

Chapter 5

Characterization of the Electronic and Geometric Structure of Non-Heme Iron Active Sites Using Fe K-Edge XAS

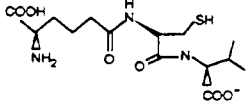
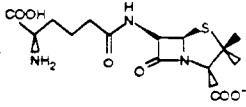
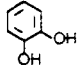
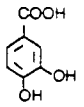
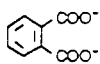
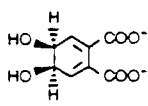
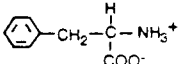
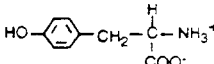
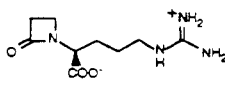
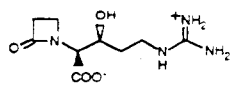
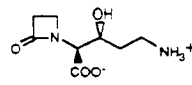
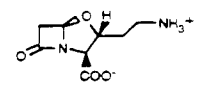
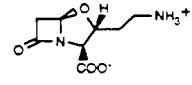
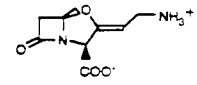
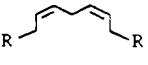
5.1. Mononuclear Non-Heme Iron Enzymes

5.1.1. Mechanistic and Structural Background

Mononuclear non-heme iron active sites are present in a variety of enzymes involved in a wide range of important biological functions requiring dioxygen. These non-heme iron enzymes include superoxide dismutases, oxidases, extra- and intradiol dioxygenases, *cis*-hydroxylases, pterin- and α -ketoglutarate-dependent hydroxylases, lipoxygenases, and bleomycin. Several recent reviews of non-heme iron enzymes have appeared in the literature.¹⁻⁴ Both the ferric and ferrous oxidation states have been determined to be involved in catalysis for different enzymes in this class with the iron usually coordinated to four, five, or six oxygen or nitrogen ligands. For several enzymes, substrate and oxygen bound intermediates are reasonably stable. Furthermore, nitric oxide derivatives of the ferrous sites have been reported for many of these enzymes which serve as reversible analogues of possible dioxygen intermediates. Representative enzymes and the reaction they catalyze are given in Table 5.1. More detailed mechanistic and structural information for these enzymes is presented below.

Iron superoxide dismutase (FeSOD) catalyzes the dismutation of superoxide anions to peroxide and molecular oxygen in procaryotes.^{5,6} The determination of the three-dimensional crystal structure of FeSOD from *E. coli* has given the first insight into the coordination chemistry of this class of enzymes and has underlined its similarity to the bacterial manganese-dependent enzymes catalyzing the same reaction.^{5,7,8} Fe(III)SOD has a distorted trigonal bipyramidal structure with four endogenous protein ligands (His-26, His-73, Asn-156, and His-160). His-26 coordinates axially with the other three ligands forming the trigonal plane.^{5,7,8} There is some controversy regarding the possible coordination of solvent in the axial fifth position. Stoddard *et al.*⁷ propose that the fifth site is devoid of a bound water molecule or an anion and place the metal at 0.5 Å out of the plane of the trigonal ligands towards the axial histidine. Stallings *et al.*⁵ position the metal ion in the plane of the trigonal ligands and find that the solvent (hydroxide) occupies the fifth, axial coordination position on the Fe³⁺. There is little structural change upon reduction to the ferrous state; however, the uptake of one proton per electron is observed from titration experiments which is accounted for in the Stallings *et al.* structure by the bound hydroxide going to water.⁸ Magnetic circular dichroism (MCD) and Mössbauer studies indicate that a five-coordinate structure is present in the reduced state,⁵ with a more square pyramidal electronic symmetry indicated from the MCD analysis.⁹ Azide is an inhibitor of dismutase activity and binds to the ferric site

Table 5.1. Mononuclear Non-Heme Iron Enzymes.

Oxygen Reactivity	Representative Enzyme	Reaction Catalyzed	
Dismutation	superoxide dismutase	$2 \text{O}_2^- + 2 \text{H}^+$	$\xrightleftharpoons[\text{Fe(II,III)SOD}]{\text{O}_2} \text{H}_2\text{O}_2 + \text{O}_2$
Oxidation	isopenicillin N synthase		$\xrightarrow[\text{2H}_2\text{O}]{\text{O}_2, \text{Fe(II)IPNS}}$ 
Monooxygenation	ω -hydroxylase	RCH_3	$\xrightarrow[\text{Fe(II)\omega H}]{\text{O}_2} \text{RCH}_2\text{OH}$
Extradiol Dioxygenation	catechol 2,3-dioxygenase		$\xrightarrow[\text{Fe(II)2,3-CTD}]{\text{O}_2} \text{HO-CO-COOH}$
Intradiol Dioxygenation	protocatechuate 3,4-dioxygenase		$\xrightarrow[\text{Fe(III)PCD}]{\text{O}_2} \text{HO-CO-COOH}$
cis-Hydroxylation	phthalate dioxygenase		$\xrightarrow[\text{NAD}^+]{\text{O}_2, \text{NADH}, \text{Fe(II)PDO}}$ 
Pterin-Dependent Hydroxylation	phenylalanine hydroxylase		$\xrightarrow[\text{H}_2\text{O}, \text{H}_2\text{biopterin}]{\text{O}_2, \text{H}_4\text{biopterin}, \text{Fe(II)PAH}}$ 
α -Ketoglutarate-Dependent Hydroxylation & Oxidative Ring Closure	clavaminate synthase		$\xrightarrow[\text{succinate, CO}_2]{\text{O}_2, \alpha\text{-KG}, \text{Fe(II)CS2}}$ 
			$\xrightarrow[\text{succinate, CO}_2, \text{H}_2\text{O}]{\text{O}_2, \alpha\text{-KG}, \text{Fe(II)CS2}}$ 
			$\xrightarrow[\text{succinate, CO}_2, \text{H}_2\text{O}]{\text{O}_2, \alpha\text{-KG}, \text{Fe(II)CS2}}$ 
Hydroperoxidation	lipoxygenases		$\xrightarrow[\text{Fe(III)LO}]{\text{O}_2} \text{HOO-}$
DNA Cleavage	bleomycin	DNA	$\xrightarrow[\text{Fe(II)BLM}]{\text{O}_2} \text{base propenals}$

reproduced in part from reference 4

with an increase in the coordination number.⁵ Superoxide binding to the ferric center is proposed to parallel azide binding, and catalysis involves a cyclic oxidation/reduction mechanism^{5,6} which ultimately results in the dismutation process.

Isopenicillin N synthase (IPNS) is a non-heme, Fe²⁺- and oxygen-dependent enzyme found in β -lactam antibiotic-producing microorganisms.¹⁰ This enzyme catalyzes the stepwise,¹¹ desaturative cyclization of δ -(L- α -amino adipoyl)-L-cysteinyl-D-valine (LLD-ACV) to form isopenicillin N,¹² the precursor of all penicillins.¹³ This key step in the biosynthesis of penicillins and cephalosporins results in the four-electron reduction of one equivalent of dioxygen to two equivalents of water.¹⁴ The loss of four hydrogen atoms is stereospecific and the internal C-N and C-S bonds are formed with complete retention of configuration.^{15,16} Although no crystal structure of this enzyme exists, information on the active site has been gained using a variety of spectroscopic techniques including optical absorption,¹⁴ electron paramagnetic resonance (EPR),¹⁷ electron spin echo envelope modulation (ESEEM),¹³ nuclear magnetic resonance (NMR),¹⁸ Mössbauer,¹⁷ and X-ray absorption spectroscopy (XAS).¹⁹⁻²¹ The native enzyme is believed to be coordinated by four endogenous residues, three histidines and one monodentate aspartate, with water or hydroxide occupying the remaining sites in a distorted octahedral geometry. There are two conserved cysteine residues which have been shown by site directed mutagenesis studies²² to affect substrate and small molecule binding, but are not directly ligated to the iron. Three independent observations support the notion that substrate binds to the metal center through a thiolate sulfur. First, the Mössbauer isomer shift of the iron center in Fe(II)IPNS is decreased from 1.3 to 1.1 mm/s upon ACV binding.¹⁷ Second, Cu(II)IPNS develops an intense band at 390 nm upon addition of ACV, which is assigned as a thiolate-to-metal charge transfer transition.¹⁴ Lastly, EXAFS analysis of the Fe(II)IPNS-ACV and Fe(II)IPNS-ACV-NO complexes require a sulfur scatterer at about 2.3 Å.¹⁹⁻²¹ Nitric oxide also binds to the native metal center to form a complex with a characteristic $S = 3/2$ EPR signal. At this point little is known about the catalytic mechanism of this enzyme, although a high-valent iron-oxo intermediate has been proposed.^{15,23,24}

The hydroxylation of fatty acids and alkanes and the epoxidation of alkenes using molecular oxygen are catalyzed by ω -*Hydroxylase* (ω H).²⁵ ω H is one of the three components, including a flavoprotein reductase and rubredoxin, of the non-heme iron monooxygenase system from *Pseudomonas oleovorans*. This system has proven difficult to purify, therefore limiting the available mechanistic and structural information.^{26,27} Phospholipids and a stoichiometry of one atom of iron per polypeptide chain are required for full activity.²⁵ NMR has shown that the epoxidation of terminal olefins to the

corresponding 1,2-oxides proceeds with a high degree of stereoselectivity and specificity, resulting primarily in inversion of the original olefin geometry.²⁸ The stepwise mechanism does not involve complex hydrogen atom abstraction but rather initial attack of "activated" oxygen and final ring closure to the epoxide product.²⁶ At most, one cysteine sulfur may be ligated to the iron of ω H. However, iron contributes only slightly to the visible absorption spectrum which displays no charge transfer transitions. Thus ω H is proposed to have principally nitrogen and/or oxygen coordination.²⁵

The *catechol dioxygenases* serve as part of nature's strategy for degrading aromatic molecules in the environment. They are found in soil bacteria such as pseudomonads and bacilli and act in the last step of transforming aromatic precursors into aliphatic products. The catechol substrates can be oxidatively cleaved by non-heme iron dioxygenases in two distinct modes: intra- and extradiol cleavage. The intradiol cleaving enzymes have a ferric active site and act on catechol and protocatechuate, while the extradiol cleaving enzymes have a ferrous active site and act on a larger number of substrates including the two already mentioned.^{2,29} The ferrous site of extradiol cleaving enzymes is stable in the presence of dioxygen, binds substrate in a bidentate fashion, and has a third coordination position available for small molecule binding and oxygen reactivity.³⁰ The intradiol cleaving enzymes involve a ferric site with two open coordination positions for substrate binding² and are the best studied with high resolution crystal structures available for *protocatechuate 3,4-dioxygenase* (PCD) from *Pseudomonas aeruginosa*³¹ and *Brevibacterium fuscum*.³² Both active sites have a trigonal bipyramidal metal environment with Tyr-147 and His-162 coordinated axially and Tyr-118, His-160, and a hydroxide bound in the equatorial plane. The substrate is thought to bind as a chelate replacing the hydroxide and axial tyrosine.³³ Binding to the ferric site is believed to activate this substrate either by inducing semiquinone-Fe²⁺ character through high covalency,³⁴ with oxygen then reacting with either the substrate or the iron,³⁵ or by a weakening of the binding of one of the catecholate oxygens with Fe³⁺ to induce ketonization of the substrate followed by oxygen attack on the coordinated hydroxyl group.²⁹ For either model of substrate activation, the enzyme-substrate-O₂ intermediate observed in the initial phase of this reaction is thought to involve a peroxy adduct of the substrate coordinated to the iron. This converts to enzyme-substrate-O₂^{*} which is a product complex. For the extradiol dioxygenase *catechol 2,3-dioxygenase* (2,3-CTD), substrate binding activates the ferrous site for small molecule binding.³⁶ A crystal structure of an extradiol dioxygenase 2,3-dihydroxybiphenyl 1,2-dioxygenase (1,2-DBD) has just been completed³⁷ and shows that this site is square pyramidal as predicted by MCD spectroscopy on the analogous enzyme 2,3-CTD. The ligation

consists of two bound water molecules, a nitrogen from His-210, and an oxygen from a carboxylate group which form the equatorial plane, and a nitrogen from His-146 coordinated axially.

Phthalate dioxygenase (PDO) catalyzes the *cis*-hydroxylation of phthalate to 1,2-dihydroxy-4,5-dicarboxy-3,5-cyclohexadiene in the presence of phthalate dioxygenase reductase (PDR), NADH as an electron source, substrate, and oxygen. PDO is substrate specific, activating only phthalate or aromatics with vicinal anionic groups. Although PDO can oxygenate phthalate in the presence of oxygen, PDR is required for efficient catalysis.³⁸ PDO is a member of a broad class of environmentally significant bacterial dioxygenases which activate aromatic substrates to their *cis*-dihydrodiols for further degradation and catabolism. Other enzymes in this family include benzene dioxygenase,³⁹ benzoate dioxygenase,⁴⁰ naphthalene dioxygenase,⁴¹ pyrazon dioxygenase,⁴² and toluene dioxygenase,⁴³ all of which contain a [2Fe-2S] Rieske site and a mononuclear non-heme iron center. In addition to the bacterial dioxygenases, there are other enzymes which also contain a Rieske cluster in addition to a mononuclear non-heme iron site but do not yield the dihydrodiol products:⁴⁴ 4-chlorophenylacetate 3,4 dioxygenase converts substrate to catechol with chloride elimination,⁴⁵ vanillate demethylase participates in the biodegradation of lignin,⁴⁶ and 4-methoxybenzoate *O*-demethylase (putidamonooxin) catalyzes the conversion of 4-methoxybenzoic acid to 4-hydroxybenzoic acid and formaldehyde.⁴⁷ In all of these systems, the mononuclear non-heme iron is believed to be the active site for catalysis and presumably binds and activates molecular oxygen. PDO is the best studied enzyme in its class because it is available in high yield and is extremely stable even at room temperature. However, spectroscopic studies that have been performed on PDO, including resonance Raman (rR),^{48,49} electron-nuclear double resonance (ENDOR),^{50,51} and XAS^{52,53} have focused primarily on investigation of the Rieske site due to its dominant spectroscopic features. The mononuclear non-heme active site has been probed indirectly through XAS studies of Co²⁺- and Zn²⁺-substituted protein.^{52,53} From XAS Co- and Zn-edge and EXAFS studies,⁵³ the mononuclear site has been shown to have predominantly oxygen ligation with a coordination number of five or six. Oxidation of the Rieske cluster and/or binding of phthalate seem to favor a five-coordinate form of the site, while reduction of the Rieske and/or removal of phthalate appear to favor a six-coordinate form of the mononuclear site. The mononuclear iron site has also been probed directly by low temperature MCD since the Rieske site can be rendered diamagnetic (*i.e.* no temperature dependent MCD) by oxidation to the antiferromagnetically-coupled [Fe^{III}-Fe^{III}] state.⁵⁴ This data shows that the resting enzyme has a six-coordinate ferrous site, while addition

of substrate causes the active site to be five-coordinate. Azide binds to the ferrous site in the enzyme-substrate form to produce a new six-coordinate form, this indicates that substrate binding causes the ferrous site to convert from six- to five-coordinate, opening a coordination position on the iron for O₂ reactivity.

The hydroxylation of phenylalanine, tyrosine and tryptophan to tyrosine, 3,4-dihydroxyphenylalanine, and 5-hydroxytryptophan, respectively, are catalyzed by hydroxylases that depend on Fe²⁺ and tetrahydropterins.⁵⁵ *Phenylalanine hydroxylase* (PAH) is the most well-studied of these enzymes. PAH is found in the liver and kidney and its deficiency is responsible for the genetic disorder phenylketonuria that is associated with severe mental retardation.⁵⁶ It has been thought that the role of the metal ion is to generate a 4a-hydroperoxy intermediate and activate it through forming a μ -peroxy pterin-iron containing complex which could further generate a non-heme oxo-ferryl intermediate and the experimentally observed 4a-hydroxypterin species.⁵⁷ In support of this, PAH from *Chromobacterium violaceum* (CVPAH), thought to be a copper enzyme, showed an ESEEM spectrum of a pterin directly coordinated to the metal ion⁵⁸ and crystallographic studies on Cu-pterin model complexes indicate that the pterin cofactor binds to the metal center through positions O4 and N5.⁵⁹ Further, paramagnetic NMR studies on Co²⁺-substituted tyrosine hydroxylase show that phenylalanine, which is also a substrate for this enzyme, binds such that the aromatic ring is in the "second coordination sphere" of the metal ion.⁶⁰ Recent studies of CVPAH⁶¹ have questioned whether the copper ion is in fact required for activity and thus whether the iron in mammalian PAHs (which is strictly required for activity) plays a direct oxygen activation role or an indirect structural role in catalysis. As reduction of the Fe²⁺ state is required for catalysis, it is critically important to probe the interaction of pterin cofactor with this reduced iron site. However, all studies thus far reported have been on the EPR-active resting ferric site. These studies^{62,63} have shown that both active (axial) and inactive (rhombic) iron sites are present which do not interconvert and have a relative ratio dependent on the preparative conditions.⁶⁴

Bacterial resistance to penicillin antibiotics is largely due to the hydrolytic activity of the β -lactamase enzymes. *Clavamate synthase* (CS) catalyzes the key biosynthetic ring closure step in the formation of clavulanic acid, a potent β -lactamase inhibitor.⁶⁵ CS is a member of a large class of non-heme iron enzymes dependent on α -ketoglutarate (α -KG) as a cofactor. This class also includes prolyl and lysyl hydroxylases (involved in collagen synthesis),⁶⁶ thymine hydroxylase,⁶⁷ and 4-hydroxyphenylpyruvate dioxygenase,⁶⁸ all of which catalyze the hydroxylation of substrate. In contrast, CS catalyzes oxidative ring closure similar to the reaction catalyzed by IPNS,²³ which is not

an α -KG-dependent enzyme. CS is a particularly interesting enzyme in that, depending on substrate, this enzyme can also catalyze hydroxylation⁶⁹ as well as ring closure and desaturation chemistry.^{65,70} The mechanism of α -KG-dependent enzymes generally involves the reaction of an α -KG-bound ferrous active site with dioxygen. Model studies⁷¹ have shown that an α -KG analog binds to the ferrous site in a bidentate fashion through one carboxylate oxygen and one carbonyl oxygen. The enzymatic reaction generates succinate, CO₂, and an activated iron-oxygen species, thought to be an oxo-ferryl unit⁷² which goes on to hydroxylate substrate or catalyze oxidative ring closure through the heteroatom.

The *lipxygenases* (LOs) catalyze the hydroperoxidation of *cis,cis*-1,4-pentadiene-containing fatty acids. Mammalian LOs catalyze the conversion of arachidonic acid to leukotrienes (5-LOs), which mediate hypersensitivity and inflammation, and lipoxins (15-LOs), which inhibit cellular immunity.⁷³ 15-LOs are also implicated in the oxidation of low density lipoprotein to the atherogenic form which leads to the growth of atherosclerotic lesions.⁷⁴ Most mechanistic studies have been performed on the plant enzyme from soybeans (SLO-1) which has linoleic acid as a substrate. The resting enzyme is air-stable in its ferrous oxidation state, but is activated by reaction with the hydroperoxide product to produce the ferric site.⁷⁵ The fatty acid substrate reacts with this ferric site to produce an intermediate, which then oxygenates to generate the hydroperoxide. The substrate-active site intermediate has been proposed to be either an organometallic complex formed by proton abstraction and coordination of the carbanion substrate to the ferric center⁷⁶ or a ferrous center with a fatty acid radical, which may not be directly coordinated to the iron.^{77,78} It has been of significant pharmacological importance to develop inhibitors of the lipxygenases which are mostly found to be reversible and function by reducing the active ferric center to the ferrous state.⁷⁹ Spectroscopic studies have generally indicated that the ferrous site is six-coordinate with at least three histidine ligands.^{9,80,81} Recently, two crystal structures have appeared^{82,83} on the resting enzyme which disagree with respect to the active site ligation. Four amino acid ligands are common to both structures: His-499(N ϵ), His-504(N ϵ), His-609 (N ϵ), and Ile-389 (OT2). The Boyington *et al.* crystallographic description⁸² of the iron site is four coordinate with a ligand arrangement described as "distorted octahedral with two adjacent unoccupied positions". Alternatively, the Minor *et al.* structure⁸³ has an additional residue as a ligand, Asn-694 (O δ 1), and further possibility of a sixth water based ligand as has been proposed from EPR line-broadening studies on the ferric enzyme.⁸⁴

Bleomycin (BLM), a histidine-containing glycopeptide antibiotic produced by strains of *Streptomyces verticillus*, is used in treatment against a variety of carcinomas and lymphomas.⁸⁵ The anticancer activity of the drug Bleomycin involves selective DNA cleavage at certain GT and GC sites in the presence of metal ions and dioxygen.⁸⁶⁻⁸⁸ The structure of BLM contains three domains: the bithiazole tail which is involved in BLM binding to DNA, the sugar moiety which is believed to be responsible for uptake by cancer cells, and the β -aminoalanine-pyrimidine-histidine region which binds metal ions. BLM is generally thought to be most reactive as a ferrous complex with histidine, deprotonated amide, pyrimidine, and secondary amine nitrogens as equatorial ligands.^{86,87} No crystal structure exists of the ferrous complex and present descriptions are based on correlations to a Cu(II) complex of the related biosynthetic precursor P-3A, which has a square-pyramidal geometry.⁸⁹ However, Cu²⁺ has strong structural preferences due to the Jahn-Teller effect which Fe²⁺ does not, and P-3A lacks the disaccharide and bithiazole moieties of BLM, the former being a potential ligand. Thus, there is some controversy with respect to axial ligation where both the carbamoyl group of the mannose sugar⁹⁰ and the primary amine from the β -aminoalanine⁹¹ have been implicated, with the sixth position being the site of exogenous ligand binding. BLM binds to DNA *via* intercalation and/or ionic interactions with the minor groove, with both the bithiazole tail and the metal chelating regions playing a significant role in the binding and specificity.⁹²⁻⁹⁴ Kinetic and spectral studies^{95,96} have demonstrated that the mechanism of activation involves a high-spin Fe(II)BLM species reacting with dioxygen to form oxygenated BLM, described as a ferric-superoxide complex. This in turn acquires an additional electron either from a second Fe(II)BLM molecule or another reductant to generate activated BLM. Activated BLM reacts with DNA by hydrogen atom abstraction from the C-4' position of the deoxyribose sugar, leading to DNA degradation concomitant with base propenal formation.⁸⁶

XAS edge and EXAFS analysis can be used to obtain information on the electronic and geometric structure of the iron active sites in the above mentioned enzymes. A detailed analysis of the intensity and splitting of the pre-edge features allows one to obtain the oxidation state, spin state, and coordination geometry of the iron active site (as described in Chapter 4). EXAFS analysis provides accurate first shell distances with information on the number and type of coordinating atoms. Not only can these types of analyses be performed on the resting enzymes, but stable substrate and oxygen bound intermediates can also be studied including the nitric oxide derivatives of the ferrous active sites which serve as reversible analogues of possible dioxygen intermediates. Mechanistic information can be gained by studying the various forms of

the enzymes and comparing them to the resting enzyme. In the following sections XAS has been used to characterize the iron site in specific enzymes. In section 5.2, edge structure analysis has been used to determine the oxidation state of the iron in {FeNO}⁷ systems. The ferrous active sites of BLM and a related model complex were characterized by both Fe K-edge and EXAFS analyses as described in section 5.3. Then, XAS was used to determine the oxidation, spin state and coordination geometry of activated BLM as shown in section 5.4. The iron active sites of both mammalian and soybean lipoxygenases were characterized utilizing XAS and the results are presented in section 5.5. An Fe K-edge and EXAFS study of phenylalanine hydroxylase is described in section 5.6. Finally, the ferrous, ferric, substrate-bound and NO-bound forms of protocatechuate 3,4-dioxygenase were studied and the results are presented in section 5.7.

5.1.2. References

- (1) Solomon, E. I.; Zhang, Y. *Acc. Chem. Res.* **1992**, *25*, 343.
- (2) Que, L., Jr. In *Bioinorganic Catalysis*; Reedijk, J., Ed.; Marcel Dekker, Inc.: New York, 1993; p 347.
- (3) Feig, A. L.; Lippard, S. J. *Chem. Rev.* **1994**, *94*, 759.
- (4) Solomon, E. I.; Pavel, E. G.; Loeb, K. E.; Campochiaro, C. *Coord. Chem. Rev.* **1995**, in press.
- (5) Stallings, W. C.; Bull, C.; Fee, J. A.; Lah, M. S.; Ludwig, M. L. In *Molecular Biology of Free Radical Scavenging Systems*; Scandolios, J. G., Ed.; Cold Spring Harbor Laboratory Press: New York, 1992; p 193.
- (6) Stalling, W.; Bull, C.; Pattridge, K. A.; Powers, T. B.; Fee, J. A.; Ludwig, M. L.; Ringe, D.; Petsko, G. A. In *Oxygen Radicals in Chemistry and Biology*; Bors, W.; Saran, M.; Tait, D., Eds.; Walter de Gruyter & Co.: Berlin, 1984; p 779.
- (7) Stoddard, B. L.; Howell, P. L.; Ringe, D.; Petsko, G. A. *Biochemistry* **1990**, *29*, 8885.
- (8) Stallings, W. C.; Metzger, A. L.; Pattridge, K. A.; Fee, J. A.; Ludwig, M. L. *Free Rad. Res. Comms.* **1991**, *12-13*, 259.
- (9) Whittaker, J. W.; Solomon, E. I. *J. Am. Chem. Soc.* **1988**, *110*, 5329.
- (10) Baldwin, J. E.; Blackburn, J. M.; Sutherland, J. D.; Wright, M. C. *Tetrahedron* **1991**, *47*, 5991.
- (11) Baldwin, J. E.; Lynch, G. P.; Schofield, C. J. *J. Chem. Soc., Chem. Commun.* **1991**, 736.

- (12) Baldwin, J. E.; Bradley, M.; Adlington, R. M.; Norris, W. J.; Turner, N. J. *Tetrahedron* **1991**, *47*, 457.
- (13) Jiang, F.; Peisach, J.; Ming, L.-J.; Que, L., Jr.; Chen, V. J. *Biochemistry* **1991**, *30*, 11437.
- (14) Ming, L.-J.; Que, L., Jr.; Kriauciunas, A.; Frolik, C. A.; Chen, V. J. *Inorg. Chem.* **1990**, *29*, 1111.
- (15) Baldwin, J. E.; Adlington, R. M.; Bradley, M.; Norris, W. J.; Turner, N. J.; Yoshida, A. *J. Chem. Soc., Chem. Commun.* **1988**, 1125.
- (16) Baldwin, J. E.; Adlington, R. M.; Marquess, D. G.; Pitt, A. R.; Russell, A. T. *J. Chem. Soc., Chem. Commun.* **1991**, 856.
- (17) Chen, V. J.; Orville, A. M.; Harpel, M. R.; Frolik, C. A.; Surerus, K. K.; Münck, E.; Lipscomb, J. D. *J. Biol. Chem.* **1989**, *264*, 21677.
- (18) Ming, L.-J.; Que, L., Jr.; Kriauciunas, A.; Frolik, C. A.; Chen, V. J. *Biochemistry* **1991**, *30*, 11653.
- (19) Fujishima, Y.; Schofield, C. J.; Baldwin, J. E.; Charnock, J. M.; Garner, C. D. *J. Inorg. Biochem.* **1991**, *43*, 564.
- (20) Scott, R. A.; Wang, S.; Eidsness, M. K.; Kriauciunas, A.; Frolik, C. A.; Chen, V. J. *Biochemistry* **1992**, *31*, 4596.
- (21) Randall, C. R.; Zang, Y.; True, A. E.; Que, L., Jr.; Charnock, J. M.; Garner, C. D.; Fujishima, Y.; Schofield, C. J.; Baldwin, J. E. *Biochemistry* **1993**, *32*, 6664.
- (22) Orville, A. M.; Chen, V. J.; Kriauciunas, A.; Harpel, M. R.; Fox, B. G.; Münck, E.; Lipscomb, J. D. *Biochemistry* **1992**, *31*, 4602.
- (23) Baldwin, J. E.; Bradley, M. *Chem. Rev.* **1990**, *90*, 1079.
- (24) Baldwin, J. E.; Lynch, G. P.; Schofield, C. J. *Tetrahedron* **1992**, *48*, 9085.
- (25) Ruettinger, R. T.; Griffith, G. R.; Coon, M. J. *Arch. Biochem. Biophys.* **1977**, *183*, 528.
- (26) Katopodis, A. G.; Wimalasena, K.; Lee, J.; May, S. W. *J. Am. Chem. Soc.* **1984**, *106*, 7928.
- (27) McKenna, E. J.; Coon, M. J. *J. Biol. Chem.* **1970**, *245*, 3882.
- (28) May, S. W.; Gordon, S. L.; Steltenkamp, M. S. *J. Am. Chem. Soc.* **1977**, *99*, 2017.
- (29) Lipscomb, J. D.; Orville, A. M. In *Metals in Biological Systems*; Sigel, H.; Sigel, A., Eds.; Marcel Dekker Inc.: New York, 1992; Vol. 28; p 243.
- (30) Arciero, D. M.; Orville, A. M.; Lipscomb, J. D. *J. Biol. Chem.* **1985**, *260*, 14035.
- (31) Ohlendorf, D. H.; Lipscomb, J. D.; Weber, P. C. *Nature* **1988**, *336*, 403.
- (32) Earhart, C. A.; Radhakrishnan, R.; Orville, A. M.; Lipscomb, J. D.; Ohlendorf, D. H. *J. Mol. Biol.* **1994**, *236*, 374.

- (33) Lipscomb, J. D. personal communication, 1994.
- (34) Jang, H. G.; Cox, D. D.; Que, L., Jr. *J. Am. Chem. Soc.* **1991**, *113*, 9200.
- (35) Funabiki, T.; Konishi, T.; Kobayashi, S.; Mizoguchi, A.; Takano, M.; Yoshida, S. *Chem. Lett.* **1987**, 719.
- (36) Mabrouk, P. A.; Orville, A. M.; Lipscomb, J. D.; Solomon, E. I. *J. Am. Chem. Soc.* **1991**, *113*, 4053.
- (37) Han, S.; Eltis, L.; Bolin, J. personal communication, 1994.
- (38) Shiman, R. In *Folates and Pterins: Chemistry and Biochemistry of Pterins*; Blakley, R. L.; Benkovic, S. J., Eds.; John Wiley and Sons: New York, 1985; Vol. 2; p 179.
- (39) Crutcher, S. E.; Geary, P. J. *Biochem. J.* **1979**, *177*, 393.
- (40) Yamaguchi, M.; Fujisawa, H. *J. Biol. Chem.* **1980**, *255*, 5058.
- (41) Ensley, B. D.; Gibson, D. T. *J. Bacteriol.* **1983**, *155*, 505.
- (42) Sauber, K.; Fröhner, C.; Rosenberg, G.; Eberspächer, J.; Lingens, F. *Eur. J. Biochem.* **1977**, *74*, 89.
- (43) Gibson, D. T.; Yeh, W.-K.; Liu, T.-N.; Subramanian, V. In *Oxygenases and Oxygen Metabolism*; Nozaki, M.; Yamamoto, S.; Ishimura, Y.; Coon, M. J.; Ernster, L.; Estabrook, R. W., Eds.; Academic Press: New York, 1982; p 51.
- (44) Batie, C. J.; Ballou, D. P.; Correll, C. C. *Chem. Biochem. Flavoenzymes* **1992**, *3*, 543.
- (45) Markus, A.; Krekel, D.; Lingens, F. *J. Biol. Chem.* **1986**, *261*, 12883.
- (46) Brunel, F.; Davison, J. *J. Bacteriol.* **1988**, *170*, 4924.
- (47) Bernhardt, F.-H.; Heymann, E.; Traylor, P. S. *Eur. J. Biochem.* **1978**, *92*, 209.
- (48) Kuila, D.; Fee, J. A.; Schoonover, J. R.; Woodruff, W. H.; Batie, C. J.; Ballou, D. P. *J. Am. Chem. Soc.* **1987**, *109*, 1559.
- (49) Kuila, D.; Schoonover, J. R.; Dyer, R. B.; Batie, C. J.; Ballou, D. P.; Fee, J. A.; Woodruff, W. H. *Biochim. Biophys. Acta* **1992**, *1140*, 175.
- (50) Gurbiel, R. J.; Batie, C. J.; Sivaraja, M.; True, A. E.; Fee, J. A.; Hoffman, B. M.; Ballou, D. P. *Biochemistry* **1989**, *28*, 4861.
- (51) Cline, J. F.; Hoffman, B. M.; Mims, W. B.; LaHaie, E.; Ballou, D. P.; Fee, J. A. *J. Biol. Chem.* **1985**, *260*, 3251.
- (52) Tsang, H.-T.; Batie, C. J.; Ballou, D. P.; Penner-Hahn, J. E. *Biochemistry* **1989**, *28*, 7233.
- (53) Penner-Hahn, J. E. *Basic Life Sci.*, **1988**, *51* (*Synchr. Radiat. in Struct. Biology*), 177.

- (54) Pavel, E. G.; Martins, L. J.; Ellis, W. R., Jr.; Solomon, E. I. *Chemistry & Biology* **1994**, *1*, 173.
- (55) Dix, T. A.; Benkovic, S. J. *Acc. Chem. Res.* **1988**, *21*, 101.
- (56) Kaufman, S. In *Advances in Neurochemistry*; Agranoff, B. W.; Aprison, M. H., Eds.; Plenum Press: New York, 1976; Vol. 2; p 1.
- (57) Dix, T. A.; Bollag, G. E.; Domanico, P. L.; Benkovic, S. J. *Biochemistry* **1985**, *24*, 2955.
- (58) McCracken, J.; Pember, S.; Benkovic, S. J.; Villafranca, J. J.; Miller, R. J.; Peisach, J. *J. Am. Chem. Soc.* **1988**, *110*, 1069.
- (59) Perkinson, J.; Brodie, S.; Yoon, K.; Mosny, K.; Carroll, P. J.; Morgan, T. V.; Burgmayer, S. J. N. *Inorg. Chem.* **1991**, *30*, 719.
- (60) Martínez, A.; Abeygunawardana, C.; Haavik, J.; Flatmark, T.; Mildvan, A. S. *Biochemistry* **1993**, *32*, 6381.
- (61) Carr, R. T.; Benkovic, S. J. *Biochemistry* **1993**, *32*, 14132.
- (62) Bloom, L. M.; Benkovic, S. J.; Gaffney, B. J. *Biochemistry* **1986**, *25*, 4204.
- (63) Wallick, D. E.; Bloom, L. M.; Gaffney, B. J.; Benkovic, S. J. *Biochemistry* **1984**, *23*, 1295.
- (64) Caradonna, J. P. personal communication, 1994.
- (65) Salowe, S. P.; Marsh, E. N.; Townsend, C. A. *Biochemistry* **1990**, *29*, 6499.
- (66) Kivirikko, K. I.; Myllylä, R. In *The Enzymology of Post-Translational Modifications of Proteins*; Freedman, R. B.; Hawkins, H. C., Eds.; Academic Press: London, 1980; Vol. 1; p 53.
- (67) Thornburg, L. D.; Lai, M.-T.; Wishnok, J. S.; Stubbe, J. *Biochemistry* **1993**, *32*, 14023.
- (68) Lindstedt, S.; Odelhög, B.; Rundgren, M. *Biochemistry* **1977**, *16*, 3369.
- (69) Baldwin, J. E.; Lloyd, M. D.; Wha-Son, B.; Schofield, C. J.; Elson, S. W.; Baggaley, K. H.; Nicholson, N. H. *J. Chem. Soc., Chem. Commun.* **1993**, 500.
- (70) Salowe, S. P.; Krol, W. J.; Iwata-Reuyl, D.; Townsend, C. A. *Biochemistry* **1991**, *30*, 2281.
- (71) Chiou, Y.-M.; Que, L., Jr. *J. Am. Chem. Soc.* **1992**, *114*, 7567.
- (72) Siegel, B. *Bioorg. Chem.* **1979**, *8*, 219.
- (73) Samuelsson, B.; Dahlén, S.-E.; Lindgren, J. Å.; Rouzer, C. A.; Serhan, C. N. *Science* **1987**, *237*, 1171.
- (74) Kühn, H.; Barnett, J.; Grunberger, D.; Baeker, P.; Chow, J.; Nguyen, B.; Bursztyn-Pettegrew, H.; Chan, H.; Sigal, E. *Biochim. Biophys. Acta* **1993**, *1169*, 80.

- (75) Feiters, M. C.; Aasa, R.; Malmström, B. G.; Slappendel, S.; Veldink, G. A.; Vliegthart, J. F. G. *Biochim. Biophys. Acta* **1985**, *831*, 302.
- (76) Corey, J.; Nagata, R. *J. Am. Chem. Soc.* **1987**, *109*, 8107.
- (77) Veldink, G. A.; Vliegthart, J. F. G. *Adv. Inorg. Biochem.* **1984**, *6*, 139.
- (78) Nelson, M. J.; Cowling, R. A.; Seitz, S. P. *Biochemistry* **1994**, *33*, 4966.
- (79) Nelson, M. J.; Batt, D. G.; Thompson, J. S.; Wright, S. W. *J. Biol. Chem.* **1991**, *266*, 8225.
- (80) Dunham, W. R.; Carroll, R. T.; Thompson, J. F.; Sands, R. H.; Funk, M. O., Jr. *Eur. J. Biochem.* **1990**, *190*, 611.
- (81) Van der Heijdt, L. M.; Feiters, M. C.; Navaratnam, S.; Nolting, H.-F.; Hermes, C.; Veldink, G. A.; Vliegthart, J. F. G. *Eur. J. Biochem.* **1992**, *207*, 793.
- (82) Boyington, J. C.; Gaffney, B. J.; Amzel, L. M. *Science* **1993**, *260*, 1482.
- (83) Minor, W.; Steczko, J.; Bolin, J. T.; Otwinowski, Z.; Axelrod, B. *Biochemistry* **1993**, *32*, 6320.
- (84) Nelson, M. J. *J. Am. Chem. Soc.* **1988**, *110*, 2985.
- (85) *Bleomycins: Current Status and New Developments*; Carter, S. K.; Crooke, S. T.; Umezawa, H., Eds.; Academic Press, Inc.: New York, 1978.
- (86) Stubbe, J.; Kozarich, J. W. *Chem. Rev.* **1987**, *87*, 1107.
- (87) Petering, D. H.; Byrnes, R. W.; Antholine, W. E. *Chem.-Biol. Interactions* **1990**, *73*, 133.
- (88) Dabrowiak, J. C. In *Metal Ions in Biological Systems*; Sigel, H., Ed.; Marcel Dekker, Inc.: New York, 1980; Vol. 11; p 305.
- (89) Iitaka, Y.; Nakamura, H.; Nakatani, T.; Muraoka, Y.; Fujii, A.; Takita, T.; Umezawa, H. *J. Antibiot.* **1978**, *31*, 1070.
- (90) Akkerman, M. A. J.; Neijman, E. W. J. F.; Wijmenga, S. S.; Hilbers, C. W.; Bermel, W. *J. Am. Chem. Soc.* **1990**, *112*, 7462.
- (91) Sugiura, Y. *J. Am. Chem. Soc.* **1980**, *102*, 5208.
- (92) Hamamichi, N.; Natrajan, A.; Hecht, S. M. *J. Am. Chem. Soc.* **1992**, *114*, 6278.
- (93) Sakai, T. T.; Riordan, J. M.; Glickson, J. D. *Biochim. Biophys. Acta* **1983**, *758*, 176.
- (94) Povirk, L. F.; Hogan, M.; Dattagupta, N. *Biochemistry* **1979**, *18*, 96.
- (95) Burger, R. M.; Peisach, J.; Horwitz, S. B. *J. Biol. Chem.* **1981**, *256*, 11636.
- (96) Burger, R. M.; Horwitz, S. B.; Peisach, J.; Wittenberg, J. B. *J. Biol. Chem.* **1979**, *254*, 12299.

5.2. {FeNO}⁷ Complexes

5.2.1. Introduction

As described in the previous section, mononuclear non-heme iron centers are present in the catalytic cycle of a number of proteins involved in oxygen activation.^{1,2} In order to understand the reactivity of these systems it is necessary to have a detailed description of the electronic as well as geometric structure of the non-heme iron active site.³ Since most of these systems are involved in oxygen activation, identification of oxygen intermediates during the catalytic cycle is necessary to obtain insight into reactivity at the molecular level. These intermediates, however, are often very short-lived and difficult to study experimentally.

As a probe of non-heme iron active sites, nitric oxide has been shown to react with the ferrous state of many mononuclear non-heme iron enzymes, *e.g.* soybean lipoxygenase,^{4,5} protocatechuate 4,5-dioxygenase,⁶ metapyrocatechase,⁷ putidamonooxin,⁸ and isopenicillin N synthase,⁹ to form stable nitrosyl complexes which can serve as reversible analogs of the possible dioxygen intermediates involved in catalysis. These non-heme iron enzyme nitrosyl derivatives have a distinctive S=3/2 ground state. This distinctive S=3/2 electron paramagnetic resonance (EPR) signal allows one to probe non-heme ferrous complexes which are normally EPR silent. For intra- and extradiol dioxygenases Fe-NO EPR has been used as an analytical probe of substrate and water coordination through superhyperfine effects on the spectrum.^{6,7} Mössbauer spectroscopy has also proved to be a very useful analytical probe,^{10,11} but conflicting descriptions of the electronic origin of the S=3/2 ground state have been suggested. The Mössbauer isomer shift for the NO complex of protocatechuate 4,5-dioxygenase has been used to argue against a ferric configuration,¹² while the equivalent isomer shift for the substrate-NO ternary complex of putidamonooxin has been used to support its description as an intermediate spin ferric site.⁸

The description of metal nitrosyl complexes is a problem of both theoretical and experimental interest. An early classic review by Enemark and Feltham gives a basic description of metal-nitrosyl complexes and their bonding.¹³ In the Enemark/Feltham notation, the metal nitrosyl unit is described as a discrete unit, *i.e.* {MNO}ⁿ, where n represents the sum of the metal d and NO π* electrons.¹³ The Fe-NO species generated in non-heme ferrous enzymes is thus designated {FeNO}⁷. A variety of descriptions of the electronic structure of these complexes have been put forth in the literature. These include: [Fe^{d7}(S=3/2) - NO^{+(S=0)}],¹⁴ [Fe²⁺d⁶(S=2) - NO⁰(S=1/2)]

antiferromagnetically coupled,¹⁵ $[\text{Fe}^{3+}d^5(S=1/2) - \text{NO}^-(S=1)]$ ferromagnetically coupled,¹⁶ and $[\text{Fe}^{3+}d^5(S=3/2) - \text{NO}^-(S=0)]$.¹¹ None of these descriptions, however, are consistent with all of the experimental and theoretical data that exist.

In this study, the XAS edge spectra of three $S=3/2$ $\{\text{FeNO}\}^7$ model complexes, FeEDTA-NO, Fe(salen)NO and $[\text{Fe}(\text{TMC})\text{NO}](\text{BF}_4)_2$,¹⁷ were compared to spectra of ferrous and ferric complexes with similar ligation to elucidate the oxidation state of the iron in the $\{\text{FeNO}\}^7$ systems. In addition, an analysis of the intensity of the pre-edge features provided information on the distortion of the iron site. The results of this XAS study were combined with results from absorption (abs), variable-temperature, variable-field magnetic circular dichroism (MCD), resonance Raman (rR), EPR, and magnetism measurements (performed by Yan Zhang and Mark Pavlosky) and self consistent field- $X\alpha$ -scattered wave (SCF- $X\alpha$ -SW) theoretical calculations (performed by Carl Brown) to develop a detailed description of the distinctive $S=3/2$ $\{\text{FeNO}\}^7$ site.^{18,19} These studies indicate that the iron is best described as high spin ferric ($S=5/2$) and the NO as NO^- ($S=1$) which are spin coupled antiferromagnetically to produce the correct total spin state of $S=3/2$.

5.2.2. Experimental Section

The X-ray absorption spectra were recorded at the Stanford Synchrotron Radiation Laboratory on unfocused beamline 7-3 during dedicated conditions (3 GeV, 25-95 mA). The radiation was monochromatized using a Si(220) double crystal monochromator detuned 50% at 7474 eV to minimize harmonic contamination. An Oxford Instruments continuous-flow liquid helium CF1208 cryostat was used to maintain a constant temperature. Data were measured to $k=9.5 \text{ \AA}^{-1}$ with 1 mm high pre-monochromator beam defining slits. Energies were calibrated using an internal Fe foil standard, assigning the first inflection point to 7111.2 eV.²⁰ The spectrometer energy resolution was approximately 1.4 eV²¹ with reproducibility of edge position determination of < 0.2 eV.

$[\text{Fe}(\text{TMC})\text{NO}](\text{BF}_4)_2$,²² $[\text{Fe}(\text{TMC})\text{N}_3](\text{BF}_4)_2$,²³ Fe(salen)NO²⁴ and Fe(salen)Cl²⁵ were prepared as described in the literature. With the exception of Fe(salen)Cl, all samples were prepared in an inert atmosphere, *i.e.* in an anaerobic wet or dry box or on a Schlenk line and handled in a nitrogen-filled inert atmosphere dry glove box during the following sample preparation. $[\text{Fe}(\text{TMC})\text{NO}](\text{BF}_4)_2$, $[\text{Fe}(\text{TMC})\text{N}_3](\text{BF}_4)_2$, Fe(salen)NO and Fe(salen)Cl crystalline samples were mixed with BN and ground into a fine powder. The BN/sample mixture was pressed into a 1 mm thick Al spacer that was sealed with

63.5 μm Mylar tape windows and frozen in liquid nitrogen. Data were measured in transmission mode with N_2 -filled ionization chambers. Data were measured at 10 K for $\text{Fe}(\text{salen})\text{Cl}$, at room temperature for $[\text{Fe}(\text{TMC})\text{N}_3](\text{BF}_4)$ and at 220 K for the $S=3/2$ forms of $\text{Fe}(\text{salen})\text{NO}$ and $[\text{Fe}(\text{TMC})\text{NO}](\text{BF}_4)_2$.

$[\text{Fe}(\text{OH}_2)\text{EDTA}]^{2-}$ solution, 50 mM in Fe, was prepared by anaerobic addition of ferrous ammonium sulfate to a 60 mM solution of Na_2EDTA in $\text{pH} = 6.5$, 0.1 M deoxygenated phosphate buffer. Oxidizing this solution produced $[\text{Fe}(\text{OH}_2)\text{EDTA}]^-$. An FeEDTA-NO solution was prepared by purging an $[\text{Fe}(\text{OH}_2)\text{EDTA}]^{2-}$ solution with NO gas under anaerobic conditions for approximately 20 minutes, or until the solution stopped changing color, indicating completion of the reaction. To form an ice crystal-free glass, solution samples were prepared by adding 50% (by volume) glycerol resulting in samples which were 25 mM in Fe. $[\text{Fe}(\text{OH}_2)\text{EDTA}]^{2-}$, $[\text{Fe}(\text{OH}_2)\text{EDTA}]^-$ and FeEDTA-NO solution samples were loaded into 140 μL Lucite EXAFS cells ($23 \times 2 \times 3$ mm) with 37 μm Kapton windows and frozen in liquid nitrogen. Data were collected in fluorescence mode at 10 K. The fluorescence signal was collected by an Ar-filled ionization chamber,^{26,27} equipped with Soller slits and a Mn filter.

Five to nine scans were averaged for each EDTA solution while two scans were averaged for each powder sample. A smooth pre-edge background was removed from the averaged spectra by fitting a first or second order polynomial to the pre-edge region and subtracting this polynomial from the entire spectrum. A one-segment spline of order one was fit to the EXAFS region and the data normalized to an edge jump of one at 7130 eV. The intensities and energies of pre-edge features were quantitated by fits to the data. The fitting program EDG_FIT, which utilizes the double precision version of the public domain MINPAK fitting library²⁸ was used. EDG_FIT was written by Dr. Graham N. George of the Stanford Synchrotron Radiation Laboratory. All spectra were fit over the range 7108-7118 eV. Pre-edge features were modeled by pseudo-Voigt line shapes (simple sums of Lorentzian and Gaussian functions).^{21,27,29,30} A fixed 50:50 ratio of Lorentzian to Gaussian contribution for the pre-edge feature successfully reproduced these spectral features. The value reported for the area of a fitted feature was calculated by multiplying the height of the feature by the full-width-at-half-maximum (FWHM).

5.2.3. Results and Analysis

To determine the oxidation state of the iron in $\{\text{FeNO}\}^7$ systems the Fe K edge X-ray absorption spectra of $S=3/2$ $\{\text{FeNO}\}^7$ complexes were compared to the spectra of ferrous and ferric complexes with similar ligation. XAS edge data were collected on

three $S=3/2$ $\{\text{FeNO}\}^7$ complexes: FeEDTA-NO , $[\text{Fe}(\text{TMC})\text{NO}](\text{BF}_4)_2$, and $\text{Fe}(\text{salen})\text{NO}$. The FeEDTA-NO spectrum was compared with spectra of ferrous and ferric complexes of EDTA, $[\text{Fe}(\text{OH}_2)\text{EDTA}]^{2-}$ and $[\text{Fe}(\text{OH}_2)\text{EDTA}]^-$. $[\text{Fe}(\text{TMC})\text{NO}](\text{BF}_4)_2$ data were compared to those for the ferrous complex $[\text{Fe}(\text{TMC})\text{N}_3](\text{BF}_4)$, and $\text{Fe}(\text{salen})\text{NO}$ data to those for the ferric complex $\text{Fe}(\text{salen})\text{Cl}$. The XAS edge spectra are shown in Figure 5.1 for $[\text{Fe}(\text{OH}_2)\text{EDTA}]^{2-}$, $[\text{Fe}(\text{OH}_2)\text{EDTA}]^-$ and FeEDTA-NO , in Figure 5.2 for $[\text{Fe}(\text{TMC})\text{NO}](\text{BF}_4)_2$ and $[\text{Fe}(\text{TMC})\text{N}_3](\text{BF}_4)$, and in Figure 5.3 for $\text{Fe}(\text{salen})\text{NO}$ and $\text{Fe}(\text{salen})\text{Cl}$. The lowest energy transitions are the weak $1s \rightarrow 3d$ pre-edge peaks at approximately 7112 eV followed by the $1s \rightarrow 4p$ transition at approximately 7123 eV. The $1s \rightarrow 3d$ pre-edge region has been expanded and is shown as insets in Figures 5.1, 5.2 and 5.3. The energies and areas of the pre-edge features were determined by fits to the data and are presented in Table 5.2. The spectrum of $[\text{Fe}(\text{OH}_2)\text{EDTA}]^{2-}$ has two low intensity pre-edge peaks that are split by ~ 2 eV (solid line in Figure 5.1 inset). The $[\text{Fe}(\text{TMC})\text{N}_3](\text{BF}_4)$ data contain an intense feature at 7111.5 eV with the second derivative of the data (not shown) clearly showing another feature at 7113.3 eV (solid line in Figure 5.2 inset). $[\text{Fe}(\text{OH}_2)\text{EDTA}]^-$, FeEDTA-NO , $[\text{Fe}(\text{TMC})\text{NO}](\text{BF}_4)_2$, $\text{Fe}(\text{salen})\text{Cl}$ and $\text{Fe}(\text{salen})\text{NO}$ all have a features whose maximum lie between 7112.6 and 7113.0 eV (Figure 5.1, 5.2, and 5.3 insets). The pre-edge features of FeEDTA-NO and $\text{Fe}(\text{salen})\text{NO}$ are more intense than the pre-edge features of $[\text{Fe}(\text{OH}_2)\text{EDTA}]^-$ and $\text{Fe}(\text{salen})\text{Cl}$ (Figure 5.1 and 5.3 insets), respectively.

The $1s \rightarrow 3d$ pre-edge feature can be used to probe the iron oxidation state in $\{\text{FeNO}\}^7$ systems. The $1s \rightarrow 3d$ transition is formally electric dipole forbidden, but gains intensity through an allowed quadrupole transition and more dominantly by $4p$ mixing into the $3d$ states as a result of the noncentrosymmetric environment of the metal site. Because the final state ($1s^1 3d^{n+1}$) has a different electronic configuration for high spin ferric and high spin ferrous ions, the $1s \rightarrow 3d$ feature is sensitive to the oxidation state of the iron site. In the weak field limit, two final states of maximum spin multiplicity can be reached in the d^7 high spin ferrous case, 4F and 4P , while only one state of maximum spin multiplicity can be reached in the d^6 high spin ferric case, 5D .³¹ The free ion splitting of the 4F and 4P is 2 eV ³² and is readily resolvable at the Fe K-edge. However, when the iron atom is placed in an octahedral ligand field the splitting of the d orbitals into the t_2 and e set causes the free ion terms to split into many-electron states. In the ferrous case, the 4F term splits into 4T_1 , 4T_2 , and 4A_2 many-electron states, while the 4P term turns into a 4T_1 state.³³ The 4A_2 many-electron state will not be allowed as it would require a two-electron transition (see Chapter 4). In a relatively weak field, the splitting of the three states is determined mainly by electron repulsion (vs.

ligand field) and the pre-edge feature that arises from transitions into the 4T_1 and 4T_2 states from the 4F term will lie ~ 2 eV lower in energy than that from a transition into the 4T_1 state from the 4P term. In the high spin ferric case, in an octahedral ligand field the 5D term splits into the 5T_2 and 5E states.³³ Thus, an octahedral high spin ferric complex has two pre-edge features from transitions into the 5T_2 and 5E states split by $10Dq$.

The splitting of the pre-edge in $[\text{Fe}(\text{OH}_2)\text{EDTA}]^{2-}$ is attributed to the splitting of the 4T_1 and 4T_2 states from the 4F term and the 4T_1 state from the 4P term (Figure 5.1 and Table 5.2). The two pre-edge features in the spectrum of $[\text{Fe}(\text{OH}_2)\text{EDTA}]^{2-}$ have an intensity ratio of $\sim 2:1$ (Table 5.2) as would be expected since the lower energy feature arises from transitions into two triplet states, while the higher energy feature arises from a transition into one triplet state. The total area of the $[\text{Fe}(\text{OH}_2)\text{EDTA}]^{2-}$ pre-edge feature is higher than that observed for octahedral high spin ferrous complexes (Table 4.1, Chapter 4) due to distortions of the iron site from variation in ligation and bond distances. The pre-edge region of $[\text{Fe}(\text{OH}_2)\text{EDTA}]^-$ was fit with two features at 7112.8 and 7113.8 eV (Figure 5.1 and Table 5.2). As in the ferrous case, the total area of the $[\text{Fe}(\text{OH}_2)\text{EDTA}]^-$ pre-edge feature is higher than that observed for octahedral high spin ferric complexes (Table 4.1, Chapter 4) due to distortions of the iron site from variation in ligation and bond distances. The pre-edge feature of FeEDTA-NO was fit with a single feature at 7112.8 eV (Figure 5.1 and Table 5.2). This feature is positioned at approximately the same energy as that for $[\text{Fe}(\text{OH}_2)\text{EDTA}]^-$, however, the pre-edge feature of FeEDTA-NO is more intense than that of $[\text{Fe}(\text{OH}_2)\text{EDTA}]^-$. One does not observe the two features at ~ 7111.5 and 7113.5 eV in the spectrum of FeEDTA-NO that are characteristic of high spin ferrous complexes (Table 4.1, Chapter 4).

The pre-edge region of the spectrum $[\text{Fe}(\text{TMC})\text{N}_3](\text{BF}_4)$ can be fit with an intense feature at 7111.5 eV and a very weak feature at 7113.3 eV (Figure 5.2 and Table 5.2). Since the high spin ferrous atom in $[\text{Fe}(\text{TMC})\text{N}_3](\text{BF}_4)$ is in a noncentrosymmetric site, $4p$ mixing into the $3d$ orbitals is allowed. As explained in detail in Chapter 4, the pre-edge feature for a high spin ferrous complex in a square pyramidal geometry has a lower energy, intense peak due to $4p_z$ character mixing into the $3d_{z^2}$ orbital with a weak peak ~ 2 eV higher in energy (see Figure 4.7 in Chapter 4). The pre-edge region for $[\text{Fe}(\text{TMC})\text{NO}](\text{BF}_4)_2$ can also be fit with two features, however, the most intense feature is the higher energy feature which is ~ 1 eV higher in energy than that for $[\text{Fe}(\text{TMC})\text{N}_3](\text{BF}_4)$. The energy of the intense pre-edge feature for $[\text{Fe}(\text{TMC})\text{NO}](\text{BF}_4)_2$ is much more similar to that of high spin ferric complexes (Table 4.1, Chapter 4). In addition to the intense feature at 7112.6 eV, the pre-edge region for $[\text{Fe}(\text{TMC})\text{NO}](\text{BF}_4)_2$ was fit with a weak feature at 7111.5 eV. This feature can be explained if the iron is in a

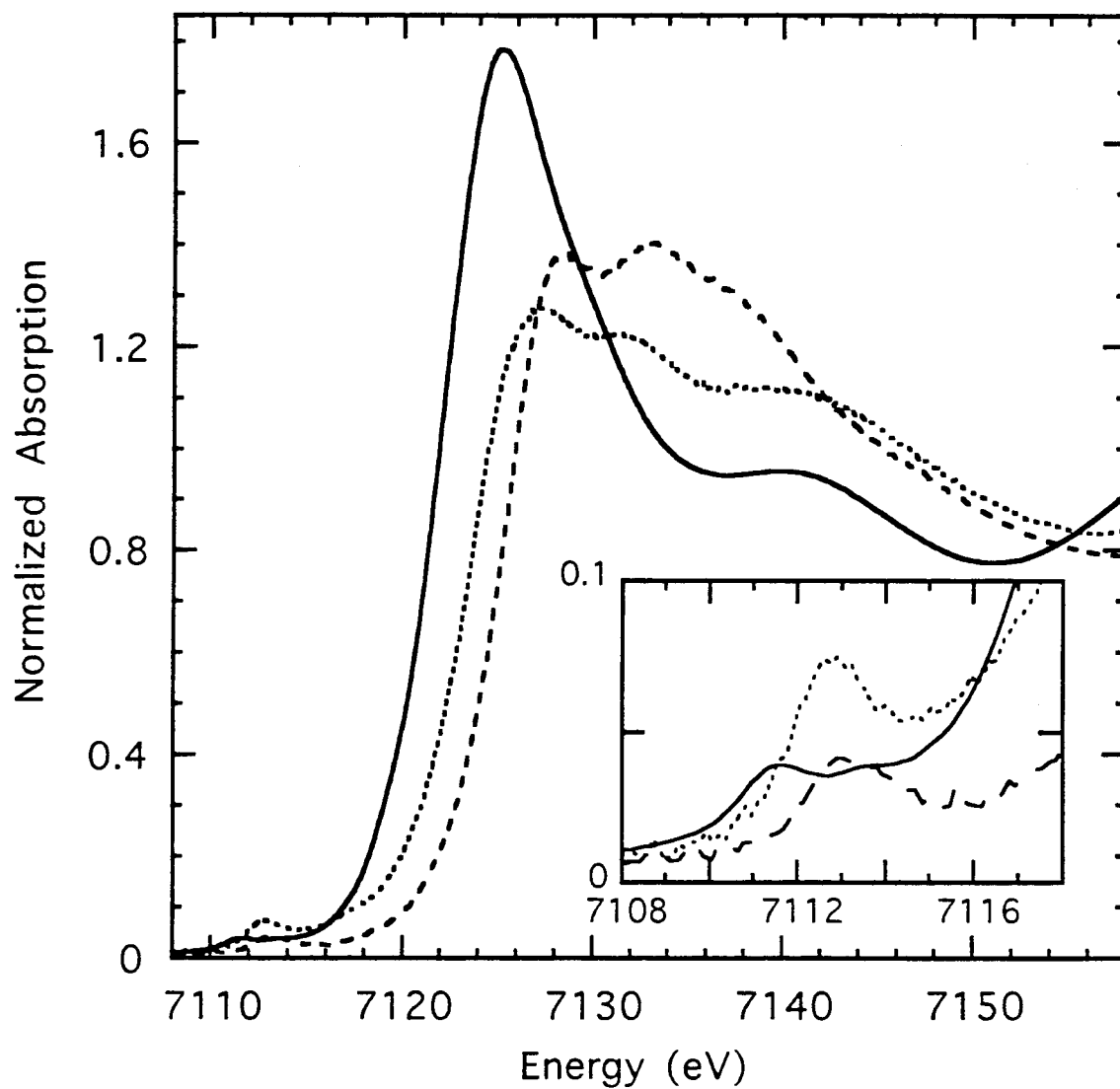


Figure 5.1. XAS Fe K-edge spectra of $[\text{Fe}(\text{OH}_2)\text{EDTA}]^{2-}$ (—), $[\text{Fe}(\text{OH}_2)\text{EDTA}]^{-}$ (---), and FeEDTA-NO (.....). The inset shows an expansion of the $1s \rightarrow 3d$ pre-edge region.

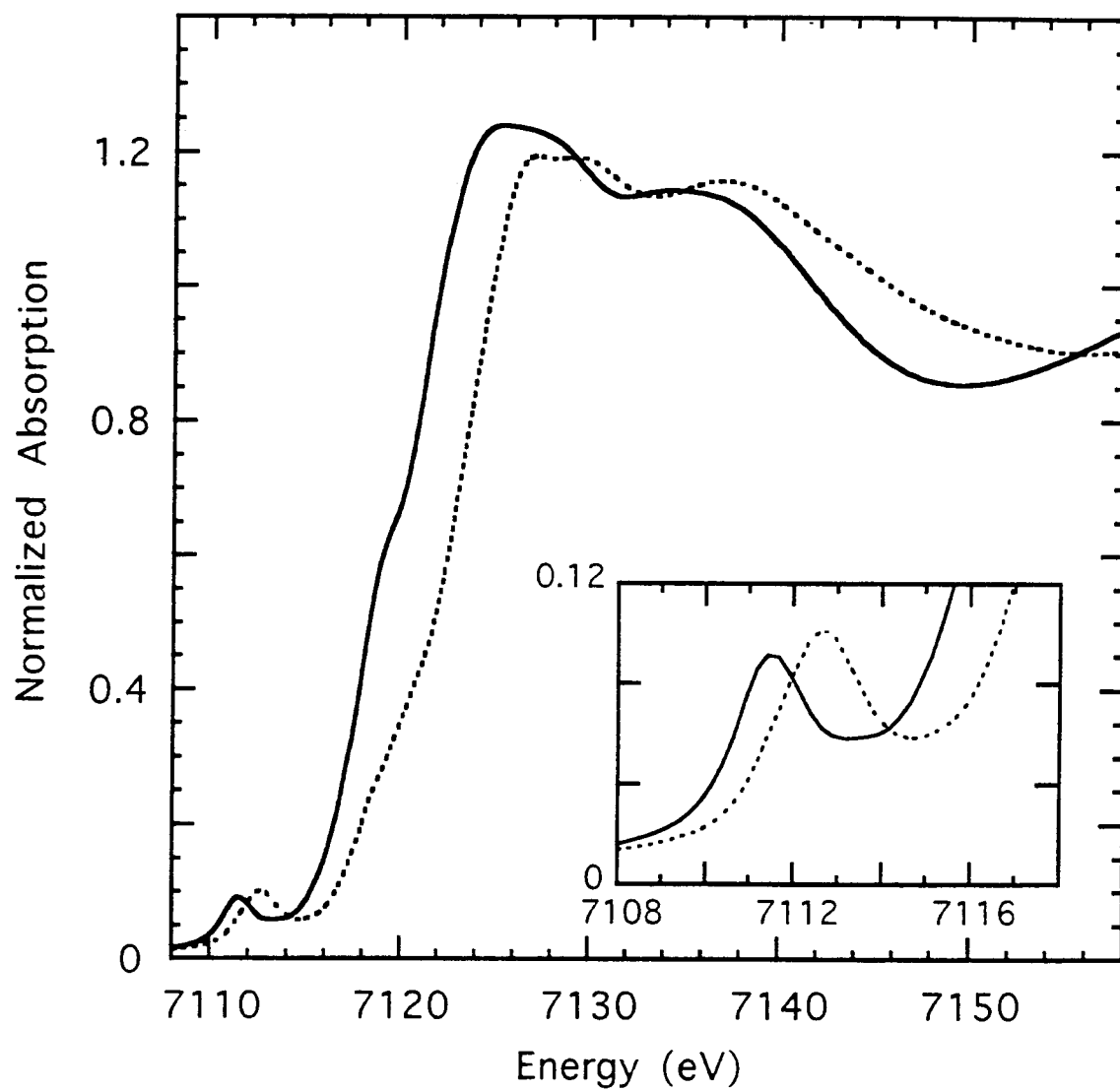


Figure 5.2. XAS Fe K-edge spectra of $[\text{Fe}(\text{TMC})\text{N}_3](\text{BF}_4)$ (—) and $[\text{Fe}(\text{TMC})\text{NO}](\text{BF}_4)_2$ (⋯). The inset shows an expansion of the $1s \rightarrow 3d$ pre-edge region.

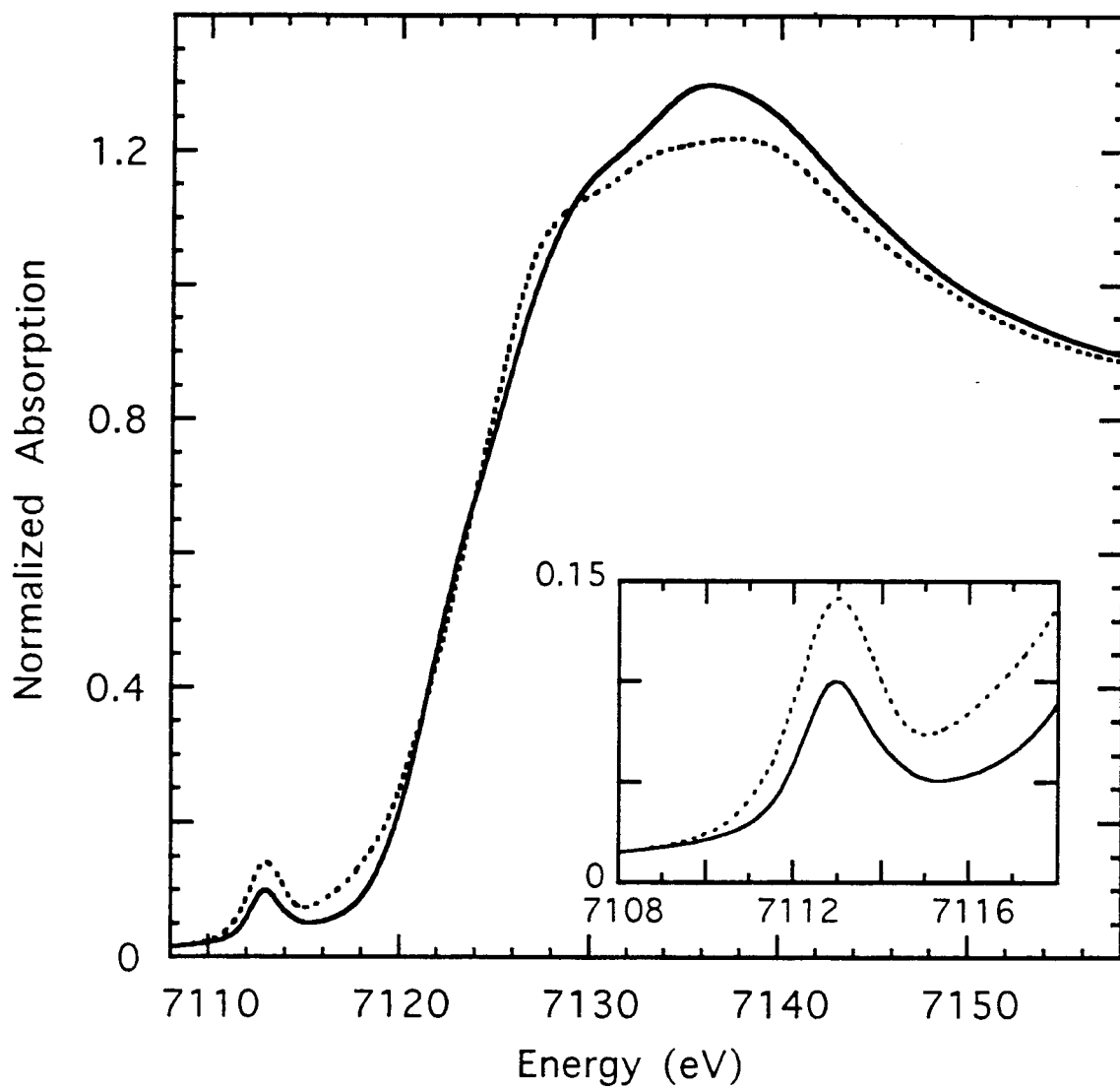


Figure 5.3. XAS Fe K-edge spectra of Fe(salen)Cl (—) and Fe(salen)NO (····). The inset shows an expansion of the $1s \rightarrow 3d$ pre-edge region.

Table 5.2. XAS Pre-Edge Energies and Areas for {FeNO}⁷ and Related Complexes.

compound	Fe oxidation state	Fe-N-O angle	pre-edge energy (eV) ^a	pre-edge area ^{a,b}	total pre-edge area ^b
[Fe(H ₂ O)EDTA] ²⁻	+2	---	7111.48 (0.02) 7113.45 (0.04)	3.9 (0.2) 1.8 (0.05)	5.7 (0.5)
[Fe(H ₂ O)EDTA] ⁻	+3	---	7112.82 (0.03) 7113.81 (0.07)	2.9 (0.4) 4.1 (0.5)	7.0 (0.2)
FeEDTA-NO	---	156° ^c	7112.75 (0.02)	10.4 (0.4)	10.4 (0.4)
[Fe(TMC)N ₃](BF ₄)	+2	---	7111.47 (0.01) 7113.30 (0.05)	12.4 (0.5) 1.0 (0.2)	13.4 (0.3)
[Fe(TMC)NO](BF ₄) ₂	---	178°	7111.52 (0.05) 7112.64 (0.02)	1.1 (0.4) 14.3 (1.4)	15.5 (1.1)
Fe(salen)Cl	+3	---	7112.91 (0.01) 7114.25 (0.07)	12.9 (0.3) 1.5 (0.4)	14.4 (0.6)
Fe(salen)NO	---	149°	7112.96 (0.01)	24.2 (0.6)	24.2 (0.6)

^a Pre-edge energies and areas were determined by fits to the data as described in the Experimental Section. ^b Pre-edge areas were calculated by multiplying the height of the fitted feature by the FWHM (the values reported for the pre-edge areas were multiplied by 100). ^c The Fe-N-O angle in this case was determined by a GNXAS analysis of the EXAFS data (see Chapter 3).

ferric oxidation state and the increased electronic repulsion from the short Fe-N(O) bond increases the energy of the d_{z^2} orbital so that it is no longer the lowest 3d orbital in energy. Hence, the weak feature at 7111.5 eV could arise from transitions into d_{xy} or d_{xz} , d_{xz} (see Scheme 6 in Chapter 4). The pre-edge feature of Fe(salen)Cl can be fit with an intense feature at 7112.91 and a weaker feature at 7114.25 eV (see Figure 4.13), while that of Fe(salen)NO can be fit with a single more intense feature at 7112.96 eV (Figure 5.3 and Table 5.2). From the energies of the pre-edge features, the iron in {FeNO}⁷ appears to be in the ferric oxidation state as the pre-edge feature of FeEDTA-NO is much more similar in shape and in energy to that of [Fe(OH₂)EDTA]⁻ than of [Fe(OH₂)EDTA]²⁻. In addition, the pre-edge feature of [Fe(TMC)NO](BF₄)₂ and of Fe(salen)NO are much more similar to that of the ferric square pyramidal complex, Fe(salen)NO, than to that of the ferrous square pyramidal complex, [Fe(TMC)N₃](BF₄).

The energy of the edge position (1s→4p transition) is dependent upon the effective nuclear charge of the absorbing metal atom. The effective nuclear charge of the metal ion is governed by a combination of effects including the formal oxidation state of the metal, the number and type of ligating atoms and the coordination geometry.^{32,34-38} Therefore, the oxidation state of a metal atom cannot be determined by the edge position without careful consideration of ligation effects on the effective nuclear charge of the metal atom. In the three cases in this study, differences between the types of ligating atoms and the coordination spheres are minimized so that changes in the edge energy can be considered to be strongly related to the oxidation state of the iron (Figure 5.1, 5.2, and 5.3). The energy of the FeEDTA-NO edge lies between that of the reduced and oxidized iron-EDTA edges (Figure 5.1). However, the FeEDTA-NO spectrum is similar in intensity and shape to the [Fe(OH₂)EDTA]⁻ spectrum. The edge of [Fe(TMC)NO](BF₄)₂ is shifted to higher energy than the edge of [Fe(TMC)N₃](BF₄) by ~2 eV (Figure 5.2), which is consistent with the difference in oxidation state between ferrous and ferric.³² The edges of Fe(salen)Cl and Fe(salen)NO (Figure 5.3) occur at the same energy indicating that the iron in each site has the same +3 oxidation state.

In a previous study (presented in Chapter 3),³⁹ iron-ligand bond distances were obtained by extended X-ray absorption fine structure (EXAFS) for [Fe(OH₂)EDTA]²⁻, [Fe(OH₂)EDTA]⁻ and FeEDTA-NO. The first shell bond distances obtained from the [Fe(OH₂)EDTA]⁻ data were 2.04 and 2.34 Å for the Fe-O and Fe-N bonds, respectively. The analogous distances obtained from the [Fe(OH₂)EDTA]²⁻ data were 2.17 and 2.34 Å. The first shell bond distance obtained from the FeEDTA-NO data were 1.76 Å for the Fe-N(O) bond and 2.05 and 2.27 Å for the Fe-O and Fe-N bond distances of the EDTA ligand. The Fe-EDTA bond distances in FeEDTA-NO are more closely matched to the

ferric-EDTA bond distances, in further experimental support of the ferric oxidation state description.

The XAS edge and pre-edge features as well as the iron-ligand distances obtained from EXAFS data are all consistent and indicate that the iron atom in these $\{\text{FeNO}\}^7$ complexes is in the ferric oxidation state. However, there are quantitative differences in the edge spectra between the ferric reference complexes and the $\{\text{FeNO}\}^7$ complexes, giving insight into the geometric and electronic structure of these $\{\text{FeNO}\}^7$ complexes. First, the pre-edge feature of the iron-nitrosyl complexes is more intense than that of their ferric counterparts. Empirically, the strength of the pre-edge transition is found to be dependent on the amount of 3d-4p mixing.³⁶ A distortion of the metal site allows for more 3d-4p mixing resulting in an increase in the pre-edge intensity since the $1s \rightarrow 4p$ transition is electric dipole allowed. This effect is the origin of the increase in the pre-edge intensity of $\text{Fe}(\text{salen})\text{Cl}$ (solid line in Figure 5.3 inset), which has a square pyramidal geometry relative to $[\text{Fe}(\text{OH}_2)\text{EDTA}]^-$ (dashed line Figure 5.1 inset), which has a distorted octahedral geometry. The effect can also be seen in a comparison of $[\text{Fe}(\text{OH}_2)\text{EDTA}]^{2-}$ (solid line in Figure 5.1 inset) and $[\text{Fe}(\text{TMC})\text{N}_3](\text{BF}_4)$ (solid line in Figure 5.2 inset) where the first pre-edge feature in $[\text{Fe}(\text{TMC})\text{N}_3](\text{BF}_4)$ increased in intensity due to the lowering of symmetry from distorted octahedral to square pyramidal. In the case of FeEDTA-NO , $[\text{Fe}(\text{TMC})\text{NO}](\text{BF}_4)_2$, and $\text{Fe}(\text{salen})\text{NO}$ complexes, the short Fe-N(O) bond lowers the symmetry around the iron site resulting in an increase in the intensity of the $1s \rightarrow 3d$ pre-edge feature (dotted lines in Figure 5.1, 5.2, and 5.3 insets).

The intensity of the $1s \rightarrow 3d$ pre-edge feature can be used to gain information on the distortion around the iron site. As described in detail in Chapter 4, the intensity of the $1s \rightarrow 3d$ pre-edge feature can be used to quantitate the amount of 4p mixing into the 3d orbitals. For example, FeEDTA-NO has a total pre-edge area of 10.4. Assuming that 5 units originate from quadrupole transition intensity (the value for centrosymmetric high spin ferric complexes, Table 4.1 in Chapter 4), 5.4 units originate from dipole transition intensity (*i.e.* 4p mixing into the 3d orbitals). If the quadrupole intensity is 1% of the dipole intensity, then there is 5.4% 4p mixing into the 3d orbitals for FeEDTA-NO . This percentage of 4p mixing is very similar to the 5.5% 4p mixing into the 3d orbitals obtained for $(\text{enH}_2)[\text{Fe}_2\text{O}(\text{HEDTA})_2] \cdot 6\text{H}_2\text{O}$ (Chapter 4), where instead of a short 1.8 Å Fe-N(O) bond as in FeEDTA-NO there is a short 1.8 Å Fe-O bond from a μ -oxo bridge. Distorting the iron site further would increase the amount of 4p mixing into the 3d orbitals and, thus, increase the pre-edge intensity. Such is the case upon removing an axial ligand and creating a square pyramidal iron site. $[\text{Fe}(\text{TMC})\text{NO}](\text{BF}_4)_2$, which has a

linear Fe-N-O unit, has a total pre-edge area of 15.5 which corresponds to 10.5% 4p mixing into the 3d orbitals. The amount of 4p mixing into the 3d orbitals is much greater for $[\text{Fe}(\text{TMC})\text{NO}](\text{BF}_4)_2$, a square-pyramidal complex, than for FeEDTA-NO, a purported seven-coordinate complex (see Chapter 3). The amount of 4p character in the 3d orbitals of $[\text{Fe}(\text{TMC})\text{NO}](\text{BF}_4)_2$ is slightly more than the value of 9.4% obtained for Fe(salen)Cl, also a square pyramidal complex, due to the shorter iron-axially ligand bond in $[\text{Fe}(\text{TMC})\text{NO}](\text{BF}_4)_2$. Fe(salen)NO, which has a bent Fe-N-O unit, has a total pre-edge area of 24.2, which corresponds to 19.2% 4p mixing into the 3d orbitals. The main difference in the iron site symmetry between $[\text{Fe}(\text{TMC})\text{NO}](\text{BF}_4)_2$ and Fe(salen)NO is a linear vs. bent Fe-N-O unit. Thus, the differences in the pre-edge area and the related 4p mixing into the 3d orbitals must be affected by the bending of the Fe-N-O unit. The increase in 4p mixing into the 3d orbitals upon bending the Fe-N-O unit has also been observed in SCF-X α -SW calculations of an $\{\text{FeNO}\}^7$ model complexes where the amount of 4p_z mixing into the 3d_{z²} orbital doubled upon bending the Fe-N-O unit from 180° to 150°. ¹⁹

The second quantitative difference involves the energy of the rising edge, with that of FeEDTA-NO being lower than that of $[\text{Fe}(\text{OH}_2)\text{EDTA}]^-$ (Figure 5.1). As has been stated previously, the 1s—>4p edge energy is affected by changes in the effective nuclear charge of the metal atom as well as ligand field effects. In this case, the H₂O of the ferric EDTA complex is replaced by NO⁻ in FeEDTA-NO. The resulting short Fe-N(O) bond causes a strong axial distortion that splits the 4p levels with the 4p_z orbital shifting to higher energy. Thus, one would expect the 1s—>4p transition to split with the transition to the 4p_{x,y} orbital occurring at approximately the same energy and the transition to the 4p_z orbital occurring at higher energy. However, experimentally the FeEDTA-NO edge is at lower energy than the $[\text{Fe}(\text{OH}_2)\text{EDTA}]^-$ edge (Figure 5.1). This shift to lower energy can be explained by charge donation from the NO⁻ to the ferric center which reduces the effective nuclear charge of the iron and causes the FeEDTA-NO edge to be at a lower energy. Alternatively, in the Fe(salen)Cl and Fe(salen)NO comparison (Figure 5.3), the edges lie at the same energy. Since Fe(salen)Cl is square pyramidal, the 4p orbitals are split with the 4p_z orbital lying lower in energy. Thus, when the NO⁻ replaces the Cl⁻ with a much shorter bond length (1.78 vs. 2.24 Å) the 1s—>4p_z should increase in energy resulting in an edge shift to higher energy. Experimentally the edges are at the same energy, thus there must also be charge donation from the NO⁻ to the ferric center of the salen complex reducing the effective nuclear charge of the iron.

5.2.4. Discussion

In summary, both the energy of the rising edge and the shape of the edge of the $\{\text{FeNO}\}^7$ complexes are similar to the ferric complexes with corresponding ligation (*i.e.* $[\text{Fe}(\text{OH}_2)\text{EDTA}]^-$ vs. FeEDTA-NO and $\text{Fe}(\text{salen})\text{Cl}$ vs. $\text{Fe}(\text{salen})\text{NO}$, Figure 5.1 and 5.3, respectively). All three of the $\{\text{FeNO}\}^7$ complexes exhibit an intense pre-edge feature at ~ 7113 eV which is consistent with a ferric complex that has a distorted iron site. In the $\{\text{FeNO}\}^7$ complexes, the short Fe-N(O) bond of ~ 1.7 Å provides a strong axial distortion of the iron active site. The bond distances obtained from EXAFS data of $[\text{Fe}(\text{OH}_2)\text{EDTA}]^{2-}$, $[\text{Fe}(\text{OH}_2)\text{EDTA}]^-$ and FeEDTA-NO show that the Fe-EDTA distances of FeEDTA-NO are much more similar to the distances in $[\text{Fe}(\text{OH}_2)\text{EDTA}]^-$ than in $[\text{Fe}(\text{OH}_2)\text{EDTA}]^{2-}$.³⁹ On a quantitative level the rising edge of FeEDTA-NO is shifted by 2 eV to lower energy relative to $[\text{Fe}(\text{OH}_2)\text{EDTA}]^-$ consistent with significant charge donation from the NO^- ligand to the Fe^{3+} center.

The results obtained from the XAS experiments on $\{\text{FeNO}\}^7$ systems can be used in conjunction with experimental (absorption, variable-temperature, variable-field MCD, resonance Raman, EPR, and magnetism) and theoretical (SCF- $X\alpha$ -SW) results to obtain a detailed electronic description of $S=3/2$ $\{\text{FeNO}\}^7$ systems. The theoretical and experimental electronic structure description we have developed for the $\{\text{FeNO}\}^7$ $S=3/2$ non-heme iron complex involves a high spin Fe^{3+} $S=5/2$ ion antiferromagnetically coupled to an NO^- ligand with $S=1$.^{18,19} From the SCF- $X\alpha$ -SW calculations, the high spin ferric description derives from the large exchange stabilization of the d^5 configuration.¹⁹ In the spin unrestricted calculations, which allow spin up and spin down electrons to occupy different orbitals, the occupied spin up d orbitals are stabilized below the unoccupied spin down counterparts by 6 eV due to this exchange interaction. The occupied spin down $\text{NO } \pi^*$ orbitals are stabilized due to their direct overlap with the spin up iron d_{xz} and d_{yz} orbitals.¹⁹ Thus, this orbital overlap leads to the $S=1$ on the NO^- unit and its antiferromagnetic coupling to the high spin ferric center.

Experimental support for this description comes from XAS, rR and abs/MCD/rR profile excited state spectroscopies.¹⁹ From the XAS, the pre-edge peak at ~ 7113 eV, rather than two peaks split by 1.9 eV as in the ferrous complexes, and the shape and energy of the rising edge both indicate that the iron is in the high spin ferric oxidation state. Furthermore, the first shell EXAFS distances of the NO complex are ~ 0.1 Å shorter than the ferrous complex with corresponding ligation but very close to those of the ferric analog. From rR, the intra-ligand frequency of ~ 1750 cm^{-1} combined with metal ligand vibrational data on the Fe- NO unit via a normal coordinate analysis give an

NO stretching force constant which, compared to molecular NO species, is significantly reduced, indicating electron transfer into the NO π^* orbital resulting in an NO⁻ species.¹⁹ From excited state spectroscopies, the ligand field and charge transfer (CT) transitions have been identified using rR profiles. The ligand field transition energies are consistent with those observed for high spin ferric complexes and the CT transitions are in an energy range and ordering consistent with predictions from the SCF-X α -SW electronic structure calculations for NO⁻ π^* \rightarrow Fe³⁺3d CT transitions.

The data further show evidence for a highly covalent Fe³⁺-NO⁻ ligand donor bond.¹⁹ First, from magnetic susceptibility the electrons of the NO⁻ are strongly antiferromagnetically coupled to the iron to give the S=3/2 spin state which requires significant orbital overlap. Secondly, the rising edges of the XAS spectra of the Fe³⁺-NO⁻ complexes are at lower energy than the respective ferric complexes, even when ligand field effects on the 4p orbitals are taken into account, indicating charge donation from the NO⁻ to the ferric center. Finally, the intra-ligand frequency and calculated force constant are significantly higher than those found for molecular NO⁻ again indicating charge donation from an antibonding orbital on the NO⁻ of the iron-nitrosyl complex. The spin unrestricted SCF-X α -SW calculations¹⁹ provide insight into the nature of the strong Fe³⁺-NO⁻ bond. There are two strong donor interactions which are, in fact, σ in character. These involve the NO⁻ 4 σ^+ and 5 σ^+ orbitals. The former is σ antibonding with respect to the NO⁻ and dominates the charge donation to the Fe³⁺ due to better overlap (*i.e.* increased N character in the antibonding NO molecular orbital). This charge donation thus removes electron density from a strongly antibonding orbital, which significantly increases the strength of the intramolecular NO⁻ bond, leading to the large increase in the bound NO force constant observed experimentally. It is important to emphasize that reduction of the NO by the ferrous complex involves electron transfer into the NO π^* orbital while charge donation of the bound NO⁻ to the Fe³⁺ dominantly involves electron transfer from an NO σ^* orbital. Thus charge donation from the bound NO⁻ to the Fe³⁺ can significantly increase the strength of the NO bond.

Thus an experimentally and theoretically consistent electronic structure has been generated for the {FeNO}⁷ S=3/2 systems, which can be described as high spin ferric (S=5/2) antiferromagnetically coupled to NO⁻ (S=1) to produce the S=3/2 ground state.¹⁹ This new bonding description provides a general understanding of the interaction of NO with the high-spin ferrous site, and the spectral features can be quantitated to provide insight into differences in bonding and electron distribution which can be related to dioxygen activation by non-heme iron enzymes.

5.2.5. Acknowledgments

The EDTA solution samples were prepared by Mark Pavlosky and Yan Zhang. Mark Pavlosky and Yan Zhang performed the absorption, variable-temperature, variable-field MCD, resonance Raman, EPR, and magnetism experiments alluded to in the discussion. Carl Brown performed the SCF-X α -SW theoretical calculations. This research was supported by grants from the NIH (GM40392, E.I.S.) and NSF (CHE-9121576, K.O.H.). The Stanford Synchrotron Radiation Laboratory is supported by the Department of Energy, Office of Basic Energy Sciences, Divisions of Chemical Science and Materials Science, and in part by the National Institutes of Health, National Center of Research Resources, Biomedical Research Technology Program (RR-01209, K.O.H.) and the DOE's Office of Health and Environmental Research.

5.2.6. References and Notes

- (1) Feig, A. L.; Lippard, S. J. *Chem. Rev.* **1994**, *94*, 759.
- (2) Howard, J. B.; Rees, D. C. *Advances in Protein Chemistry*; Academic Press: New York, 1991; Vol. 42, p 199.
- (3) Solomon, E. I.; Zhang, Y. *Acc. Chem. Res.* **1992**, *25*, 343.
- (4) Nelson, M. J. *J. Biol. Chem.* **1987**, *262*, 12137.
- (5) Galpin, J. R.; Veldink, G. A.; Vliegthart, J. F. G.; Boldingh, J. *Biochim. Biophys. Acta* **1978**, *536*, 356.
- (6) Arciero, D. M.; Lipscomb, J. D. *J. Biol. Chem.* **1986**, *261*, 2170.
- (7) Arciero, D. M.; Orville, A. M.; Lipscomb, J. D. *J. Biol. Chem.* **1985**, *260*, 14035.
- (8) Twilfer, H.; Bernhardt, F.-H.; Gersonde, K. *Eur. J. Biochem.* **1985**, *147*, 171.
- (9) Chen, V. J.; Orville, A. M.; Harpel, M. R.; Frolik, C. A.; Surerus, K. K.; Münck, E.; Lipscomb, J. D. *J. Biol. Chem.* **1989**, *264*, 21677.
- (10) Ming, L.-J.; Que, L., Jr.; Kriauciunas, A.; Frolik, C. A.; Chen, V. J. *Biochemistry* **1991**, *30*, 11653.
- (11) Bill, E.; Bernhardt, F.-H.; Trautwein, A. X.; Winkler, H. *Eur. J. Biochem.* **1985**, *147*, 177.
- (12) Arciero, D. M.; Lipscomb, J. D.; Huynh, B. H.; Kent, T. A.; Münck, E. *J. Biol. Chem.* **1983**, *258*, 14981.
- (13) Enemark, J. H.; Feltham, R. D. *Coord. Chem. Rev.* **1974**, *13*, 339.
- (14) Wells, F. V.; McCann, S. W.; Wickman, H. H.; Kessel, S. L.; Hendrickson, D. N.; Feltham, R. D. *Inorg. Chem.* **1982**, *21*, 2306.

- (15) Salerno, J. C.; Siedown, J. N. *Biochim. Biophys. Acta* **1979**, *579*, 246.
- (16) Pohl, K.; Wiegardt, K.; Nuber, B.; Weiss, J. *J. Chem. Soc. Dalton Trans.* **1987**, 187.
- (17) Abbreviations used: EDTA = ethylenediaminetetraacetic acid; TMC = 1,4,8,11-tetramethyl-1,4,8,11-tetraazacyclotetradecane; salen = *N,N*-ethylenebis(salicylideneiminato).
- (18) Zhang, Y.; Pavlosky, M. A.; Brown, C. A.; Westre, T. E.; Hedman, B.; Hodgson, K. O.; Solomon, E. I. *J. Am. Chem. Soc.* **1992**, *114*, 9189.
- (19) Brown, C. A.; Pavlosky, M. A.; Westre, T. E.; Zhang, Y.; Hedman, B.; Hodgson, K. O.; Solomon, E. I. *J. Am. Chem. Soc.* **1995**, *117*, 715.
- (20) Scott, R. A.; Hahn, J. E.; Doniach, S.; Freeman, H. C.; Hodgson, K. O. *J. Am. Chem. Soc.* **1982**, *104*, 5364.
- (21) Lytle, F. W. In *Applications of Synchrotron Radiation*; Winick, H.; Xian, D.; Ye, M.-h.; Huang, T., Eds.; Gordon & Breach: New York, 1989; p 135.
- (22) Hodges, K. D.; Wollmann, R. G.; Kessel, S. L.; Hendrickson, D. N.; Van Derveer, D. G.; Barefield, E. K. *J. Am. Chem. Soc.* **1979**, *101*, 906.
- (23) Hodges, K. D.; Wollmann, R. G.; Barefield, E. K.; Hendrickson, D. N. *Inorg. Chem.* **1977**, *16*, 2746.
- (24) Haller, K. J.; Johnson, P. L.; Feltham, R. D.; Enemark, J. H.; Ferraro, J. R.; Basile, L. J. *Inorg. Chim. Acta* **1979**, *33*, 119.
- (25) Gerloch, M.; Mabbs, F. E. *J. Chem. Soc. (A)* **1967**, 1598.
- (26) Stern, E. A.; Heald, S. M. *Rev. Sci. Instrum.* **1979**, *50*, 1579.
- (27) Lytle, F. W.; Greigor, R. B.; Sandstrom, D. R.; Marques, E. C.; Wong, J.; Spiro, C. L.; Huffman, G. P.; Huggins, F. E. *Nucl. Instrum. Meth. Phys. Res.* **1984**, *226*, 542.
- (28) Argonne National Laboratory; B. S. Garbow, K. E. Hillstrom, J. J. More.
- (29) Agarwal, B. K. *X-ray Spectroscopy*; Springer-Verlag: New York, 1979, p 276.
- (30) Tyson, T. A.; Roe, A. L.; Frank, P.; Hodgson, K. O.; Hedman, B. *Phys. Rev. B* **1989**, *39*, 6305.
- (31) Sugano, S.; Tanabe, Y.; Kamimura, H. *Multiplets of Transition-Metal Ions in Crystals*; Academic Press: New York, 1970.
- (32) Shulman, R. G.; Yafet, Y.; Eisenberger, P.; Blumberg, W. E. *Proc. Natl. Acad. Sci. USA* **1976**, *73*, 1384.
- (33) Griffith, J. S. *The Theory of Transition Metal Ions*; Cambridge University Press: Cambridge, 1961.
- (34) Srivastava, U. C.; Nigam, H. L. *Coord. Chem. Rev.* **1973**, *9*, 275.

- (35) Cramer, S. P.; Eccles, T. K.; Kutzler, F. W.; Hodgson, K. O. *J. Am. Chem. Soc.* **1976**, *98*, 1287.
- (36) Roe, A. L.; Schneider, D. J.; Mayer, R. J.; Pyrz, J. W.; Widom, J.; Que, L., Jr. *J. Am. Chem. Soc.* **1984**, *106*, 1676.
- (37) Wong, J.; Lytle, F. W.; Messmer, R. P.; Maylotte, D. H. *Phys. Rev. B.* **1984**, *30*, 5596.
- (38) Kau, L.-S.; Spira-Solomon, D. J.; Penner-Hahn, J. E.; Hodgson, K. O.; Solomon, E. I. *J. Am. Chem. Soc.* **1987**, *109*, 6433.
- (39) Westre, T. E.; Di Cicco, A.; Filipponi, A.; Natoli, C. R.; Hedman, B.; Solomon, E. I.; Hodgson, K. O. *J. Am. Chem. Soc.* **1994**, *116*, 6757.

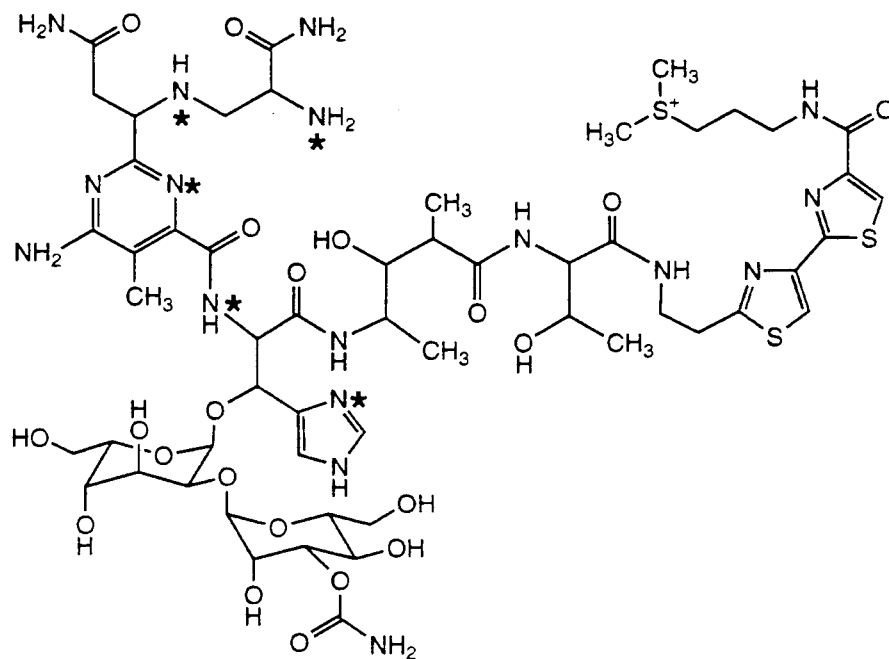
5.3. Iron(II) Bleomycin

5.3.1. Introduction

Bleomycin (BLM) is a histidine-containing glycopeptide antibiotic isolated as a Cu(II) complex from the fungus *Streptomyces verticillus*.¹⁻³ The drug Blenoxane, composed mainly of BLM A₂, is used in treatment against a variety of carcinomas because of its ability to degrade DNA with sequence specificity.⁴ The structure of BLM A₂ (Figure 5.4a) includes three domains: the bithiazole tail is believed to be involved in BLM binding to DNA,⁵⁻⁷ the sugar moiety is thought to control uptake of BLM by cancer cells,^{8,9} and the β-aminoalanine-pyrimidine-histidine region is responsible for metal chelation.^{10,11} DNA degradation by BLM is oxygen and metal ion dependent¹²⁻¹⁵ with the greatest enhancement observed for iron.^{12,16-21} Oxygen binds to Fe(II)BLM producing a ternary complex (oxygenated BLM) that is stable in the presence of excess DNA.²²⁻²⁴ Transfer of an additional electron from a second Fe(II)BLM molecule (or other reductant) to oxygenated BLM produces activated BLM, the species responsible for DNA strand scission.²⁵ The similarity in mechanism to cytochrome P-450 has led researchers to postulate a ferryl (Fe(IV)=O) BLM intermediate,^{10,19} as has generally been considered to be present in heme chemistry.²⁶ Alternatively, electron paramagnetic resonance (EPR),¹⁹ Mössbauer,²⁴ mass spectrometry,²⁷ and X-ray absorption spectroscopy (XAS)²⁸ of activated BLM are most consistent with a low spin Fe(III)-peroxide site (see section 5.4. Activated BLM).

No crystal structure exists for the ferrous complex of BLM and there is some controversy concerning the ligation of BLM to Fe²⁺. Present descriptions are based on correlation to a Cu(II) complex of the related biosynthetic precursor P-3A, which has been crystallographically defined and shown to have a five-coordinate, square pyramidal geometry with pyrimidine, imidazole, deprotonated amide, and secondary amine functions forming the equatorial plane, and a primary amine function coordinating axially.²⁹ However, Cu²⁺ has strong structural preferences due to the Jahn-Teller effect which Fe²⁺ does not and P-3A lacks the disaccharide and bithiazole moieties of BLM, the former being a potential ligand. Axial coordination in Fe(II)BLM of the carbamoyl group of the mannose sugar has been implicated by ¹H nuclear magnetic resonance (NMR) studies³⁰⁻³² and two-dimensional NMR studies of the carbon monoxide bound form.³³ In contrast, earlier studies of CO-bound Fe(II)BLM maintained axial coordination of the primary amine and proposed that the sugar portion played a steric role in governing CO binding constants via hydrogen bonding to the β-amino-propionamide group.³⁴ EPR spectroscopy on the

(a) Bleomycin A₂



(b) PMAH

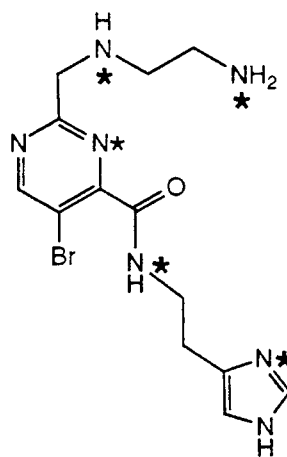


Figure 5.4. Structural ligand framework of (a) Bleomycin A₂ and (b) the analogous model complex PMAH. Coordinating nitrogens are denoted with asterisks (*) for each structure.

nitrosyl complex of Fe(II)BLM has been used to further support the model that the axial donor *trans* to the bound NO is the primary nitrogen of the α -amino group of the β -aminoalanine portion.³⁵⁻³⁷ Additional evidence for axial coordination of the primary amine derives from the variation in EPR parameters for Fe(III)BLM and the ferric complexes of depyruvamide BLM and deamido BLM.³⁸

There is little direct spectroscopic evidence available on Fe(II)BLM as the Mössbauer spectra exhibit broad, unresolved magnetic features and high spin Fe²⁺ non-Kramers ions generally do not exhibit EPR signals.²⁴ As a result, most experiments have focused on the spectroscopically accessible ferric forms of the drug. In this study Fe K-edge XAS was used to characterize the electronic and geometric structure of Fe(II)BLM. Examination of the pre-edge feature can give insight into the coordination number and geometry of the iron site, while the position of the edge is dependent upon the effective nuclear charge of the iron. In addition, an EXAFS analysis can be used to accurately determine the distances to the ligands. Due to the complexity of the glycopeptide and the range of possible metal coordinating functional groups in BLM, synthetic models have been prepared in an effort to obtain insight into the structure.³⁹⁻⁴⁵ The synthetic analog PMAH⁴⁶ which has a similar metal binding domain but lacks the sugar moiety and the bithiazole tail (Figure 5.4b) has also been investigated. The ferrous complex serves as a good model of Fe(II)BLM in that it reacts with dioxygen to generate an analog of activated BLM which has a nearly identical EPR spectrum and causes DNA cleavage with similar specificity.³⁹ XAS data was collected on [Fe(II)PMA]⁺ both in the solid and solution form. The results from this study were combined with results from optical absorption (Abs), magnetic circular dichroism (MCD), and resonance Raman (rR) spectroscopies to develop a detailed description of the geometric and electronic structure of the Fe(II)BLM active site.⁴⁷

5.3.2. Experimental Section

Bleomycin sulfate (Blenoxane), a mixture of 60% BLM A2, 30% BLM B2, and 10% other BLM fractions, was obtained as a gift from Bristol-Meyers Squibb and used without further purification. The individual components differ only in the terminal amine functionality which has no influence on the spectroscopic characteristics of the metal binding domain.¹⁹ All concentrations were calculated with a molecular weight of ~1510 Daltons. The Fe(II)BLM sample was prepared as a glass in 50% (v/v) glycerol-d₃ (98 atom % D; Aldrich), HEPES buffer (Sigma) dissolved in D₂O (99.9 atom % D; Aldrich) and adjusted to a pD in the range 6.0 to 9.0 with 40 wt % NaOD (Aldrich) in D₂O.

Septum stoppered reaction flasks were not sufficient to prevent O₂ reaction, therefore, all solutions were rigorously degassed with 10-15 freeze, pump, thaw cycles at 10⁻³ Torr in Teflon or ground glass stoppered flasks and immediately placed in a N₂ atmosphere (< 10 ppm O₂). Solid forms of metal free BLM and Fe(NH₄)₂(SO₄)₂•6H₂O (FeAS; MCB Manufacturing Chemists, Inc.) were solvated just prior to use in an inert atmosphere with buffered solution and D₂O, respectively. Fe(II)BLM was prepared in the presence of 20% excess ligand by addition of 5 μL of the FeAS stock solution to 5 mM metal free BLM to give a final sample concentration of ~4 mM. Sample integrity was confirmed by optical absorption ($\epsilon_{476} = 380 \text{ M}^{-1} \text{ cm}^{-1}$)¹⁸ and EPR. The use of reducing agents to inhibit Fe²⁺ oxidation was strictly avoided as it was determined to significantly alter both the CD and MCD spectra of Fe(II)BLM.

The ligand PMAH,⁴⁸ was synthesized according to published procedures, followed by anaerobic complexation with Fe²⁺ to form [Fe(II)(PMA)]Cl•MeOH. A [Fe(II)PMA]⁺ solution was prepared in a N₂ atmosphere with degassed methanol-d₄ (99.9 atom % D; Aldrich) and ethanol-d₆ (99+ atom % D; Aldrich) in a ratio of 1 to 4 to facilitate glassing. Sample concentration was determined by optical absorption ($\epsilon_{670}([\text{Fe(II)PMA}]^+) = 1850 \text{ M}^{-1} \text{ cm}^{-1}$) to be ~4 mM.

X-ray absorption spectra were recorded at the Stanford Synchrotron Radiation Laboratory on unfocused beamline 7-3 during dedicated conditions (3 GeV, 50-100 mA). The radiation was monochromatized using a Si(220) double-crystal monochromator. Unless specified otherwise, data were measured to $k = 15 \text{ \AA}^{-1}$ with 1 mm high pre-monochromator beam defining slits and the monochromator was detuned by 50% at 7998 eV to minimize harmonic contamination. An Oxford Instruments continuous-flow liquid helium CF1208 cryostat was used to maintain a constant temperature of 10 K. Energies were calibrated using an internal Fe foil standard, assigning the first inflection point to 7111.2 eV.⁴⁹ The spectrometer energy resolution was ~1.4 eV with reproducibility in edge position determination of < 0.2 eV.

The [Fe(II)PMA]⁺ solution and Fe(II)BLM XAS samples were prepared as described above. The solution samples were syringed into Lucite EXAFS cells (23 x 1 x 3 mm) with 37 μm Kapton windows under a N₂ atmosphere and subsequently frozen in liquid nitrogen prior to exposure to air. The fluorescence signal was monitored by using a 13-element Ge solid-state array detector⁵⁰ windowed on the Fe K α signal. During the experiment, count rates of approximately 30,000 s⁻¹ total per element were not exceeded. Approximately thirty scans were averaged for Fe(II)BLM and eleven scans were averaged for the [Fe(II)PMA]⁺ solution. The powder [Fe(II)PMA]⁺ sample was mixed with BN and ground into a fine powder in a N₂-filled glove box. This BN/sample mixture was

pressed into a 1 mm thick Al spacer that was sealed with 63.5 μm Mylar tape windows and frozen in liquid nitrogen. Data were measured in transmission mode with N_2 -filled ionization chambers. The final spectrum represents a six scan average.

EXAFS data reduction was performed on the averaged spectra according to established methods.⁵¹⁻⁵³ A smooth pre-edge background was removed from the averaged spectra by fitting a second order polynomial to the pre-edge region and subtracting this polynomial from the entire spectrum. A three-segment spline approximately even in k -space was fit to the EXAFS region and the data normalized to an edge jump of one at 7130 eV. The spline was chosen so that it minimized residual low-frequency background but did not reduce the EXAFS amplitude as checked by monitoring the Fourier transform of the EXAFS during the background subtraction process. The normalized data were converted to k -space. The photoelectron wave vector, k , is defined by $[2m_e(E-E_0)/\hbar^2]^{1/2}$ where m_e is the electron mass, E is the photon energy, \hbar is Planck's constant divided by 2π , and E_0 is the threshold energy of the absorption edge, which was defined to be 7130 eV for the Fe K absorption edge. The empirical EXAFS data analyses were performed with nonlinear least-square curve-fitting^{49,51-53} techniques using empirical phase and amplitude parameters. The following models were used to obtain the empirical Fe-X backscattering parameters of interest: Fe-O from $[\text{Fe}(\text{acetylacetonate})_3]$ ^{54,55} and Fe-N from $[\text{Fe}(1,10\text{-phenanthroline})_3](\text{ClO}_4)_3$.^{56,57} Fourier transforms (from k to R space) were performed for the data range 3.5-12.5 \AA^{-1} with a Gaussian window of 0.1 \AA^{-1} . The window widths used in the backtransforms (from R to k space) are given in the Results and Analysis section. The window widths were kept as similar as possible to those used to extract amplitude and phase parameters from the model compounds to minimize artifacts introduced by the Fourier filtering technique. All curve-fitting was based on k^3 -weighted data and applied to the individual filtered shell of interest. Only the structure-dependent parameters, the distance and coordination number, were varied unless stated otherwise. A "goodness of fit" parameter, F , was calculated as $F = \{[k^6(\text{data} - \text{fit})^2]/(\text{no. of points})\}^{1/2}$ for each fit.

Fe K-edge spectra were also collected on a five- and a six-coordinate ferrous model complex. $[\text{Fe}(\text{TMC})\text{N}_3]\text{BF}_4$ ⁵⁸ (where TMC refers to tetramethylcylcam) and $[\text{Fe}(\text{imidazole})_6]\text{Cl}_2$ ⁵⁹ were prepared as described in the literature. The XAS samples were prepared in the same manner as the $[\text{Fe}(\text{II})\text{PMA}]^+$ solid sample. Data were measured in transmission mode with N_2 -filled ionization chambers to $k = 9.5 \text{\AA}^{-1}$ detuning the monochromator 50% at 7474 eV to minimize harmonic contamination. Two to three scans were averaged for each sample. A smooth pre-edge background was removed from the averaged spectra by fitting a first order polynomial to the pre-edge region and subtracting

this polynomial from the entire spectrum. A two segment spline of order two was fit to the EXAFS region and the data normalized to an edge jump of one at 7130 eV.

5.3.3. Results and Analysis

5.3.3.1. Fe K-Edge XAS. Fe K edge spectra of [Fe(II)PMA]⁺ solid, [Fe(II)PMA]⁺ solution and Fe(II)BLM are shown in Figure 5.5A. The lowest energy peaks arise from the weak 1s→3d pre-edge transition which is at ~7113 eV followed by the 1s→4p transition at ~7127 eV. An expanded view of the 1s→3d pre-edge region is shown for the same samples in Figure 5.5B. Figure 5.5C contains the 1s→3d pre-edge region of representative five- and six-coordinate high spin ferrous model complexes, [Fe(TMC)N₃]BF₄⁵⁸ and [Fe(imidazole)₆]Cl₂,⁵⁹ respectively. The [Fe(imidazole)₆]Cl₂ spectrum (solid line) has two very weak pre-edge features at ~7111.5 and ~7113.5 eV, while the [Fe(TMC)N₃]BF₄ spectrum (dashed line) has a much more intense feature at 7111.5 eV (Figure 5.5C). The spectra of [Fe(II)PMA]⁺ solid (solid line) and [Fe(II)PMA]⁺ solution (dashed line) show two features at ~7112 and ~7113.5 eV with the first transition at 7112 eV for [Fe(II)PMA]⁺ solid being more intense (Figure 5.5B). The spectrum of Fe(II)BLM (dotted line) has two weak features at approximately 7111.5 and 7113.5 eV (Figure 5.5B). The feature at ~7127 eV, attributed to the 1s→4p transition, is more intense and at slightly lower energy for Fe(II)BLM relative to that of [Fe(II)PMA]⁺ samples. The [Fe(II)PMA]⁺ solid feature lies ~1 eV above that of [Fe(II)PMA]⁺ in solution (Figure 5.5A).

The energy of the 1s→4p transition is dependent upon the effective nuclear charge of the absorbing metal atom. This charge is governed by a combination of effects including the formal oxidation state of the metal, the number and type of ligating atoms, and the coordination geometry.⁶⁰⁻⁶³ Differences in the edge energy position of the ferrous BLM and PMA complexes in Figure 5.5A thus reflect variation in the coordination number and the ligand-iron bonding interactions. One would expect the edge of a five-coordinate complex to be at lower energy than that of a six-coordinate complex⁶³ due to reduced ligand repulsion, however the edge of [Fe(II)PMA]⁺ solid occurs at slightly higher energy than [Fe(II)PMA]⁺ solution indicating increased charge donation to the ligand set. This likely reflects the pyrimidine backbonding (*vide infra*), which from the edge energy positions, follows the trend: [Fe(II)PMA]⁺ solid > [Fe(II)PMA]⁺ solution > Fe(II)BLM.

As discussed in detail in Chapter 4, the 1s→3d pre-edge feature can be used to probe the coordination number of an iron active site. The 1s→3d transition is formally electric dipole forbidden, but gains intensity through an allowed quadrupole transition and

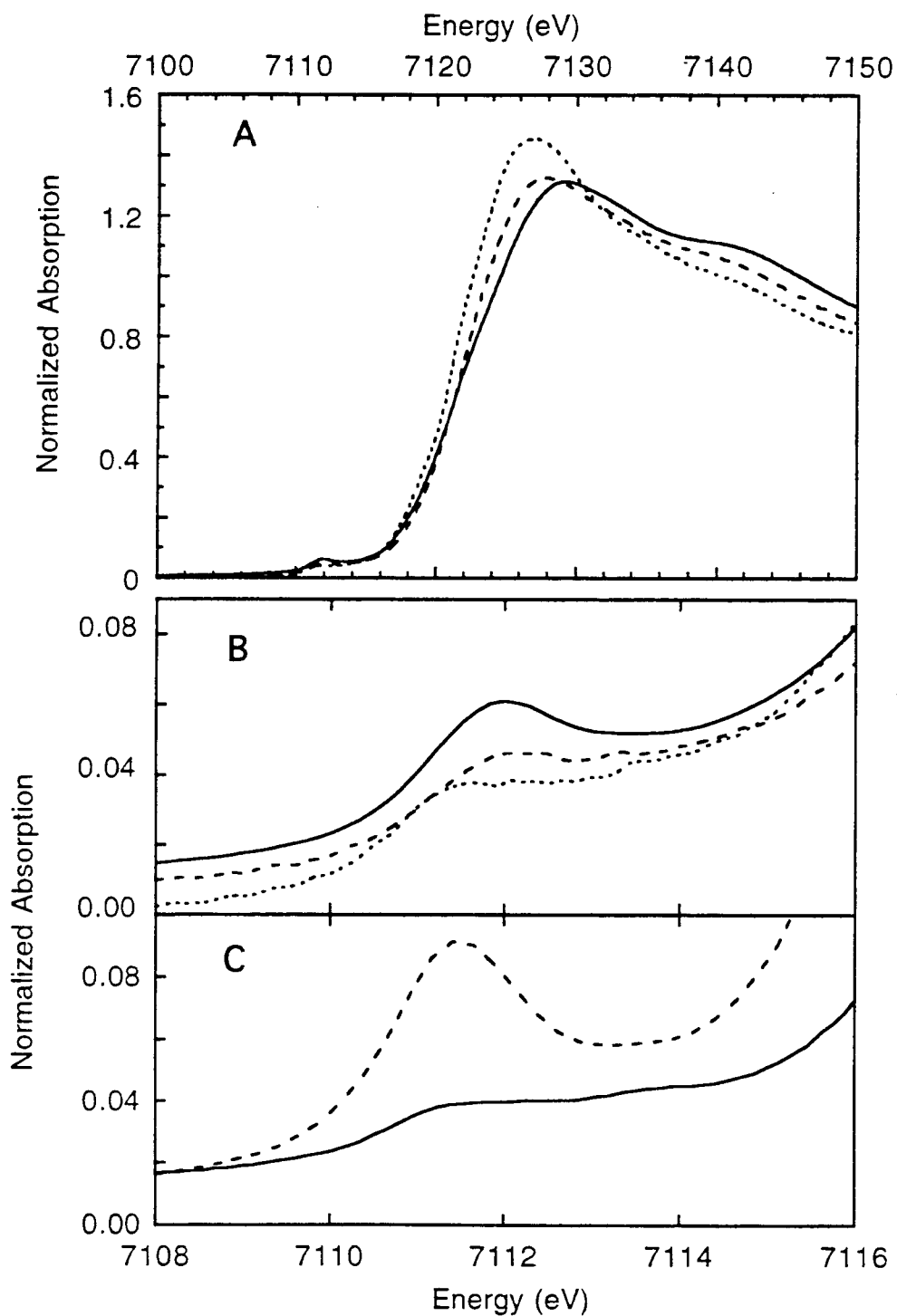


Figure 5.5. A) Fe-K XAS edge spectra of [Fe(II)PMA]⁺ solid (—), [Fe(II)PMA]⁺ solution (---), and Fe(II)BLM (.....). B) Expansion of the 1s→3d pre-edge region of A. C) The 1s→3d pre-edge region of a six-coordinate high spin ferrous model complex [Fe(imidazole)₆]Cl₂ (—) and a five-coordinate complex [Fe(TMC)N₃]BF₄ (---).

more dominantly by 4p mixing into the 3d states as a result of the non-centrosymmetric environment of the metal site. It has been shown for ferric and ferrous complexes that when the symmetry of the iron site is lowered, the pre-edge intensity increases due to an increase in the 3d-4p mixing.^{63,64} When a high spin ferrous atom is in an octahedral site, three transitions are observed into $4T_1$, $4T_2$, and $4T_1$ many-electron excited states (see Chapter 4). The transitions into these states are only quadrupole allowed as the iron is in a centrosymmetric site and therefore there is no 4p-3d mixing. Therefore, one observes three weak peaks (solid line in Figure 5.5C) positioned at approximately 7111.2, 7112.3, and 7113.67 eV for octahedral high spin ferrous complexes with nitrogen ligation. The pre-edge area of five-coordinate high spin ferrous model complexes is greater than that of six-coordinate complexes (Figure 5.5C). This increase in intensity is due to 4p mixing into the 3d orbitals as a result of the loss of the inversion center at the iron site. When an axially ligand is removed and the high spin ferrous atom is in a square pyramidal site, the intensity of the lower energy feature increases dramatically since there is now $4p_z$ mixing into the $3d_{z^2}$ orbital due to the loss of a center of inversion, as can be seen in the $(BF_4)[Fe(TMC)N_3]$ spectrum (dashed line in Figure 5.5C). Empirically the pre-edge of the $[Fe(II)PMA]^+$ solution and Fe(II)BLM look much more similar in shape and intensity to the six-coordinate ferrous complex (Figure 5.5B and 5.5C). The pre-edge of $[Fe(II)PMA]^+$ solid has more intensity in the lowest energy feature, as does $[Fe(TMC)N_3]BF_4$, which is consistent with the MCD results of $[Fe(II)PMA]^+$ solid being five-coordinate.⁴⁷ However, the first pre-edge transition of $[Fe(II)PMA]^+$ solid is not as intense as that of $[Fe(TMC)N_3]BF_4$. This could be due to the Fe $4p_z$ orbital of $[Fe(II)PMA]^+$ solid mixing with the π^* orbital of the pyrimidine. This would diminish the intensity of the pre-edge feature since for square pyramidal geometry the $4p_z$ orbital should be the dominant iron p-orbital mixing into the d-orbitals based on its lower energy⁶² and the lack of inversion along the z-axis. This $4p_z$ -pyrimidine π^* mixing would shift electric dipole intensity from the pre-edge into a higher energy region of the XAS spectrum.

5.3.3.2. EXAFS. EXAFS studies of $[Fe(II)PMA]^+$ solid, $[Fe(II)PMA]^+$ solution and Fe(II)BLM were also pursued to obtain metrical information on the iron active site. The EXAFS spectra of $[Fe(II)PMA]^+$ solid, $[Fe(II)PMA]^+$ solution and Fe(II)BLM are shown in Figure 5.6A and the Fourier transforms (FTs), taken over the k range of 3.5 - 12.5 \AA^{-1} , are shown Figure 5.6B. Curve-fitting was performed on filtered first coordination shell contributions with FT backtransform windows given in Table 5.3 over the k range 4 - 12 \AA^{-1} varying bond distances and coordination numbers. The results from the curve-fitting analysis are presented in Table 5.3. It should be noted that EXAFS analysis cannot readily distinguish between O and N coordination. However, given the

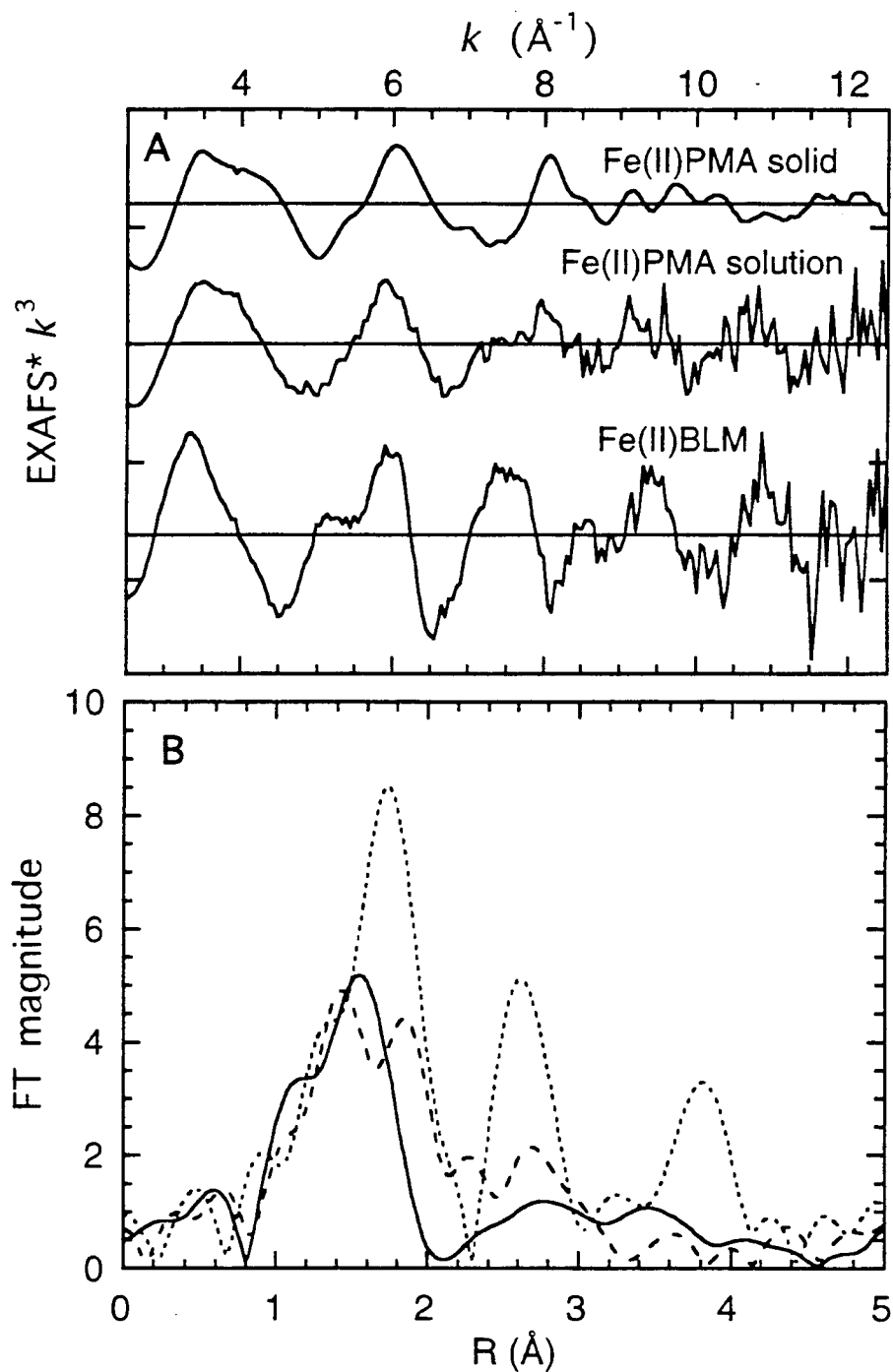


Figure 5.6. A) EXAFS data ($*k^3$) for $[\text{Fe}(\text{II})\text{PMA}]^+$ solid, $[\text{Fe}(\text{II})\text{PMA}]^+$ solution, and Fe(II)BLM (the ordinate scale is 5 between major tick marks on an absolute scale from the abscissa with solid horizontal lines indicating the zero point of each plot). B) The Fourier transforms (non-phase shift corrected) over the k -range $3.5 - 12.5 \text{ \AA}^{-1}$ of the EXAFS data for $[\text{Fe}(\text{II})\text{PMA}]^+$ solid (—), $[\text{Fe}(\text{II})\text{PMA}]^+$ solution (-----), and Fe(II)BLM (.....).

Table 5.3. Summary of EXAFS Curve-Fitting Results.

compound	Fit #	FT window		element	bond length	
		width (Å)	CN ^{a,b}		(Å) ^b	<i>F</i>
[Fe(II)PMA] ⁺ solid	1	0.8 - 2.1	1.5	N	2.04	0.53
	2	0.8 - 2.1	1.8	N	1.98	0.31
			1.6	N	2.12	
			1.3	N	1.93	
	3	0.8 - 2.1	2.9	N	2.07	0.25
		1.1	N	2.23		
[Fe(II)PMA] ⁺ solution	4	0.8 - 2.2	1.4	N	2.13	0.75
	5	0.8 - 2.2	2.0	N	2.00	0.17
			2.9	N	2.17	
			2.1	N	1.99	
	6	0.8 - 2.2	3.3	N	2.15	0.14
		0.6	N	2.29		
Fe(II)BLM	7	1.0 - 2.25	3.0	N	2.16	0.41
	8	1.0 - 2.25	1.4	N	2.08	0.29
			3.0	N	2.19	
			1.6	N	2.06	
	9	1.0 - 2.25	4.2	N	2.19	0.23
		0.8	N	2.40		

^a CN = coordination number. ^b Errors in distances (± 0.02 Å) and coordination numbers ($\pm 25\%$) are estimated from the variance between EXAFS fitting results and values from models of crystallographically known structure.⁵¹

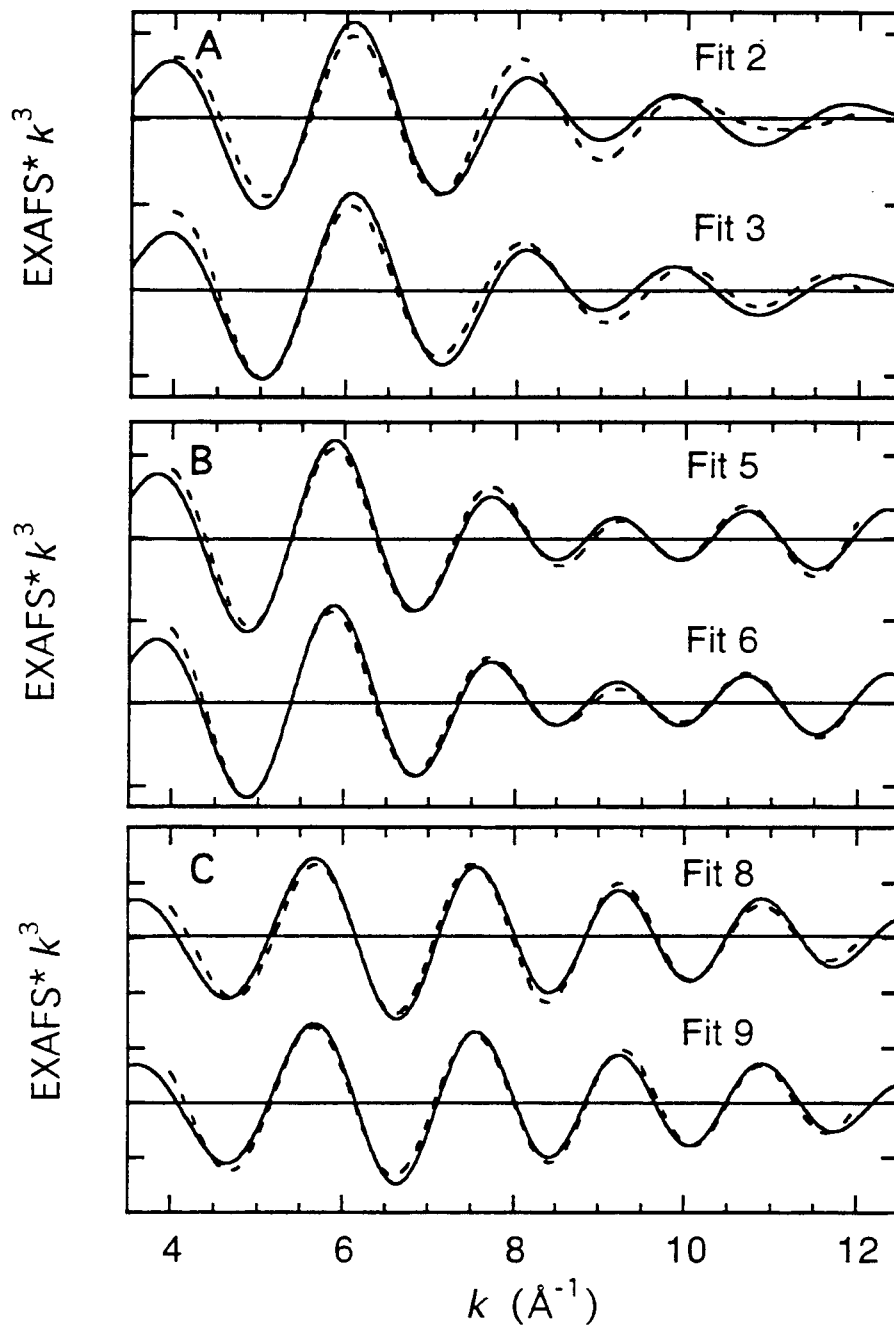


Figure 5.7. Empirical first shell fits to the Fourier-filtered EXAFS data with the solid lines representing the experimental data and the dashed lines representing the fits to the data. A) Fits 2 and 3 to the $[\text{Fe}(\text{II})\text{PMA}]^+$ solid data (Table 5.3). B) Fits 5 and 6 to the $[\text{Fe}(\text{II})\text{PMA}]^+$ solution data. C) Fits 8 and 9 to the $\text{Fe}(\text{II})\text{BLM}$ data. (The ordinate scale is 2 between consecutive tick marks with solid horizontal lines going through the zero point of each plot.)

likely ligation, only N parameters were used in the fits to the data. The EXAFS data of [Fe(II)PMA]⁺ solid could not be adequately fit with one shell of N atoms (Fit 1). The "goodness of fit parameter", *F*, was dramatically reduced when a second shell of N was added to the fit (Fit 2) giving N distances of 1.98 and 2.12 Å. However, the coordination number of 3.4 was still low and there was a mismatch in the fit to the data in the higher *k* region. Thus, a third shell of N was added to the fit (Fit 3). The *F* value was somewhat reduced and the fit matched the data more closely in the higher *k* region, (Figure 5.7A) giving the best fit to the data with 1 N at 1.93 Å, 3 N at 2.07 Å, and 1 N at 2.23 Å. The [Fe(II)PMA]⁺ solution data also could not be fit adequately with a single shell of N (Fit 4). The *F* value dropped by a factor of 4 when a second shell of N was added (Fit 5), giving 2 N at 2.00 Å and 3 N at 2.17 Å. Inclusion of a third shell of N (Fit 6) did not substantially improve the fit (Figure 5.7B) and this contribution had a relatively low coordination number of 0.6. Thus, the physical significance of the contribution at 2.29 Å is more questionable. The Fe(II)BLM EXAFS data could be fit reasonably well with one shell of N at 2.16 Å (Fit 7). A two shell fit (Fit 8) improved the *F* value and increased the coordination numbers. A three shell fit was also tried (Fit 9), however the fit to the data did not improve substantially (Figure 5.7C). The *F* value improved slightly and the total coordination numbers increased to 6.6 (vs. 4.4 for Fit 8).

The average first shell distance of [Fe(II)PMA]⁺ in solution is ~0.1 Å longer than that of the [Fe(II)PMA]⁺ solid, consistent with the Fe K-edge data which indicates that [Fe(II)PMA]⁺ solid is five-coordinate while [Fe(II)PMA]⁺ solution is six-coordinate. Both [Fe(II)PMA]⁺ solid and [Fe(II)PMA]⁺ solution have a first coordination sphere that has several contributions, as is evident from the curve-fitting results and the multiple peaks in the FTs (Figure 5.6B). Fe(II)BLM has a more regular first shell with an average first shell distance of 2.16 Å which is consistent with that of other six-coordinate high spin ferrous complexes (2.16 ± 0.03 Å).⁶⁵⁻⁶⁸ Importantly, a short Fe(II)-N contribution is present in all three complexes, which increases in length along the series [Fe(II)PMA]⁺ solid (1.93 Å) < [Fe(II)PMA]⁺ solution (2.00 Å) < Fe(II)BLM (2.06-2.08 Å). This short N can reasonably be assigned to the pyrimidine based upon the high degree of covalency derived from Abs, MCD, and rR results.⁴⁷ The trend in Fe-N_{pm} distances correlates with the Fe K-edge energy positions and with differences in π-backbonding as discussed below.

5.3.4. Discussion

The results obtained from these XAS experiments on Fe(II)BLM and [Fe(II)PMA]⁺ can be used in conjunction with results from Abs, MCD, and rR spectroscopies to develop

a detailed description of the geometric and electronic of the Fe(II)BLM active site.⁴⁷ With the array of data in the literature regarding the solution structure of Fe(II)BLM, some controversy still remains as to the definitive metal-chelating mode of this ligand. This problem has been addressed by comparison to [Fe(II)PMA]⁺, which has been found by molecular modeling to be most stable with the pyrimidine, imidazole, deprotonated amide and secondary amine coordinated equatorially and the primary amine bound axially, and is thought to have a solvent molecule coordinated at the open site in solution.⁶⁹ Binding of solvent to the sixth site is confirmed from the ligand field MCD spectra of solid and solution [Fe(II)PMA]⁺.⁴⁷ Solid [Fe(II)PMA]⁺ has a ⁵E_g splitting of 6100 cm⁻¹ indicating a five-coordinate, square pyramidal structure. In solution the ⁵E_g splitting for [Fe(II)PMA]⁺ decreases to 2110 cm⁻¹ indicating addition of a solvent molecule to the vacant axial position. The increase in coordination number is consistent with a decrease in the XAS pre-edge intensity as shown in Figure 5.5 and an increase in Fe–N bond lengths proceeding from five- to six-coordination as determined from the EXAFS analysis in Table 5.3. The similarities in the MCD ligand field spectrum and Δ^5E_g splitting of Fe(II)BLM to that of the [Fe(II)PMA]⁺ in solution,⁴⁷ as well as the comparable pre-edge shapes and intensities suggest that the coordination spheres of Fe(II)BLM and [Fe(II)PMA]⁺ in solution are not markedly different. The EXAFS analysis does indicate an overall increase in the Fe–N bond lengths of Fe(II)BLM relative to those of [Fe(II)PMA]⁺ which is consistent with the increased steric bulk of the BLM ligand compared with the more compact PMAH framework. Thus, a proposed solution structure of Fe(II)BLM is given in Figure 16 of reference 47 which is based on the PMAH ligand set and the experimental evidence that solvent coordinates at the sixth position.

The steric constraints of the BLM ligand framework coupled with the labile coordination site occupied by the solvent molecule suggest that oxygen binding to the Fe²⁺ center occurs via a dissociative mechanism. This is supported by the fact that in solution the Δ^5E_g splitting in the room temperature CD spectrum of Fe(II)BLM increases to ~3600 cm⁻¹ indicating that an axial ligand, likely H₂O or OH⁻, in Fe(II)BLM is weakly coordinated to the iron. Our spectral studies⁴⁷ of solid [Fe(II)PMA]⁺ have defined the five-coordinate complex as being square pyramidal which produces an open coordination position available for O₂ reaction. On the basis of the similarity in spectral features and activation chemistry of [Fe(II)PMA]⁺ and Fe(II)BLM in solution, this square pyramidal structure is reasonably correlated with the reactive intermediate in the mechanism of O₂ binding to Fe(II)BLM.

In addition to the geometric structure obtained for Fe(II)BLM through the MCD excited state ligand field and XAS analyses, the electronic structures of Fe(II)BLM and

[Fe(II)PMA]⁺ have been elucidated through MCD ligand field ground state, charge transfer excited state, and rR spectroscopies.⁴⁷ From the ligand field analysis, [Fe(II)PMA]⁺ solid exhibits nested saturation magnetization curves consistent with the five-coordinate, square pyramidal geometry. The value of $V/2\Delta$ (0.33) derived from this analysis indicates that the structure is highly rhombic due to the short Fe–N bond distance in the equatorial plane determined from the EXAFS results which supports the presence of strong metal-ligand π backbonding. In solution [Fe(II)PMA]⁺ and Fe(II)BLM also exhibit nested saturation magnetization curves that result in unusually small values of the spin Hamiltonian parameter (δ), not generally observed for six-coordinate non-heme ferrous active sites. This corresponds to a large splitting of the t_{2g} set of d-orbitals ($-\Delta$) which requires strong π -bonding interactions between the metal and pyrimidine π^* orbitals. The values of $V/2\Delta$ of 0.24 for [Fe(II)PMA]⁺ and 0.18 for Fe(II)BLM indicate a more moderate degree of rhombic distortion which decreases with increasing Fe–N bond length. Thus the magnitudes of δ (and $-\Delta$) are different from typical six-coordinate model complexes indicating that strong π -bonding effects are present, consistent with the EXAFS results exhibiting a short Fe–N distance.

An important deviation from non-heme ferrous behavior demonstrated by Fe(II)BLM and [Fe(II)PMA]⁺ is the existence of low energy CT transitions analogous to $d_{\pi} \rightarrow \pi^*$ MLCT transitions in heme systems.⁷⁰ The presence of moderately intense, low energy MLCT transitions in the low temperature Abs and MCD spectra of [Fe(II)PMA]⁺ and Fe(II)BLM⁴⁷ represents an important deviation from other non-heme iron centers and reflects high covalency. The MLCT transition energies and intensities determine the degree of metal-ligand π -backbonding which decreases along the series solid [Fe(II)PMA]⁺ > solution [Fe(II)PMA]⁺ > Fe(II)BLM. Assignment of these bands as Fe(II) \rightarrow pyrimidine MLCT transitions is derived from the strong resonance enhancement of the pyrimidine normal modes at 680, 744, 1519, and 1542 cm^{-1} in the [Fe(II)PMA]⁺ Raman spectrum, thereby implicating pyrimidine as the specific ligand associated with the large d_{π} splitting and short Fe–N bond.⁴⁷

These MLCT transitions in Fe(II)BLM and [Fe(II)PMA]⁺ indicate the presence of significant π -backbonding not observed for other non-heme iron centers. This results from the presence of five strong field nitrogen ligands (with solvent occupying the sixth site) complexed to the Fe²⁺ which raises the energy of the d-manifold, reduces the energy gap between the d_{π} and ligand π^* orbitals, and increases the propensity for metal-ligand backbonding at the site. This π -backbonding contributes to the unique chemistry and reactivity of Fe(II)BLM. Unlike other non-heme iron active sites, Fe(II)BLM reversibly binds CO and reacts with NO and other strong field ligands to form low spin complexes.

Addition of this sixth strong field ligand induces the low spin conversion through an increase in the already sizable splitting (*i.e.*, all nitrogen ligands) of the d-orbitals (10Dq) which overcomes the electron-spin pairing energy. The unusual binding of CO derives from the tendency of the Fe(II)BLM site to backbond. Similar "symbiotic" behavior is common in inorganic coordination complexes and is rationalized by the relative softness (*i.e.*, polarizability) of the metal center induced by the coordination sphere.⁷¹ Formation of the Fe(II)BLM–CO complex is further promoted by the increased ligand field stabilization energy of the resultant low spin d⁶ configuration. The presence of backbonding also contributes to the unusual O₂ reactivity of this site relative to other non-heme Fe systems. Backbonding to the pyrimidine ligand decreases the extent of charge transfer to the O₂ which shifts the equilibrium in eq. (1) to the left, making FeBLM less likely to dissociate O₂⁻, and contributing to the reversible binding of O₂ by the site.



This reduced charge transfer to the bound superoxide also enhances its propensity for further reduction to form the Fe(III)–O₂²⁻ site of activated BLM. This is in contrast to a pathway observed in other non-heme iron systems where strong π-backbonding is absent. In these cases, a diffusible superoxide radical may be formed by direct autoxidation of the Fe²⁺ site (eq. (1), right).^{72,73} In the presence of DNA, a superoxide radical would lead to non-selective cleavage products which are not observed in BLM chemistry.¹⁰

The low energy MLCT transitions, the reversible binding of O₂, and the formation of low spin complexes with CO and NO suggest that Fe(II)BLM more closely parallels heme rather than non-heme iron chemistry. Yet the differences in these ferrous centers are significant as heme systems exhibit more intense ($\epsilon \approx 10,000 \text{ M}^{-1} \text{ cm}^{-1}$), lower energy ($\sim 10,000 \text{ cm}^{-1}$) MLCT transitions than Fe(II)BLM indicating much greater Fe²⁺ backbonding into the tetrapyrrole macrocycle.⁷⁰ This difference in backbonding correlates with differences in the O₂ reactivity of BLM relative to heme iron centers. In particular, the oxygen intermediate of cytochrome P-450 is thought to be a ferryl species^{26,74} which is structurally distinct from the peroxide-level intermediate of activated BLM.^{27,28} Our results suggest that other non-heme Fe enzymes which exhibit little or no low energy MLCT transitions relative to Fe(II)BLM may be expected to form intermediates which more closely resemble the ferric-peroxide species of activated BLM than the ferryl species of heme systems.

In summary, these studies have provided significant insight into the oxygen reactivity of Fe(II)BLM. The lability of high spin iron combined with steric constraints of

the BLM ligand framework and its weaker axial interaction with solvent support a dissociative mechanism for O₂ reactivity. These spectroscopic studies of solid [Fe(II)PMA]⁺ have defined the nature of such a five-coordinate intermediate as square pyramidal which provides an open coordination position for reaction with O₂. A major electronic structure difference between Fe(II)BLM (and [Fe(II)PMA]⁺) and other non-heme ferrous sites is the presence of low energy CT transitions which reflect strong Fe(II)->pyrimidine backbonding. Relative to non-heme iron complexes this backbonding results in reduced charge donation to the O₂ which 1) contributes to the reversible binding of O₂ exhibited by Fe(II)BLM, 2) stabilizes the initial Fe(III)-O₂⁻ intermediate from loss of O₂⁻ and reaction with substrate, and 3) promotes the further reduction of Fe(III)BLM-O₂⁻ to form activated BLM. Despite generally being considered a non-heme iron system due to the absence of an extensive delocalized π network, the existence of low energy MLCT transitions with reasonable intensity, hence the presence of some backbonding, identify BLM as an important link bridging the chemistry of non-heme and heme active sites.

5.3.5. Acknowledgments

Pradip Mascharak and Richard Guarjardo of UC Santa Cruz provided the [Fe(II)(PMA)]Cl•MeOH sample. Kelly Loeb and Jeff Zaleski prepared the Fe(II)BLM sample and performed the Abs, rR, and MCD experiments alluded to in the Discussion. This work was supported by grants from the National Institutes of Health (GM40392, E.I.S.) and National Science Foundation (CHE-9121576, K.O.H.). SSRL is supported by the U.S. Department of Energy, Office of Basic Energy Science, Divisions of Chemical and Materials Sciences, and in part by the National Institutes of Health, Biomedical Research Technology Program (RR-01209), and the US Department of Energy, Office of Health and Environmental Research.

5.3.6. References and Notes

- (1) Umezawa, H.; Maeda, K.; Takeuchi, T.; Oakami, Y. *J. Antibiot.* **1966**, *19*, 200.
- (2) Umezawa, H.; Surhara, Y.; Takita, T.; Maeda, K. *J. Antibiot.* **1966**, *19*, 210.
- (3) Umezawa, H. *Biomed.* **1973**, *18*, 459.
- (4) Hutchinson, F.; Povirk, L. F. In *Bleomycin: Chemical, Biochemical, and Biological Aspects*; Hecht, S. M., Ed.; Springer-Verlag: New York, 1979; p 255.
- (5) Chien, M.; Grollman, A. P.; Horwitz, S. B. *Biochemistry* **1977**, *16*, 3641.

- (6) Kross, J.; Henner, W. D.; Haseltine, W. A.; Rodriguez, L.; Levin, M. D.; Hecht, S. M. *Biochemistry* **1982**, *21*, 3711.
- (7) Fisher, L. M.; Kuroda, R.; Sakai, T. T. *Biochemistry* **1985**, *24*, 3199.
- (8) Umezawa, H. *Pure Appl. Chem.* **1971**, *28*, 665.
- (9) DeReimer, L. H.; Meares, C. F.; Goodwin, D. A.; Diamanti, C. I. *J. Med. Chem.* **1979**, *22*, 1019.
- (10) Stubbe, J.; Kozarich, J. W. *Chem. Rev.* **1987**, *87*, 1107.
- (11) Petering, D. H.; Byrnes, R. W.; Antholine, W. E. *Chem.-Biol. Interactions* **1990**, *73*, 133.
- (12) Sausville, E. A.; Peisach, J.; Horwitz, S. B. *Biochemistry* **1978**, *17*, 2740.
- (13) Ishida, R.; Takahashi, T. *Biochem. Biophys. Res. Commun.* **1975**, *66*, 1432.
- (14) Oppenheimer, N. J.; Chang, C.; Rodriguez, L. O.; Hecht, S. M. *J. Biol. Chem.* **1981**, *256*, 1514.
- (15) Ehrenfeld, G. M.; Murugesan, N.; Hecht, S. M. *Inorg. Chem.* **1984**, *23*, 1496.
- (16) Lown, J. W.; Sim, S.-K. *Biochem. Biophys. Res. Commun.* **1977**, *77*, 1150.
- (17) Sausville, E. A.; Peisach, J.; Horwitz, S. B. *Biochem. Biophys. Res. Commun.* **1976**, *73*, 814.
- (18) Sausville, E. A.; Stein, R. W.; Peisach, J.; Horwitz, S. B. *Biochemistry* **1978**, *17*, 2746.
- (19) Burger, R. M.; Peisach, J.; Horwitz, S. B. *J. Biol. Chem.* **1981**, *256*, 11636.
- (20) Giloni, L.; Takeshita, M.; Johnson, F.; Iden, C.; Grollman, A. P. *J. Biol. Chem.* **1981**, *256*, 8608.
- (21) Burger, R. M.; Berkowitz, A. R.; Peisach, J.; Horwitz, S. B. *J. Biol. Chem.* **1980**, *255*, 11832.
- (22) Fulmer, P.; Petering, D. H. *Biochemistry* **1994**, *33*, 5319.
- (23) Albertini, J.-P.; Garnier-Suillerot, A.; Tosi, L. *Biochem. Biophys. Res. Commun.* **1982**, *104*, 557.
- (24) Burger, R. M.; Kent, T. A.; Horwitz, S. B.; Münck, E.; Peisach, J. *J. Biol. Chem.* **1983**, *258*, 1559.
- (25) Hecht, S. M. *Acc. Chem. Res.* **1986**, *19*, 383.
- (26) Ortiz de Montellano, P. R. *Cytochrome P-450: Structure, Mechanism, and Biochemistry*; Plenum Press: New York, 1986, p 429.
- (27) Sam, J. W.; Tang, X.-J.; Peisach, J. *J. Am. Chem. Soc.* **1994**, *116*, 5250.
- (28) Westre, T. E.; Loeb, K. E.; Zaleski, J. M.; Hedman, B.; Hodgson, K. O.; Solomon, E. I. *J. Am. Chem. Soc.* **1995**, *117*, 1309.

- (29) Iitaka, Y.; Nakamura, H.; Nakatani, T.; Muraoka, Y.; Fujii, A.; Takita, T.; Umezawa, H. *J. Antibiot.* **1978**, *31*, 1070.
- (30) Sugiura, Y.; Suzuki, T.; Otsuka, M.; Kobayashi, S.; Ohno, M.; Takita, T.; Umezawa, H. *J. Biol. Chem.* **1983**, *258*, 1328.
- (31) Oppenheimer, N. J.; Chang, C.; Chang, L.-H.; Ehrenfeld, G.; Rodriguez, L. O.; Hecht, S. M. *J. Biol. Chem.* **1982**, *257*, 1606.
- (32) Oppenheimer, N. J.; Rodriguez, L. O.; Hecht, S. M. *Proc. Natl. Acad. Sci. USA* **1979**, *76*, 5616.
- (33) Akkerman, M. A. J.; Neijman, E. W. J. F.; Wijmenga, S. S.; Hilbers, C. W.; Bermel, W. *J. Am. Chem. Soc.* **1990**, *112*, 7462.
- (34) Sugiura, Y.; Kuwahara, J.; Suzuki, T. *FEBS Letters* **1985**, *182*, 39.
- (35) Sugiura, Y.; Ishizu, K. *J. Inorg. Biochem.* **1979**, *11*, 171.
- (36) Sugiura, Y. *J. Antibiot.* **1978**, *31*, 1206.
- (37) Sugiura, Y.; Ishizu, K.; Miyoshi, K. *J. Antibiot.* **1979**, *32*, 453.
- (38) Sugiura, Y. *J. Am. Chem. Soc.* **1980**, *102*, 5208.
- (39) Guajardo, R. J.; Hudson, S. E.; Brown, S. J.; Mascharak, P. K. *J. Am. Chem. Soc.* **1993**, *115*, 7971.
- (40) Henichart, J.-P.; Bernier, J.-L.; Helbecque, N.; Houssin, R. *Nucl. Acid Res.* **1985**, *13*, 6703.
- (41) Kenani, A.; Bailly, C.; Helbecque, N.; Houssin, R.; Bernier, J.-L.; Henichart, J.-P. *Eur. J. Med. Chem.* **1989**, *24*, 371.
- (42) Sugiyama, T.; Ohno, M.; Shibasaki, M.; Otsuka, M.; Sugiura, Y.; Kobayashi, S.; Maeda, K. *Heterocycles* **1994**, *37*, 275.
- (43) Shepherd, R. E.; Lomis, T. J.; Koepsel, R. R.; Hedge, R.; Mistry, J. S. *Inorg. Chim. Acta* **1990**, *171*, 139.
- (44) Brown, S. J.; Tao, X.; Wark, T. A.; Stephan, D. W.; Mascharak, P. K. *Inorg. Chem.* **1988**, *27*, 1581.
- (45) Muetterties, M.; Mascharak, P. K.; Cox, M. B.; Arora, S. K. *Inorg. Chim. Acta* **1989**, *160*, 123 .
- (46) The chemical formula for PMAH is 2-((N-(aminoethyl)amino)methyl)-4-(N-(2-(4-imidazolyl)ethyl)carbomoyl)-5-bromopyrimidine where H is the dissociable amide proton. PMAH forms a 1:1 iron complex with pyrimidine, imidazole, amide, secondary and primary amine functionalities.
- (47) Loeb, K. E.; Zaleski, J. M.; Westre, T. E.; Guajardo, R. J.; Mascharak, P. K.; Hedman, B.; Hodgson, K. O.; Solomon, E. I. *J. Am. Chem. Soc.* **1995**, *117*, 4545.

- (48) Brown, S. J.; Mascharak, P. K.; Stephan, D. W. *J. Am. Chem. Soc.* **1988**, *110*, 1996.
- (49) Scott, R. A.; Hahn, J. E.; Doniach, S.; Freeman, H. C.; Hodgson, K. O. *J. Am. Chem. Soc.* **1982**, *104*, 5364.
- (50) Cramer, S. P.; Tench, O.; Yocum, M.; George, G. N. *Nucl. Instrum. Methods Phys. Res.* **1988**, *A266*, 586.
- (51) Cramer, S. P.; Hodgson, K. O.; Stiefel, E. I.; Newton, W. E. *J. Am. Chem. Soc.* **1978**, *100*, 2748.
- (52) Cramer, S. P.; Hodgson, K. O. *Prog. Inorg. Chem.* **1979**, *25*, 1.
- (53) Scott, R. A. *Methods Enzymol.* **1985**, *117*, 414.
- (54) Iball, J.; Morgan, C. H. *Acta Crystallogr.* **1967**, *23*, 239.
- (55) Roof, R. B., Jr. *Acta Crystallogr.* **1956**, *9*, 781.
- (56) Johansson, L.; Molund, M.; Oskarsson, Å. *Inorg. Chim. Acta.* **1978**, *31*, 117.
- (57) Johansson, L. *Chemica Scripta.* **1976**, *9*, 30.
- (58) Hodges, K. D.; Wollman, R. G.; Barefield, E. K.; Hendrickson, D. N. *Inorg. Chem.* **1977**, *16*, 2746.
- (59) Burbridge, C. D.; Goodgame, D. M. L. *Inorg. Chim. Acta* **1970**, *4*, 231.
- (60) Shulman, R. G.; Yafet, Y.; Eisenberger, P.; Blumberg, W. E. *Proc. Natl. Acad. Sci. USA* **1976**, *73*, 1384.
- (61) Cramer, S. P.; Eccles, T. K.; Kutzler, F. W.; Hodgson, K. O.; Mortenson, L. E. *J. Am. Chem. Soc.* **1976**, *98*, 1287.
- (62) Kau, L.-S.; Spira-Solomon, D. J.; Penner-Hahn, J. E.; Hodgson, K. O.; Solomon, E. I. *J. Am. Chem. Soc.* **1987**, *109*, 6433.
- (63) Roe, A. L.; Schneider, D. J.; Mayer, R. J.; Pyrz, J. W.; Widom, J.; Que, L., Jr. *J. Am. Chem. Soc.* **1984**, *106*, 1676.
- (64) Randall, C. R.; Shu, L.; Chiou, Y.-M.; Hagen, K. S.; Ito, M.; Kitajima, N.; Lachicotte, R. J.; Zang, Y.; Que, L., Jr. *Inorg. Chem.* **1995**, *34*, 1036.
- (65) Montgomery, H.; Chastain, R. V.; Natt, J. J.; Witkowska, A. M.; Lingafelter, E. *C. Acta Cryst.* **1967**, *22*, 775.
- (66) Price, D. C. *Can. J. Phys.* **1987**, *65*, 1280.
- (67) Miller, L. L.; Jacobsen, R. A.; Chen, Y.-S.; Kurtz, D. M., Jr. *Acta Cryst.* **1989**, *C45*, 527.
- (68) Kitajima, N.; Fukui, H.; Moro-oka, Y. *J. Am. Chem. Soc.* **1990**, *112*, 6402.
- (69) Wu, Y.-D.; Houk, K. N.; Valentine, J. S.; Nam, W. *Inorg. Chem.* **1992**, *31*, 718.

- (70) Lever, A. B. P.; Gray, H. B. *Iron Porphyrins: Part One*; Addison-Wesley Publishing Co., Inc.: Reading, 1983.
- (71) Jørgensen, C. K. *Inorg. Chem.* **1964**, 3, 1201.
- (72) Feig, A. L.; Lippard, S. J. *Chem. Rev.* **1994**, 94, 759.
- (73) Brown, E. R.; Mazzarella, J. D. *J. Electroanal. Chem.* **1987**, 222, 173.
- (74) Dawson, J. H. *Science* **1988**, 240, 433.
- (75) Solomon, E. I.; Pavel, E. G.; Loeb, K. E.; Campochiaro, C. *Coord. Chem. Rev.* in press.

5.4. Activated Bleomycin

5.4.1. Introduction

Bleomycin (BLM), a glycopeptide antibiotic produced by strains of *Streptomyces verticillus*, is currently used in treatment against a variety of carcinomas and lymphomas.¹ Its therapeutic activity involves selective DNA cleavage at certain GT and GC sites in the presence of metal ions (in particular Fe²⁺) and dioxygen.^{2,3} The coordination environment of the iron is believed to be square pyramidal with the iron ligated to five nitrogens from histidine, pyrimidine, a deprotonated peptide function, and primary and secondary amine groups (see section 5.3).⁴ Kinetic and spectral studies have demonstrated that the activation mechanism involves high spin Fe(II)BLM reacting with dioxygen and an electron to form activated BLM which is formally at the peroxo-ferric level.⁵ Activated BLM (and the activated form of the analogous PMA model complex)⁶ is the first mononuclear non-heme iron oxygen intermediate stable enough for detailed spectroscopic study. DNA degradation by activated BLM involves C-H bond cleavage at the C4' position of deoxyribose moieties and results in the production of base propenals.^{3,7} This mechanism is similar to the monooxygenation mechanism of cytochrome P-450 and has led researchers to postulate an oxo-ferryl BLM intermediate,³ as has been generally considered to be present in P-450 chemistry. Alternatively, spectroscopic model studies^{6,8} and mass spectrometric studies⁹ have indicated activated BLM to have an iron (III)-peroxide site. In this study, X-ray absorption spectroscopy (XAS) has been used to directly probe the oxidation and spin state of the iron in activated BLM and to determine if a short iron-oxo bond is present, which would be characteristic of the oxo-ferryl species of heme iron. Both the pre-edge and edge regions of the Fe K-edge spectra indicate that activated BLM is a low spin ferric complex. Bond distances obtained from extended X-ray absorption fine structure (EXAFS) are similar to those in low spin Fe(III)BLM and show no evidence for a short iron-oxo bond. These data indicate that the Fe(III)-peroxide formalism is an appropriate description of the iron center in activated BLM and suggest that such an intermediate may play an important role in activating O₂ for further chemistry in the catalytic cycles of mononuclear non-heme iron enzymes.

5.4.2. Experimental Section

Blenoxane (a mixture of 60% BLM A₂, 30% BLM B₂, and 10% other BLMs) was obtained as a gift from Bristol-Meyers Squibb and used without further purification. For all XAS samples a 5 mM apo-BLM solution consisting of equal volumes of 300 mM, pH 7.0, HEPES buffer (Sigma) and ethylene glycol (Mallinckrodt) was prepared. Subsequent anaerobic and aerobic additions of 5 μ L of a Fe(NH₄)₂(SO₄)₂·6H₂O (FeAS; MCB Manufacturing Chemists, Inc.) stock solution yielded ~4 mM Fe(II)BLM and Fe(III)BLM, respectively. Sample integrity (< 5% ferric impurity) was confirmed by optical absorption with an HP 8452A diode array spectrophotometer and by electron paramagnetic resonance (EPR) using a Bruker ER 220D-SRC spectrometer interfaced to an IBM XT computer and a Bruker ER 042MRH microwave bridge (X-band). The Fe(II)BLM sample was syringed into the XAS sample cell (Lucite cell 23 x 1 x 3 mm with 37 μ m Kapton windows) under a N₂ atmosphere and frozen in liquid N₂ before exposure to air. Activated BLM was formed from the reaction of low spin Fe(III)BLM with H₂O₂ (Mallinckrodt),⁵ because the reaction of Fe(II)BLM with O₂ yields a 50:50 mixture of activated BLM and low spin Fe(III)BLM. The intermediate was prepared at 4 °C by rapid addition of 3.8 μ L of H₂O₂ (100-fold excess) to 80 μ L Fe(III)BLM followed by simultaneous freezing in the XAS sample cell and a 3 mm EPR tube, after a 25 sec incubation. This method resulted in samples with superimposable EPR spectra. The concentrations of the individual components of the activated BLM sample were determined by spin quantitation of the sample in the EPR tube using a 1 mM CuSO₄·5H₂O (Mallinckrodt) solution, in 2 mM HCl and 2 M NaClO₄ (Fisher), and a 3 mM Fe(III)EDTA solution in 50/50 glycerol (Baker)/water (prepared by stirring Fe(III)Cl₃·6H₂O (Baker) with excess Na₂EDTA·2H₂O (Aldrich) for 12 hours) as standards in the g=2.0 and g=4.3 regions, respectively. The proportionality of the high field feature in the Fe(III)BLM EPR spectrum (g=1.89) to the total low spin ferric signal was used to account for this contribution to the overlapping features in the EPR spectrum of the intermediate and quantitate the remaining low spin signal attributed to activated BLM. Quantitation of the EPR silent degradation product was achieved by subtracting the percentages of the EPR detectable components from the total Fe(III)BLM concentration determined by quantitation of the sample prior to activation and accounting for the 3.8 μ L H₂O₂ dilution. This revealed a sample composed of 81(4)% activated BLM, 7(1)% low spin Fe(III)BLM, 4(1)% high spin ferric, and 8(1)% Fe degradation product undetectable by EPR at 77 K. A separate sample with the degradation product of

the Fe(III)BLM-H₂O₂ reaction was generated by allowing activated BLM to decay for 12 hours producing 8% high spin ferric with the remaining 92% Fe EPR silent at 77 K.

X-ray absorption spectra were recorded at the Stanford Synchrotron Radiation Laboratory (SSRL) on unfocused wiggler beamline 7-3 during dedicated conditions (3 GeV, 50-100 mA). The radiation was monochromatized using a Si(220) double-crystal monochromator. An Oxford Instruments continuous-flow liquid helium CF1208 cryostat was used to maintain a constant temperature of 10 K. Energies were calibrated using an internal Fe foil standard, assigning the first inflection point to 7111.2 eV.¹⁰ The spectrometer energy resolution was approximately 1.4 eV¹¹ with reproducibility in edge position determination of < 0.2 eV.

Data were collected on Fe(II)BLM, Fe(III)BLM, 81(4)% activated BLM, and the degradation product of the Fe(III)BLM-H₂O₂ reaction. Data were measured to $k = 15 \text{ \AA}^{-1}$ with 1 mm high pre-monochromator beam defining slits, detuning the monochromator 50% at 7998 eV to minimize harmonic contamination. The fluorescence signal was monitored by using a 13-element Ge solid-state array detector¹² windowed on the Fe K α signal. During the experiment, count rates of approximately 30,000 s⁻¹ total per element were not exceeded. Approximately thirty scans were averaged for each sample. A smooth pre-edge background was removed from the averaged spectra by fitting a second order polynomial to the pre-edge region and subtracting this polynomial from the entire spectrum. A three-segment spline approximately even in k -space was fit to the EXAFS region and the data normalized to an edge jump of one at 7130 eV. The spline was chosen so that it minimized residual low-frequency background but did not reduce the EXAFS amplitude as checked by monitoring the Fourier transform of the EXAFS during the background subtraction process.

Fe K-edge spectra were also collected on several iron model complexes. [Fe(Prpep)₂] \cdot 2CH₃OH and [Fe(Prpep)₂] \cdot ClO₄ \cdot 2CH₃OH \cdot CH₃CN were obtained as gifts from Pradip Mascharak.¹³ [Fe(imidazole)₆] \cdot Cl₂¹⁴ and Fe(acac)₃^{15,16} were prepared as described in the literature. [Fe(Prpep)₂] \cdot 2CH₃OH, [Fe(Prpep)₂] \cdot ClO₄ \cdot 2CH₃OH \cdot CH₃CN, and [Fe(imidazole)₆] \cdot Cl₂ are air-sensitive and thus the following procedure was carried out in a nitrogen-filled glove box. The crystalline samples were each mixed with boron nitride (BN) and ground into a fine powder. The BN/sample mixture was pressed into a 1 mm thick Al spacer that was sealed with 63.5 μ m Mylar tape windows and frozen in liquid nitrogen. Data were measured in transmission mode with N₂-filled ionization chambers to $k = 9.5 \text{ \AA}^{-1}$ detuning the monochromator 50% at 7474 eV to minimize harmonic contamination. Two to three scans were averaged for each sample. A smooth pre-edge background was removed from the averaged spectra by fitting a first order

polynomial to the pre-edge region and subtracting this polynomial from the entire spectrum. A two segment spline of order two was fit to the EXAFS region and the data normalized to an edge jump of one at 7130 eV.

EXAFS data reduction was performed on the normalized BLM spectra according to established methods.¹⁷⁻¹⁹ The normalized data were converted to k -space. The photoelectron wave vector, k , is defined by $[2m_e(E-E_0)/\hbar^2]^{1/2}$ where m_e is the electron mass, E is the photon energy, \hbar is Planck's constant divided by 2π , and E_0 is the threshold energy of the absorption edge, which was defined to be 7130 eV for the Fe K absorption edge. The empirical EXAFS data analyses were performed with nonlinear least-square curve-fitting^{10,17-19} techniques using empirical phase and amplitude parameters. The following models were used to obtain the empirical Fe-X backscattering parameters of interest: Fe-O from $\text{Fe}(\text{acac})_3$ ^{15,16} and Fe-N from $[\text{Fe}(1,10\text{-phenanthroline})_3](\text{ClO}_4)_3$ ^{20,21}. Fourier transforms (from k to R space) were performed for the data range 3.5-12.5 \AA^{-1} with a Gaussian window of 0.1 \AA^{-1} . The window widths used in the backtransforms (from R to k space) for the BLM samples are given in the Results and Analysis section. The window widths were kept as similar as possible to those used to extract amplitude and phase parameters from the model compounds to minimize artifacts introduced by the Fourier filtering technique. All curve-fitting was based on k^3 -weighted data and applied to the individual filtered shell of interest. Only the structure-dependent parameters, the distance and coordination number, were varied unless stated otherwise. A "goodness of fit" parameter, F , was calculated as $F = \{[k^6(\text{data} - \text{fit})^2]/(\text{no. of points})\}^{1/2}$ for each fit.

Contributions to the XAS spectrum due to low spin Fe(III)BLM and degradation product were subtracted from the normalized data of the 81% activated BLM spectrum to obtain a 96% activated BLM spectrum. As stated above, all the averaged spectra were normalized to an edge jump of one. Fe(III)BLM and degradation product data were used to subtract off 7% and 8%, respectively, from the normalized 81% activated BLM spectrum, giving a 96% pure activated BLM spectrum which was then re-normalized to an edge jump of one. The remaining 4% corresponds to a high spin ferric impurity for which no reference is available. The 96% activated BLM edge spectrum was identical in shape to that of the 81% pure sample, however, the edge shifted 0.7 eV to higher energy. The 96% activated BLM spectrum was used in the edge analysis, whereas the original 81% activated BLM spectrum was used in the EXAFS analysis.

5.4.3. Results and Analysis

5.4.3.1. Fe K-Edge XAS. The Fe-K edge spectra of Fe(II)BLM, Fe(III)BLM, and activated BLM are shown in Figure 5.8, whereas the inset shows an expanded view of the $1s \rightarrow 3d$ pre-edge region. The lowest energy peaks arise from the weak $1s \rightarrow 3d$ transition at ~ 7113 eV followed by the $1s \rightarrow 4p$ transition at ~ 7125 eV. The spectrum of Fe(II)BLM (solid line) has two low-intensity pre-edge peaks at 7111.4 and 7113.6 eV (Figure 5.8 inset). The data for both Fe(III)BLM (dashed line) and activated BLM (dotted line) have similar pre-edge features, each with a maximum at 7112.5 eV with similar intensity and a barely resolvable low energy shoulder for Fe(III)BLM at ~ 7111 eV and a sloping tail in this lower energy region in activated BLM. The rising edge inflection points occur at 7121.3 eV for Fe(II) BLM, 7127.0 eV for Fe(III)BLM, and 7127.3 eV for activated BLM. Figure 5.9 displays the $1s \rightarrow 3d$ pre-edge region for representative iron model complexes: a) a low spin ferrous complex, $[\text{Fe}(\text{Prpep})_2] \cdot 2\text{CH}_3\text{OH}$ ²²; b) a high spin ferrous complex, $[\text{Fe}(\text{imidazole})_6]\text{Cl}_2$ ¹⁴; c) a low spin ferric complex, $[\text{Fe}(\text{Prpep})_2]\text{ClO}_4 \cdot 2\text{CH}_3\text{OH} \cdot \text{CH}_3\text{CN}$ ²²; and d) a high spin ferric complex, $\text{Fe}(\text{acac})_3$.^{15,16} The $[\text{Fe}(\text{Prpep})_2] \cdot 2\text{CH}_3\text{OH}$ spectrum has a single peak in the pre-edge region located at 7112.1 eV, while the $[\text{Fe}(\text{imidazole})_6]\text{Cl}_2$ spectrum has three features positioned at approximately 7111.2, 7112.3, and 7113.67 eV. The data for $[\text{Fe}(\text{Prpep})_2]\text{ClO}_4 \cdot 2\text{CH}_3\text{OH} \cdot \text{CH}_3\text{CN}$ shows three pre-edge features: a low-energy shoulder at 7111.0 eV, a more intense peak at 7112.7 eV, and a weaker feature at 7114.4 eV. The pre-edge region in the spectrum for $\text{Fe}(\text{acac})_3$ has two features positioned at 7112.8 and 7114.3 eV.

The energy of the edge position (dominated by the $1s \rightarrow 4p$ transition) is dependent upon the effective nuclear charge of the absorbing metal atom. This charge is governed by a combination of effects, including the formal metal oxidation state, the number and type of ligating atoms, and the coordination geometry.²³⁻²⁸ In this case, the types of ligating atoms and the coordination sphere are similar, thus changes in the edge energy can be correlated to the iron oxidation state. From Figure 5.8, the edge spectrum of activated BLM is very close in energy and similar in shape to that of Fe(III)BLM, in contrast to the Fe(II)BLM spectrum which is ~ 4 eV lower in energy and has a more intense $1s \rightarrow 4p$ feature, indicating that activated BLM contains a ferric metal center. It should be noted that the edge inflection point of horseradish peroxidase compound I, which has a purported Fe(IV)=O metal site, was observed to be at ~ 2 eV higher in energy than that of the resting ferric horseradish peroxidase.²⁹

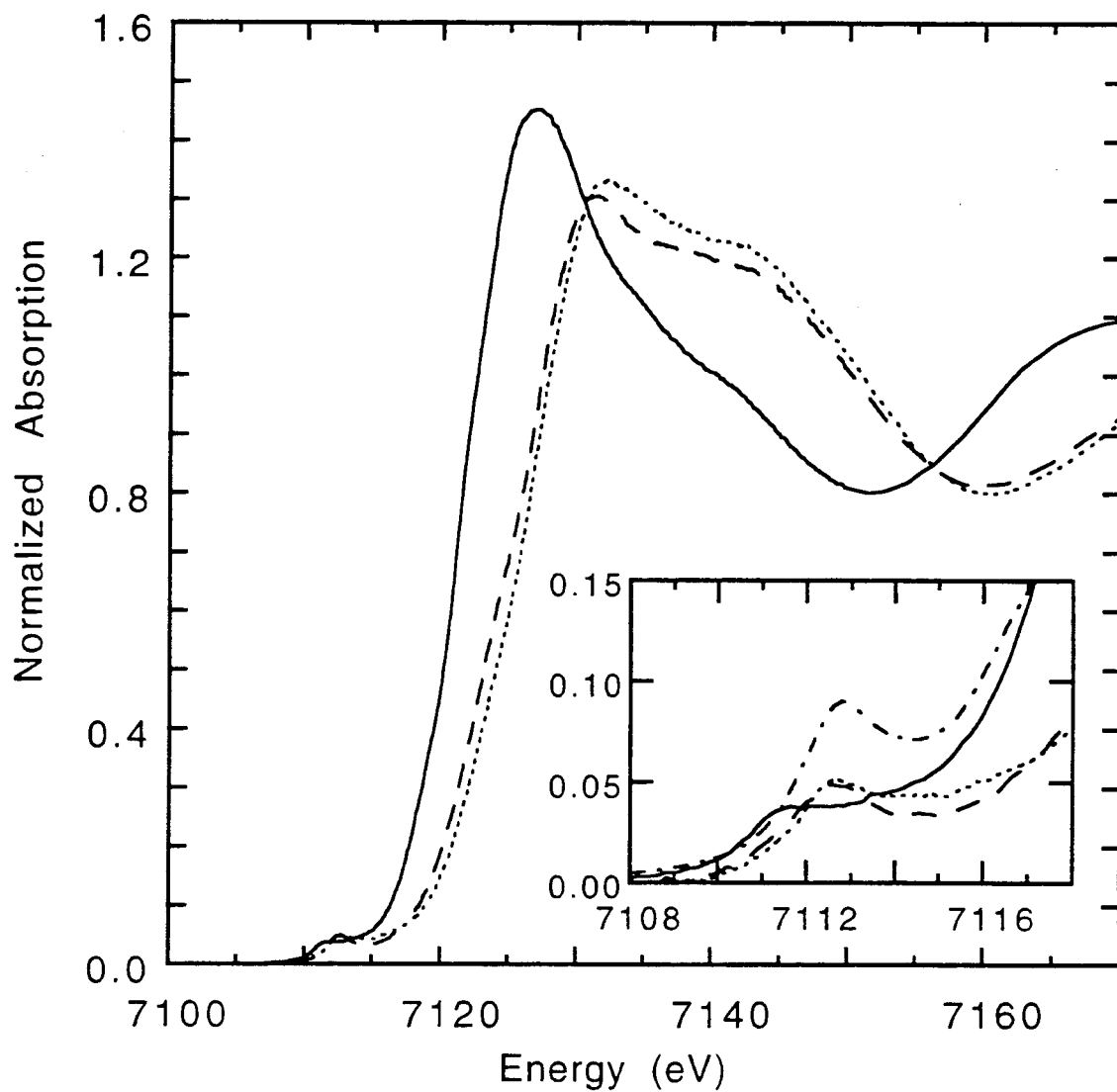


Figure 5.8. Fe-K XAS edge spectra of Fe(II)BLM (—), Fe(III)BLM (---), and activated BLM (.....). The inset shows an expansion of the 1s→3d pre-edge region and includes pre-edge data of Fe(Me₃TACN)(NO)(N₃)₂ (— · —), which has a Fe-N(O) bond of 1.74 Å.

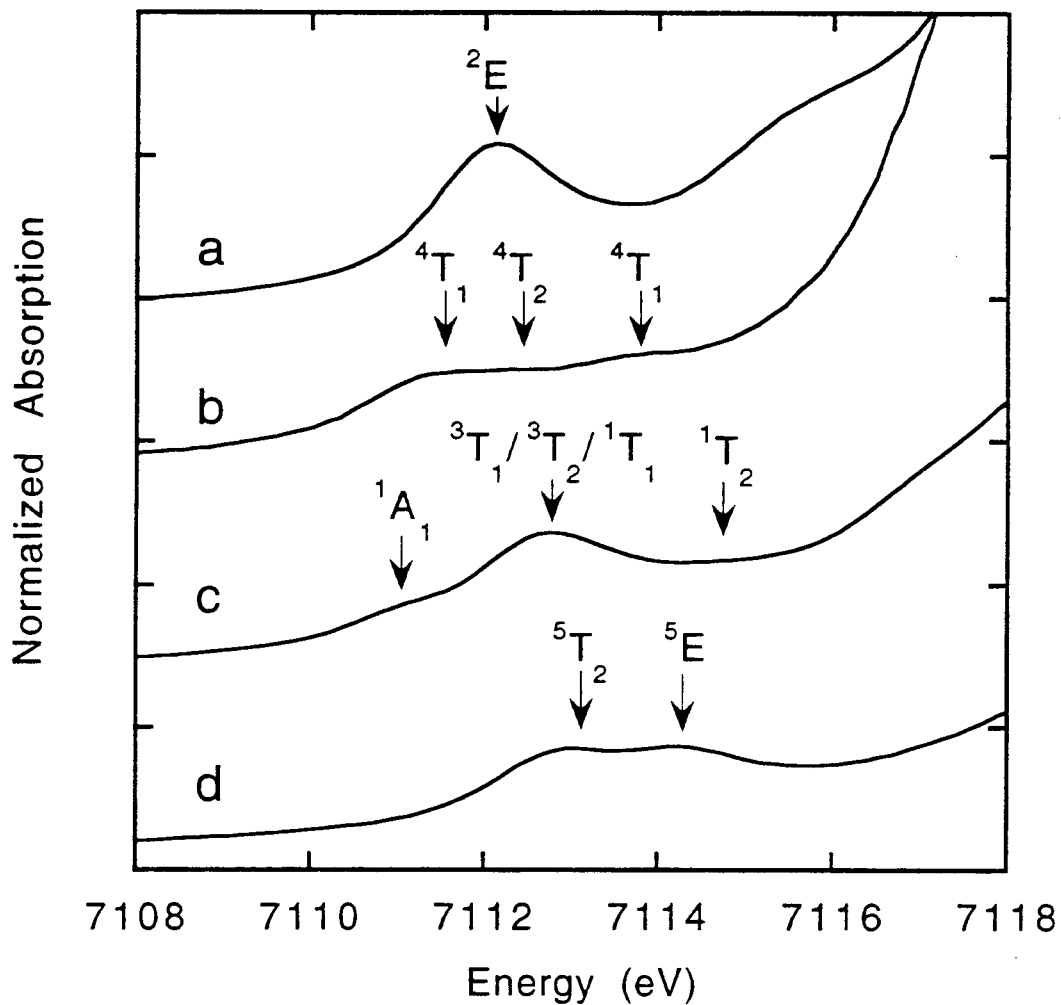


Figure 5.9. The $1s \rightarrow 3d$ pre-edge region of representative iron model complexes. a) a low spin ferrous complex, $[\text{Fe}(\text{Prpep})_2] \cdot 2\text{CH}_3\text{OH}$; b) a high spin ferrous complex, $[\text{Fe}(\text{imidazole})_6]\text{Cl}_2$; c) a low spin ferric complex, $[\text{Fe}(\text{Prpep})_2]\text{ClO}_4 \cdot 2\text{CH}_3\text{OH} \cdot \text{CH}_3\text{CN}$; and d) a high spin ferric complex, $\text{Fe}(\text{acac})_3$. The individual spectra are offset vertically by increments of 0.05 on the y-scale.

The $1s \rightarrow 3d$ pre-edge feature can be used to probe the spin and oxidation states of the iron site in activated BLM, since the $3d^{n+1}$ final state has a different multiplet splitting for high spin ferrous ($^4T_1, ^4T_2, ^4T_1$), high spin ferric ($^5T_2, ^5E$), low spin ferrous (2E), and low spin ferric ($^1A_1, ^3T_1, ^3T_2, ^1T_1, ^1T_2$) cases (as described in detail in Chapter 4). The number, intensity ratio, and energies of the pre-edge multiplet features are indicative of the specific oxidation and spin states of the iron. As can be seen in Figure 5.9, the low spin ferrous complex has a single pre-edge feature which has a maximum at ~ 7112 eV (Figure 5.9a), while high spin ferrous complexes have three features positioned at approximately 7111.2, 7112.3, and 7113.7 eV (Figure 5.9b). This correlates with the fact that there is a single allowed final state for low spin ferrous complexes (2E) while there are three final states of maximum spin multiplicity for the high spin ferrous complexes ($^4T_1, ^4T_2, ^4T_1$). A typical pre-edge for a low spin ferric complex has a low energy feature at ~ 7111 eV with a more intense feature at ~ 7112.5 eV (Figure 5.9c), corresponding to transitions into the 1A_1 and $^3T_1, ^3T_2$, and 1T_1 many-electron states, respectively (features from transitions into the higher energy 1T_2 state are much harder to resolve due to the onset of the rising edge). There are two features in pre-edge region of $\text{Fe}(\text{acac})_3$ (Figure 5.9d) corresponding to transitions into the two final states of maximum spin multiplicity allowed for high spin ferric complexes, the 5T_2 and 5E states. The pre-edge region for $\text{Fe}(\text{II})\text{BLM}$ (inset Figure 5.8 solid line) exhibits a weak broad feature that is similar in shape and energy to that observed for octahedral high spin ferrous complexes. $\text{Fe}(\text{III})\text{BLM}$ and activated BLM both have a pre-edge feature with maximum at 7112.5 eV with a lower energy shoulder being barely resolved in the $\text{Fe}(\text{III})\text{BLM}$ data. The energy position of the pre-edge features and the shape of both the $\text{Fe}(\text{III})\text{BLM}$ and the activated BLM indicate that both complexes have a low spin ferric active site.

The pre-edge features can also provide information on the geometric structure of the active site. The $1s \rightarrow 3d$ pre-edge feature is formally electric dipole forbidden, but gains intensity through an allowed quadrupole transition and through $4p$ mixing into the $3d$ states as a result of the non-centrosymmetric environment of the metal site. When the symmetry of the iron site is lowered, the pre-edge intensity increases due to an increase in the $3d$ - $4p$ mixing (see Chapter 4).^{27,30} Iron-oxo³¹ and iron-nitrosyl³² complexes typically have pre-edge features that are a factor of two more intense than their centrosymmetric counterparts, due to their short ~ 1.8 Å Fe-O/N bond. See, for example, the factor of two increase for $\text{Fe}(\text{Me}_3\text{TACN})(\text{NO})(\text{N}_3)_2$ ³³ (where TACN = N,N',N'' -trimethyl-1,4,7-triazacyclononane) which has been included in inset in Figure 5.8 (dot dashed line) as a reference. This iron-nitrosyl complex has an Fe-N(O) bond length of 1.74 Å. The pre-edge intensity of a five-coordinate oxo-ferryl porphyrin complex with an

Fe-O bond of 1.65 Å is even greater than that of Fe(Me₃TACN)(NO)(N₃)₂, due to the shorter Fe-O bond length.³⁴ In contrast, the spectrum of activated BLM (inset Figure 5.8 dotted line) has a pre-edge intensity which is typical of a six coordinate low spin ferric complex with no severe distortion around the iron site, eliminating the possibility of a short Fe-O bond.

5.4.3.2. EXAFS. The EXAFS spectra of Fe(II)BLM, Fe(III)BLM, and activated BLM are shown in Figure 5.10A and the Fourier transforms (FTs), calculated over the k range of 3.5-12.5 Å⁻¹, are shown in Figure 5.10B. Curve-fitting was performed on filtered first shell contributions over the k range 4-12 Å⁻¹ varying bond distances and coordination numbers. The results of the curve-fitting are presented in Table 5.4 with the best fits shown in Figure 5.11. The first shell of each sample could not be adequately fit with a single low-Z wave (Fits 1,3,5 in Table 5.4). The Fe(II)BLM data were well fit by 2 shells of N atoms (Fit 2 in Table 5.4 and Figure 5.11) with an average Fe-N distance of 2.16 Å. The Fe(III)BLM and activated BLM data were also fit with two shells of low Z atoms (Fits 4,6 in Table 5.4 and Figure 5.11), but with an average first shell distance 0.2 Å shorter than in Fe(II)BLM (see FTs in Figure 5.10B). The two N shells from the fit to the Fe(III)BLM and activated BLM data have very similar distances with slight changes in the coordination numbers consistent with both being low spin ferric complexes. In contrast, an oxo-ferryl species would have a bond length of ~1.65 Å.²⁹ The presence of a short Fe-O was further examined by fixing an Fe-O distance of 1.65 and 1.75 Å with a coordination number of 1, while varying the coordination numbers and distances of the two longer shells of N. These fits to the data do not support a shorter Fe-O distance, in that there was a much worse fit to the data when a 1.65 or 1.75 Å contribution was added (Fit 7, Figure 5.11) and the coordination numbers of the other N shells became unreasonable (total CN of ~11). When the third shell distance was allowed to vary it refined to a value of 1.83 Å with the fit having a similar F value as Fit 6 (Table 5.4). These studies indicate that an oxo-ferryl species is clearly not present from the analysis of the EXAFS data.

5.4.4. Discussion

Both the energy position and shape of the rising edge of the activated BLM XAS spectrum are very similar to those for Fe(III)BLM, indicating that the iron in activated BLM is ferric. Both Fe(III)BLM and activated BLM exhibit a weak pre-edge feature at 7112.5 eV with a lower energy shoulder, indicative of a low spin ferric active site with no severe distortion (*i.e.* no short iron-oxo bond). The first shell distances obtained from the

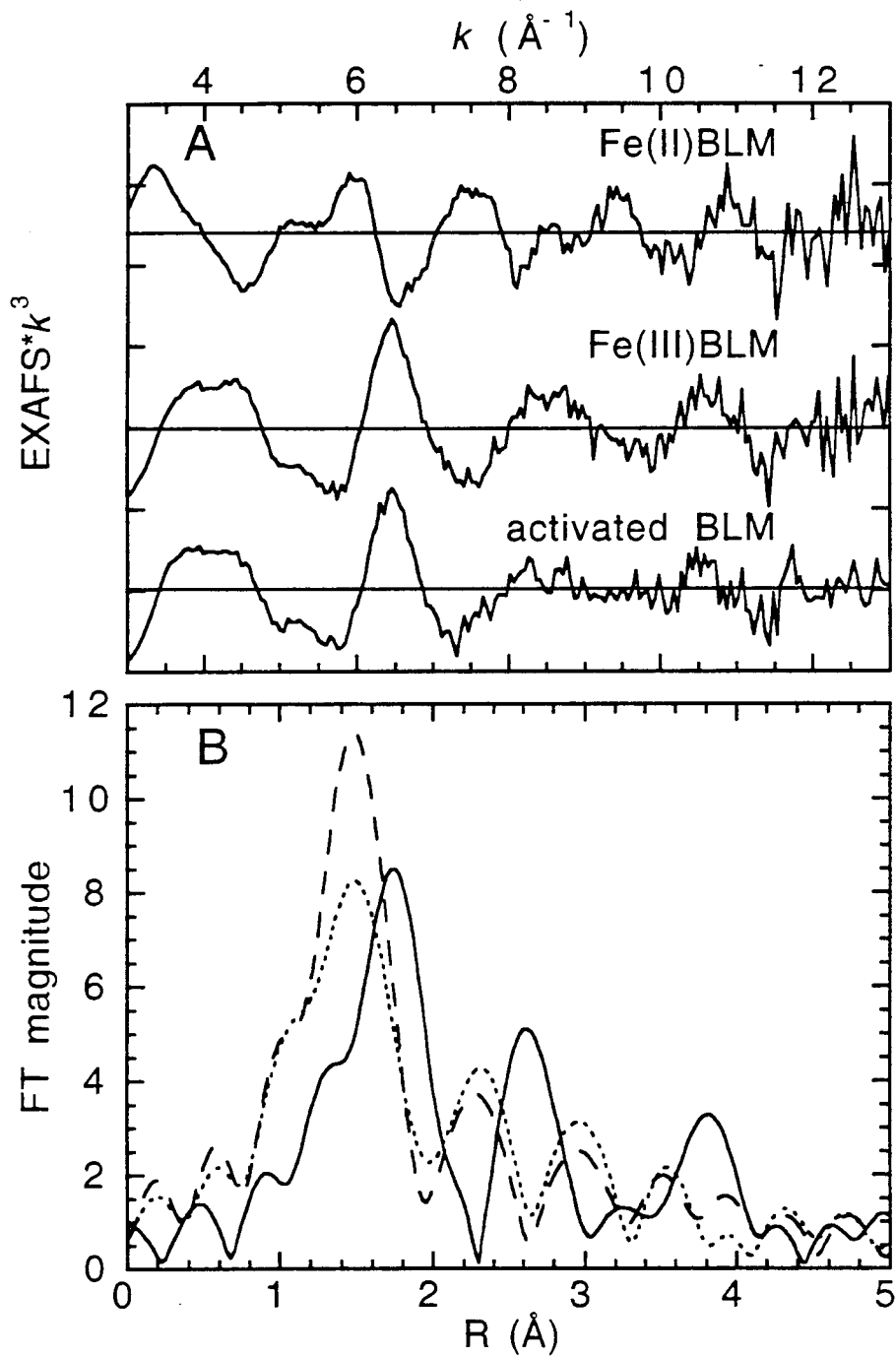


Figure 5.10. A) EXAFS data ($*k^3$) for Fe(II)BLM, Fe(III)BLM, and activated BLM (the ordinate scale is 5 between major tick marks on an absolute scale from the abscissa with solid horizontal lines indicating the zero point of each plot). B) The Fourier transforms (non-phase shift corrected) over the k -range 3.5 - 12.5 Å⁻¹ of the EXAFS data for Fe(II)BLM (—), Fe(III)BLM (---), and activated BLM (.....).

Table 5.4. Summary of EXAFS Curve-Fitting Results.

sample	Fit #	FT window		CN ^{a,b}	bond length	
		width (Å)	element		(Å) ^b	<i>F</i>
Fe(II)BLM	1	[1.0-2.25]	N	3.0	2.16	0.41
	2	[1.0-2.25]	N	1.4	2.08	0.29
Fe(III)BLM	3	[0.75-2.0]	N	3.0	2.19	
			N	3.3	1.94	0.73
	4	[0.75-2.0]	N	3.4	1.90	0.31
activated BLM	5	[0.7-2.0]	N	2.5	2.03	
			N	2.5	1.96	0.84
	6	[0.7-2.0]	N	2.5	1.89	0.36
			N	3.0	2.03	
			N	3.0	2.03	
7	[0.7-2.0]	O	1*	1.65*	0.75	
		N	7.0	1.91		
		N	2.9	2.07		

^a CN = coordination number. ^b Errors in distances (± 0.02 Å) and coordination numbers ($\pm 25\%$) are estimated from the variance between EXAFS fitting results and values from models of crystallographically known structure.¹⁷ * values fixed.

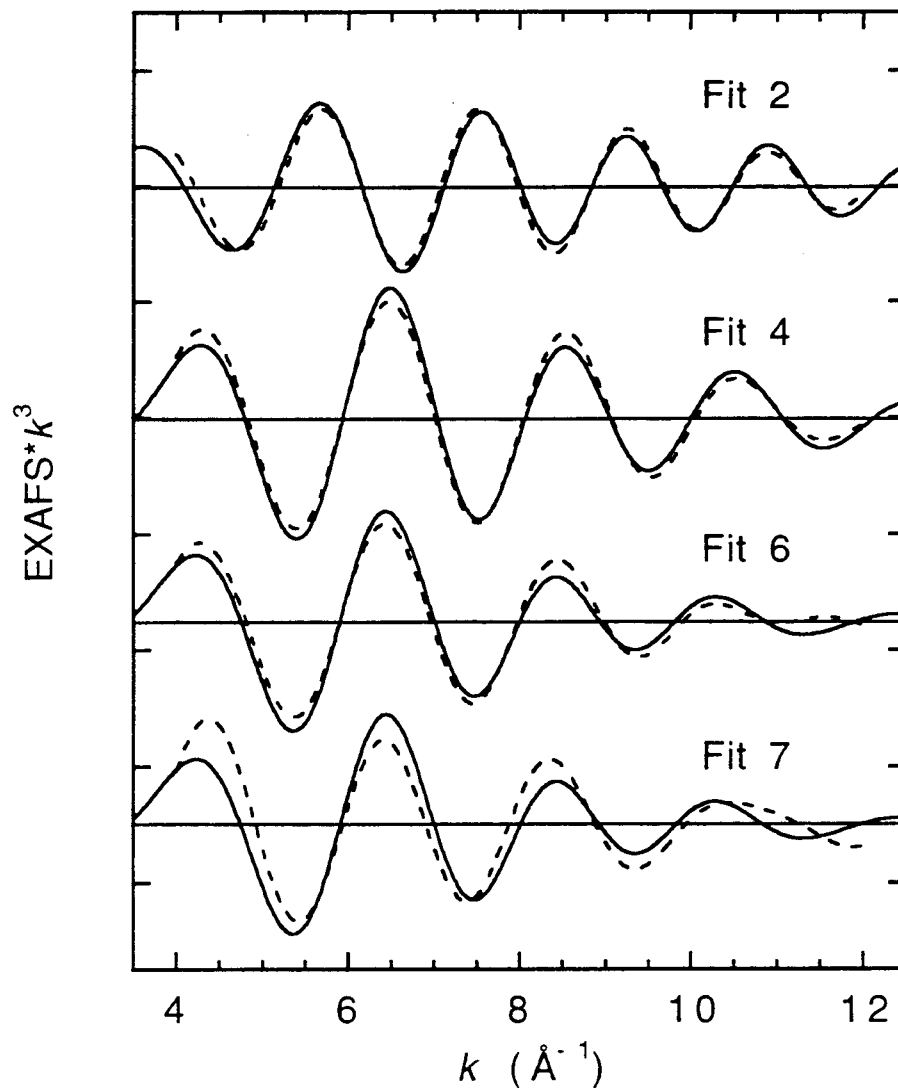


Figure 5.11. Empirical first shell fits to the Fourier-filtered EXAFS data with the solid lines representing the experimental data and the dashed line representing the fit to the data. Fits 2, 4, and 6 are the best empirical fits to the Fe(II)BLM, Fe(III)BLM and activated BLM data, respectively. Fit 7 is a fit to the activated BLM data where a short 1.65 Å Fe-O bond distance was included. (The ordinate scale is 4 between major tick marks on an absolute scale from the abscissa with solid horizontal lines indicating the zero point of each plot.)

EXAFS data of activated BLM are within 0.01 Å of the Fe(III)BLM distances with slight changes in the coordination numbers. Thus, the XAS data of activated BLM are *not* consistent with a Fe(IV)=O species, but rather with a low spin ferric-peroxide description of the active site. These results confirm the description of activated BLM being a peroxy-Fe(III)BLM species presented in a recent mass spectrometry study.⁹ The XAS results provide a *direct* determination of both the iron oxidation and spin states and the fact that there is no short iron-oxo bond. Activated BLM is the first mononuclear non-heme iron oxygen intermediate to be characterized and its description suggests that such a peroxy-ferric complex may play an important role in O₂ activation by this class of enzymes. Experiments are currently underway to define the peroxide binding mode and to generate a detailed electronic structure description of activated BLM in order to understand the nature of the oxygen activation.

5.4.5. Acknowledgments

The BLM samples were prepared by Kelly Loeb and Jeffrey Zaleski. This research is supported by grants from the NIH (GM40392, E.I.S.) and NSF (CHE-9121576, K.O.H.). SSRL is supported by the U.S. Department of Energy, Office of Basic Energy Science, Divisions of Chemical and Materials Sciences, and in part by the National Institutes of Health, Biomedical Research Technology Program (RR-01209) and the US Department of Energy, Office of Health and Environmental Research.

5.4.6. References and Notes

- (1) Carter, S. K. *Bleomycin Chemotherapy*; Academic Press: New York, 1985, p 3.
- (2) Hecht, S. M. *Acc. Chem. Res.* **1986**, *19*, 383.
- (3) Stubbe, J.; Kozarich, J. W. *Chem. Rev.* **1987**, *87*, 1107.
- (4) Sugiura, Y. *Biochem. Biophys. Res. Commun.* **1979**, *87*, 643.
- (5) Burger, R. M.; Peisach, J.; Horwitz, S. B. *J. Biol. Chem.* **1981**, *256*, 11636.
- (6) Guajardo, R. J.; Hudson, S. E.; Brown, S. J.; Mascharak, P. K. *J. Am. Chem. Soc.* **1993**, *115*, 7971.
- (7) McGall, G. H.; Rabow, L. E.; Ashley, G. W.; Wu, S. H.; Kozarich, J. W.; Stubbe, J. *J. Am. Chem. Soc.* **1992**, *114*, 4958.
- (8) Burger, R. M.; Kent, T. A.; Horwitz, S. B.; Münck, E.; Peisach, J. *J. Biol. Chem.* **1983**, *258*, 1559.
- (9) Sam, J. W.; Tang, X.-J.; Peisach, J. *J. Am. Chem. Soc.* **1994**, *116*, 5250.

- (10) Scott, R. A.; Hahn, J. E.; Doniach, S.; Freeman, H. C.; Hodgson, K. O. *J. Am. Chem. Soc.* **1982**, *104*, 5364.
- (11) Lytle, F. W. In *Applications of Synchrotron Radiation*; Winick, H.; Xian, D.; Ye, M.-h.; Huang, T., Eds.; Gordon and Breach Science Publishers: New York, 1989; p 135.
- (12) Cramer, S. P.; Tench, O.; Yocum, M.; George, G. N. *Nucl. Instrum. Methods Phys. Res.* **1988**, *A266*, 586.
- (13) Abbreviations used: PrpepH = N-(2-(4-imidazolyl)ethyl)pyrimidine-4-carboxamide; acac = acetylacetonate.
- (14) Burbridge, C. D.; Goodgame, D. M. L. *Inorg. Chim. Acta* **1970**, *4*, 231.
- (15) Roof, R. B., Jr. *Acta Crystallogr* **1956**, *9*, 781.
- (16) Iball, J.; Morgan, C. H. *Acta Crystallogr.* **1967**, *23*, 239.
- (17) Cramer, S. P.; Hodgson, K. O.; Stiefel, E. I.; Newton, W. E. *J. Am. Chem. Soc.* **1978**, *100*, 2748.
- (18) Cramer, S. P.; Hodgson, K. O. *Prog. Inorg. Chem.* **1979**, *25*, 1.
- (19) Scott, R. A. *Methods Enzymol.* **1985**, *117*, 414.
- (20) Johansson, L. *Chem. Scr.* **1976**, *9*, 30.
- (21) Johansson, L.; Molund, M.; Oskarsson, Å. *Inorg. Chim. Acta* **1978**, *31*, 117.
- (22) Brown, S. J.; Olmstead, M. M.; Mascharak, P. K. *Inorg. Chem.* **1990**, *29*, 3229.
- (23) Srivastava, U. C.; Nigam, H. L. *Coord. Chem. Rev.* **1973**, *9*, 275.
- (24) Shulman, R. G.; Yafet, Y.; Eisenberger, P.; Blumberg, W. E. *Proc. Natl. Acad. Sci. USA* **1976**, *73*, 1384.
- (25) Cramer, S. P.; Eccles, T. K.; Kutzler, F. W.; Hodgson, K. O. *J. Am. Chem. Soc.* **1976**, *98*, 1287.
- (26) Wong, J.; Lytle, F. W.; Messmer, R. P.; Maylotte, D. H. *Phys. Rev. B.* **1984**, *30*, 5596.
- (27) Roe, A. L.; Schneider, D. J.; Mayer, R. J.; Pyrz, J. W.; Widom, J.; Que, L., Jr. *J. Am. Chem. Soc.* **1984**, *106*, 1676.
- (28) Kau, L.-S.; Spira-Solomon, D. J.; Penner-Hahn, J. E.; Hodgson, K. O.; Solomon, E. I. *J. Am. Chem. Soc.* **1987**, *109*, 6433.
- (29) Penner-Hahn, J. E.; McMurry, T. J.; Renner, M.; Latos-Grazynsky, L.; Eble, K. S.; Davis, I. M.; Balch, A. L.; Groves, J. T.; Dawson, J. H.; Hodgson, K. O. *J. Biol. Chem.* **1983**, *258*, 12761.
- (30) Randall, C. R.; Shu, L.; Chiou, Y.-M.; Hagen, K. S.; Ito, M.; Kitajima, N.; Lachicotte, R. J.; Zang, Y.; Que, L., Jr. *Inorg. Chem.* **1995**, *34*, 1036.
- (31) DeWitt, J. G., Ph.D. Thesis, Stanford University, 1993.

- (32) Brown, C. A.; Pavlosky, M. A.; Westre, T. E.; Zhang, Y.; Hedman, B.; Hodgson, K. O.; Solomon, E. I. *J. Am. Chem. Soc.* **1995**, *117*, 715.
- (33) Pohl, K.; Wieghardt, K.; Nuber, B.; Weiss, J. *J. Chem. Soc., Dalton Trans.* **1987**, 187.
- (34) Liu, H. I.; Gold, A.; Dawson, J. H.; Hedman, B.; Hodgson, K. O. unpublished data.

5.5. Lipoxygenases

5.5.1. Introduction

Lipoxygenases (LOs) are non-heme iron enzymes which catalyze the reaction of dioxygen with *cis,cis*-1,4-pentadiene-containing fatty acids, *e.g.*, linoleic and arachidonic acids, to form hydroperoxide products (see Table 5.1). Certain LOs are positionally specific and are classified by the carbon position at which the hydroperoxidation of arachidonic acid occurs. Mammalian 5-, 12-, and 15-LOs catalyze the formation of the direct precursors to leukotrienes and lipoxins,¹ compounds which mediate inflammation, hypersensitivity, and cellular immunity. LOs have also been implicated in the oxidation of low-density lipoprotein to its atherogenic form.^{2,3} Thus, the development of LO inhibitors has been the target of many pharmaceutical companies. In plants, LOs are involved in immunity and growth regulation.⁴ Soybean lipoxygenase-1 (SLO-1) and mammalian 5- and 15-LOs have regions of high amino acid sequence identity.⁵ Maximal alignment of the LOs shows that the middle and COOH terminal portions are very similar. The non-homology of the first 117 residues of SLO-1 (MW ~95,000) with the mammalian LOs (MW ~75,000) is thought to be due to an additional region present only in plant LOs.^{5,6}

SLO-1, a 15-LO, catalyzes the reaction of O₂ with linoleic acid to give primarily 13(*S*)-hydroperoxy-9,11-(*E,Z*)-octadecadienoic acid (13-HPOD) as product. The native ferrous enzyme is stable in air⁷ and must be oxidized to the active ferric form for reaction with substrate. There are two classes of proposed mechanisms for LO catalysis. The first is a radical-based mechanism in which the fatty acid is activated through oxidation by the ferric center to form a fatty acid radical.^{8,9} The ferrous site generated may then activate O₂ for reaction with the radical, or O₂ may react with the radical to generate product. The second mechanism involves a direct reaction of the ferric center and the substrate, forming an organo-iron complex¹⁰ to which O₂ inserts, forming a ferric peroxo complex and subsequently product.

Two recent X-ray crystal structures^{6,11} of ferrous SLO-1 have identified four common amino acid active site ligands: histidine₄₉₉Ne, histidine₅₀₄Ne, histidine₆₉₀Ne, and isoleucine₈₃₉OT2, the terminal carboxylate. Each of these residues is conserved in all sequenced lipoxygenases, with the exception of a valine replacement of the isoleucine in rat leukocyte 5-LO.¹² One crystallographic active site description is four-coordinate distorted octahedral with two adjacent unoccupied ligand positions.⁶ The other crystal structure¹¹ has an additional ligand, asparagine₆₉₄Oδ1, with the further possibility of a sixth water-based ligand; such a ligand has been proposed from electron paramagnetic resonance

(EPR) line broadening studies on the ferric enzyme.¹³ This asparagine residue is conserved in all sequenced LOs with the exception of rabbit reticulocyte and human 15-LOs, in which a histidine is in the analogous position.⁵

There have been a limited number of spectroscopic studies aimed at defining the geometric and electronic structure of the ferrous site of SLO-1. Magnetic susceptibility measurements⁷ show that the ferrous active site ground state is high-spin with $S = 2$. X-ray absorption (XAS),¹⁴ Mössbauer,¹⁵ and circular and magnetic circular dichroism¹⁶ (CD/MCD) studies predicted a distorted octahedral geometry. However, a more recent XAS study on a frozen solution of ferrous SLO-1 found the $1s \rightarrow 3d$ pre-edge intensity greater than what was found for six-coordinate high-spin iron(II) model complexes, but comparable to that of a five-coordinate model.¹⁷ These studies now appear to have been complicated by solvent effects as a recent CD/MCD study¹⁸ in the near-infrared (NIR) region on native SLO-1 in solution using sucrose as a non-perturbing low-temperature glassing agent showed that native ferrous SLO-1 exists as a mixture of two forms, one five-coordinate and one six-coordinate, and that the addition of glycerol converts the mixture to the pure six-coordinate form.¹⁹

Considering the discrepancies between the two crystals structures^{6,11} (which predict a four- and five-coordinate active site, respectively) and the spectroscopic studies (which predict a five-¹⁷ and six-coordinate¹⁴⁻¹⁶ active site), both Fe K-edge and extended X-ray absorption fine structure (EXAFS) measurements were performed on SLO-1 in glycerol to obtain information on the coordination number and geometry of the iron active site in a pure form.¹⁸ In addition Fe K-edge XAS data were obtained for two mammalian LOs, rabbit reticulocyte 15-LO (15-RLO) and recombinant human 15-LO (15-HLO), to compare to SLO-1. The XAS results have been combined with the results from a NIR CD/MCD study of SLO-1, 15-RLO and 15-HLO in solution and glycerol to obtain an understanding of the geometric and electronic structure of these three LOs.

5.5.2. Experimental Section

SLO-1 was purified from soybeans (Williams Variety, Tabor Seed Division, Decatur, IL) following published procedures.²⁰ Enzyme activity was determined by monitoring the absorption of 13-HPOD product formed during the enzymatic reaction at 234 nm ($\epsilon_{234} = 2.5 \times 10^4 \text{ M}^{-1} \text{ cm}^{-1}$). The specific activity of the final enzyme was ~200 units/mg. Native SLO-1 samples were buffered in 0.1 M sulfonic acid solutions: MES, $5.6 < \text{pD} < 7$; HEPES, $7.5 < \text{pD} < 8.2$; CHES, $8.5 < \text{pD} < 9.5$; CAPS, $10 < \text{pD} < 11$. Human 15-lipoxygenase was purified from an baculovirus/insect cell expression system by

anion-exchange chromatography on a Mono Q column.²¹ Rabbit 15-lipoxygenase was purified from a 55% ammonium sulfate precipitate of rabbit reticulocyte lysate to greater than 98% purity according to the published method with the following modifications: desalting the protein with a PD-10 column instead of dialysis and replacement of the Mono S with a Mono Q column.²² The Bradford method was used for determining protein concentration.²¹ All purification steps were carried out at 4 °C or on ice.

X-ray absorption spectra were recorded at the Stanford Synchrotron Radiation Laboratory on unfocused beamline 7-3 during dedicated conditions (3 GeV, 50-100 mA). The radiation was monochromatized using a Si(220) double-crystal monochromator. An Oxford Instruments continuous-flow liquid helium CF1208 cryostat was used to maintain a constant temperature of 10 K. Energies were calibrated using an internal Fe foil standard, assigning the first inflection point to 7111.2 eV.²³ The spectrometer energy resolution was approximately 1.4 eV with reproducibility in edge position determination of < 0.2 eV.

The SLO-1, 15-RLO, and 15-HLO XAS samples were prepared as described above with 50% glycerol. The samples were loaded into Lucite EXAFS cells (23 x 1 x 3 mm) with 37 μm Kapton windows and frozen in liquid nitrogen. Data were measured to $k = 13 \text{ \AA}^{-1}$ with 1 mm high pre-monochromator beam defining slits, detuning the monochromator 50% at 7824 eV to minimize harmonic contamination. The fluorescence signal was monitored by using a 13-element Ge solid-state array detector²⁴ windowed on the Fe $K\alpha$ signal. During the experiment, count rates of approximately $30,000 \text{ s}^{-1}$ total per element were not exceeded. Approximately 30 scans were averaged for each protein sample. A pre-edge subtraction was performed by fitting the tail of a Gaussian to the pre-edge region and subtracting this polynomial from the averaged spectra.²⁵ A three-segment spline approximately even in k -space was fit to the EXAFS region and the data normalized to an edge jump of one at 7130 eV. The spline was chosen so that it minimized residual low-frequency background but did not reduce the EXAFS amplitude as checked by monitoring the Fourier transform of the EXAFS during the background subtraction process.

Fe K-edge spectra were also collected on four-, five-, and six-coordinate ferrous model complexes. $\text{Fe}(\text{HB}(3,5\text{-}i\text{Pr}_2\text{pz})_3)\text{Cl}$ ²⁶ was obtained as a gift from N. Kitajima.²⁸ $[\text{Fe}(\text{imidazole})_6]\text{Cl}_2$ ²⁹ and $(\text{BF}_4)[\text{Fe}(\text{TMC})\text{Cl}]$ ²⁷ was prepared as described in the literature. These three samples are air-sensitive and thus the following procedure was carried out in a nitrogen-filled glove box. The crystalline samples were each mixed with BN and ground into a fine powder. The BN/sample mixture was pressed into a 1 mm thick Al spacer that was sealed with 63.5 μm Mylar tape windows and frozen in liquid nitrogen. Data were measured in transmission mode with N_2 -filled ionization chambers to $k =$

9.5 Å⁻¹, detuning the monochromator 50% at 7474 eV to minimize harmonic contamination. Two to three scans were averaged for each sample. A smooth pre-edge background was removed from the averaged spectra by fitting a first order polynomial to the pre-edge region and subtracting this polynomial from the entire spectrum. A two-segment spline of order two was fit to the EXAFS region and the data normalized to an edge jump of one at 7130 eV.

EXAFS data reduction was performed on the normalized protein spectra according to established methods.³⁰⁻³² The normalized data were converted to *k*-space. The photoelectron wave vector, *k*, is defined by $[2m_e(E-E_0)/\hbar^2]^{1/2}$ where *m_e* is the electron mass, *E* is the photon energy, *h* is Planck's constant divided by 2π, and *E₀* is the threshold energy of the absorption edge, which was defined to be 7130 eV for the Fe K absorption edge. The empirical EXAFS data analyses were performed with nonlinear least-squares curve-fitting^{23,30-32} techniques using empirical phase and amplitude parameters. The following models were used to obtain the empirical Fe-X backscattering parameters of interest: Fe-O from [Fe(acetylacetonate)₃]^{33,34} and Fe-N from [Fe(1,10-phenanthroline)₃](ClO₄)₃.^{35,36} Fourier transforms (from *k* to *R* space) were performed for the data range 3.5-12.5 Å⁻¹ with a Gaussian window of 0.1 Å⁻¹. The window widths used in the backtransforms (from *R* to *k* space) for the proteins are given in the Results and Analysis. The window widths were kept as similar as possible to those used to extract amplitude and phase parameters from the model compounds to minimize artifacts introduced by the Fourier filtering technique. All curve-fitting was based on *k*³-weighted data and applied to the individual filtered shell of interest. Only the structure-dependent parameters, the distance and coordination number, were varied unless stated otherwise. A "goodness of fit" parameter, *F*, was calculated as $F = \{[k^6(\text{data} - \text{fit})^2]/(\text{no. of points})\}^{1/2}$ for each fit.

The intensities and energies of pre-edge features of the model complex and protein data were quantitated by fits to the data. The fitting program EDG_FIT, which utilizes the double precision version of the public domain MINPAK fitting library³⁷ was used. EDG_FIT was written by Dr. Graham N. George of the Stanford Synchrotron Radiation Laboratory. All spectra were fit over the range 7108 - 7118 eV. Pre-edge features were modeled by pseudo-Voigt line shapes (simple sums of Lorentzian and Gaussian functions).³⁸⁻⁴¹ A fixed 50:50 ratio of Lorentzian to Gaussian contribution for the pre-edge feature successfully reproduced these spectral features. Functions modeling the background underneath the pre-edge features were chosen empirically to give the best fit. The second derivative of the data was compared to the second derivative of the fit. In all cases, a number of fits were obtained which reproduced the data and the second derivative.

The value reported for the area of a fitted feature (where the peak area was approximated by the height x full width at half-maximum (FWHM)) is the average of all the pseudo-Voigts which successfully fit the feature. For each sample, the standard deviation of the average of the areas was calculated to quantitate the error.

5.5.3. Results and Analysis

5.5.3.1. Fe K-Edge XAS. Fe K-edge X-ray absorption spectra of ferrous SLO-1, 15-RLO, and 15-HLO have been compared to spectra of four-, five-, and six-coordinate ferrous model complexes to obtain information on the coordination number of the iron active site in the LOs. All three protein samples contained glycerol to ensure that a pure form was being studied.^{18,19} The XAS edge spectra for SLO-1, 15-RLO, and 15-HLO are shown in the upper portion of Figure 5.12, while the lower portion contains spectra of representative four-, five-, and six-coordinate ferrous model complexes: Fe(HB(3,5-*i*Pr₂pz)₃)Cl,²⁶ (BF₄)[Fe(TMC)Cl],²⁷ and [Fe(imidazole)₆]Cl₂,²⁹ respectively. The lowest energy peaks arise from the weak 1s→3d transition which is at ~7112 eV followed by the 1s→4p transition at ~7125 eV. An expanded view of the 1s→3d pre-edge region is shown for the three LOs as well as for the model complexes in Figure 5.12 insets A and B, respectively. The energies and areas of the pre-edge features were determined by fits to the data and are presented in Table 5.5. The SLO-1, 15-RLO, and 15-HLO spectra all have a very broad low-intensity pre-edge feature which can be fit with two features that have a total pre-edge area of ~8. The three ferrous model complexes, Fe(HB(3,5-*i*Pr₂pz)₃)Cl, (BF₄)[Fe(TMC)Cl], and [Fe(imidazole)₆]Cl₂, all have what appear to be two pre-edge features split by ~2 eV with varying intensities (Figure 5.12 inset B). The four-coordinate complex has the most intense pre-edge feature with a total area of 19.8, while the six-coordinate complex has the least intense pre-edge feature with a total pre-edge area of 3.8. The "white line", attributed to the 1s→4p transition at ~7125 eV, is very similar in shape and intensity in all three LO samples, while this feature differs drastically in shape between the four-, five-, and six-coordinate ferrous complexes (Figure 5.12).

The 1s→3d pre-edge feature can be used to probe the coordination number of the iron in the active site of the LOs. The 1s→3d transition is formally electric dipole forbidden, but gains intensity through an allowed quadrupole transition and more dominantly by 4p mixing into the 3d states as a result of the noncentrosymmetric environment of the metal site. It has been shown for ferric and ferrous complexes that when the symmetry of the iron site is lowered, the pre-edge intensity increases due to an

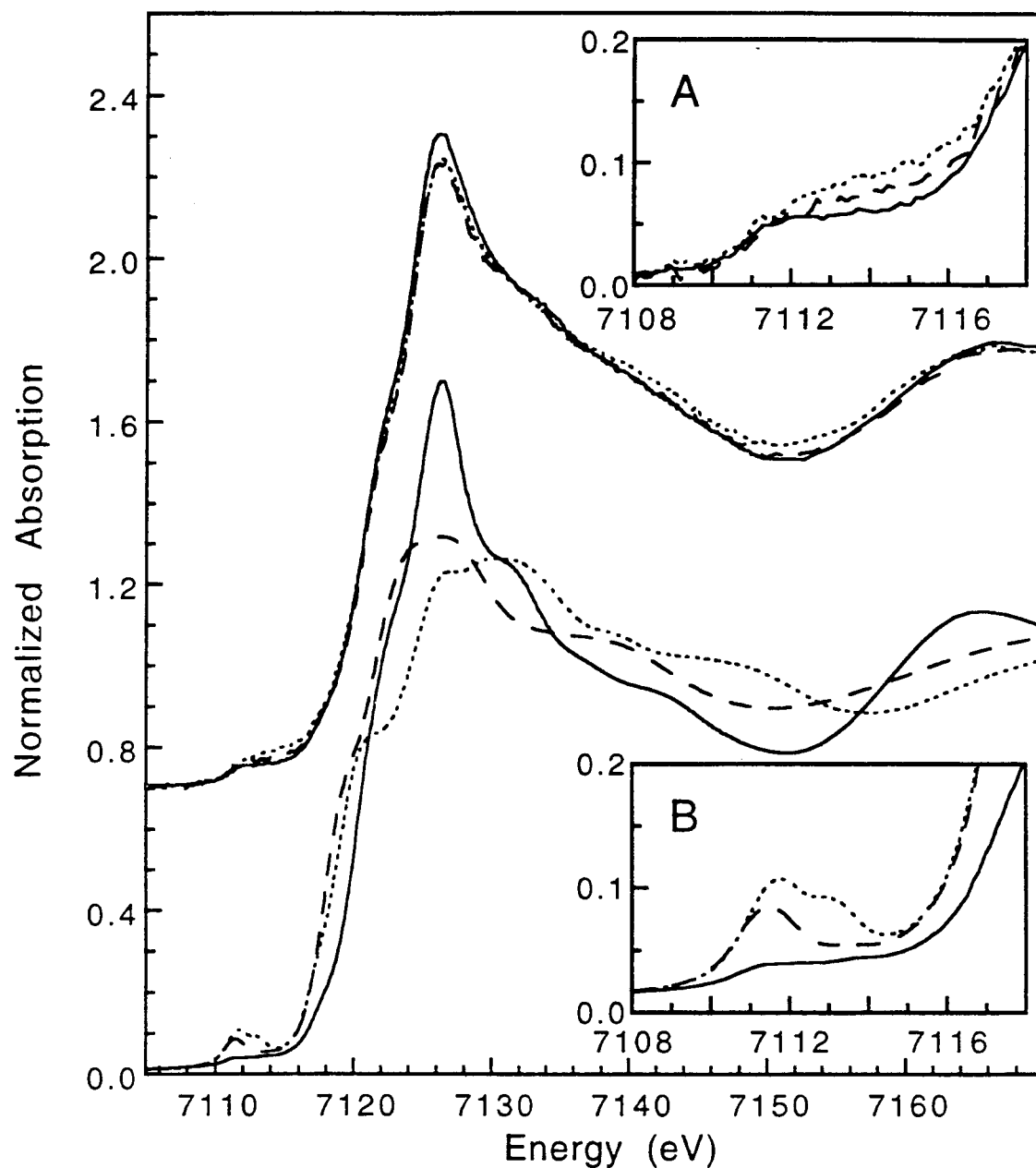


Figure 5.12. Fe K-edge XAS spectra (offset by +0.7) of SLO-1 (—), 15-RLO (---), and 15-HLO (····) are shown in the upper portion, where inset A shows an expansion of the $1s \rightarrow 3d$ pre-edge region. The lower portion shows the Fe K-edge XAS spectra of four-, five- and six-coordinate ferrous model complexes: $\text{Fe}(\text{HB}(3,5\text{-}i\text{Pr}_2\text{pz})_3)\text{Cl}$ (····), $(\text{BF}_4)[\text{Fe}(\text{TMC})\text{Cl}]$ (---), and $[\text{Fe}(\text{imidazole})_6]\text{Cl}_2$ (—). Inset B is an expansion of the $1s \rightarrow 3d$ pre-edge region for the model complexes.

Table 5.5. XAS Pre-Edge Energies and Areas for LO's and Ferrous Model Complexes.

sample	CN ^a	pre-edge energy (eV) ^b	pre-edge area ^{b,c}	total pre-edge area ^c
Fe(HB(3,5- <i>i</i> Pr ₂ pz) ₃)Cl	4	7111.64 (0.02)	14.2 (0.5)	19.8 (0.9)
		7113.17 (0.02)	5.6 (0.9)	
(BF ₄)[Fe(TMC)Cl]	5	7111.41 (0.01)	10.9 (0.1)	12.9 (0.2)
		7113.43 (0.02)	2.0 (0.3)	
[Fe(imidazole) ₆]Cl ₂	6	7111.24 (0.03)	1.6 (0.5)	3.8 (0.3)
		7112.35 (0.16)	1.6 (0.8)	
		7113.66 (0.02)	0.6 (0.2)	
SLO-1 in glycerol	--	7111.64 (0.07)	4.4 (0.9)	8.7 (1.1)
		7113.34 (0.15)	4.3 (1.2)	
15-RLO	--	7111.85 (0.08)	4.1 (1.4)	8.1 (2.6)
		7113.35 (0.32)	4.0 (1.7)	
15-HLO	--	7111.69 (0.08)	4.0 (0.9)	7.9 (1.4)
		7113.35 (0.19)	3.9 (0.7)	

^a CN = coordination number. ^b Pre-edge energies and areas were determined by fits to the data as described in the Experimental Section. ^c Pre-edge areas were calculated by multiplying the height of the fitted feature by the FWHM (the values reported were multiplied by 100).

increase in the 3d-4p mixing.^{42,43} As described in more detail in Chapter 4, the pre-edge splitting and intensity distribution is indicative of the site symmetry of the iron atom. When a high spin ferrous atom is in an octahedral site, three transitions are observed into 4T_1 , 4T_2 , and 4T_1 excited states (a transition into the 4A_2 state is not observed as it would involve a two electron transition). The transitions into these states are only quadrupole allowed as the iron is in a centrosymmetric site and therefore there is no 4p-3d mixing. Thus, one observes three weak peaks as can be seen in the $[\text{Fe}(\text{imidazole})_6]\text{Cl}_2$ spectrum (Figure 5.12 inset B) with the first two features being barely resolvable and centered at 7111.2 and 7112.4 eV and the third feature positioned at 7113.7 eV. Since the difference in energy between the lowest energy 4T_1 state and the 4T_2 state is about the same as the energy resolution at the Fe K-edge, occasionally only two pre-edge features are observed for high spin ferrous complexes with the first feature attributed to transitions into both the 4T_1 and the 4T_2 states and the second feature ~ 2 eV higher in energy attributed to a transition into the higher energy 4T_1 state. When a high spin ferrous atom is in a square pyramidal site, the intensity of the lower energy feature increases dramatically since there is now $4p_z$ mixing into the $3d_{z^2}$ orbital due to the loss of a center of inversion, as can be seen in the $(\text{BF}_4)[\text{Fe}(\text{TMC})\text{Cl}]$ spectrum (dashed line in Figure 5.12 inset B). When a high spin ferrous atom is in a tetrahedral site, there are two intense pre-edge features due to 4p mixing into the d_{xy} , d_{xz} , d_{yz} orbitals, with the lower energy feature being more intense than the higher energy feature, as can be seen in the $(\text{Fe}(\text{HB}(3,5\text{-}i\text{Pr}_2\text{pz})_3)\text{Cl})$ spectrum (dotted line in Figure 5.12 inset B). See Chapter 4 for a more detailed analysis of the distribution of the dipole intensity in the $1s \rightarrow 3d$ pre-edge features of high spin ferrous complexes.

Empirically the pre-edge features of SLO-1, 15-RLO, and 15-HLO look much more similar in shape and intensity to that of the six-coordinate ferrous model and quite different from those of the four- and five-coordinate model complexes. The total fitted area of the pre-edge features of the LOs at ~ 8 is higher than that of $[\text{Fe}(\text{imidazole})_6]\text{Cl}_2$ at 4. The larger pre-edge in the LOs can be attributed to an overall less symmetric iron site caused by mixed ligation and variation in bond lengths. However, the shape of the LOs' pre-edge feature is very similar to that of the $[\text{Fe}(\text{imidazole})_6]\text{Cl}_2$ and other six-coordinate ferrous complexes (see Chapter 4). In addition, the shapes of the "white line" in the SLO-1, 15-RLO, and 15-HLO spectra at ~ 7127 eV are very much alike and similar to that in the six-coordinate $[\text{Fe}(\text{imidazole})_6]\text{Cl}_2$ spectrum. These results indicate that all three LOs in glycerol have a six-coordinate iron active site.

5.5.3.2. EXAFS. EXAFS studies of SLO-1 in glycerol were also pursued to obtain metrical information on the iron active site of the pure six-coordinate form.^{18,19} High-quality, high- k EXAFS data could not be obtained on the 15-HLO or 15-RLO

samples due to the low protein concentration of ~1 mM. The EXAFS spectrum of SLO-1 in glycerol is shown in Figure 5.13A, and the Fourier transform (FT), taken over the k range of 3.5 - 12.5 Å⁻¹, is shown in Figure 5.13C. Curve-fitting was performed on filtered first shell contributions over the k range 4 - 12 Å⁻¹. Fits were performed by stepping through fixed coordination numbers while allowing the bond distance and $c2$ to vary. $c2$ is the amplitude parameter which has the functional form of the Debye-Waller factor, *i.e.*, $\exp(xk^2)$, where $x = c2$ or $x = -2\sigma_{as}^2$.^{23,30-32} As determined in these fits, the value of $c2$ is correlated to σ_{as}^2 only in a relative manner. Since $\Delta c2 = -2\Delta\sigma_{as}^2$, a more negative value of $c2$ denotes a larger value of σ_{as}^2 and thus a weaker bond or a greater distribution of distances for scatterers. The values of $c2$ for Fe–O from Fe(acetylacetonate)₃ and Fe–N from [Fe(1,10-phenanthroline)₃](ClO₄)₃ were -0.02391 and -0.02083, respectively. These values correspond to a well-ordered shell of nearest neighbors.

The FT peak centered at ~1.8 Å (non-phase shift corrected) could be adequately fit with either one shell of O's or N's (Fits 1-6 in Table 5.6; Figure 5.13B) with an average first shell distance of 2.15 and 2.18 Å, respectively. Fits 1-3 with all O ligation matched the data better in the lower k region, while Fits 4-6 with all N ligation matched the data better in the higher k region. The coordination number and $c2$ are highly correlated, as can be seen in Fits 1-3 and 4-6 in Table 5.6, with the $c2$ values becoming more negative as the coordination number is increased. The F value is lowest with a coordination number of 4 using the Fe-O parameters (Fit 1) and a coordination number of 5 or 6 using the Fe-N parameters (Fit 6, Figure 5.13B). Two shell fits with both an O and a N contribution were also attempted (Fits 7-9). These fits gave no indication that the first shell has two components since the distances remained the same (and thus not separable), the $c2$ parameters were highly correlated, and the $c2$ parameter of O increased to such a level where its resulting contribution was negligible. Previous results on SLO-1 in frozen buffered solution¹⁴ indicated that there were 2 O at a distance of 1.94 Å. Therefore, the possibility of a shorter low Z contribution was further examined by fixing an Fe–O distance at 1.95, 2.00, 2.05 and 2.10 Å (Fits 10-15) and varying both the $c2$ value and the second shell distance. When both distances of these two shell fits were allowed to vary, the same results as in Fits 7-9 were obtained. These fits to the data on SLO-1 in glycerol thus do not support a shorter Fe–O distance. The fit became significantly worse with the addition of a second shell in that the $c2$ value for the shorter Fe–O contribution is more than an order a magnitude more negative than is chemically reasonable.

Fits were also performed where $c2$ was fixed to -0.02391 and -0.02083 for the Fe–O and Fe–N contributions, respectively, letting both the distance and coordination

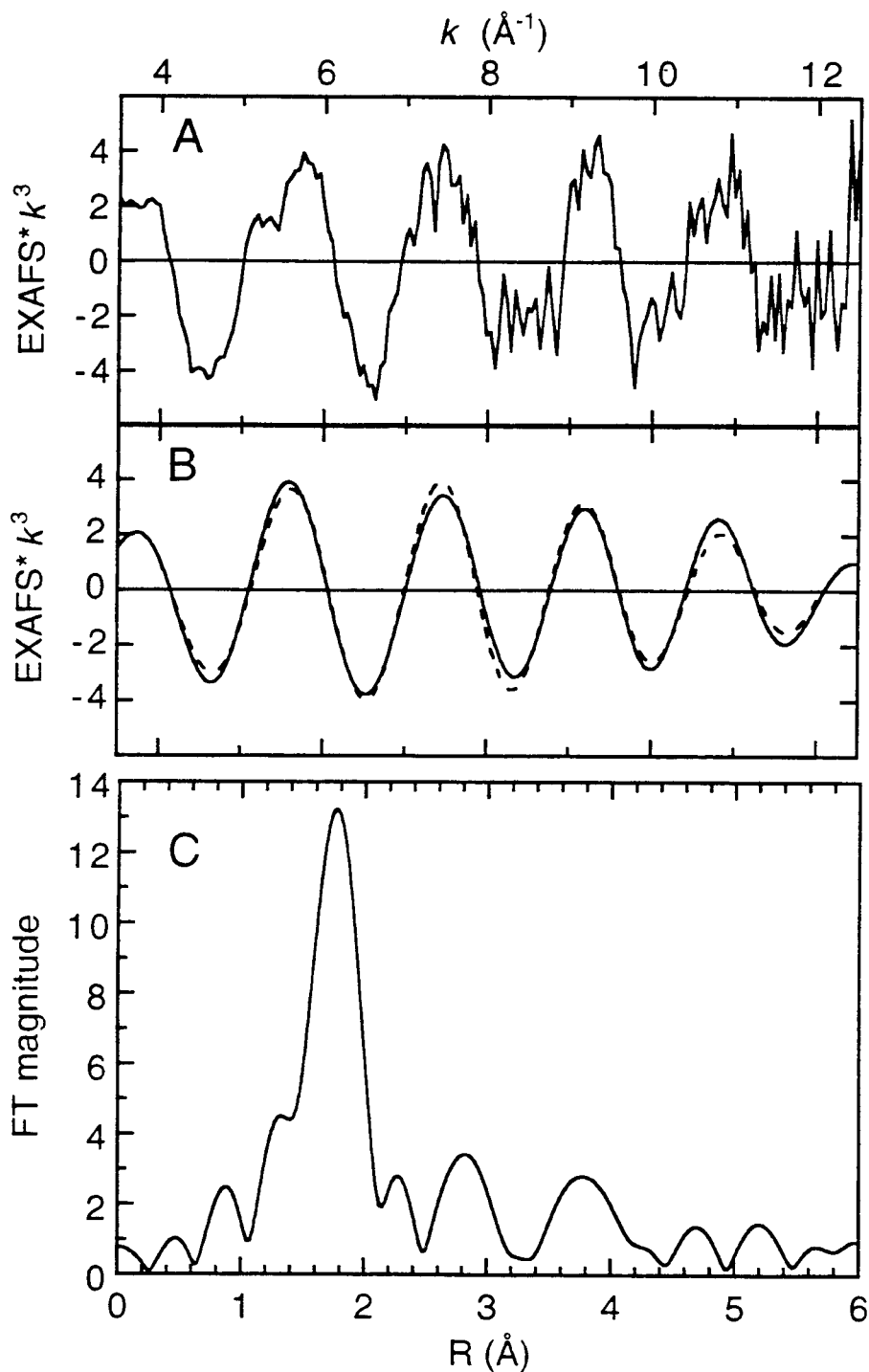


Figure 5.13. A) EXAFS data ($\cdot k^3$) for SLO-1 in glycerol. B) Fit to the Fourier filtered data. The solid line represents the data (FT backtransform range 1.0 - 2.25 \AA) while the dashed line is the fit to the data with one shell of N (Table 5.6, Fit 6). C) Fourier transform (non-phase shift corrected) over the k range 3.5 - 12.5 \AA^{-1} of the EXAFS data of SLO-1.

Table 5.6. Summary of EXAFS Curve-Fitting Results for SLO-1 in Glycerol.

Fit	element	CN ^b		distance ^c	c2 ^d	F
		(fixed)				
1	O	4		2.15	-0.02449	0.32
2	O	5		2.15	-0.02814	0.47
3	O	6		2.15	-0.03158	0.63
4	N	4		2.18	-0.01973	0.45
5	N	5		2.18	-0.02250	0.34
6	N	6		2.18	-0.02500	0.32
7	O	1		2.15	-0.05671	0.28
	N	5		2.18	-0.02299	
8	O	2		2.15	-0.05148	0.25
	N	4		2.18	-0.02086	
9	O	3		2.15	-0.04811	0.22
	N	3		2.18	-0.01830	
10	O	1		1.95*	-0.69547	0.34
	N	5		2.18	-0.02250	
11	O	2		1.95*	-0.64971	0.45
	N	4		2.18	-0.01973	
12	O	3		1.95*	-0.65984	0.63
	N	3		2.18	-0.01650	
13	O	2		2.00*	-0.68207	0.45
	N	4		2.18	-0.01973	
14	O	2		2.05*	-0.07232	0.42
	N	4		2.18	-0.01978	
15	O	2		2.10*	-0.04990	0.30
	N	4		2.18	-0.02053	

^a FT range 3.5 - 12.5 Å⁻¹; FT back-transform range 1.0 - 2.5 Å. ^b CN = coordination number. ^c Errors in distances (±0.02 Å) are estimated from the variance between EXAFS fitting results and values from models of crystallographically known structure.³⁰ ^d c2 values for Fe-O from Fe(acetylacetonate)₃ and Fe-N from [Fe(1,10-phenanthroline)₃](ClO₄)₃ were -0.02391 and -0.02083, respectively. * Values fixed.

number vary. As expected, this gave the same results. The coordination numbers obtained from these fits were low, 3.8 for a fit with one O shell and 4.6 for a fit with one N shell. The low coordination numbers from these fits and the fact that the c_2 values (when CN = 6) are more negative than the respective values for $\text{Fe}(\text{acetylacetonate})_3$ and $[\text{Fe}(1,10\text{-phenanthroline})_3](\text{ClO}_4)_3$ indicate that SLO-1 has a greater distribution of scatterers than the model complexes, as would be expected for the active site of a protein. Experimentally for a spread in first shell distances of 0.15 Å for a six-coordinate complex with mixed O and N ligation, it has been observed that the c_2 values were -0.03408 for a fit with one shell of O and -0.02816 for a fit with one shell of N. The fact that Fits 3 and Fit 6 have less negative c_2 values, respectively, suggests that the spread of first shell distances in SLO-1 is less than 0.15 Å. This is also supported by the fact that a two shell fit (Fits 7-9) does not match the data significantly better than a one shell fit (Fits 1-6) and that two shells should be readily discernible over the k range 4 - 12 Å⁻¹ if the spread of first-shell distances is greater than ~0.1 Å.

5.5.4. Discussion

In summary, the Fe K-edge shape and pre-edge intensity for all three 15-LO active sites are very similar to each other and all consistent with six-coordination. The EXAFS data of SLO-1 show that the iron active site has 5 ± 1 O/N ligands at ~2.16 Å. The average bond length also supports a six-coordinate site: crystallographic information on ferrous model complexes with oxygen and nitrogen ligation reports average bond lengths of 2.16 ± 0.03 Å for six-coordinate sites,⁴⁴⁻⁴⁸ 2.12 ± 0.01 Å for five-coordinate sites,^{26,27} and 2.00 ± 0.01 Å for four-coordinate sites.²⁶ There is no indication of the previously reported shorter Fe–O distance of Van der Heijdt *et. al.*¹⁴ Furthermore, these results show an average first shell distance that is ~0.1 Å longer than the previous result of 2.05 Å.¹⁴ However, the EXAFS data collected by Van der Heijdt *et. al.* was of a pH 9 sodium borate buffered frozen solution and lyophilized native SLO-1 samples. There is now evidence that native SLO-1 consists of more than one form.¹⁸ The fact that native SLO-1 contains a five-coordinate and a six-coordinate form could also explain the higher pre-edge intensity observed by Scarrow *et. al.* in the active site of native SLO-1.¹⁷ The edge and EXAFS analysis of SLO-1 in 50% glycerol from this work and that of SLO-1^N·MeOH of Scarrow *et. al.* give very similar first-shell coordination and distances,¹⁷ indicating that iron active site in SLO-1 in glycerol and methanol is six-coordinate.

The XAS results can be combined with NIR CD/MCD and VTVH MCD to better understand the coordination geometries of the iron active site in plant and mammalian LOs.¹⁹ NIR CD and MCD spectroscopies allow the direct determination of the splitting of the ferrous 5E_g excited state which through ligand field (LF) theory is dependent on the coordination geometry.^{49,50} Through analysis of the NIR CD and MCD spectra, it has been determined that native SLO-1 in solution exists as a nearly equal mixture of five- and six-coordinate forms.¹⁸ Addition of linoleate substrate or alcohols shifts the mixture to the purely six-coordinate form, which is consistent with the XAS pre-edge results and the EXAFS results of SLO-1 in glycerol which show the iron active site to have 5 ± 1 N/O at ~ 2.16 Å.

The two crystal structures^{6,11} of SLO-1 have four common ligands, three histidines and the carboxylate terminus isoleucine. The NIR CD/MCD and XAS spectroscopic results indicate that one and two additional ligands are present in the five- and six-coordinate forms of SLO-1, respectively. One ligand is likely a water or hydroxide, as Nelson¹³ has performed a EPR line broadening experiment on Fe^{+3} SLO-1 in $H_2^{17}O$ which showed evidence that in the ferric enzyme a water or hydroxide is present. Minor *et al.* leave a water-based ligand open as a possibility in their structure, while Boyington *et al.* find no evidence for a water-based ligand. A significant difference in the crystal structures is in the binding of Asn₆₉₄. Minor *et al.* show this residue bound through the carbonyl oxygen of the amide side chain, while the side chain is 3.3 Å from the Fe^{+2} in the Boyington *et al.* structure. An amide carbonyl oxygen would be a relatively weak ligand which could be perturbed by hydrogen bonding or steric effects. Boyington *et al.* have the asparagine side chain hydrogen bonded to a neighboring glycine. The asparagine is also conserved in all sequenced LOs, *except* for rabbit reticulocyte and human 15-LOs. It is reasonable for the sixth ligand in the native six-coordinate SLO-1 site to be this asparagine.

Since the ligands perturb the d-orbital energy levels in a way dependent on their arrangement around the ferrous center,^{51,52} LF calculations⁵¹ were performed on two spectroscopically effective active site models¹⁹ (one five-coordinate without Asn₆₉₄ bound and one six-coordinate with Asn₆₉₄ bound) of SLO-1 built upon the crystallography^{6,11} as well as on the four-coordinate structure of Boyington *et al.* (described as a distorted octahedron missing two *cis* ligands). Comparison of the calculated 5E_g energy levels to those of the experimental 5E_g splittings shows that the five- and six-coordinate LF calculations accurately model the experimentally observed splittings of the two components in the native SLO-1 spectrum. The four-coordinate SLO-1 calculation show the presence of two transitions in the 5000 - 13,000 cm^{-1} region and an additional high-energy transition at $>13,000$ cm^{-1} . Since the experimental NIR CD/MCD data on SLO-1 do not

exhibit such high-energy transitions, the four-coordinate crystal structure does not accurately describe the ferrous site in solution. The observed CD/MCD transitions for native ferrous SLO-1 are consistent with the five- and six-coordinate sites.

The effect of alcohols on the NIR CD/MCD data for the native ferrous SLO-1 site is also dramatic, shifting the mixture of forms to a purely six-coordinate site which has very similar spectral features to the six-coordinate component of the native enzyme. The ferric enzyme has been shown by EPR studies^{53,54} to be a mixture of two fairly axial forms with $g = 6.2$ and 7.4 . Addition of alcohols causes the mixture of EPR signals to shift to the clean $g = 6.2$ peak.⁵³ The coordination number of the two ferric forms is not known, but MCD studies⁵⁵ indicate that a six-coordinate site may also be appropriate for the $g = 6.2$ species, as it is the only form present when alcohols and glycerol are added to the ferric enzyme. NMR studies⁵⁶ of the ferric enzyme showed that alcohols bind near the active site but not directly to the iron, likely in the hydrophobic fatty acid substrate binding site. This may also relate to the alcohol effects on the native ferrous site, which have the same effect as substrate binding to native ferrous SLO-1, and thus the alcohols are likely to bind at the substrate binding site. Asn₆₉₄ is at the end of a cavity which starts at the surface of the enzyme⁶ and which may relate to the fatty acid binding site. It appears that when linoleate (or alcohols) are present at the fatty acid binding site, a change in the active site environment occurs allowing the O δ 1 of Asn₆₉₄ to bind to the iron, converting the active site to the purely six-coordinate form. Thus the ferrous SLO-1 plus linoleate substrate form may be the most relevant with respect to catalysis.

The NIR CD and MCD studies on the two native mammalian 15-LO active sites show that in contrast to SLO-1, they exist as purely six-coordinate structures rather than a mixture of five- and six-coordinate sites.¹⁹ XAS pre-edge intensities also indicate that the mammalian 15-LOs in glycerol are six-coordinate. The edge shapes are also very similar to those of six-coordinate model complexes. The corresponding Asn₆₉₄ amino acid position in SLO-1 is substituted with histidine in rabbit reticulocyte and human 15-LOs.⁵ The differences in the NIR CD/MCD spectra of the native plant vs. these mammalian 15-LOs is reasonably associated with this substitution, as histidine would be a stronger ligand than the carbonyl oxygen of asparagine and lead to a stronger bond. A LF calculation was also performed on a model structure, in which the asparagine O has been replaced with a histidine N.¹⁹ Comparison of the resulting calculated d-orbital energy levels to the experimentally observed transitions for 15-RLO and 15-HLO shows general agreement for the 5E_g splittings. The calculated $^5T_{2g}$ splittings for both the soybean and mammalian enzymes are also qualitatively similar to the ground-state splittings obtained though the

VTVH MCD analysis, showing a larger $^5T_{2g}$ splitting for the five-coordinate SLO-1 site than for the six-coordinate LOs.

The saturation magnetization data for the mammalian 15-LOs are qualitatively different from those of the six-coordinate SLO-1, exhibiting tighter nesting compared to the plant enzyme data. The VTVH MCD analysis of these data shows that both the five- and six-coordinate sites of SLO-1 have a positive zero field splitting (+D), while the mammalian LOs have a negative zero field splitting (-D). Thus replacing one ligand going from the plant to the mammalian enzymes causes large perturbations in the electronic structure of the ferrous site which are clearly exhibited in the behavior of the VTVH MCD data. LF calculations which differ only by the parameters associated with the Asn→His substitution along the molecular z-axis (with the asparagine O weaker than the histidine N) reproduce the +D ground state d-orbital pattern for six-coordinate SLO-1 and the -D pattern for the mammalian LOs. Therefore, although the spectra of six-coordinate SLO-1 and 15-R/HLO are qualitatively similar, the ground-state VTVH MCD and LF analyses demonstrate significant differences in the electronic structure of the ferrous site between the soybean and mammalian enzymes reasonably ascribed to the Asn→His ligand substitution.

5.5.5. Acknowledgments

Mark Pavlosky prepared the SLO-1 sample. The 15-RLO and 15-HLO samples were prepared by Yan Zhang and Qing-Fen Gan of Syntex. Dr. Elliott Sigal, Executive Director of Cell Biology of Syntex Discovery Research, provided the human recombinant 15-lipoxygenase and rabbit reticulocyte 15-lipoxygenase protein samples. Mark Pavlosky, Yan Zhang, Elizabeth Pavel, and Cecelia Campochiaro performed the NIR CD/MCD experiments and the LF calculations alluded to in the Discussion. This research was supported by grants from the NIH (GM40392, E. I. Solomon) and NSF (CHE-9121576, K. O. Hodgson). The Stanford Synchrotron Radiation Laboratory is supported by the Department of Energy, Office of Basic Energy Sciences, Divisions of Chemical Science and Materials Science, and in part by the National Institutes of Health, National Center of Research Resources, Biomedical Research Technology Program (RR-01209, K. O. Hodgson) and the DOE's Office of Health and Environmental Research.

5.5.6. References and Notes

- (1) Samuelsson, B.; Dahlén, S.-E.; Lindgren, J. Å.; Rouzer, C. A.; Serhan, C. N. *Science* **1987**, *237*, 1171.

- (2) Sigal, E.; Laughton, C. W.; Mulkins, M. A. *Ann. New York Acad. Sci.* **1994**, *714*, 211.
- (3) Steinberg, D.; Parthasarathy, S.; Carew, T. E.; Khoo, J. C.; Witztum, J. L. *N. Engl. J. Med.* **1989**, *320*, 915.
- (4) Gardner, H. W. *Biochim. Biophys. Acta* **1991**, *1084*, 221.
- (5) Sigal, E. *Am. J. Physiol.* **1991**, *260*, L13.
- (6) Boyington, J. C.; Gaffney, B. J.; Amzel, L. M. *Science* **1993**, *260*, 1482.
- (7) Petersson, L.; Slappendel, S.; Vliegthart, J. F. G. *Biochim. Biophys. Acta* **1985**, *828*, 81.
- (8) Veldink, G. A.; Vliegthart, J. F. G. *Adv. Inorg. Biochem.* **1984**, *6*, 139.
- (9) Nelson, M. J.; Cowling, R. A.; Seitz, S. P. *Biochemistry* **1994**, *33*, 4966.
- (10) Corey, E. J.; Nagata, R. *J. Am. Chem. Soc.* **1987**, *109*, 8107.
- (11) Minor, W.; Steczko, J.; Bolin, J. T.; Otwinowski, Z.; Axelrod, B. *Biochemistry* **1993**, *32*, 6320.
- (12) Sigal, E.; Craik, C. S.; Highland, E.; Grunberger, D.; Costello, L. L.; Dixon, R. A. F.; Nadel, J. A. *Biochem. Biophys. Res. Comm.* **1988**, *157*, 457.
- (13) Nelson, M. J. *J. Am. Chem. Soc.* **1988**, *110*, 2985.
- (14) Van der Heijdt, L. M.; Feiters, M. C.; Navaratnam, S.; Nolting, H.-F.; Hermes, C.; Veldink, G. A.; Vliegthart, J. F. G. *Eur. J. Biochem.* **1992**, *207*, 793.
- (15) Dunham, W. R.; Carroll, R. T.; Thompson, J. F.; Sands, R. H.; Funk, M. O., Jr. *Eur. J. Biochem.* **1990**, *190*, 611.
- (16) Whittaker, J. W.; Solomon, E. I. *J. Am. Chem. Soc.* **1988**, *110*, 5329.
- (17) Scarrow, R. C.; Trimitsis, M. G.; Buck, C. P.; Grove, G. N.; Cowling, R. A.; Nelson, M. J. *Biochemistry* **1994**, *33*, 15023.
- (18) Pavlosky, M. A.; Solomon, E. I. *J. Am. Chem. Soc.* **1994**, *116*, 11610.
- (19) Pavlosky, M. A.; Zhang, Y.; Westre, T. E.; Gan, Q.-F.; Pavel, E. G.; Campochiaro, C.; Hedman, B.; Hodgson, K. O.; Solomon, E. I. *J. Am. Chem. Soc.* **1995**, *117*, 4316.
- (20) Nelson, M. J. *Biochemistry* **1988**, *27*, 4273.
- (21) Kühn, H.; Barnett, J.; Grunberger, D.; Baeker, P.; Chow, J.; Nguyen, B.; Bursztyn-Pettegrew, H.; Chan, H.; Sigal, E. *Biochim. Biophys. Acta* **1993**, *1169*, 80.
- (22) Sloane, D. L.; Browner, M. F.; Dauter, Z.; Wilson, K.; Fletterick, R. J.; Sigal, E. *Biochem. Biophys. Res. Comm.* **1990**, *173*, 507.
- (23) Scott, R. A.; Hahn, J. E.; Doniach, S.; Freeman, H. C.; Hodgson, K. O. *J. Am. Chem. Soc.* **1982**, *104*, 5364.

- (24) Cramer, S. P.; Tench, O.; Yocum, M.; George, G. N. *Nucl. Instrum. Methods Phys. Res.* **1988**, *A266*, 586.
- (25) George, G. N.; Pickering, I., to be published.
- (26) Kitajima, N., private communication.
- (27) Hodges, K.D.; Wollmann, R.G.; Barfield, E.K.; Hendrickson, D.N. *Inorg. Chem.* **1977**, *16*, 2746.
- (28) Abbreviations used: HB(3,5-*i*Pr₂pz)₃ = hydrotris(3,5-diisopropyl-1-pyrazolyl)borate; TMC = 1,4,8,11-tetramethyl-1,4,8,11-tetraazacyclotetradecane.
- (29) Burbridge, C. D.; Goodgame, D. M. L. *Inorg. Chim. Acta* **1970**, *4*, 231.
- (30) Cramer, S. P.; Hodgson, K. O.; Stiefel, E. I.; Newton, W. E. *J. Am. Chem. Soc.* **1978**, *100*, 2748.
- (31) Cramer, S. P.; Hodgson, K. O. *Prog. Inorg. Chem.* **1979**, *25*, 1.
- (32) Scott, R. A. *Methods Enzymol.* **1985**, *117*, 414.
- (33) Iball, J.; Morgan, C. H. *Acta Crystallogr.* **1967**, *23*, 239.
- (34) Roof, R. B., Jr. *Acta Crystallogr.* **1956**, *9*, 781.
- (35) Johansson, L. *Chem. Scripta* **1976**, *9*, 30.
- (36) Johansson, L.; Molund, M.; Oskarsson, Å. *Inorg. Chim. Acta.* **1978**, *31*, 117.
- (37) Argonne National Laboratory; Garbow, B.S.; Hillstrom, K.E.; More, J.J.
- (38) Agarwal, B. K. *X-ray Spectroscopy*; Springer-Verlag: New York, 1979; p 276.
- (39) Lytle, F. W.; Greigor, R. B.; Sandstrom, D. R.; Marques, E. C.; Wong, J.; Spiro, C. L.; Huffman, G. P.; Huggins, F. E. *Nucl. Instrum. Methods Phys. Res.* **1984**, *226*, 542.
- (40) Lytle, F. W. In *Applications of Synchrotron Radiation*; Winick, H.; Xian, D.; Ye, M.-h.; Huang, T., Eds.; Gordon and Breach Science Publishers: New York, 1989; p 135.
- (41) Tyson, T. A.; Roe, A. L.; Frank, P.; Hodgson, K. O.; Hedman, B. *Phys. Rev. B* **1989**, *39*, 6305.
- (42) Roe, A. L.; Schneider, D. J.; Mayer, R. J.; Pyrz, J. W.; Widom, J.; Que, L., Jr. *J. Am. Chem. Soc.* **1984**, *106*, 1676.
- (43) Randall, C. R.; Shu, L.; Chiou, Y.-M; Hagen, K.S.; Ito, M.; Kitajima, N.; Lachicotte, R.J.; Zang, Y.; Que, L., Jr. *Inorg. Chem.* **1995**, *34*, 1036.
- (44) Miller, L. L.; Jacobson, R. A.; Chen, Y.-S.; Kurtz, D. M., Jr. *Acta Crystallogr.* **1989**, *C45*, 527.
- (45) Oliver, J. D.; Mullica, D. F.; Hutchinson, B. B.; Milligan, W. O. *Inorg. Chem.* **1980**, *19*, 165.

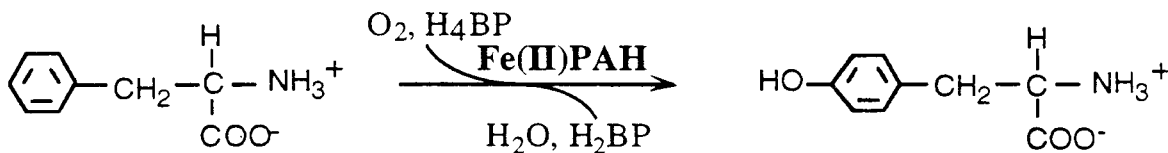
- (46) Kitajima, N.; Fukui, H.; Moro-oka, Y.; Mizutani, Y.; Kitagawa, T. *J. Am. Chem. Soc.* **1990**, *112*, 6402.
- (47) Montgomery, H.; Chastain, R. V.; Natt, J. J.; Witkowska, A. M.; Lingafelter, E. C. *Acta Crystallogr.* **1967**, *22*, 775.
- (48) Price, D. C. *Can. J. Phys.* **1987**, *65*, 1280.
- (49) Solomon, E. I.; Zhang, Y. *Acc. Chem. Res.* **1992**, *25*, 343.
- (50) Solomon, E. I.; Pavel, E. G.; Loeb, K. E.; Campochiaro, C. *Coord. Chem. Rev.* in press.
- (51) Companion, A. L.; Komarynsky, M. A. *J. Chem. Ed.* **1964**, *41*, 257.
- (52) Pulver, S.; Froland, W. A.; Fox, B. G.; Lipscomb, J. D.; Solomon, E. I. *J. Am. Chem. Soc.* **1993**, *115*, 12409.
- (53) Slappendel, S.; Aasa, R.; Malmström, B. G.; Verhagen, J.; Veldink, G. A.; Vliegthart, J. F. G. *Biochim. Biophys. Acta* **1982**, *708*, 259.
- (54) Gaffney, B. J.; Mavrophilipos, D. V.; Doctor, K. S. *Biophys. J.* **1993**, *64*, 773.
- (55) Zhang, Y.; Gebhard, M. S.; Solomon, E. I. *J. Am. Chem. Soc.* **1991**, *113*, 5162.
- (56) Slappendel, S.; Aasa, R.; Falk, K.-E.; Malmström, B. G.; Vänngård, T.; Veldink, G. A.; Vliegthart, J. F. G. *Biochim. Biophys. Acta* **1982**, *708*, 266.

5.6. Phenylalanine Hydroxylase

5.6.1. Introduction

Phenylalanine hydroxylase (PAH), tyrosine hydroxylase (TH), and tryptophan hydroxylase (TPH) are mammalian aromatic amino acid hydroxylases that uniquely use tetrahydropterins as obligatory cofactors. The reactions catalyzed by these enzymes are all used in amino acid metabolism: PAH initiates the detoxification of high levels of phenylalanine^{1,2} while TH and TPH catalyze the committed steps in the biosynthesis of the neurotransmitters dihydroxyphenylalanine^{3,4} and serotonin,^{5,6} respectively. A role for the non-heme iron in oxygen activation is strongly suggested, since all of the mammalian hydroxylases contain one non-heme iron per subunit and each enzyme requires the presence of its metal center for reactivity.⁷⁻⁹ It appears certain that Fe(II) is the catalytically important oxidation state,¹⁰ but the Fe(III) state may play a role in feedback regulation.¹¹ Due to the relatively large quantity of PAH available from rat liver as well as its soluble nature and ease of purification by substrate-induced hydrophobic binding, much more work has been done on this enzyme than the other hydroxylases. Thus, PAH serves as the prototype aromatic amino acid hydroxylase.¹²

PAH catalyzes the rate-limiting step in the removal of phenylalanine from blood. Dysfunction of this enzyme leads to a condition called phenylketonuria, which is characterized by irreversible, progressive brain damage that results from the buildup of phenylalanine and its neurotoxic metabolites.¹³ PAH is a tetramer of ~50 kDa subunits, each of which contains a non-heme iron that is absolutely required for reactivity.⁷⁻⁹ During the hydroxylation of phenylalanine, the enzyme uses molecular oxygen and one tetrahydrobiopterin (H₄BP) to generate tyrosine and a molecule of oxidized pterin cofactor:



Dioxygen is partitioned heterolytically between the phenolic hydroxy group of tyrosine and the initial C4a-carbinolamine form of the oxidized pterin, which subsequently dehydrates to yield the oxidized, quinonoid dihydropterin. In order to avoid depletion of phenylalanine from the liver, the enzyme is only active in the presence of elevated levels of its amino acid substrate. In studies of the protein, it has been observed that phenylalanine binds to an allosteric effector site (as distinguished from the active phenylalanine binding site) concomitant with an increase in the specific activity of the protein. This "activation"

process has a large energetic barrier (30 - 40 kcal/mol by Arrhenius analysis) and is accompanied by a large structural rearrangement of the PAH protein.¹⁴ The transition between the resting low affinity state (the "T" state) and the activated high affinity state (the "R" state) is required for the enzyme to achieve catalytic competence.¹⁴ Enzyme activation can also be accomplished using lysolecithin, α -chymotrypsin, or N-ethylmaleimide.² For the reaction of the resting enzyme with H₄BP an ordered sequential mechanism is observed,¹⁵ phenylalanine + H₄BP + O₂, because tight binding of the pterin to the resting enzyme inhibits its conversion to the activated state.

By analogy to flavin chemistry, it was originally proposed that dioxygen reacts directly with the pterin cofactor to generate 4a-hydroperoxy-tetrahydrobiopterin (4a-OOH), which decays to form the active oxidant. Substantial experimental evidence supports this hypothesis.^{12,16,17} According to this mechanism, Fe(II) would react with the peroxidated cofactor, rather than with dioxygen itself, forming an Fe(II)peroxypterine (Fe-OO-4a) adduct. Heterolytic decomposition of this intermediate is proposed to yield 4a-OH (which has been observed experimentally¹²) and a ferryl species that is the active oxidant. This theory appeared to be supported by the existence of a "copper-free" form of PAH from *Chromobacterium violaceum*,¹⁸ since the heterolytic cleavage of hydroperoxides is known to occur under certain metal free conditions. Conversely, a reaction between the reduced metal and dioxygen may precede formation of the 4a-OOH intermediate. The strongest evidence for such a role for iron in PAH is the diminished oxidation rate of the cofactor in absence of the metal ion.¹² On the basis of chemistry observed in other enzymes and model systems and the clear requirement for reduced iron, it may be that a ferric-superoxide/ferrous-dioxygen adduct forms initially which then peroxidizes the H₄BP.¹⁹ The reaction would yield the same Fe(II)-OO-4a cofactor adduct discussed above and result in possibly the same heterolytic decomposition pathway. The current experimental data unfortunately cannot differentiate these two pathways.

As isolated from either rat liver or an *E. coli*-based overexpression system,¹⁴ PAH is oxidized and in the "T" state (Fe(III)PAH^T). Either reduction or activation may occur next, to give Fe(II)PAH^T or Fe(III)PAH^R, respectively. Finally, the generation of active enzyme follows activation or reduction to give Fe(II)PAH^R. Note that Fe(II)PAH^R has phenylalanine in both the allosteric and the active site. It is this activated form of the ferrous enzyme that reacts with H₄BP and O₂ to generate tyrosine and an oxidized form of the pterin cofactor (see previous page).

X-ray absorption spectroscopy (XAS) can be used to characterize the essential non-heme iron site, both in the absence and presence of substrates and competitive inhibitors of substrates. An understanding of the structure of this iron site will aid in

elucidating the complex mechanism of PAH catalysis. In the study presented here, XAS was used to define the geometric and electronic structure of the non-heme iron active site of Fe(II)PAH^R, Fe(II)PAH^T, Fe(III)PAH^R, and Fe(III)PAH^T. Fe K-edge data were collected for these four forms of PAH and compared to data of four-, five-, and six-coordinate ferrous and ferric model complexes to determine the coordination number of the non-heme active site. In addition, an extended X-ray absorption fine structure (EXAFS) analysis was performed on the data of Fe(II)PAH^R, Fe(II)PAH^T, Fe(III)PAH^R, and Fe(III)PAH^T to provide information on the types of ligands surrounding the iron site and the distances to those ligands.

5.6.2. Experimental Section

The PAH samples were prepared in Prof. John Caradonna's laboratory at Yale University using an *E. coli*-based overexpression system.¹⁴ As-isolated PAH is in the Fe(III)PAH^T form. Each of the four samples (Fe(II)PAH^R, Fe(II)PAH^T, Fe(III)PAH^R, and Fe(III)PAH^T) were exchanged into low-salt 50 mM 3-(*N*-morpholino)propanesulfonic acid (MOPS) buffer and concentrated over a YM30 ultrafiltration membrane to ~2 ml. At this point, 2 volumes of 50 mM MOPS/75% glycerol were added and then the samples were concentrated back down to ~0.2 mL. The Fe(II)PAH^T sample was obtained by reducing the Fe(III)PAH^T sample with one equivalent of dithionite. The R state samples were generated by dissolving the protein in 50 mM MOPS buffer (pH 7.3 at 25 °C) that contained 1 mM phenylalanine and activated by heating the sample to 25 °C for 10 minutes. The samples were then concentrated as described above. Two volumes of 50 mM MOPS/75% glycerol/10 mM phenylalanine were added and then the R state samples were concentrated back down to ~0.2 mL. The iron concentrations of all four samples were between 2.0 - 2.7 mM in Fe. The starting specific activity for the Fe(III)PAH^T sample was 7.9 U/mg with about 0.75 Fe/subunit. The starting specific activity for the Fe(III)PAH^R sample was 6.0 U/mg with about 0.75 Fe/subunit. The samples were loaded into Lucite EXAFS cells (23 x 1 x 3 mm) with 37 μm Kapton windows and frozen in liquid nitrogen. The samples were characterized before and after exposure to the X-ray beam using electron paramagnetic resonance (EPR).

X-ray absorption spectra were recorded at the Stanford Synchrotron Radiation Laboratory (SSRL) on unfocused beamline 7-3 during dedicated conditions (3 GeV, 50-100 mA). The radiation was energy resolved using a Si(220) double-crystal monochromator with 1 mm high pre-monochromator beam defining slits. An Oxford Instruments continuous-flow liquid helium CF1208 cryostat was used to maintain a

constant temperature of 10 K. Energies were calibrated using an internal Fe foil standard, assigning the first inflection point to 7111.2 eV.²⁰ The spectrometer energy resolution was approximately 1.4 eV with reproducibility in edge position determination of < 0.2 eV.⁴⁰ Data were measured to $k = 15 \text{ \AA}^{-1}$, detuning the monochromator 50% at 7998 eV to minimize harmonic contamination. The fluorescence signal was monitored using a 13-element Ge solid-state array detector²¹ windowed on the Fe K α signal. During the experiment, count rates of approximately 30,000 s⁻¹ total per element were not exceeded. Thirty scans were collected on the Fe(II)PAH^T sample and twenty-two scans were collected on the Fe(II)PAH^R sample. Both the Fe(III)PAH^R and Fe(III)PAH^T samples photo-reduced in the beam, as was evident by changes in the edge shape and position. Therefore, the Fe(III)PAH^T sample was exposed to the beam in two different spots and thus two 'first' scans and a total of eleven scans were collected. Since the photo-reduction of Fe(III)PAH^R was anticipated, the sample was exposed in four different spots giving four 'first' scans and a total of twenty scans. The edge position of the data in the 'fifth' scans was at ~1 eV lower in energy than that in the 'first' scans for both ferric protein samples. From comparison of 'first' scan data to 'second' scan data to 'third' scan data, *etc.*, no discernible changes in the EXAFS could be detected. Therefore, the edge spectra of Fe(III)PAH^T and Fe(III)PAH^R presented in this section are an average of the 'first' scans only, while the EXAFS data shown are an average of all the scans collected. A pre-edge subtraction was performed by fitting the tail of a Gaussian to the pre-edge region and subtracting this polynomial from the averaged spectra.²² A three-segment spline approximately even in k -space was fit to the EXAFS region and the data normalized to an edge jump of one at 7130 eV. The spline was chosen so that it minimized residual low-frequency background but did not reduce the EXAFS amplitude as checked by monitoring the Fourier transform of the EXAFS during the background subtraction process.

Fe K-edge spectra were also collected on four-, five-, and six-coordinate ferrous and ferric model complexes. Fe(acac)₃ was purchased from Aldrich.²³ Fe(HB(3,5-*i*Pr₂pz)₃)Cl²⁴ was obtained as a gift from N. Kitajima. (BF₄)[Fe(TMC)Cl],²⁵ [Fe(imidazole)₆]Cl₂,²⁶ Fe(salen)Cl,²⁷ and (Et₄N)[FeCl₄]²⁸ were prepared as described in the literature. The model complex XAS samples were prepared in the following manner. [Fe(imidazole)₆]Cl₂, Fe(HB(3,5-*i*Pr₂pz)₃)Cl, and (BF₄)[Fe(TMC)Cl] are air-sensitive and thus the following procedure was carried out in a nitrogen-filled glove box for these three samples. The crystalline samples were each mixed with BN and ground into a fine powder. The BN/sample mixture was pressed into a 1 mm thick Al spacer that was sealed with 63.5 μm Mylar tape windows and frozen in liquid nitrogen. Data were measured in

transmission mode with N₂-filled ionization chambers to $k = 9.5 \text{ \AA}^{-1}$ detuning the monochromator 50% at 7474 eV to minimize harmonic contamination. Two to three scans were averaged for each sample. A smooth pre-edge background was removed from the averaged spectra by fitting a first order polynomial to the pre-edge region and subtracting this polynomial from the entire spectrum. A two segment spline of order two was fit to the EXAFS region and the data normalized to an edge jump of one at 7130 eV. The intensities and energies of the pre-edge features were determined as described below.

EXAFS data reduction was performed on the normalized protein spectra according to established methods.²⁹⁻³¹ The normalized data were converted to k -space. The photoelectron wave vector, k , is defined by $[2m_e(E-E_0)/\hbar^2]^{1/2}$ where m_e is the electron mass, E is the photon energy, \hbar is Planck's constant divided by 2π , and E_0 is the threshold energy of the absorption edge, which was defined to be 7130 eV for the Fe K absorption edge. The empirical EXAFS data analyses were performed with nonlinear least-square curve-fitting techniques^{20,29-31} using empirical phase and amplitude parameters. The following models were used to obtain the empirical Fe-X backscattering parameters of interest: Fe-O from $[\text{Fe}(\text{acac})_3]$ ^{32,33} and Fe-N from $[\text{Fe}(1,10\text{-phenanthroline})_3](\text{ClO}_4)_3$.^{34,35} Fourier transforms (from k to R space) were performed for the data range 3.5-12.5 \AA^{-1} with a Gaussian window of 0.1 \AA^{-1} . The window widths used in the backtransforms (from R to k space) for the proteins are given in the results section. The window widths were kept as similar as possible to those used to extract amplitude and phase parameters from the model compounds to minimize artifacts introduced by the Fourier filtering technique. All curve-fitting was based on k^3 -weighted data and applied to the individual filtered shell of interest. Only the structure-dependent parameters, the distance and coordination number, were varied unless stated otherwise. A "goodness of fit" parameter, F , was calculated as $F = \{[k^6(\text{data} - \text{fit})^2]/(\text{no. of points})\}^{1/2}$ for each fit.

The intensities and energies of pre-edge features of the model complex and protein data were quantitated by fits to the data. The fitting program EDG_FIT, which utilizes the double precision version of the public domain MINPAK fitting library was used. EDG_FIT was written by Dr. Graham N. George of the Stanford Synchrotron Radiation Laboratory. All spectra were fit over the range 7108-7118 eV. Pre-edge features were modeled by pseudo-Voigt line shapes (simple sums of Lorentzian and Gaussian functions).³⁶⁻³⁹ A fixed 50:50 ratio of Lorentzian to Gaussian contribution for the pre-edge feature successfully reproduced these spectral features. Functions modeling the background underneath the pre-edge features were chosen empirically to give the best fit. The second derivative of the data was compared to the second derivative of the fit. In all

cases, a number of fits were obtained which reproduced the data and the second derivative. The value reported for the area of a fitted feature (where peak area was approximated by the height x full-width-at-half-maximum (FWHM)) is the average of all the pseudo-Voigts which successfully fit the feature. For each sample, the standard deviation of the average of the areas was calculated to quantitate the error.

5.6.3. Results and Analysis

5.6.3.1. Fe K-Edge XAS. Fe K-edge XAS data of Fe(II)PAH^R, Fe(II)PAH^T, Fe(III)PAH^R, and Fe(III)PAH^T have been compared to data of four-, five-, and six-coordinate ferrous and ferric model complexes to obtain information on the coordination number and the geometry of the iron active site of PAH. The XAS edge spectra for Fe(II)PAH^R and Fe(II)PAH^T are shown in Figure 5.14A and those of Fe(III)PAH^R and Fe(III)PAH^T are shown in Figure 5.14B. Figure 5.15 contains spectra of representative four-, five-, and six-coordinate ferrous model complexes: Fe(HB(3,5-*i*Pr₂pz)₃)Cl,²⁴ (BF₄)[Fe(TMC)Cl],²⁵ and [Fe(imidazole)₆]Cl₂²⁶ in part A and ferric model complexes (Et₄N)[FeCl₄],²⁸ Fe(salen)Cl,²⁷ and Fe(acac)₃^{32,33} in part B. The lowest energy peaks arise from the weak 1s→3d transition which is at ~7112 eV followed by the 1s→4p transition at ~7125 eV. An expanded view of the 1s→3d pre-edge region is shown for the proteins as well as for the model complexes as insets in figures 5.14 and 5.15, respectively. The energies and areas of the pre-edge features were determined by fits to the data and are presented in Table 5.7.

The spectra for Fe(II)PAH^R, Fe(II)PAH^T, Fe(III)PAH^R, and Fe(III)PAH^T all have a very broad, low-intensity pre-edge feature which can be fit with two features. The three ferrous complexes, Fe(HB(3,5-*i*Pr₂pz)₃)Cl, (BF₄)[Fe(TMC)Cl], and [Fe(imidazole)₆]Cl₂, all have what appear to be two pre-edge features split by ~2 eV with varying intensities. The four-coordinate complex has the most intense pre-edge feature (19.8 total area), while the six-coordinate complex has the least intense pre-edge feature (3.8). The ferric four-coordinate complex, (Et₄N)[FeCl₄], has a single intense pre-edge feature (20.7), while the five-coordinate model, Fe(salen)Cl, has two pre-edge peaks with the lower energy peak being much more intense. The ferric six-coordinate complex has two relatively weak features (4.6 total area) with an intensity ratio of 3:2. The most intense edge feature, attributed to the 1s→4p transition at ~7125 eV, is very similar in shape and intensity in Fe(II)PAH^R and Fe(II)PAH^T (Figure 5.14A). The main edge features of Fe(III)PAH^R and Fe(III)PAH^T also look very similar and lie at approximately 4 eV higher than the respective ferrous proteins. The edge features of the ferric four-, five-

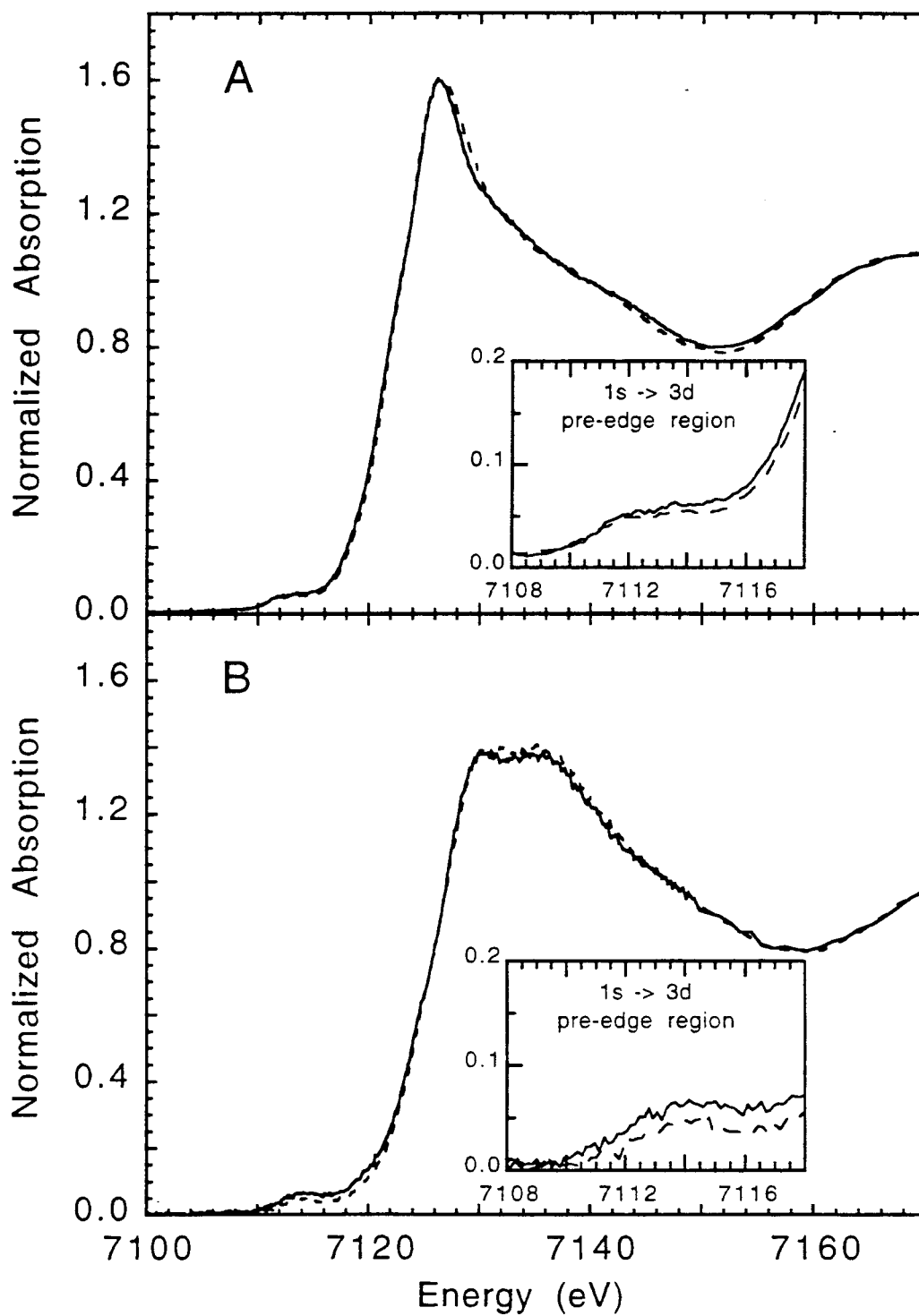


Figure 5.14. Fe K-edge XAS spectra of Fe(II)PAHT^T (—) and Fe(II)PAHR^R (---) are shown in part A and the spectra of Fe(III)PAHT^T (—) and Fe(III)PAHR^R (---) are shown in part B. The insets are expansions of the 1s → 3d pre-edge region.

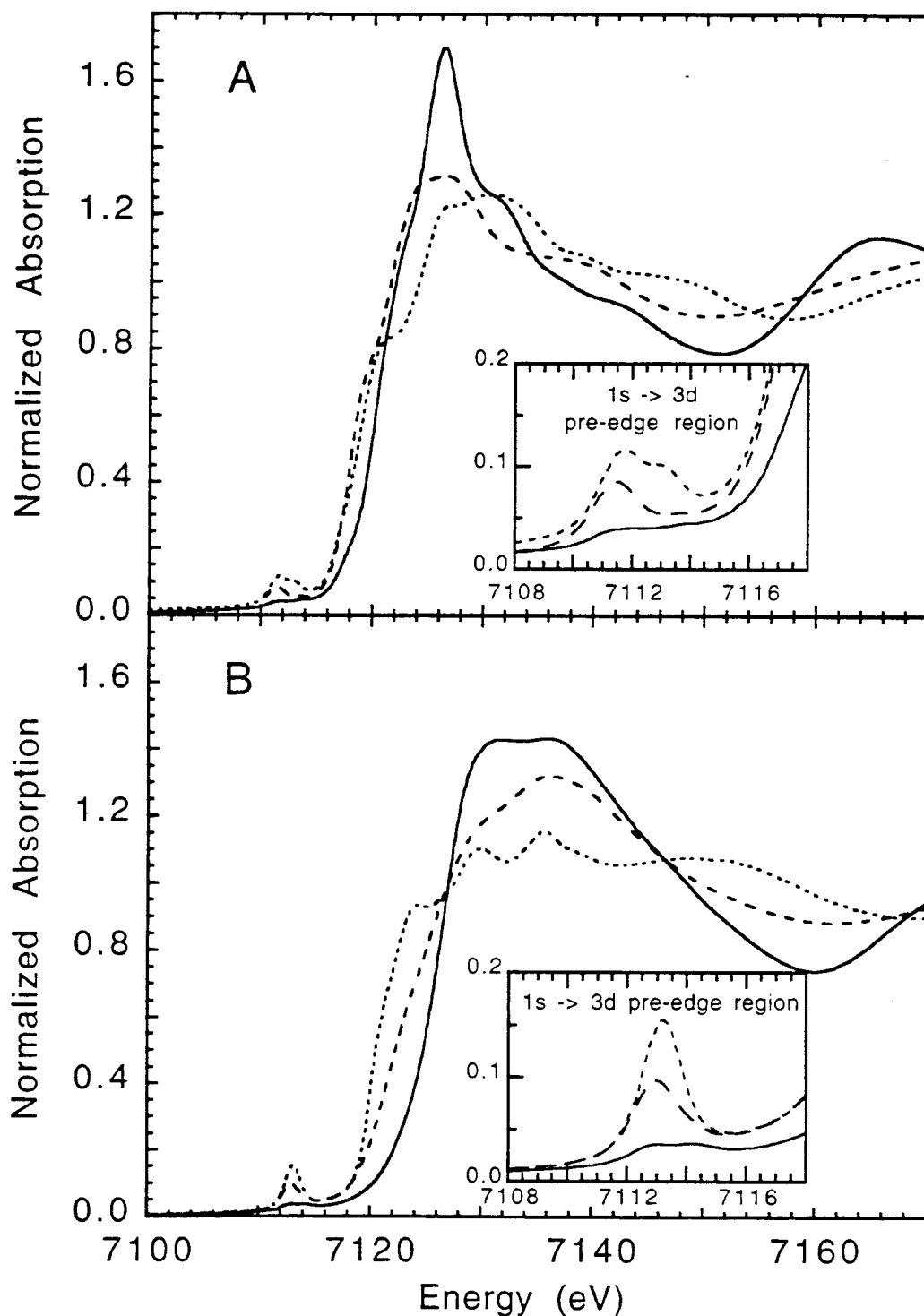


Figure 5.15. Fe K-edge XAS spectra of four-, five-, and six-coordinate ferrous model complexes are shown in part A: $\text{Fe}(\text{HB}(3,5\text{-}i\text{Pr}_2\text{pz})_3)\text{Cl}$ (.....), $(\text{BF}_4)[\text{Fe}(\text{TMC})\text{Cl}]$ (---), and $[\text{Fe}(\text{imidazole})_6]\text{Cl}_2$ (—). XAS spectra of four-, five-, and six-coordinate ferric model complexes are shown in part B: $(\text{Et}_4\text{N})[\text{FeCl}_4]$ (.....), $[\text{Fe}(\text{salen})\text{Cl}]$ (---), and $\text{Fe}(\text{acac})_3$ (—). The insets are expansions of the 1s \rightarrow 3d pre-edge region.

Table 5.7. XAS Pre-Edge Energies and Areas for PAH and Model Complexes.

sample	oxid. state	CN ^a	pre-edge energy (eV)	pre-edge area ^b	total area ^b
Fe(HB(3,5- <i>i</i> Pr ₂ pz) ₃)Cl	2+	4	7111.64 (0.02)	14.2 (0.5)	19.8 (0.9)
			7113.17 (0.02)	5.6 (0.9)	
(BF ₄)[Fe(TMC)Cl]	2+	5	7111.41 (0.01)	10.9 (0.1)	12.9(0.2)
			7113.43 (0.02)	2.0 (0.3)	
[Fe(imidazole) ₆]Cl ₂	2+	6	7111.24 (0.03)	1.6 (0.5)	3.8 (0.3)
			7112.35 (0.16)	1.6 (0.8)	
			7113.66 (0.02)	0.6 (0.2)	
Fe(II)PAH ^T	2+	--	7111.72 (0.06)	4.6 (0.7)	9.9 (1.4)
			7113.58 (0.11)	5.3 (0.7)	
Fe(II)PAH ^R	2+	--	7111.75 (0.07)	5.1 (0.7)	8.2 (1.0)
			7113.60 (0.08)	3.1 (0.7)	
(Et ₄ N)[FeCl ₄]	3+	4	7113.16 (0.00)	20.7 (0.8)	20.7 (0.8)
Fe(salen)Cl	3+	5	7112.91 (0.01)	12.9 (0.3)	14.4 (0.6)
			7114.25 (0.07)	1.5 (0.4)	
Fe(acac) ₃	3+	6	7112.79 (0.02)	2.7 (0.3)	4.6 (0.3)
			7114.31 (0.04)	1.9 (0.1)	
Fe(III)PAH ^T	3+	--	7112.41 (0.06)	5.4 (1.4)	13.7 (4.1)
			7114.28 (0.06)	8.3 (4.5)	
Fe(III)PAH ^R	3+	--	7112.75 (0.07)	2.3 (0.4)	8.2 (1.1)
			7114.24 (0.08)	5.9 (1.0)	

^a CN = coordination number. ^b Pre-edge areas and errors were determined from fits to the data and the values reported were multiplied by 100. See the Experimental Section for a discussion of fitting procedure and error determination.

six-coordinate model complexes differ drastically in shape (Figure 5.15) with the edge position of the ferric complexes being ~4 eV higher in energy than the ferrous complexes.

The $1s \rightarrow 3d$ pre-edge feature can be used to probe the coordination number of the iron in the active site of PAH. The $1s \rightarrow 3d$ transition is formally electric dipole forbidden, but gains intensity through an allowed quadrupole transition and also by $4p$ mixing into the $3d$ states as a result of the noncentrosymmetric environment of the metal site. It has been shown for ferric and ferrous complexes that when the symmetry of the iron site is lowered, the pre-edge intensity increases due to an increase in the $3d$ - $4p$ mixing.^{40,41} As described in more detail in Chapter 4, the pre-edge splitting and intensity distribution is indicative of the site symmetry of the iron.

When a high spin ferrous ion is in an octahedral site, three transitions are observed for an $1s$ electron into 4T_1 , 4T_2 , and ${}^4T_1 d^{(n+1)}$ excited states (a transition into the 4A_2 state is not observed as it would involve a two electron transition). The transitions into these states are only quadrupole allowed as the iron is in a centrosymmetric site and therefore there is no $4p$ - $3d$ mixing. Thus, one observes three weak peaks in the pre-edge region, as can be seen in the $[\text{Fe}(\text{imidazole})_6]\text{Cl}_2$ spectrum (Figure 5.15A). However, in some cases only two transitions are observed since the difference in energy between the lowest 4T_1 and the 4T_2 states is about the same as the energy resolution at the Fe K-edge. When a high spin ferrous atom is in a square pyramidal site, the intensity of the lower energy pre-edge feature increases dramatically, since there is now $4p_z$ mixing into the $3d_{z^2}$ orbital due to the loss of center of symmetry, as can be seen in the $(\text{BF}_4)[\text{Fe}(\text{TMC})\text{Cl}]$ spectrum (Figure 5.15A). When a high spin ferrous atom is in a tetrahedral site, there are two intense pre-edge features due to $4p$ mixing into the d_{xy} , d_{xz} , d_{yz} orbitals, with the lower energy feature being more intense than the higher energy feature, as can be seen in the $(\text{Fe}(\text{HB}(3,5\text{-}i\text{Pr}_2\text{pz})_3)\text{Cl})$ spectrum in Figure 5.15A.

Empirically the pre-edge features of $\text{Fe}(\text{II})\text{PAH}^{\text{R}}$ and $\text{Fe}(\text{II})\text{PAH}^{\text{T}}$ (Figure 5.14A) look much more similar in shape and intensity to those of the six-coordinate ferrous complex and quite different from those of the four- and five-coordinate complexes. The broad pre-edge feature of $\text{Fe}(\text{II})\text{PAH}^{\text{R}}$ and $\text{Fe}(\text{II})\text{PAH}^{\text{T}}$ can be fit with two peaks, with the first peak having a wider FWHM than second peak, indicating that the first feature contains transitions into both the 4T_1 and the 4T_2 states. The first pre-edge feature of $\text{Fe}(\text{II})\text{PAH}^{\text{R}}$ is more intense than the second, similar to what is seen in an octahedral ferrous case. In $\text{Fe}(\text{II})\text{PAH}^{\text{T}}$ both features are approximately equal intensity. The energies of the pre-edge peaks of both $\text{Fe}(\text{II})\text{PAH}^{\text{R}}$ and $\text{Fe}(\text{II})\text{PAH}^{\text{T}}$ are consistent with those seen in octahedral ferrous complexes. The total fitted area of the pre-edge features is higher in the two ferrous proteins than in the octahedral ferrous model complex, which can be attributed to an overall

less symmetric iron site caused by mixed ligation and variation in bond lengths. However, the shape of the ferrous PAH pre-edge feature is very similar to that of the $[\text{Fe}(\text{imidazole})_6]\text{Cl}_2$ and other six-coordinate ferrous complexes. In addition, the shapes of the main edge feature at ~ 7126 eV in the $\text{Fe}(\text{II})\text{PAH}^{\text{R}}$ and $\text{Fe}(\text{II})\text{PAH}^{\text{T}}$ spectra are very much alike and similar to that of the six-coordinate $[\text{Fe}(\text{imidazole})_6]\text{Cl}_2$ spectrum. The results are consistent in indicating that both $\text{Fe}(\text{II})\text{PAH}^{\text{R}}$ and $\text{Fe}(\text{II})\text{PAH}^{\text{T}}$ have a six-coordinate iron active site with little difference between the "R" and "T" forms of the enzyme.

The intensity pattern and energy splittings of the pre-edge features of ferric iron are also indicative of the iron's site symmetry. When a high spin ferric atom is in an octahedral site, two features are observed from transitions of an $1s$ electron into ${}^5\text{T}_2$ and ${}^5\text{E}$ $d^{(n+1)}$ excited states. The transitions into these states are only quadrupole allowed as the iron is in a centrosymmetric site and therefore there is no $4p$ - $3d$ mixing. Thus, one observes two weak transitions with an intensity ratio of 3:2 as can be seen in the $\text{Fe}(\text{acac})_3$ spectrum (Figure 5.15B). When a high spin ferric atom is in a square pyramidal site, the intensity of the lower energy transition increases dramatically, since there is now $4p_z$ mixing into the $3d_{z^2}$ orbital due to the loss of center of symmetry, as can be seen in the $\text{Fe}(\text{salen})\text{Cl}$ spectrum (Figure 5.15B). When a high spin ferric atom is in a tetrahedral site, there is a single very intense pre-edge feature due to $4p$ mixing into the d_{xy} , d_{xz} , d_{yz} orbitals, as can be seen in the $(\text{Et}_4\text{N})[\text{FeCl}_4]$ spectrum in Figure 5.15B.

Empirically the pre-edge features of $\text{Fe}(\text{III})\text{PAH}^{\text{R}}$ and $\text{Fe}(\text{III})\text{PAH}^{\text{T}}$ (Figure 5.14B) look much more similar in shape and intensity to that of the six-coordinate ferric complex and quite different than that of the four- and five-coordinate complexes. The broad pre-edge feature of $\text{Fe}(\text{III})\text{PAH}^{\text{R}}$ and $\text{Fe}(\text{III})\text{PAH}^{\text{T}}$ can be fit with two peaks that are very similar in energy to the two features in the $\text{Fe}(\text{acac})_3$ spectrum (Table 5.7). However, the area of the higher energy pre-edge feature in both the $\text{Fe}(\text{III})\text{PAH}^{\text{R}}$ and $\text{Fe}(\text{III})\text{PAH}^{\text{T}}$ data is larger than that of the lower energy feature with the total area of the fitted features being between that of the five- and six-coordinate model complexes. This could arise from two possible origins, first it is possible that the background subtraction is less accurate in protein data due to the increased noise level and second the iron site will be less symmetric due to mixed ligation and variation in bond lengths. However, the shapes of the main edge feature at ~ 7135 eV in the $\text{Fe}(\text{III})\text{PAH}^{\text{R}}$ and $\text{Fe}(\text{III})\text{PAH}^{\text{T}}$ spectra are very much alike and similar to that of the six-coordinate $\text{Fe}(\text{acac})_3$ spectrum, indicating that both $\text{Fe}(\text{III})\text{PAH}^{\text{R}}$ and $\text{Fe}(\text{III})\text{PAH}^{\text{T}}$ have a six-coordinate iron active site with little difference between the "R" and "T" forms of the enzyme.

5.6.3.2. EXAFS. EXAFS studies of Fe(II)PAH^R, Fe(II)PAH^T, Fe(III)PAH^R, and Fe(III)PAH^T were pursued to obtain metrical information on the iron active site of each of these species. The EXAFS spectra of Fe(II)PAH^R and Fe(II)PAH^T are shown in Figure 5.16A with the Fourier transforms (FTs) taken over the k range of 3.5 - 12.5 Å⁻¹ shown in 5.16B. Figure 5.17A contains the EXAFS spectra of Fe(III)PAH^R and Fe(III)PAH^T with the FTs taken over the k range of 3.5 - 12.5 Å⁻¹ shown in 5.17B. Curve-fitting was performed on filtered first shell contributions over the k range 4 - 12 Å⁻¹ varying bond distances and coordination numbers. Note that curve-fitting was also performed over the k range of 3.8 - 10 Å⁻¹ for the Fe(III)PAH^R and Fe(III)PAH^T data and over the k range of 4 - 14 Å⁻¹ for the Fe(II)PAH^R and Fe(II)PAH^T data. In addition, the averaged 'first scan' data of Fe(III)PAH^R and Fe(III)PAH^T were fit over the k range of 3.8 - 10 Å⁻¹. The curve-fitting results over the different k ranges were all very similar (all within the error of the technique) to those over the k range of 4 - 12 Å⁻¹ that are presented in Table 5.8. In each of the four cases, the FT peak centered at ~1.8 Å (non-phase shift corrected) could not be adequately fit with a single shell of either O's or N's (Fits 1, 2, 7, 8, 13, 14, 19, and 20), although this was the least prominent for Fe(II)PAH^R. In particular, these single shell fits did not match the frequency of the data at higher k and gave unreasonably low coordination numbers. The F values were significantly reduced (typically by a factor of 2) when a second shell was included in the fit. The tabulated results show fits with two O waves, an O (shorter) and a N wave, an O and a N (shorter) wave, and two N waves. The coordination numbers obtained from these two shell fits are 6±1 for Fe(II)PAH^T, 5±1 for Fe(II)PAH^R, 6±1 for Fe(III)PAH^T, and 6±1 for Fe(III)PAH^R. There are only subtle differences between an Fe-O and Fe-N EXAFS wave and they can generally not be distinguished in EXAFS fits. Furthermore, it is even more difficult to distinguish the two elements in non-heme iron enzymes due to the quality of the data and the fact that there is usually both O and N in the first coordination sphere. Usually Fe-O distances are shorter than Fe-N distances, with octahedral Fe(II)-N distances being ~2.20 Å,⁴² Fe(II)-O distances being ~2.15 Å,⁴³⁻⁴⁶ Fe(III)-N distances being ~2.15 Å,⁴⁷⁻⁵² and Fe(III)-O distances being ~1.98 Å.⁴⁷⁻⁵⁴ The two shell fits with the O shell at a shorter distance than the N shell (Fits 4, 10, 16, and 22) are therefore presented in comparison to the backtransformed data in Figure 5.18.

There are subtle differences between the fits to the Fe(II)PAH^T and Fe(II)PAH^R EXAFS data. In comparing Fits 4 and 10, the distances of both the O and N shell lengthen by ~0.04 Å in going from Fe(II)PAH^T to Fe(II)PAH^R and the total coordination number decreases from 6.2 to 4.5 with a marked decrease in the coordination number of the second shell in Fe(II)PAH^R. However, the pre-edge and edge features of Fe(II)PAH^T and

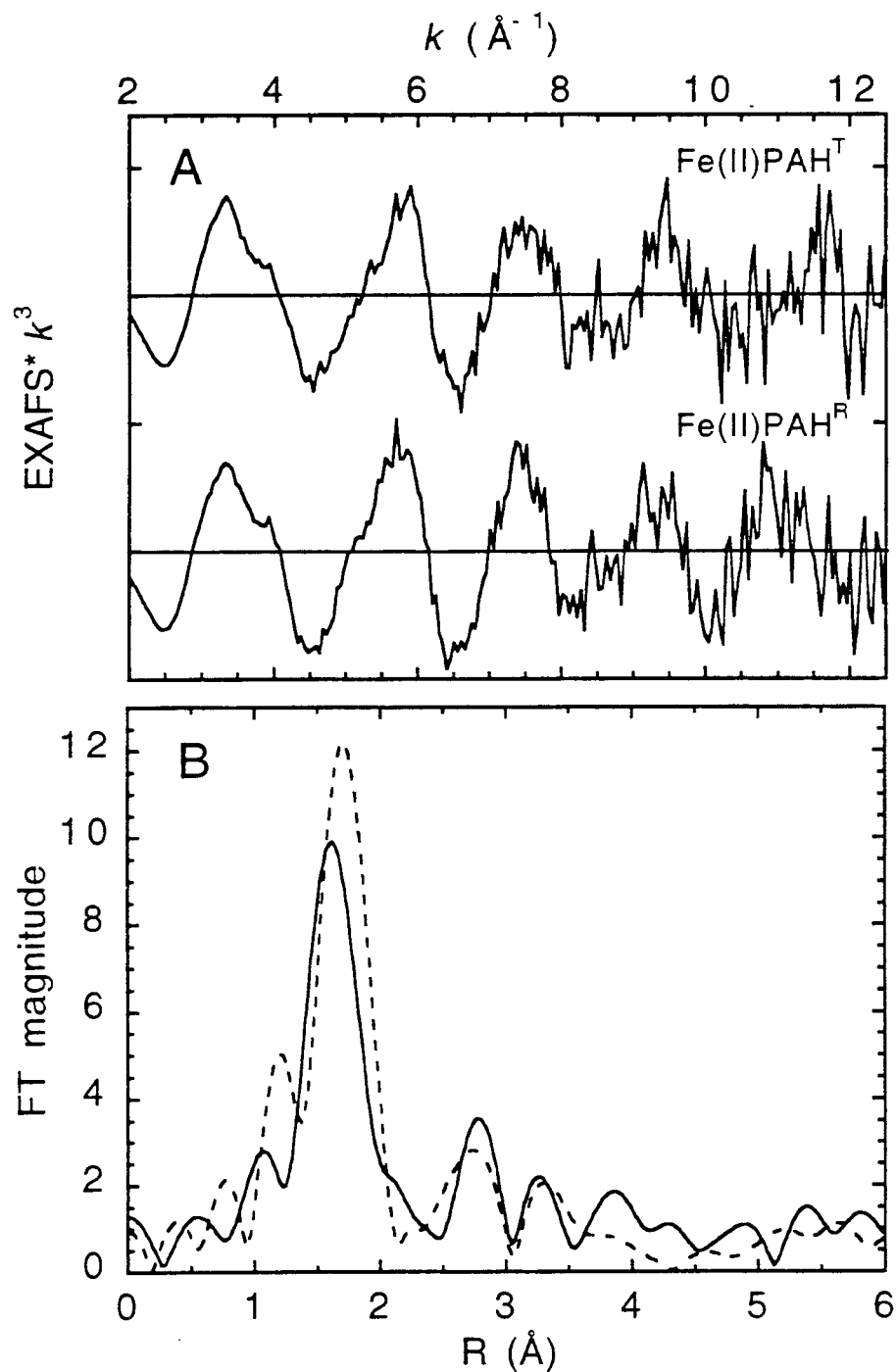


Figure 5.16. A) EXAFS data ($\cdot k^3$) for Fe(II)PAH^T and Fe(II)PAH^R (the ordinate scale is 5 between tick marks with solid horizontal lines indicating the zero point of each plot). B) Fourier transform (non-phase shift corrected) over the k -range 3.5 - 12.5 \AA^{-1} of the EXAFS data of Fe(II)PAH^T (—) and Fe(II)PAH^R (---).

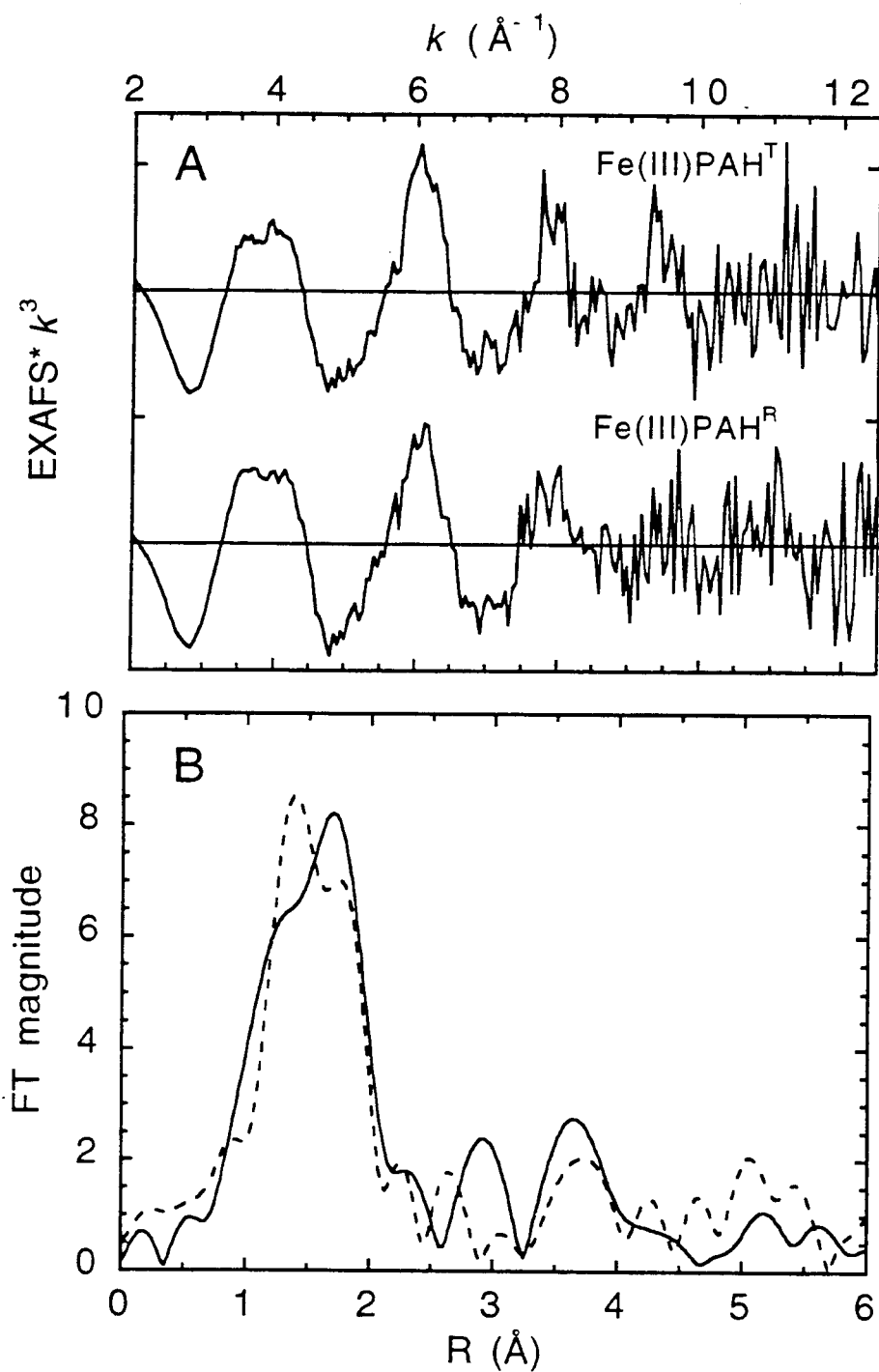


Figure 5.17. A) EXAFS data ($\cdot k^3$) for Fe(III)PAH^T and Fe(III)PAH^R (the ordinate scale is 5 between tick marks with solid horizontal lines indicating the zero point of each plot). B) Fourier transform (non-phase shift corrected) over the k -range 3.5 - 12.5 \AA^{-1} of the EXAFS data of Fe(III)PAH^T (—) and Fe(III)PAH^R (---).

Table 5.8. Summary of EXAFS Curve-Fitting Results.

sample	Fit #	FT window width (Å)	element	CN ^{a,b}	bond length (Å) ^b	<i>F</i>
Fe(II)PAH ^T	1	[0.8-2.3]	N	2.9	2.14	0.91
	2	[0.8-2.3]	O	2.5	2.12	0.75
	3	[0.8-2.3]	O	3.2	2.09	0.36
			O	2.0	2.25	
	4	[0.8-2.3]	O	3.5	2.10	0.34
			N	2.4	2.29	
5	[0.8-2.3]	O	2.5	2.22	0.27	
		N	3.7	2.10		
Fe(II)PAH ^R	6	[0.8-2.3]	N	4.3	2.11	0.25
			N	3.2	2.27	
	7	[1.0-2.15]	N	4.1	2.17	0.58
			O	3.4	2.15	0.39
	9	[1.0-2.15]	O	3.6	2.14	0.32
			O	0.7	2.29	
10	[1.0-2.15]	O	3.7	2.14	0.32	
		N	0.8	2.33		
11	[1.0-2.15]	O	2.2	2.20	0.36	
		N	2.8	2.13		
Fe(III)PAH ^T	12	[1.0-2.15]	N	4.2	2.15	0.37
			N	2.1	2.27	
	13	[0.7-2.2]	N	2.8	2.08	1.1
			O	2.5	2.05	0.94
	15	[0.7-2.2]	O	1.9	1.93	0.44
			O	3.4	2.09	
16	[0.7-2.2]	O	2.4	1.96	0.46	
		N	4.0	2.14		
17	[0.7-2.2]	O	3.7	2.08	0.44	
		N	2.1	1.94		
Fe(III)PAH ^R	18	[0.7-2.2]	N	2.9	1.97	0.49
			N	4.6	2.13	
	19	[0.9-2.15]	N	2.4	2.07	1.2
			O	2.2	2.04	0.99
	21	[0.9-2.15]	O	2.3	1.94	0.32
			O	3.2	2.10	
22	[0.9-2.15]	O	2.7	1.96	0.33	
		N	3.7	2.15		
23	[0.9-2.15]	O	3.5	2.09	0.24	
		N	2.6	1.95		
24	[0.9-2.15]	N	3.3	1.97	0.29	
		N	4.4	2.13		

^a CN = coordination number. ^b Errors in distances (± 0.02 Å) and coordination numbers ($\pm 25\%$) are estimated from the variance between EXAFS fitting results and values from models of crystallographically known structure.²⁹

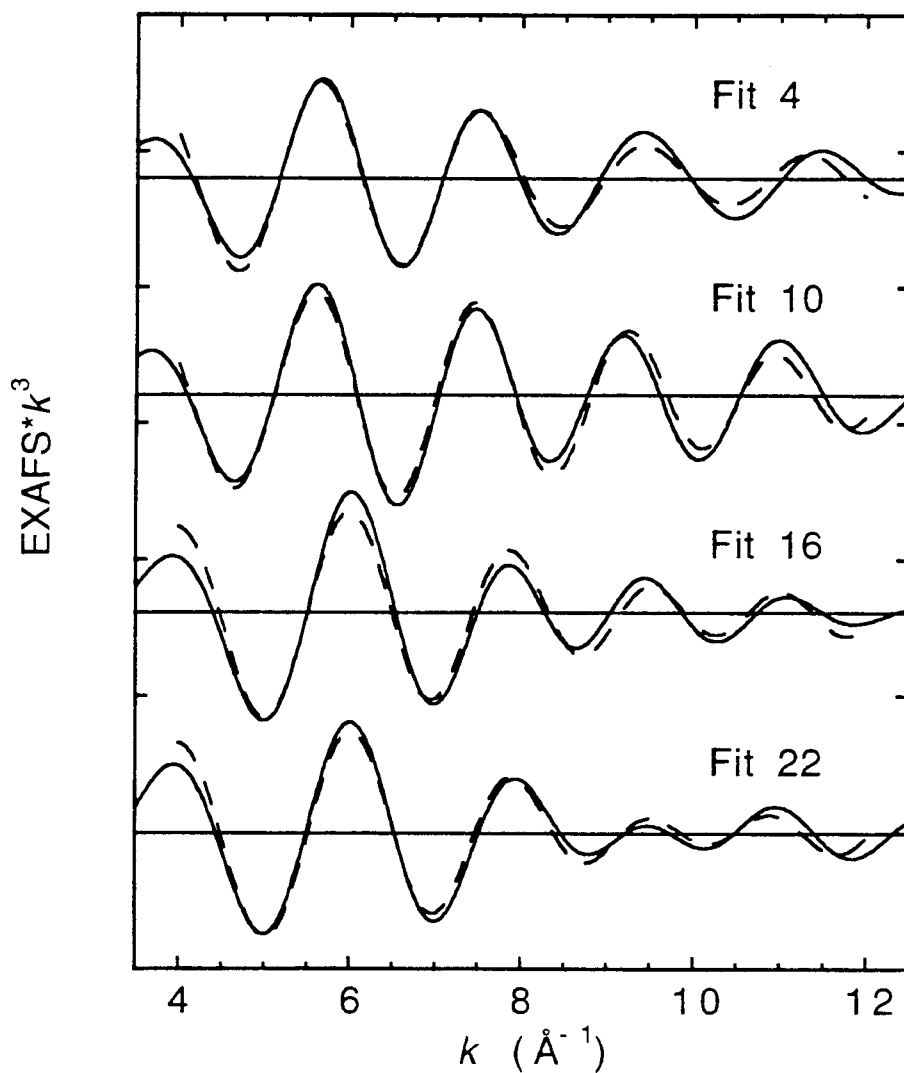


Figure 5.18. Fits to the Fourier filtered data of Fe(II)PAH^T (Fit 4), Fe(II)PAH^R (Fit 10), Fe(III)PAH^T (Fit 16), and Fe(III)PAH^R (Fit 22), where the solid line represents the backtransformed data while the dashed line is the fit to the data. (The ordinate scale is 5 between tick marks with solid horizontal lines indicating the zero point of each plot).

Fe(II)PAH^R looked very similar and similar to that of six-coordinated model complexes. This suggests that the coordination number of 4.5 extracted from the fit to the Fe(II)PAH^R EXAFS data is low due to correlation of the two EXAFS waves. In addition, the average distance to all the ligands in the first coordination sphere is 2.18 Å for Fe(II)PAH^T and 2.17 Å for Fe(II)PAH^R. These distances are typical of six-coordinate ferrous iron as crystallographic information on ferrous model complexes with oxygen and nitrogen ligation reports average bond lengths of 2.17±0.03 Å for six-coordinate sites,^{43-46,55-57} 2.11±0.02 Å for five-coordinate sites,^{58,59} and 2.00±0.01 Å for four-coordinate sites.²⁴ The fits to the Fe(III)PAH^T and Fe(III)PAH^R EXAFS data are extremely similar with Fits 16 and 22 having nearly identical Fe-O and Fe-N distances and similar coordination numbers. The average ligand distance is 2.07 Å in both of these fits, typical of six-coordinate ferric iron. Crystallographic information on ferric model complexes with O and N ligation reports average bond lengths of 2.03±0.03 Å for six-coordinate sites,^{32,33,47-54} 1.97 Å for a five-coordinate site,⁶⁰ and 1.86±0.01 Å for four-coordinate sites.⁶¹

5.6.4. Discussion

In summary, the Fe K-edge and pre-edge features of Fe(II)PAH^T and Fe(II)PAH^R look very similar to each other and to that of ferrous six-coordinate model complexes. The fits to the EXAFS data of these two forms of PAH give ligand distances typical of ferrous six-coordinate model complexes with oxygen and nitrogen ligation. However, there are subtle differences in the fits to the EXAFS to these two proteins suggesting a slight change in ligand environment between Fe(II)PAH^T and Fe(II)PAH^R with both iron sites looking six-coordinate. The edge and pre-edge features of Fe(III)PAH^T and Fe(III)PAH^R look nearly identical and also very similar to six-coordinate ferric model with oxygen and nitrogen ligation. The average ligand distance of 2.07 Å, obtained from the fits to the EXAFS data of Fe(III)PAH^T and Fe(III)PAH^R, is typical of six-coordinate ferric iron.

There are subtle differences in the EXAFS fits to the data of Fe(II)PAH^T and Fe(II)PAH^R with there being an increase in the contribution of the ligands at shorter distance with respect to the contribution of the ligands at the longer distance in the Fe(II)PAH^R data. Magnetic circular dichroism (MCD) data of Fe(II)PAH^T and Fe(II)PAH^R also show that the iron site in both of these forms of PAH is six-coordinate with the data of Fe(II)PAH^R having features slightly higher in energy indicative of a larger 10Dq value.⁶² This increase in ligand field strength is consistent with an increase in the contribution of the ligands at shorter distance seen in the fits to the EXAFS data. The

differences seen in the EXAFS and MCD data of Fe(II)PAH^T and Fe(II)PAH^R can either be attributed to changes caused by phenylalanine in the active site or by the activation process (*i.e.* phenylalanine in the allosteric site). Previous EPR studies on ferric forms of PAH have shown that data for Fe(III)PAH^T, Fe(III)PAH^R activated with lysolecithin (*i.e.* activated but with no phenylalanine in the active site), and Fe(III)PAH^R activated with *N*-ethylmaleimide (*i.e.* activated but with no phenylalanine in the active site) are similar. Data for Fe(III)PAH^R and Fe(III)PAH^T with tryptophan in the active site are similar to each other, but different than those of the previous three samples discussed.¹⁴ This indicates that phenylalanine in the active site causes the differences seen in the EPR data of the ferric forms of the enzyme. It is unclear as to whether the changes observed in the EXAFS and MCD data of Fe(II)PAH^T and Fe(II)PAH^R are caused by the same effect. Thus, further XAS and MCD studies need to be done on Fe(II)PAH^R activated with lysolecithin, α -chymotrypsin, or *N*-ethylmaleimide (*i.e.* activated but with no phenylalanine in the active site) and Fe(II)PAH^T with tryptophan in the active site to sort out the effects of phenylalanine in the active site *vs.* the allosteric site. In addition, an EXAFS study of Fe(II)PAH^R with iodinated phenylalanine could be used to help define the proximity of phenylalanine to the iron active site. Further XAS studies additionally can be used to determine the effects of the ferrous site in both activated and non-activated forms with pterin and non-reactive small molecule analogs of O₂. An understanding of the changes that occur to the iron active site upon activation and addition of pterin cofactor will aid in elucidating the mechanism of catalysis.

5.6.5. Acknowledgments

The PAH samples were provided by Joe Kappock in Prof. John Caradonna's laboratory at Yale University. Kelly Loeb measured liquid He EPR data for the four PAH samples before and after the samples were exposed to the X-ray beam. This research was supported by grants from the NIH (GM40392, E. I. Solomon) and NSF (CHE-9423181, K. O. Hodgson). The Stanford Synchrotron Radiation Laboratory is supported by the Department of Energy, Office of Basic Energy Sciences, Divisions of Chemical Science and Materials Science, and in part by the National Institutes of Health, National Center of Research Resources, Biomedical Research Technology Program (RR-01209, K. O. Hodgson) and the DOE's Office of Health and Environmental Research.

5.6.6. References and Notes

- (1) Goodman, B. L. In *Aromatic Amino Acid Hydroxylases and Mental Disease*; Youdim, M. B. H., Ed.; Wiley-Interscience: New York, 1979; p 5.
- (2) Shiman, R. In *Folates and Pterins*; Blakely, R. L.; Benkovic, S. J., Eds.; Wiley-Interscience: New York, 1985; Vol. 2; p 179.
- (3) Weiner, N. In *Aromatic Amino Acid Hydroxylases and Mental Disease*; Youdim, M. B. H., Ed.; Wiley-Interscience: New York, 1979; p 141.
- (4) Kaufman, S.; Kaufman, E. E. In *Folates and Pterins*; Blakely, R. L.; Benkovic, S. J., Eds.; Wiley-Interscience: New York, 1985; Vol. 2; p 251.
- (5) Hamon, M.; Bourgoin, S.; Youdim, M. B. H. In *Aromatic Amino Acid Hydroxylases and Mental Disease*; Youdim, M. B. H., Ed.; Wiley-Interscience: New York, 1979; p 233.
- (6) Kuhn, D. M.; Lovenberg, W. In *Folates and Pterins*; Blakely, R. L.; Benkovic, S. J., Eds.; Wiley-Interscience: New York, 1985; Vol. 2; p 353.
- (7) Dix, T. A.; Kuhn, D.; Benkovic, S. J. *Biochemistry* **1987**, *26*, 3354.
- (8) Gottschall, D. W.; Dietrich, R. F.; Benkovic, S. J.; Shiman, R. *Biochemistry* **1982**, *21*, 845.
- (9) Kuhn, D. M.; Ruskin, B.; Lovenberg, W. *J. Biol. Chem.* **1980**, *255*, 4137.
- (10) Wallick, D. E.; Bloom, L. M.; Gaffney, B. J.; Benkovic, S. J. *Biochemistry* **1984**, *23*, 1295.
- (11) Andersson, K. K.; Cox, D. D.; Que, L., Jr.; Petersson, L.; Flatmark, T.; Haavik, J. *J. Biol. Chem.* **1988**, *263*, 18621.
- (12) Dix, T. A.; Benkovic, S. J. *Acc. Chem. Res.* **1988**, *21*, 101.
- (13) Kaufman, S. In *Advances in Neurochemistry*; Agranoff, B. W.; Aprison, M. H., Eds.; Plenum Press: New York, 1976; Vol. 2; p 1.
- (14) Caradonna, J. P. private communication.
- (15) Tourian, A. *Biochim. Biophys. Acta* **1971**, *242*, 345.
- (16) Dix, T. A.; Benkovic, S. J. *Biochemistry* **1985**, *24*, 5839.
- (17) Dix, T. A.; Bollag, G. E.; Domanico, P. L.; Benkovic, S. J. *Biochemistry* **1985**, *24*, 2955.
- (18) Carr, R. T.; Benkovic, S. J. *Biochemistry* **1993**, *32*, 14132.
- (19) Feig, A. L.; Lippard, S. J. *Chem. Rev.* **1994**, *94*, 759.
- (20) Scott, R. A.; Hahn, J. E.; Doniach, S.; Freeman, H. C.; Hodgson, K. O. *J. Am. Chem. Soc.* **1982**, *104*, 5364.

- (21) Cramer, S. P.; Tench, O.; Yochum, M.; George, G. N. *Nucl. Instrum. Methods Phys. Rev.* **1988**, A266, 586.
- (22) George, G. N.; Pickering, I. to be published.
- (23) Abbreviations used: HB(3,5-*i*Pr₂pz)₃ = hydrotris(3,5-diisopropyl-1-pyrazolyl)borate; TMC = tetramethylcyclam; salen = N,N'-ethylenebis(salicylideneiminato); acac = acetylacetonate.
- (24) Kitajima, N. private communication.
- (25) Hodges, K. D.; Wollman, R. G.; Barfield, E. K.; Hendrickson, D. N. *Inorg. Chem.* **1977**, 16, 2746.
- (26) Burbridge, C. D.; Goodgame, D. M. L. *Inorg. Chim. Acta* **1970**, 4, 231.
- (27) Gerloch, M.; Mabbs, F. E. *J. Chem. Soc. (A)* **1967**, 1598.
- (28) Kistenmacher, T. J.; Stucky, G. D. *Inorg. Chem.* **1968**, 7, 2150.
- (29) Cramer, S. P.; Hodgson, K. O.; Stiefel, E. I.; Newton, W. E. *J. Am. Chem. Soc.* **1978**, 100, 2748.
- (30) Cramer, S. P.; Hodgson, K. O. *Prog. Inorg. Chem.* **1979**, 15, 1.
- (31) Scott, R. A. *Methods Enzymol.* **1985**, 117, 414.
- (32) Iball, J.; Morgan, C. H. *Acta Crystallogr.* **1967**, 23, 239.
- (33) Roof, R. B. J. *Acta Crystallogr.* **1956**, 9, 781.
- (34) Johansson, L. *Chem. Scr.* **1976**, 9, 30.
- (35) Johansson, L.; Molund, M.; Oskarsson, Å. *Inorg. Chim. Acta.* **1978**, 31, 117.
- (36) Agarwall, B. K. X-ray Spectroscopy; Springer-Verlag: New York, 1979; p 276.
- (37) Lytle, F. W.; Greigor, R. B.; Sandstrom, D. R.; Marques, E. C.; Wong, J.; Spiro, C. L.; Huffman, G. P.; Huggins, F. E. *Nucl. Instrum. Methods* **1984**, 226, 542.
- (38) Lytle, F. W. In *Applications of Synchrotron Radiation*; Winick, H.; Xiam, D.; Ye, M. -h.; Huang, T., Eds.; Gordon and Breach Science Publishers: New York, 1989; p 135.
- (39) Tyson, T. A.; Roe, A. L.; Frank, P.; Hodgson, K. O.; Hedman, B. *Phys. Rev. B* **1989**, 39, 6305.
- (40) Roe, A. L.; Schneider, D. J.; Mayer, R. L.; Pyrz, J. W.; Widom, J.; Que, L., Jr. *J. Am. Chem. Soc.* **1984**, 106, 1676.
- (41) Randall, C. R.; Shu, L.; Chiou, Y.-M.; Hagen, K. S.; Ito, M.; Kitajima, N.; Lachicotte, R. J.; Zang, Y.; Que, L., Jr. *Inorg. Chem.* **1995**, 34, 1036.
- (42) Butcher, R. J.; Addison, A. W. *Inorg. Chim. Acta* **1989**, 158, 211.
- (43) Hamilton, W. C. *Acta Crystallogr.* **1962**, 15, 353.

- (44) Montgomery, H.; Chastain, R. V.; Natt, J. J.; Witkowska, A. M.; Lingafelter, E. C. *Acta Crystallogr.* **1967**, *22*, 775.
- (45) Cingi, M. B.; Lanfredi, A. M. M.; Tiripicchio, A.; Cornelissen, J. P.; Haasnoot, J. G.; Reedijk, J. *Acta Crystallogr.* **1986**, *C42*, 1296.
- (46) Kitajima, N.; Fukui, H.; Moro-oka, Y.; Mizutani, Y.; Kitagawa, T. *J. Am. Chem. Soc.* **1990**, 6402.
- (47) Ainscough, E. W.; Brodie, A. M.; Plowman, J. E.; Brown, K. L.; Addison, A. W.; Gainsford, A. R. *Inorg. Chem.* **1980**, *19*, 3655.
- (48) Cox, D. D.; Que, L., Jr. *J. Am. Chem. Soc.* **1988**, *110*, 8085.
- (49) Lauffer, R. B.; Heistand, R. H., II; Que, L., Jr. *Inorg. Chem.* **1983**, *22*, 50.
- (50) Malfant, I.; Morgenstern-Badarau, I.; Philoche-Levisalles, M.; Lloret, F. *J. Chem. Soc., Chem. Commun.* **1990**, 1338.
- (51) McDevitt, M. R.; Addison, A. W.; Sinn, E.; Thompson, L. K. *Inorg. Chem.* **1990**, *29*, 3425.
- (52) Okamoto, K.-I.; Kanamori, K.; Hidaka, J. *Acta Crystallogr.* **1990**, *C46*, 1640.
- (53) Raymond, K. N.; Isied, S. S.; Brown, L. D.; Fronczek, F. R.; Nibert, J. H. *J. Am. Chem. Soc.* **1976**, *98*, 1767.
- (54) Clarke, E. T.; Martell, A. E.; Reibenspies, J. *Inorg. Chim. Acta* **1992**, *196*, 177.
- (55) Miller, L. L.; Jacobson, R. A.; Chen, Y.-S.; Kurtz, D. M., Jr. *Acta Crystallogr.* **1989**, *C45*, 527.
- (56) Chiou, Y.-M.; Que, L., Jr. *J. Am. Chem. Soc.* **1992**, *114*, 7567.
- (57) Zang, Y.; Elgren, T. E.; Dong, Y.; Que, L., Jr. *J. Am. Chem. Soc.* **1993**, *115*, 811.
- (58) Kitajima, N.; Tamura, N.; Amagai, H.; Fukui, H.; Moro-oka, Y.; Mizutani, Y.; Kitagawa, T.; Mathur, R.; Heerwegh, K.; Reed, C. A.; Randall, C. R.; Que, L., Jr.; Tatsumi, K. *J. Am. Chem. Soc.* **1994**, *116*, 9071.
- (59) Hagen, K. private communication.
- (60) Heistand, R. H., II; Roe, A. L.; Que, L., Jr. *Inorg. Chem.* **1982**, *21*, 676.
- (61) Koch, S. A.; Millar, M. *J. Am. Chem. Soc.* **1982**, *104*, 5255.
- (62) Loeb, K.; Solomon, E. I. private communication.

5.7. Protocatechuate 3,4-Dioxygenase

5.7.1. Introduction

The catechol dioxygenases serve as part of nature's strategy for degrading aromatic molecules in the environment.¹ A critical point of this degradation is the opening of the chemically stable aromatic ring. In typical aerobic pathways, the ring is first activated by hydroxylation on adjacent carbons to form a catecholate-like complex. Ring cleavage, catalyzed by dioxygenase, then proceeds between the hydroxylated carbon atoms (intradiol- or *ortho*-cleavage) or adjacent to one of these carbon atoms (extradiol- or *meta*-cleavage).² The intradiol cleaving enzymes utilize a ferric active site and act on catechol and protocatechuate resulting in muconic acids, while the extradiol cleaving enzymes utilize a ferrous active site and act on a larger number of substrates producing muconic semialdehydes (Table 5.1).^{3,4}

The most well-characterized intradiol dioxygenase is protocatechuate 3,4-dioxygenase (PCD). Crystal structures of PCD from *Pseudomonas aeruginosa*^{5,6} and *Brevibacterium fuscum*⁷ both have trigonal bipyramidal iron sites with a tyrosine (Tyr) and histidine (His) coordinated axially and a Tyr, His, and water-based molecule bound in the equatorial plane. The iron coordination environment defined by the crystal structure corresponds remarkably well to the active site proposed on the basis of spectroscopic studies.⁸ The enzyme exhibits a distinct burgundy red color ($\lambda_{\max} \sim 460$ nm) that is associated with a tyrosinate \rightarrow Fe(III) charge transfer (CT) transition with the presence of two distinct tyrosine ligands indicated by the appearance of two ν_{CO} bands in the resonance Raman (rR) spectrum.^{9,10} Histidine ligation was also suggested by rR studies with the observation of a low-energy $\nu_{\text{Fe-N(Im)}}$ feature at 276.5 cm^{-1} and by the presence of second and third shell features in the Fourier transform (FT) of the extended X-ray absorption fine structure (EXAFS) data ascribable to the imidazole ring.¹¹ A bound water ligand was indicated by the line broadening found in the electron paramagnetic resonance (EPR) spectrum of the native enzyme from *Brevibacterium fuscum* when dissolved in H_2^{17}O .¹² A subsequent EXAFS study suggested that the bound water-based molecule is a hydroxide based on the Fe-O distance.¹³

The extradiol dioxygenases are less understood in comparison to their intradiol counterparts, since the active iron site is in the ferrous oxidation state and thus more difficult to study spectroscopically. However, a recent crystal structure of extradiol dioxygenase 2,3 dihydroxybiphenyl 1,2-dioxygenase (1,2-DBD) showed a square-pyramidal iron site with ligands from two histidine and one glutamate residues and two

water molecules.¹⁴ A square pyramidal geometry was predicted by magnetic circular dichroism (MCD) spectroscopy on an analogous enzyme, catechol 2,3-dioxygenase (2,3-CTD).¹⁵

Knowing the structure of the iron active site of the native enzymes is only the first step in the broader objective of understanding the iron's role in the enzyme mechanism. It is clear that the native intradiol dioxygenases have a high spin ferric active site¹⁶ and that the enzyme mechanism involves initial substrate binding followed by O₂ attack.¹⁷ An attractive mechanism postulated early on suggested reduction of the ferric site by substrate, followed by dioxygen binding to the ferrous center. However, Mössbauer and EPR studies have shown that the iron retains its ferric oxidation state even after the substrate is bound.^{18,19} Stopped-flow kinetic studies have revealed the involvement of three intermediates subsequent to O₂ attack on the enzyme-substrate complex, all of which retain their visible chromophores, indicating that the metal center remains high spin ferric.^{20,21} These results led to the postulation of a substrate activation mechanism in which the coordination of catechol to the ferric center activates the catechol for direct attack by the O₂. The mechanism of the extradiol dioxygenases is less understood. The active form of the extradiol dioxygenases have a high spin ferrous site, as has been ascertained from Mössbauer spectroscopy.^{22,23} It is also known from MCD studies on 2,3-CTD that substrate binding activates the ferrous site for small molecule binding.¹⁵

The changes that occur to the iron active site due to substrate binding and O₂ activation in catechol dioxygenases can be further probed using NO as an O₂ analog. Intradiol dioxygenases do not bind NO in their native ferric state, however, the ferrous form of the enzyme binds NO to form an S=3/2 {FeNO}⁷ species.²⁴ A different S=3/2 complex is formed when NO binds to a preformed enzyme-substrate complex.²⁴ Additionally, substrate does not bind to the enzyme-NO complex indicating that initial NO binding blocks the single site for exogenous ligand binding to the iron, thereby inhibiting substrate association. In contrast, substrate binding before NO appears to evoke an enzyme conformational change that allows simultaneous NO binding in another site.²⁴ On the other hand, native extradiol dioxygenases bind NO to form a {FeNO}⁷ S=3/2 species, as does the enzyme-substrate form. Particularly interesting is the fact that the NO binding constant increases by two orders of magnitude upon substrate binding.^{25,26} From EPR studies on the NO forms of protocatechuate 4,5-dioxygenase and gentisate 1,2-dioxygenase, it has been shown that substrate binds in a bidentate manner in the NO complex and thus there are three available sites on the iron for exogenous ligand binding, two for substrate and one for NO (and presumably O₂).^{25,26}

This fact is supported by the MCD studies on 2,3-CTD¹⁵ and the crystal structure of 1,2-DBD.¹⁴

Since X-ray absorption spectroscopy (XAS) is not dependent on the oxidation or spin state of the iron, comparable data can be obtained on the different forms of the intra- and extradiol dioxygenases to obtain more detailed information on the electronic and geometric structures of the iron active site. The ferrous and ferric forms of these enzymes can be studied, as well as the enzyme-NO, enzyme-substrate, and enzyme-substrate-NO forms. The changes observed in the edge and EXAFS region of the XAS spectra can be used to obtain a detailed description of the iron active site in stages of the mechanism for which forms can be isolated or stabilized. In this study, both Fe K edge and EXAFS data were collected on Fe(III)PCD, Fe(II)PCD, Fe(III)PCD + 3,4 dihydroxybenzoic acid (Fe(III)PCA), and FePCD-NO. The intensities and energy splitting of the 1s→3d pre-edge features and the energy and shape of the rising edge indicate that Fe(II)PCD has a six-coordinate iron site, while Fe(III)PCD, Fe(III)PCA, and FePCD-NO have five-coordinate active sites. The edge shape and intensity of FePCD-NO indicates that the iron is in the ferric oxidation state. An EXAFS analysis provided iron-ligand distances for each of the four forms of the protein. Additionally, the GNXAS approach was used to fit the experimental EXAFS data of Fe(III)PCD and FePCD-NO in order to investigate the Fe-N-O angle in FePCD-NO.

5.7.2. Experimental Section

5.7.2.1. Sample Preparation. PCD was isolated from *Brevibacterium fuscum* as previously described.^{12,19,27} All XAS samples had a concentration of ~3 mM in Fe in 50 mM 3-(*N*-morpholino)propanesulfonic acid (MOPS) buffer at pH 7.0 and contained 50% glycerol by volume. As isolated, the protein is in the ferric oxidation state and thus the Fe(III)PCD sample was obtained by concentrating isolated PCD in 50 mM MOPS to ~6 mM in Fe and then adding 50% glycerol by volume. The sample was then syringed into a Lucite XAS cell (23 x 1 x 3 mm) with 37 μm Kapton windows and frozen in liquid nitrogen. The Fe(III)PCD XAS sample was characterized using liquid He EPR and showed the typical high spin ferric signal at 4.3.¹⁹ Fe(II)PCD was obtained by reducing degassed Fe(III)PCD (~6 mM in Fe in 50 mM MOPS) with 5 μl of ~1 M degassed dithionite solution (~15-fold reducing equivalents of Fe) anaerobically. The protein sample turned from burgundy to clear indicating a complete reduction of the iron site. Degassed glycerol was then added to the sample under anaerobic conditions. The Fe(II)PCD sample was loaded into the XAS cell in a nitrogen-filled glove box and

immediately frozen in liquid nitrogen. FePCD-NO was prepared by bubbling NO gas over the headspace of Fe(II)PCD (~3 mM in Fe in 50 mM MOPS with 50% glycerol by volume) while tipping/mixing for ~20 min. under anaerobic conditions until the color of the sample changed to a yellowish green and stopped changing color. The FePCD-NO sample was then loaded into an XAS cell in a nitrogen-filled glove box and immediately frozen in liquid nitrogen. The quality of the FePCD-NO XAS sample was characterized by the $S=3/2$ He EPR signal. EPR spectra taken before and after the sample was exposed to the X-ray beam showed the characteristic $\{\text{FeNO}\}^7 S=3/2$ EPR signal,²⁴ thus showing that NO was bound. In addition, there is a significant change in the edge feature between Fe(II)PCD and FePCD-NO (*vide infra*), indicative of the NO being bound to the iron. The edge shape and position of FePCD-NO was closely monitored during data collection to ensure that the NO was not photo-dissociating with there being no change in the edge feature for the duration of the experiment. Fe(III)PCA was prepared by anaerobically mixing Fe(III)PCD (~6 mM in Fe in 50 mM MOPS) with 3,4-dihydroxybenzoic acid (30 mM in MOPS) and glycerol (all three solutions were thoroughly degassed prior to mixing). The sample was then loaded into an XAS cell in a nitrogen-filled glove box and immediately frozen in liquid nitrogen. The liquid He EPR signal of Fe(III)PCA was identical to that previously reported.¹⁹

5.7.2.2. Data Collection and Reduction. X-ray absorption spectra were recorded at the Stanford Synchrotron Radiation Laboratory (SSRL) on unfocused beamline 7-3 during dedicated conditions (3 GeV, 50-100 mA). The radiation was energy resolved using a Si(220) double-crystal monochromator with 1 mm vertical pre-monochromator beam defining slits. An Oxford Instruments continuous-flow liquid helium CF1208 cryostat was used to maintain a constant temperature of 10 K. Energies were calibrated using an internal Fe foil standard, assigning the first inflection point to 7111.2 eV.²⁸ The spectrometer energy resolution was approximately 1.4 eV²⁹ with reproducibility in edge position determination of < 0.2 eV. Data were measured to $k = 15 \text{ \AA}^{-1}$, detuning the monochromator 50% at 7998 eV to minimize harmonic contamination. The fluorescence signal was monitored using a 13-element Ge solid-state array detector³⁰ windowed on the Fe $K\alpha$ signal. During the experiment, count rates of approximately $30,000 \text{ s}^{-1}$ total per element were not exceeded. Thirty-five scans were collected on the Fe(II)PCD sample. Thirty-two scans were collected on the Fe(III)PCD and Fe(III)PCA samples. Both the Fe(III)PCD and Fe(III)PCA samples photo-reduced in the beam, as was evident by changes in the edge shape and position. Therefore, these samples were exposed to the beam in eight different spots (four spots on two separate cells) producing eight 'first' scans and a total of thirty-two scans. There was less than a

0.5 eV energy shift between the 'first' and 'fourth' scans. There was no discernible change in the EXAFS data from comparison of the average of the 'first' scan data to the average of the 'fourth' scan data. Therefore, the spectra of Fe(III)PCD and Fe(III)PCA presented in this section are an average all thirty-two scans. Two data sets were collected on FePCD-NO (on separate protein samples). The first data set contained a thirty-four scan average and the second data set contained a thirty scan average. The data presented in this section is an average of the two data sets (*i.e.* a sixty-four scan average), since both the edge and EXAFS features of the two data sets were identical within the noise level. A pre-edge subtraction was performed by fitting the tail of a Gaussian to the pre-edge region and subtracting this polynomial from the averaged spectra.³¹ A three-segment spline approximately even in k -space was fit to the EXAFS region and the data normalized to an edge jump of one at 7130 eV. The spline was chosen so that it minimized residual low-frequency background but did not reduce the EXAFS amplitude as checked by monitoring the FT of the EXAFS during the background subtraction process.

Fe K-edge spectra were also collected on four-, five-, and six-coordinate ferrous and ferric model complexes. Fe(acac)₃ was purchased from Aldrich.³² Fe(HB(3,5-*i*Pr₂pz)₃)Cl³³ was obtained as a gift from N. Kitajima. (BF₄)[Fe(TMC)Cl],³⁴ [Fe(imidazole)₆]Cl₂,³⁵ Fe(salen)Cl,³⁶ (AsPh₄)[Fe(N₃)₅],³⁷ and (Et₄N)[FeCl₄]³⁸ were prepared as previously described. The model complex XAS samples were prepared in the following manner. The crystalline samples were each mixed with BN and ground into a fine powder. The BN/sample mixture was pressed into a 1 mm thick Al spacer that was sealed with 63.5 μ m Mylar tape windows and frozen in liquid nitrogen. [Fe(imidazole)₆]Cl₂, Fe(HB(3,5-*i*Pr₂pz)₃)Cl, and (BF₄)[Fe(TMC)Cl] are air-sensitive and thus the preparation was carried out in a nitrogen-filled glove box for these three samples. Data were measured in transmission mode with N₂-filled ionization chambers to $k = 9.5 \text{ \AA}^{-1}$ detuning the monochromator 50% at 7474 eV to minimize harmonic contamination. Two to three scans were averaged for each sample. A smooth pre-edge background was removed from the averaged spectra by fitting a first order polynomial to the pre-edge region and subtracting this polynomial from the entire spectrum. A two segment spline of order two was fit to the EXAFS region and the data normalized to an edge jump of one at 7130 eV. The intensities and energies of the pre-edge features were determined as described below.

5.7.2.3. Empirical EXAFS Analysis. EXAFS data analysis was performed on the normalized protein spectra according to established methods.³⁹⁻⁴¹ The normalized data were converted to k -space. The photoelectron wave vector, k , is defined by

$[2m_e(E-E_0)/\hbar^2]^{1/2}$ where m_e is the electron mass, E is the photon energy, \hbar is Planck's constant divided by 2π , and E_0 is the threshold energy of the absorption edge, which was defined to be 7130 eV for the Fe K absorption edge. The empirical EXAFS data analyses were performed with nonlinear least-square curve-fitting techniques^{28,39-41} using empirical phase and amplitude parameters. The following models were used to obtain the empirical Fe-X backscattering parameters of interest: Fe-O from $[\text{Fe}(\text{acac})_3]$ ^{42,43} and Fe-N from $[\text{Fe}(1,10\text{-phenanthroline})_3](\text{ClO}_4)_3$.^{44,45} Fourier transforms (from k to R space) were performed for the data range 3.5 - 14.5 \AA^{-1} with a Gaussian window of 0.1 \AA^{-1} . The window widths used in the backtransforms (from R to k space) for the proteins are given in the results section. The window widths were kept as similar as possible to those used to extract amplitude and phase parameters from the model compounds to minimize artifacts introduced by the Fourier filtering technique. All curve-fitting was based on k^3 -weighted data and applied to the individual filtered shell of interest. Only the structure-dependent parameters, the distance and coordination number, were varied unless stated otherwise. A "goodness of fit" parameter, F , was calculated as $F = \{[k^6(\text{data} - \text{fit})^2]/(\text{no. of points})\}^{1/2}$ for each fit.

5.7.2.4. GNXAS Data Analysis. As described in detail in Chapter 2 and elsewhere,⁴⁶⁻⁴⁸ the GNXAS programs generate model EXAFS signals for each shell around the photoabsorber based on an initial structural model. Both single-scattering and multiple-scattering contributions are summed to generate a theoretical spectrum for the model which is then fit to the non-Fourier-filtered experimental data.⁴⁶⁻⁴⁸

The crystallographic coordinates were used as input for Fe(III)PCD.⁶ Phase shifts were calculated using the standard muffin-tin approximation with all the atoms associated with each compound and up to an energy limit of 70 Ry (950 eV) above the Fe K edge. The Mattheiss prescription⁴⁹ of overlapping, self-consistent atomic charge densities of the atoms of the cluster was used to construct the Coulomb portion of the effective one-electron potential. Proper account of the charge relaxation around the core hole was taken. The Hedin-Lundqvist plasmon-pole approximation was used to model its exchange and correlation part.⁵⁰ The imaginary part of the latter takes into account inelastic scattering processes of the photoelectron propagating out of the system and models *a priori* its mean-free path. The muffin-tin radii were chosen by scaling Norman radii of the cluster atoms by a factor of about 0.8 as to match the nearest neighbor distance.

The theoretical EXAFS spectrum was calculated to include contributions from two-atom and three-atom configurations. Within each n -atom configuration, all the MS contributions were taken into account.⁴⁶⁻⁴⁸ The two-atom and three-atom configurations

were identified in each cluster up to 4.5 Å and averaged with a frequency tolerance of 0.1 Å. The resultant information was used to calculate the various EXAFS $\gamma^{(2)}$ and $\gamma^{(3)}$ signals associated with each two-atom and three-atom contribution using the crystallographic bond lengths and distances.

The GNXAS fitting program constructs the theoretical absorption spectrum by summing all the $\gamma^{(2)}$ and $\gamma^{(3)}$ signals and compares this theoretical spectrum with the experimental absorption spectrum with the residual function R being a measure of the quality of the fit.⁴⁸ Least-squares fits are performed on the averaged, energy-calibrated, raw absorption data without prior background subtraction or Fourier filtering. Raw data are compared directly with a model absorption coefficient composed of an appropriate background plus the oscillatory structural contribution from the theoretically calculated EXAFS.⁴⁸ A spline of orders 4,4,4 with defining energy points of 7147, 7269, 7577, and 7998 eV was used for Fe(III)PCD. The first spline point used for FePCD-NO was 7149 eV to reduce low-frequency noise in the FT. Least-squares fits were done with k^3 -weighting where the first and the last spline points determined the range of the fit.

The structural parameters varied in the refinements were the distance (R) and the bond variance (σ_R^2), the mean square variation in the bond distance, for each two-atom configuration and the distances, the angle and the covariance matrix elements⁴⁶⁻⁴⁸ for the three-atom configurations. Distances and angles were allowed to vary within a preset range, typically ± 0.05 Å and $\pm 5^\circ$. Bond and angle variances were also allowed to vary in restricted ranges: ± 0.005 Å² and ± 50 (degrees)², respectively. The off-diagonal covariance matrix elements were kept fixed at zero. The coordination numbers were kept fixed. The nonstructural parameters in the fits were E_0 (a parameter that aligns the experimental energy scale to the theoretical energy scale), S_0^2 (many-body amplitude reduction factor), Γ_c (core-hole lifetime), and E_r (experimental resolution). These parameters were refined within narrow limits around expected values.^{51,52}

5.7.2.5. 1s—>3d Pre-Edge Analysis. The intensities and energies of pre-edge features of the model complex and protein data were quantitated by fits to the data. The fitting program EDG_FIT, which utilizes the double precision version of the public domain MINPAK fitting library was used. EDG_FIT was written by Dr. Graham N. George of the Stanford Synchrotron Radiation Laboratory. All spectra were fit over the range 7108-7118 eV. Pre-edge features were modeled by pseudo-Voigt line shapes (simple sums of Lorentzian and Gaussian functions).^{29,53-55} A fixed 50:50 ratio of Lorentzian to Gaussian contribution for the pre-edge feature successfully reproduced these spectral features. Functions modeling the background underneath the pre-edge features were chosen empirically to give the best fit. The second derivative of the data

was compared to the second derivative of the fit. In all cases, a number of fits were obtained which reproduced the data and the second derivative. The value reported for the area of a fitted feature (where peak area was approximated by the height x full-width-at-half-maximum (FWHM)) is the average of all the pseudo-Voigts which successfully fit the feature. For each sample, the standard deviation of the average of the areas was calculated to quantitate the error.

5.7.3. Results and Analysis

5.7.3.1. Fe K-Edge XAS. Fe K-edge XAS data for Fe(II)PCD, Fe(III)PCD, Fe(III)PCA, and FePCD-NO were measured to obtain information on the electronic and geometric structure of the iron sites of these forms of the protein. The protein data were compared to data of four-, five-, and six-coordinate ferrous and ferric model complexes to obtain information on the coordination number and the geometry of the non-heme iron site. Information on the oxidation state and the site symmetry of the iron in FePCD-NO was also obtained from the edge spectra. The XAS edge spectra for Fe(II)PCD, Fe(III)PCD, Fe(III)PCA, and FePCD-NO are shown in Figure 5.19. Figure 5.20 displays spectra of representative four-, five-, and six-coordinate ferrous model complexes, Fe(HB(3,5-*i*Pr₂pz)₃)Cl,³³ (BF₄)[Fe(TMC)Cl],³⁴ and [Fe(imidazole)₆]Cl₂,³⁵ in part A and ferric model complexes, (Et₄N)[FeCl₄],³⁸ Fe(salen)Cl,³⁶ (AsPh₄)[Fe(N₃)₅],³⁷ and Fe(acac)₃,^{42,43} in part B. The lowest energy peaks arise from the weak 1s→3d transition which is at ~7112 eV followed by the 1s→4p transition at ~7125 eV. An expanded view of the 1s→3d pre-edge region is shown for the proteins as well as for the model complexes as insets in Figures 5.19 and 5.20, respectively. The energies and areas of the pre-edge features were determined by fits to the data and are presented in Table 5.9.

Fe(II)PCD has a broad, low-intensity pre-edge feature which can be fit with two peaks. Fe(III)PCD has an intense pre-edge feature centered at ~7113.4 eV, while Fe(III)PCA has a broader feature centered ~0.1 eV lower in energy. FePCD-NO has a relatively intense, broad pre-edge feature that can be fit with two pre-edge peaks. The three ferrous model complexes, Fe(HB(3,5-*i*Pr₂pz)₃)Cl, (BF₄)[Fe(TMC)Cl], and [Fe(imidazole)₆]Cl₂, all have what appear to be two pre-edge features split by ~2 eV with varying intensities (Figure 5.20A). The four-coordinate complex has the most intense pre-edge feature with a total area of 19.8, while the six-coordinate complex has the least intense pre-edge feature with a total pre-edge area of 3.8. The ferric four-coordinate complex, (Et₄N)[FeCl₄], has a single intense pre-edge feature with a total fitted pre-edge

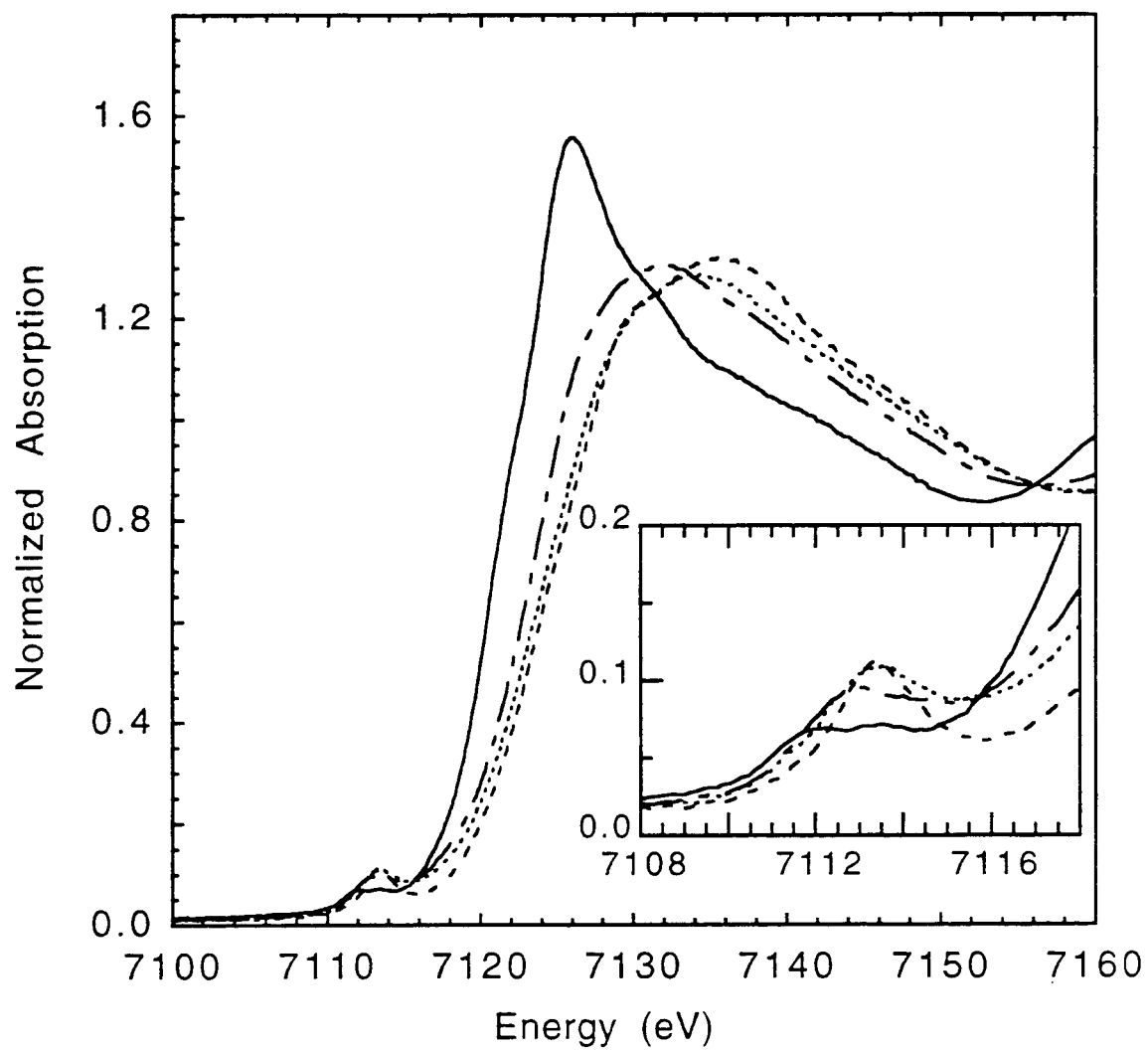


Figure 5.19. Fe K-edge XAS spectra of Fe(II)PCD (—), Fe(III)PCD (---), Fe(III)PCA (···), and FePCD-NO (— ·). The inset is an expansion of the 1s → 3d pre-edge region.

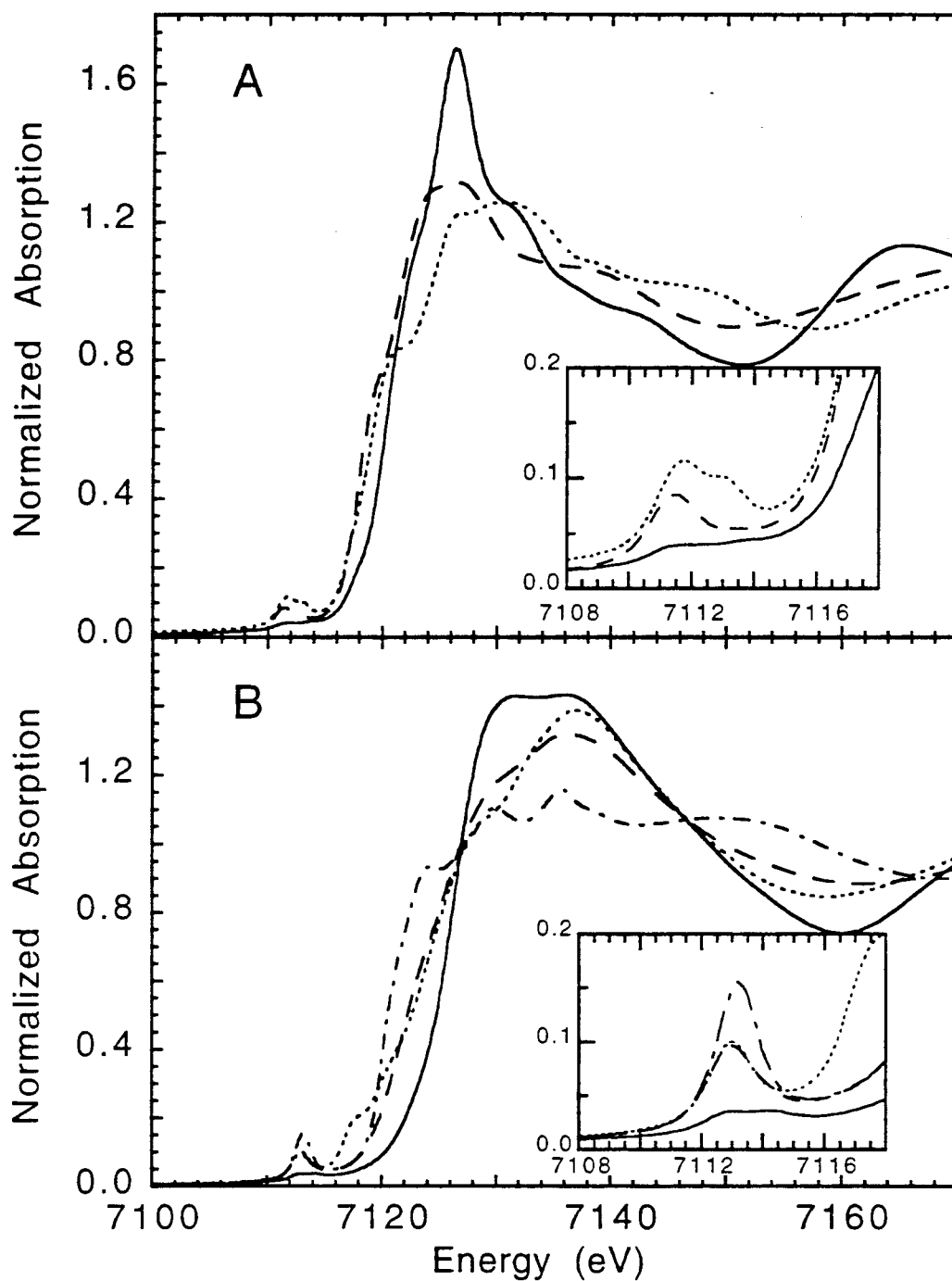


Figure 5.20. Fe K-edge XAS spectra of four-, five-, and six-coordinate ferrous model complexes are shown in part A: $\text{Fe}(\text{HB}(3,5\text{-}i\text{Pr}_2\text{pz})_3)\text{Cl}$ (····), $(\text{BF}_4)[\text{Fe}(\text{TMC})\text{Cl}]$ (---), and $[\text{Fe}(\text{imidazole})_6]\text{Cl}_2$ (—). XAS spectra of four-, five-, and six-coordinate ferric model complexes are shown in part B: $(\text{Et}_4\text{N})[\text{FeCl}_4]$ (—), $[\text{Fe}(\text{salen})\text{Cl}]$ (---), $(\text{AsPh}_4)[\text{Fe}(\text{N}_3)_5]$ (····), and $\text{Fe}(\text{acac})_3$ (—). The insets are expansions of the $1s \rightarrow 3d$ pre-edge region.

Table 5.9. XAS Pre-Edge Energies and Areas for PCD and Model Complexes.

sample	Fe		pre-edge		total
	oxid. state	CN ^a	energy (eV) ^b	area ^{b,c}	pre-edge area ^c
Fe(HB(3,5- <i>i</i> Pr ₂ pz) ₃)Cl	2+	4	7111.64 (0.02)	14.2 (0.5)	19.8 (0.9)
			7113.17 (0.02)	5.6 (0.9)	
(BF ₄)[Fe(TMC)Cl]	2+	5	7111.41 (0.01)	10.9 (0.1)	12.9(0.2)
			7113.43 (0.02)	2.0 (0.3)	
[Fe(imidazole) ₆]Cl ₂	2+	6	7111.24 (0.03)	1.6 (0.5)	3.8 (0.3)
			7112.35 (0.16)	1.6 (0.8)	
			7113.66 (0.02)	0.6 (0.2)	
Fe(II)PCD	2+	--	7111.81 (0.02)	5.7 (0.8)	8.8 (0.9)
			7113.43 (0.03)	3.0 (0.4)	
(Et ₄ N)[FeCl ₄]	3+	4	7113.16 (0.00)	20.7 (0.8)	20.7 (0.8)
Fe(salen)Cl	3+	5	7112.91 (0.01)	12.9 (0.3)	14.4 (0.6)
			7114.25 (0.07)	1.5 (0.4)	
(AsPh ₄)[Fe(N ₃) ₅]	3+	5	7112.94 (0.01)	11.7 (0.6)	11.7 (0.6)
Fe(acac) ₃	3+	6	7112.79 (0.02)	2.7 (0.3)	4.6 (0.3)
			7114.31 (0.04)	1.9 (0.1)	
Fe(III)PCD	3+	--	7113.35 (0.02)	16.4 (1.7)	16.4 (1.7)
Fe(III)PCA	3+	--	7113.27 (0.01)	20.3 (0.7)	20.3 (0.7)
FePCD-NO	--	--	7112.71 (0.04)	14.2 (2.0)	18.3 (2.8)
			7114.47 (0.08)	4.1 (1.6)	

^a CN = coordination number. ^b Pre-edge energies and areas were determined by fits to the data as described in the Experimental Section. ^c Pre-edge areas were calculated by multiplying the height of the fitted feature by the FWHM (the values reported were multiplied by 100).

area of 20.7 at 7113.2 eV. The two five-coordinate models, Fe(salen)Cl and (AsPh₄)[Fe(N₃)₅], have pre-edge features that are less intense with fitted areas of 14.4 and 11.7, respectively (Figure 5.20B and Table 5.9). The ferric six-coordinate complex, Fe(acac)₃, has two relatively weak features with a total fitted area of 4.6 and an intensity ratio of 3:2 (Figure 5.20B and Table 5.9). The main edge feature, attributed to the 1s→4p transition at ~7125 eV, is very narrow and intense for the Fe(II)PCD data (Figure 5.19). The main edge feature of Fe(III)PCD, Fe(III)PCA, and FePCD-NO all look similar with the onset of the edge at approximately 4 eV higher in energy than that of the respective ferrous protein with that of FePCD-NO being slightly lower in energy (Figure 5.19). The edge features of the ferrous and ferric model complexes differ significantly in shape (Figure 5.20) with the onset of the edge for the ferric complexes being ~4 eV higher in energy than that of the ferrous complexes.

The 1s→3d pre-edge feature can be used to probe the coordination number of the non-heme iron site in these various forms of PCD. The 1s→3d transition is formally electric dipole forbidden, but gains intensity through an allowed quadrupole transition and also by 4p mixing into the 3d states as a result of the noncentrosymmetric environment of the metal site. It has been shown for ferric and ferrous complexes that when the symmetry of the iron site is lowered, the pre-edge intensity increases due to an increase in the 3d-4p mixing.^{56,57}

As described in more detail in Chapter 4, the pre-edge splitting and intensity distribution is indicative of the site symmetry of the iron atom. When a high spin ferrous atom is in an octahedral site, three transitions are observed into ⁴T₁, ⁴T₂, and ⁴T₁ d⁽ⁿ⁺¹⁾ excited states (a transition into the ⁴A₂ state is not observed as it would involve a two electron transition). The transitions into these states are only quadrupole allowed as the iron is in a centrosymmetric site and therefore there is no 4p-3d mixing. Thus, one observes three weak peaks as can be seen in the [Fe(imidazole)₆]Cl₂ spectrum (Figure 5.20A) with the first two features being barely resolvable and centered at 7111.2 and 7112.4 eV and the third feature positioned at 7113.7 eV. Since the difference in energy between the lowest energy ⁴T₁ state and the ⁴T₂ state is about the same as the energy resolution at the Fe K-edge, occasionally only two pre-edge features are observed for high spin ferrous complexes with the first feature attributed to transitions into both the ⁴T₁ and the ⁴T₂ states and the second feature ~2 eV higher in energy attributed to a transition into the higher energy ⁴T₁ state.

When a high spin ferrous atom is in a square pyramidal site, the intensity of the lower energy feature increases dramatically since there is now 4p_z mixing into the 3d_{z²} orbital due to the loss of a center of inversion, as can be seen in the (BF₄)[Fe(TMC)Cl]

spectrum (dashed line in Figure 5.20A). When a high spin ferrous atom is in a tetrahedral site, there are two intense pre-edge features due to 4p mixing into the d_{xy} , d_{xz} , d_{yz} orbitals, with the lower energy feature being more intense than the higher energy feature, as can be seen in the $(\text{Fe}(\text{HB}(3,5\text{-}i\text{Pr}_2\text{pz})_3)\text{Cl})$ spectrum (dotted line in Figure 5.20A). See Chapter 4 for a more detailed analysis of the distribution of the dipole intensity in the $1s \rightarrow 3d$ pre-edge features of high spin ferrous complexes.

Empirically the pre-edge feature of $\text{Fe}(\text{II})\text{PCD}$ looks much more similar in shape and intensity to that of the six-coordinate ferrous complex and quite different from that of the four- and five-coordinate complexes (Figure 5.19 and 5.20A). The broad pre-edge feature of $\text{Fe}(\text{II})\text{PCD}$ can be fit with two peaks, with the lower energy peak having a wider FWHM than the higher energy peak (solid line in Figure 5.19). In addition, the area of the pre-edge feature centered at 7111.8 eV is twice as large as that of the feature centered at 7113.4 eV (Table 5.9), indicating that the first feature contains transitions into both the ${}^4\text{T}_1$ and the ${}^4\text{T}_2$ states while the second feature contains the transition into the higher energy ${}^4\text{T}_1$ state. The energies of the pre-edge peaks of $\text{Fe}(\text{II})\text{PCD}$ are consistent with those seen in octahedral high spin ferrous complexes (Table 4.1 in Chapter 4). The total fitted area of the pre-edge features is higher for $\text{Fe}(\text{II})\text{PCD}$ than for octahedral ferrous model complexes (Table 4.1 in Chapter 4), which can be attributed to an overall less symmetric iron site caused by mixed ligation and variation in bond lengths. Additional support of a six-coordinate iron site for $\text{Fe}(\text{II})\text{PCD}$ comes from the shape of the edge feature. The shape of the main edge feature in the $\text{Fe}(\text{II})\text{PCD}$ spectrum (solid line in Figure 5.19) is very similar to that in the six-coordinate $[\text{Fe}(\text{imidazole})_6]\text{Cl}_2$ spectrum (solid line in Figure 5.20A) and other octahedral high spin ferrous model complexes with oxygen and nitrogen ligation (Figure 4.2 in Chapter 4). The results from the pre-edge and edge analysis are consistent in indicating that $\text{Fe}(\text{II})\text{PCD}$ has a six-coordinate iron active site.

The intensity pattern and energy splitting of the pre-edge feature of high spin ferric iron are also indicative of the iron's site symmetry. When a high spin ferric atom is in an octahedral site, two pre-edge features are observed from transitions to ${}^5\text{T}_2$ and ${}^5\text{E}_{d^{(n+1)}}$ many-electron excited states. The transitions into these states are only quadrupole allowed as the iron is in a centrosymmetric site and therefore there is no 4p-3d mixing. Thus, one observes two weak features with an intensity ratio of 3:2 as can be seen in the $\text{Fe}(\text{acac})_3$ spectrum (solid line in Figure 5.20B). When a high spin ferric atom is in a five-coordinate site (either square pyramidal or trigonal bipyramidal), the intensity of the pre-edge feature increases dramatically due to 4p mixing into the 3d orbital due to the loss of a center of inversion, as can be seen in the $\text{Fe}(\text{salen})\text{Cl}$ and $(\text{AsPh}_4)[\text{Fe}(\text{N}_3)_5]$

spectra (dashed and dotted lines in Figure 5.20B). When a high spin ferric atom is in a tetrahedral site, there is a single very intense pre-edge feature due to 4p mixing into the d_{xy} , d_{xz} , d_{yz} orbitals, as can be seen in the $(Et_4N)[FeCl_4]$ spectrum shown in Figure 5.20B.

The pre-edge feature of Fe(III)PCD and Fe(III)PCA (dashed and dotted line, respectively, in Figure 5.19) can be fit with a single broad peak at ~ 7113.3 eV (Table 5.9). The fitted area of this feature, which is 16.4 for Fe(III)PCD and 20.3 for Fe(III)PCA, is more similar to that of the five-coordinate models, where Fe(salen)Cl and $(AsPh_4)[Fe(N_3)_5]$ have areas of 14.4 and 11.7, respectively, than to that of the six-coordinate model, Fe(acac)₃, which has an intensity of 4.6. The total pre-edge area of Fe(III)PCA is more similar to that of the four-coordinate model $(Et_4N)[FeCl_4]$ (Table 5.9), however, the shape of the pre-edge feature more closely resembles that of the five-coordinate models. Also, the fitted area of the pre-edge features for protein complexes is typically higher than that of model complexes, since the iron sites of the proteins are often more distorted than the iron sites in model complexes due to mixed ligation and varying bond distances. A further indication of the coordination number of the iron is the shape of the main edge feature. Fe(III)PCD and Fe(III)PCA have a main edge feature that is very similar to the five-coordinate ferric model complexes with a feature at ~ 7128 eV that is slightly lower in intensity than a feature at ~ 7135 eV (Figure 5.19 and 5.20B). In contrast, the features at 7128 and 7135 eV are of equal intensity in the six-coordinate octahedral complex (solid line in Figure 20B) and the four-coordinate complex has three features at approximately 7124, 7130, and 7136 eV (dashed-dotted line in Figure 20B). Thus, the pre-edge and edge features of both Fe(III)PCD and Fe(III)PCA indicate that the iron is in a five-coordinate site.

The pre-edge and edge features were used to probe the oxidation state of the iron in FePCD-NO. The pre-edge region of FePCD-NO was fit with an intense feature at 7112.7 eV and a weaker feature at 7114.5 eV. The energies of these peaks are much more similar to those of ferric complexes than ferrous complexes (Table 5.9), with the lower energy feature of ferrous complexes typically being below 7111.8 eV in energy (see Table 4.1 in Chapter 4). The pre-edge peak energies and areas for FePCD-NO is very similar to that of the ferric five-coordinate model complex, Fe(salen)Cl (Table 5.9). The rising edge of FePCD-NO lies between that of Fe(II)PCD and Fe(III)PCD in energy with the shape and intensity of the edge being much more similar to that of Fe(III)PCD (Figure 5.19). The differences in the edge spectra of Fe(II)PCD, Fe(III)PCD, and FePCD-NO are very similar to the differences observed in the spectra of Fe(II)EDTA, Fe(III)EDTA, and FeEDTA-NO (Figure 5.1). Previous studies on FeEDTA-NO and

other $S=3/2$ $\{\text{FeNO}\}^7$ complexes indicate that the iron in these systems is in the high spin ferric form and that there is significant charge donation from the NO^- to the ferric atom.⁵⁸ The pre-edge and edge features of FePCD-NO also indicate that the iron atom in FePCD-NO is in the high spin ferric state with the Fe^{3+} - NO^- bond being very covalent, as is evident by the fact that the FePCD-NO rising edge is at lower energy than the Fe(III)PCD rising edge.

The intensity of the $1s \rightarrow 3d$ pre-edge feature of FePCD-NO was used to determine the coordination environment of the iron site. As has been previously discussed the intensity of the $1s \rightarrow 3d$ pre-edge feature is sensitive to the coordination environment and geometry of the iron site. $\{\text{FeNO}\}^7$ complexes have been shown to have intense pre-edge features due to the distortion caused by the short Fe-N(O) bond.^{57,58} Additionally, the pre-edge feature has been shown to also be sensitive to the Fe-N-O angle in $\{\text{FeNO}\}^7$ complexes (section 5.2). Bending of the Fe-N-O unit increases the distortion around the iron site, thus, increasing the amount of 4p mixing into the 3d orbitals. The increase of $1s \rightarrow 3d$ pre-edge intensity upon bending of the Fe-N-O angle has been observed for $[\text{Fe}(\text{TMC})\text{NO}](\text{BF}_4)_2$ which has a total pre-edge intensity of 15.5 and Fe(salen)NO which has a total pre-edge intensity of 24.2 (Table 5.2) where the main difference in the iron site symmetry between $[\text{Fe}(\text{TMC})\text{NO}](\text{BF}_4)_2$ and Fe(salen)NO is a linear vs. bent Fe-N-O unit, respectively.^{59,60} The increase of 4p mixing into the 3d orbitals upon bending of the Fe-N-O unit has also been predicted by self consistent field- $X\alpha$ -scattered wave calculations.⁵⁸ Hence, an analysis of the intensity of the pre-edge feature for FePCD-NO allows for determination of the coordination number of the iron site as well as the mode of NO binding (linear vs. bent).

The fitted pre-edge area for FePCD-NO of 18.3 is much higher than that of FeEDTA-NO, a seven-coordinate $\{\text{FeNO}\}^7$ complex, which has a pre-edge area of 10.4 and $\text{Fe}(\text{Me}_3\text{TACN})(\text{NO})(\text{N}_3)_2$,⁶¹ a six-coordinate $\{\text{FeNO}\}^7$ complex, which has a pre-edge area of 10.8 (Table 5.2). In fact, the pre-edge area of FePCD-NO is in the range of the five-coordinate $\{\text{FeNO}\}^7$ complexes as $[\text{Fe}(\text{TMC})\text{NO}](\text{BF}_4)_2$ has a total pre-edge intensity of 15.5 and Fe(salen)NO has a total pre-edge intensity of 24.2 (Table 5.2). From a first-shell empirical EXAFS analysis of FePCD-NO (*vide infra*), the Fe-N(O) bond length in FePCD-NO is ~ 1.9 Å, substantially longer than the 1.74 and 1.78 Å Fe-N(O) bond lengths for $[\text{Fe}(\text{TMC})\text{NO}](\text{BF}_4)_2$ ⁶⁰ and Fe(salen)NO⁵⁹, respectively. The increase in the Fe-N(O) bond length in FePCD-NO should decrease the distortion around the iron site and thus the pre-edge intensity should be lower than that of a $\{\text{FeNO}\}^7$ model complexes of similar geometry and shorter Fe-N(O) bond length. Thus, it appears

that the FePCD-NO has a bent Fe-N-O unit where the pre-edge area of 18.3 is lower the value of 24.2 for Fe(salen)NO.

5.7.3.2. First-Shell Empirical EXAFS Analysis. Analysis of the EXAFS data for Fe(II)PCD, Fe(III)PCD, Fe(III)PCA, and FePCD-NO was pursued to obtain metrical information on the iron active site of each of these forms of the protein. The EXAFS spectra are shown in Figure 5.21. The EXAFS oscillations for Fe(II)PCD have a higher frequency than those for Fe(III)PCD (Figure 5.21), indicative of longer first-shell bond distances in the ferrous protein. The EXAFS data for Fe(III)PCD and Fe(III)PCA are similar in the low- k region, but differ in the higher k region. The EXAFS data for FePCD-NO are unique with respect to the other three forms of the protein.

The FTs of the EXAFS data taken over the k range of 3.5 - 14.5 \AA^{-1} are shown in Figure 5.22. The FTs of the EXAFS data for Fe(II)PCD and FePCD-NO are fairly similar, however, Fe(II)PCD has a feature at ~ 2.8 \AA that is nearly absent in the data for FePCD-NO (Figure 5.22). The FT of the EXAFS data for Fe(III)PCD has a very intense feature at ~ 1.5 \AA , while that for Fe(III)PCA has a split feature at this distance and has additional features at ~ 2.1 and 4.1 \AA . Curve-fitting was performed on filtered first-shell contributions over the k range 4 - 14 \AA^{-1} varying bond distances and coordination numbers (the FT backtransform windows are given in Table 5.10). Note that curve-fitting was also performed over the k range of 4 - 12 \AA^{-1} for all four of the protein samples. The results over the shorter k range were all very similar (all within the error of the technique) to the results over the k range of 4 - 14 \AA^{-1} that are presented in Table 5.10. In each of the four cases, the FT peak centered at ~ 1.8 \AA (non-phase shift corrected) could not be adequately fit with waves representing a single shell of oxygens or nitrogens (Fits 1, 4, 5, 6, and 9). These fits did not match the frequency of the data at higher k and gave unreasonably low coordination numbers. The F values were significantly reduced when a wave from a second oxygen or nitrogen contribution was included in the fit to the data. Since most non-heme iron active sites contain both oxygen and nitrogen ligation, fits were performed with two oxygen waves, an oxygen (shorter) and a nitrogen wave, an oxygen and a nitrogen (shorter) wave, and two nitrogen waves. All four types of fits gave similar results, since distinguishing between an oxygen and nitrogen wave from EXAFS data on proteins is inherently extremely difficult due to their strong similarity in backscattering properties and further exacerbated by the relatively low quality of the data. Only the fits with nitrogen signals are therefore reported in Table 5.10.

The EXAFS data of Fe(II)PCD were reasonably well fit with two nitrogen waves (Fit 2) having 1 N at 1.99 \AA and 3 N at 2.15 \AA with an F value of 0.37 (Table 5.10 and

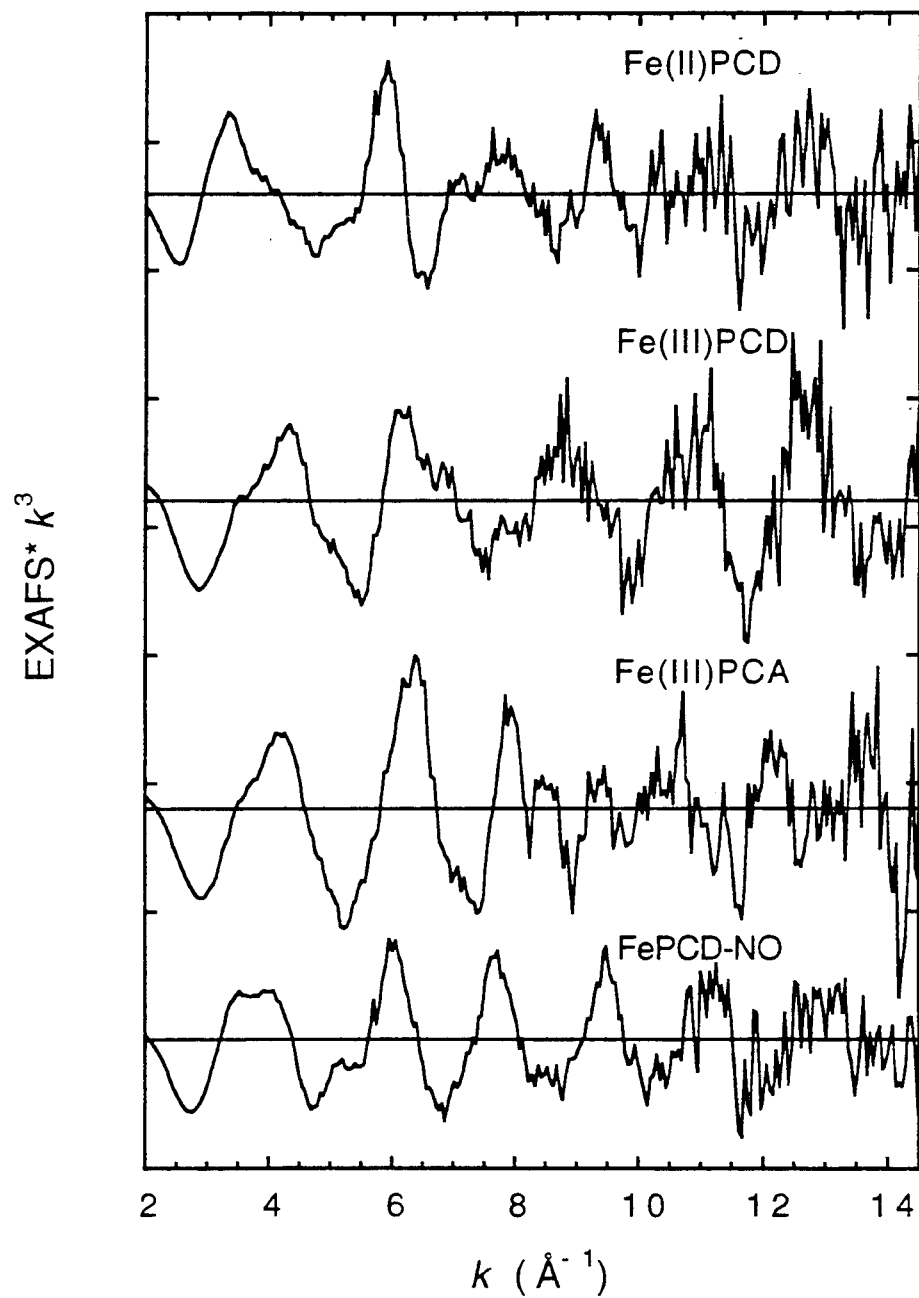


Figure 5.21. EXAFS data ($*k^3$) for Fe(II)PCD, Fe(III)PCD, Fe(III)PCA, and FePCD-NO (the ordinate scale is 5 between tick marks with solid horizontal lines indicating the zero point of each plot).

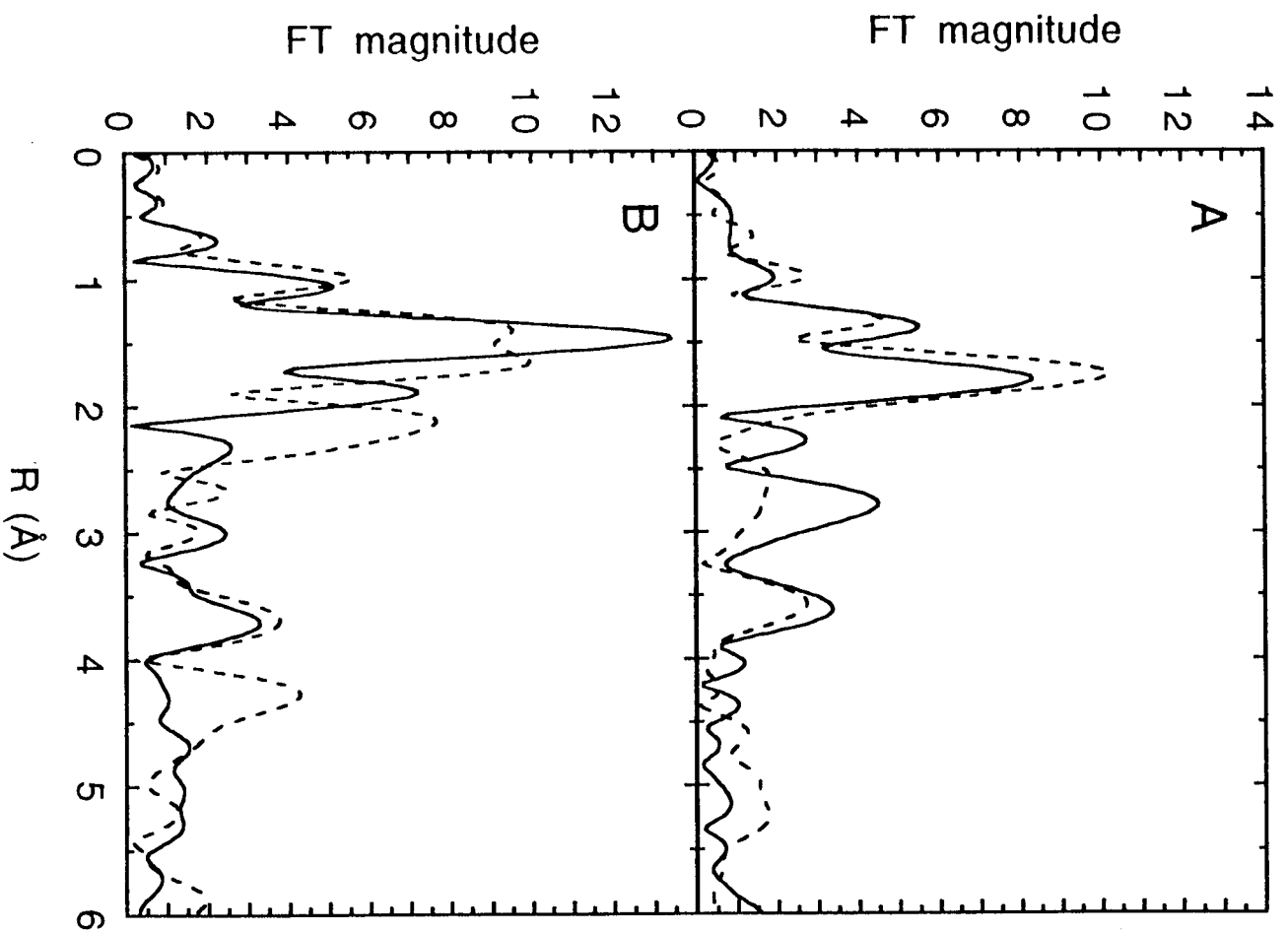


Figure 5.22. Fourier transforms over the k -range $3.5 - 14.5 \text{ \AA}^{-1}$ (non-phase shift corrected) for the EXAFS data of Fe(II)PCD (—) and FePCD-NO (---) (shown in part A) and Fe(III)PCD (—) and Fe(III)PCA (---) (shown in part B).

Table 5.10. Summary of EXAFS Curve-Fitting Results.*

sample	Fit #	FT window		CN ^{a,b}	bond length		<i>F</i>
		width (Å)	element		(Å) ^b		
Fe(II)PCD	1	[1.1-2.1]	N	2.3	2.14	0.56	
	2	[1.1-2.1]	N	1.0	1.99	0.37	
	3	[1.1-2.1]	N	3.1	2.15	0.31	
			N	1.5	1.98		
			N	4.1	2.15		
Fe(III)PCD	4	[0.88-2.15]	N	1.0	2.31	1.2	
	5	[0.88-2.15]	N	2.6	1.91		
	N	4.3	1.92	0.38			
Fe(III)PCA	6	[0.75-2.55]	N	3.1	2.12	1.4	
			N	2.7	2.00		
	7	[0.75-2.55]	N	3.7	1.97	1.2	
			N	2.5	2.11		
			N	3.0	1.97		0.80
FePCD-NO	9	[0.8-2.3]	N	1.8	2.10	0.58	
			O	2.2	2.47		
	10	[0.8-2.3]	N	2.8	2.12	0.33	
			N	1.1	1.94		
			N	3.7	2.12		
	11	[0.8-2.3]	N	1.1	1.91	0.31	
			N	1.9	2.07		
			N	2.6	2.14		
12	[0.8-2.3]	N	1.0	1.94	0.27		
		N	3.6	2.12			
		N	0.5	2.50			

* EXAFS data were fit over the k -range 4 -14 Å⁻¹. ^a CN = coordination number. ^b Errors in distances (± 0.02 Å) and coordination numbers ($\pm 25\%$) are estimated from the variance between EXAFS fitting results and values from models of crystallographically known structure.³⁹

Figure 5.23). However, this fit gave a total coordination number of four which is much lower than the value of six predicted by the edge analysis. The F value decreased to 0.31 when a third contribution of 1 N at 2.31 Å was added to the fit (Fit 3). This fit matches the data more accurately at higher k (Figure 5.23) and has a total coordination number of 6.6, which is more consistent with the edge data. Also, the average first-shell distance for Fit 3 of 2.14 Å is more consistent with six-coordination than the average first-shell distance for Fit 2 of 2.11 Å. Crystallographic determination of ferrous model complexes with oxygen and nitrogen ligation reports average bond lengths of 2.17 ± 0.03 Å for six-coordinate sites,⁶²⁻⁶⁸ 2.11 ± 0.02 Å for five-coordinate sites,^{69,70} and 2.00 ± 0.01 Å for four-coordinate sites.³³

The EXAFS data of Fe(III)PCD could not be simulated with a wave from a single shell of nitrogens (Fit 4, Table 5.10). Inclusion of a second nitrogen signal (Fit 5) decreased the F value by a factor of three (Table 5.10) and gave a fit that matched the EXAFS data extremely well (Fit 5, Figure 5.23). Fit 5 has 4.3 N at 1.92 Å and 3.1 N at 2.12 Å. The total coordination number of Fit 5 is 7.4 which is much higher than the coordination number of five predicted by the edge analysis. However, the two EXAFS waves from nitrogens at 1.92 Å and 2.12 Å are $\sim 180^\circ$ out-of-phase with one another in the k region where the signals are the strongest, 6 - 10 Å⁻¹. This causes high correlation and thus high uncertainty in the coordination numbers. The distances and the relative strengths of the two O/N waves obtained from these fits to the EXAFS data are consistent with a previous study¹³ which reported a best fit to the EXAFS data for Fe(III)PCD of 3 O/N at 1.90 Å and 2 O/N at 2.08 Å.

The EXAFS data of Fe(III)PCA could not be reproduced accurately with fits that contained only one (Fit 6) or two Fe-N waves (Fit 7). Fits 6 and 7 have F values of 1.4 and 1.2, respectively (Table 5.10). A fit that included signals from nitrogens at 1.97 and 2.10 Å and oxygens at 2.47 Å was necessary to simulate the EXAFS data in the higher k region (Fit 8, Figure 5.23). The addition of the longer oxygen distance in the fit is also justified by the fact that there is a feature in the FT at ~ 2.2 Å (non-phase shift corrected). Fit 8 has a total coordination number of seven, which is inconsistent with the pre-edge and edge analysis that indicates that the iron site is five-coordinate.

The EXAFS data of FePCD-NO could be simulated accurately with fits that contained either two or three Fe-N signals (Fit 10, 11, and 12 in Table 5.10 and Figure 5.23). The F values of Fits 10 and 11 are nearly identical (0.33 and 0.31, respectively). Both fits have a contribution from a single nitrogen at ~ 1.9 Å with another contribution of approximately four nitrogens at 2.1 Å. The only difference between Fits 10 and 11 is that the contribution at 2.1 Å is split into two contributions in Fit 11. Fit 12 contains an

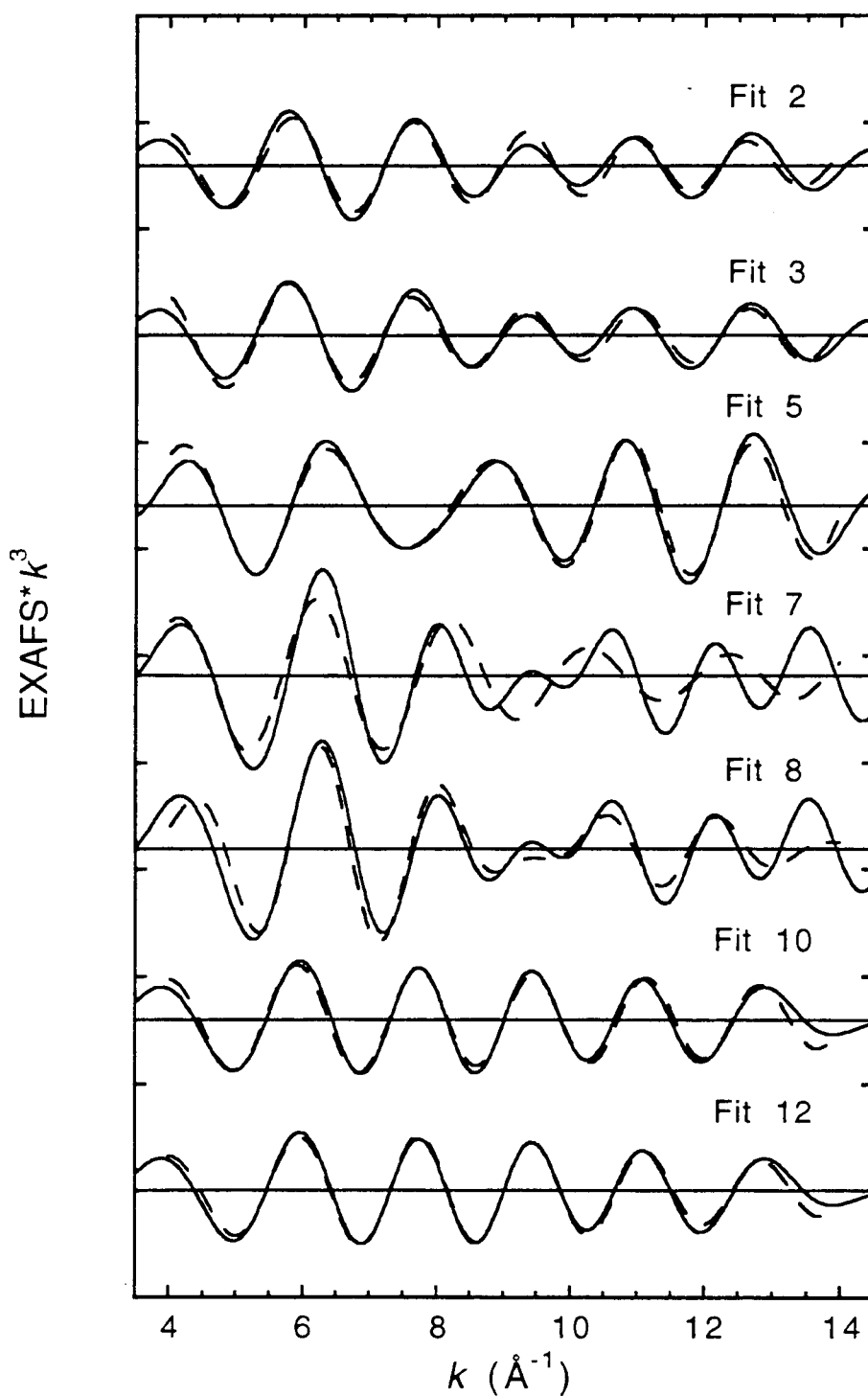


Figure 5.23. Fits to the Fourier filtered data of Fe(II)PCD (Fit 2 and 3), Fe(III)PCD (Fit 5), Fe(III)PCA (Fit 7 and 8), and FePCD-NO (Fit 10 and 12), where the solid line represents the backtransformed data while the dashed line is the fit to the data. (The ordinate scale is 5 between tick marks with solid horizontal lines indicating the zero point of each plot).

additional contribution from a N at ~ 2.5 Å. The contribution from an O/N at 2.5 Å is questionable as the F value only decreases slightly to 0.27 when this contribution is added and the match to the experimental data is only slightly better (Figure 5.23). The short 1.9 Å distance can be assigned as the Fe-N(O) bond with this distance being longer than the typical Fe-N(O) distance of ~ 1.75 Å reported for {FeNO}⁷ model complexes⁵⁹⁻⁶¹ and isopenicillin N synthase-substrate-NO.⁷¹ The presence of a shorter Fe-N interaction was further examined by fixing a Fe-N distance at 1.75 Å with a coordination number of 1, while varying the distances and coordination numbers of the other two N contributions. Including the shorter Fe-N distance at 1.75 Å increased the F value to 0.6 indicating that there is no contribution from a shorter Fe-N distance.

5.7.3.3. Fe-N-O Angle Determination Using GNXAS. The GNXAS approach was used to fit the experimental EXAFS data of Fe(III)PCD and FePCD-NO in order to investigate the Fe-N-O angle in FePCD-NO. GNXAS requires an initial structural model. Since the crystal structure of Fe(III)PCD is known, the EXAFS data of Fe(III)PCD were fit using the GNXAS approach to determine the accuracy of the technique for studying the active site of this protein. The GNXAS approach was then used to fit the EXAFS data of FePCD-NO to gain information on the Fe-N-O angle.

Crystal structures of Fe(III)PCD from *Psuedomonas aeruginosa*^{5,6} and *Brevibacterium fuscum*⁷ both show that the iron atom is coordinate axially by a Tyr and His with a Tyr, His, and water-based molecule bound in the equatorial plane. Crystallographic coordinates from the *Psuedomonas aeruginosa* structure at 2.15 Å⁶ were used as input to build the initial structural model. EXAFS contributions for each two-atom and three-atom configuration were calculated using the crystallographic bond distances and angles. The individual contributions were then summed to generate a theoretical EXAFS spectrum which was then fit to the non-Fourier-filtered experimental EXAFS data without prior background subtraction. In the fits the crystallographic bond distances and angles were allowed to vary to fit the experimental EXAFS data unless stated otherwise.

Due to the complexity of the structure, contributions to the fits of the Fe(III)PCD EXAFS data were systematically introduced. The first-shell fit contained waves from the following two-atom configurations: Fe-O(H) [1], Fe-O(Tyr) [2], and Fe-N(His) [2], where the number in brackets indicates the coordination number. This first-shell fit (not shown) gave an R value of 0.286×10^{-5} with good agreement between the FT of the experimental data and the theoretical signal up to 2.0 Å (corresponding to ~ 2.4 Å in the cluster when the phase shift is taken into account). The major contributions in the EXAFS signal were accounted for using the three first-shell distances with especially

good agreement at higher k . The next fit included signals from three-body configurations: Fe-O2-C4 [2], Fe-N1-C7 [2], and Fe-N1-C6 [2] (with the atom designations shown in Figure 5.24A and B). The R value decreased only slightly to 0.222×10^{-5} when these three signals from the second-shell carbon atoms were included. The four Fe-N1-C6/C7 contributions could not be summed together as the His ligand is bound in such a way that the Fe-N1-C6 angle is $\sim 140^\circ$ while the Fe-N1-C7 angle is $\sim 110^\circ$ in the crystal structure. Fits that included signals from third and fourth shells were then performed to investigate the dominant multiple-scattering pathways. There were approximately 35 unique three-atom configurations which ranged in distance from 3.0 to 4.5 Å. The seven main contributions were from Fe-O2-C4, Fe-N1-C7, Fe-N1-C6, Fe-O2-C3, Fe-C7-N2, Fe-N1-N2, and Fe-N1-C8 (with the atom designations shown in Figure 5.24A and B).

The best fit to the data was obtained when the last seven contributions were included with the three Fe-O/N first-shell contributions. This fit had an R value of 0.178×10^{-5} . A comparison of the theoretical EXAFS spectrum to the experimental data (along with the individual EXAFS signal from each contribution) is presented in Figure 5.24C for this fit to the Fe(III)PCD data with the FTs shown in Figure 5.25. A comparison of the bond distances and angles obtained from the GNXAS fit to the crystallographic values is given in Table 5.11. The low-frequency EXAFS is dominated by the three waves from the first-shell contributions. The Fe-O distances obtained from the GNXAS fit show excellent agreement with the crystallographic values for Fe(III)PCD⁶ with the Fe-O1 (H) distance being 1.92 Å (vs. the crystallographic value of 1.91 Å) and the average of the two Fe-O2 (Tyr) distances being 1.88 Å, which is within the crystallographic range of 1.80 - 1.90 Å. The Fe-N1 (His) distance obtained from the GNXAS fit to the data is 2.14 Å which is ~ 0.15 Å shorter than the crystallographic value. The experimental EXAFS data could not be reproduced with an Fe-N1 (His) distance of ~ 2.29 Å. The shorter Fe-N1 (His) distance obtained from the GNXAS fit is consistent with the value obtained from the first-shell empirical fits to the EXAFS data of Fe(III)PCD in this study (see Fit 5 in Table 5.10 and Figure 5.23) and in the study by True *et. al.*¹³

The EXAFS data of Fe(III)PCD was fit reasonably well including signals from the three two-atom configurations and the seven main three-body configurations (Figure 5.24C and 5.25). The bond distances and angles obtained from this fit were all within 10% of the crystallographic values (Table 5.11). However, the frequency distribution of the signals from the three-body configurations does not match the data particularly well in the 2 - 4 Å region of the FT (Figure 5.25A). The match to the data was significantly

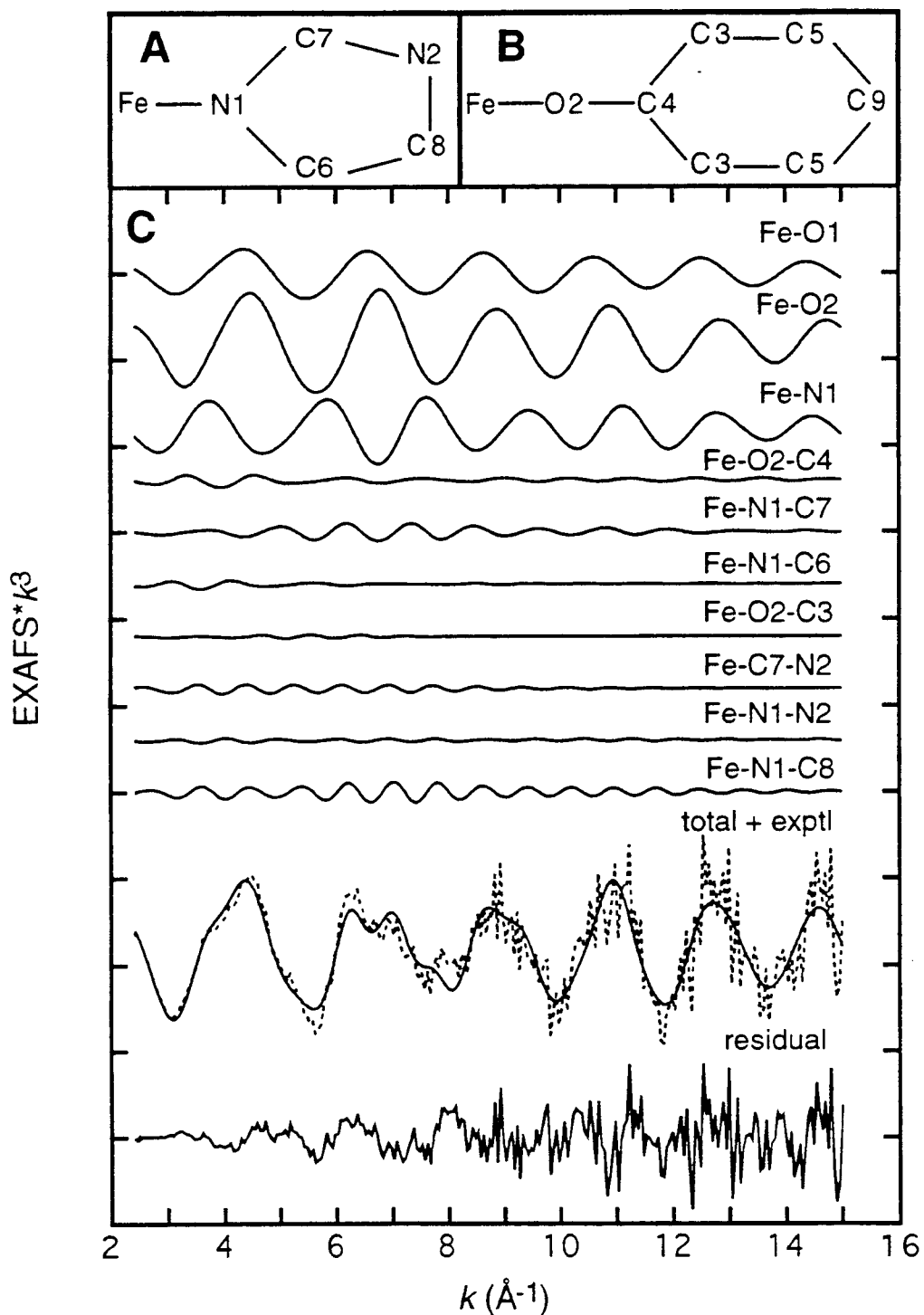


Figure 5.24. Atom designations for the A) Fe-His and the B) Fe-Tyr subunits. C) EXAFS signals for individual contributions in the best fit for the Fe(III)PCD data. The total signal (—) is also shown and compared with the experimental data (····) with the residual being the difference between the experimental EXAFS and the theoretical EXAFS. (The ordinate scale is 5 between two consecutive tick marks.)

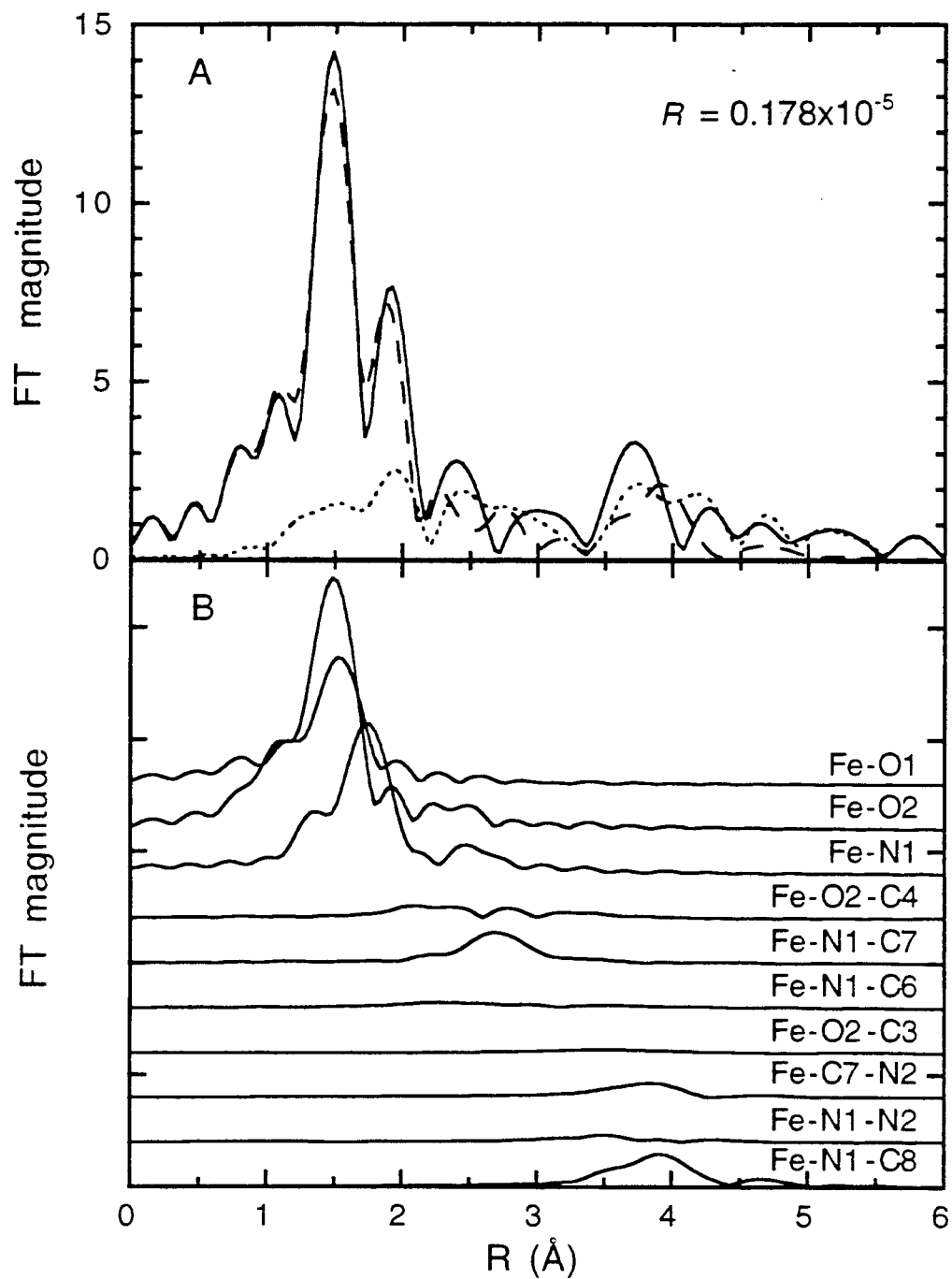


Figure 5.25. A) A comparison of the theoretical (---) and experimental (—) non-phase shift corrected FT of Fe(III)PCD EXAFS data, along with the FT of the EXAFS residual (⋯). The R value is an indication of the goodness of the fit. B) FT of the EXAFS signals of Fe(III)PCD for the individual contributions shown in Figure 5.24C. This display is a useful way to determine which signals contribute in which regions. (The ordinate scale is 5 between two consecutive tick marks.)

Table 5.11. Crystallographic Bond Distances and Angles Compared to GNXAS Results for Fe(III)PCD.

structural feature ^a (CN ^b)	GNXAS		crystallographic values [range]
	distance/ angle	bond variance (σ_R^2)/ angle variance (σ_θ^2) ^c	
Fe-O1 (H) (1)	1.92 Å	0.002	1.91 Å
Fe-O2 (Tyr) (2)	1.88 Å	0.002	1.85 Å [1.80-1.90]
Fe-N (His) (2)	2.14 Å	0.002	2.29 Å [2.26-2.33]
O2-C4 (2)	1.30 Å	0.003	1.37 Å [1.36-1.38]
N1-C7 (2)	1.37 Å	0.004	1.32 Å [1.31-1.32]
N1-C6 (2)	1.32 Å	0.006	1.37 Å [1.36-1.38]
O2-C3 (4)	2.45 Å	0.007	2.4 Å [2.35-2.42]
C7-N2 (2)	1.32 Å	0.004	1.31 Å [1.30-1.31]
Fe-C7 (2)	3.14 Å	0.007	3.01 Å [2.97-3.05]
N1-N2 (2)	2.11 Å	0.004	2.13 Å [2.11-2.14]
N1-C8 (2)	2.25 Å	0.004	2.18 Å [2.16-2.20]
Fe-O2-C4 (1)	139°	3×10^1	138° [130-145]
Fe-N1-C7 (2)	119°	5×10^0	110° [1.09-110]
Fe-N1-C6 (2)	136°	6×10^1	141° [140-142]
Fe-O2-C3 (2)	130°	9×10^1	132° [111-166]
Fe-C7-N2 (2)	154°	5×10^0	154° [153-155]
Fe-N1-N2 (2)	146°	3×10^0	146° [145-146]
Fe-N1-C8 (2)	176°	5×10^0	177° [176-178]

^a Atom designation are shown in Figure 5.24. ^b CN = number of configurations in the complex. ^c Bond and angle variances are reported in Å² and degrees², respectively.

worse when the bond angles and distances were fixed to crystallographic values. Numerous fits were tried including signals from other three-body configurations with none of the fits having a good match to the data in the FT range of 2 - 4 Å. The inability to match the signals from second-, third-, and fourth-shell atoms is most likely due to the number of and the complexity of the multiple-scattering pathways. As mentioned earlier there were 35 unique three-body configurations in the range of 3.0 to 4.5 Å. Since all the atoms surrounding the iron site are low Z (O, N, and C), the signals are weak and there is no dominant signal. In addition, this fit is slightly underdetermined with 40 fitting parameters compared with 38 independent points, where the number of independent points was calculated by the expression $N_I = (2\delta k \delta R/\pi) + 2$.⁷² It is difficult to say whether the mismatch in the FT region between the experimental data and the theoretical signal is due to an inaccuracy in the bond distances and angles of the initial structural model as it was derived from the crystal structure determined at a resolution of 2.15 Å or from the fact that there are so many unique multiple-scattering pathways all contributing very weak signals, or both.

The GNXAS approach was then applied to the EXAFS data of FePCD-NO using the theoretical signals that were generated from the Fe(III)PCD crystallographic bond distances and angles. Since the structure of FePCD-NO is unknown, the EXAFS data was fit with signals from differing first-shell two-body configurations to develop an understanding of the first coordination sphere of the iron atom. The data could not be reproduced well with a single contribution of oxygen or nitrogen ligands. A fit (not shown) with 5 O at 2.06 Å had an R value of 0.826×10^{-5} . The match to the experimental data improved significantly when a second Fe-O wave was included with the R value decreasing by almost a factor of four to 0.246×10^{-5} . This fit included signals from a single O at 1.85 Å and four O at 2.05 Å. These distances are similar to those observed in the first-shell empirical fit to the FePCD-NO EXAFS data (see Fit 10 in Table 5.10 and Figure 5.23). Yet, there was still a mismatch between the data and the theoretical signal in the FT at 2 Å (corresponding to ~2.4 Å in the cluster). Thus, a third first-shell contribution was included. The best first-shell fit to the data had an R value of 0.134×10^{-5} and included signals from one O at 1.89 Å, four N at 2.11 Å, and one N at 2.45 Å (see Figure 5.26 and Table 5.12). Fits to the data were also tried where the distance of the short Fe-O contribution was fixed to 1.85, 1.80 and 1.75 Å. In each of these cases the R values increased with the greatest increase for the shortest distance and there was not a good match between the experimental and theoretical signal. The distance of the longer Fe-N contribution was also fixed to shorter values. Again the R values increased with the greatest increase for the shortest distance and there was not a

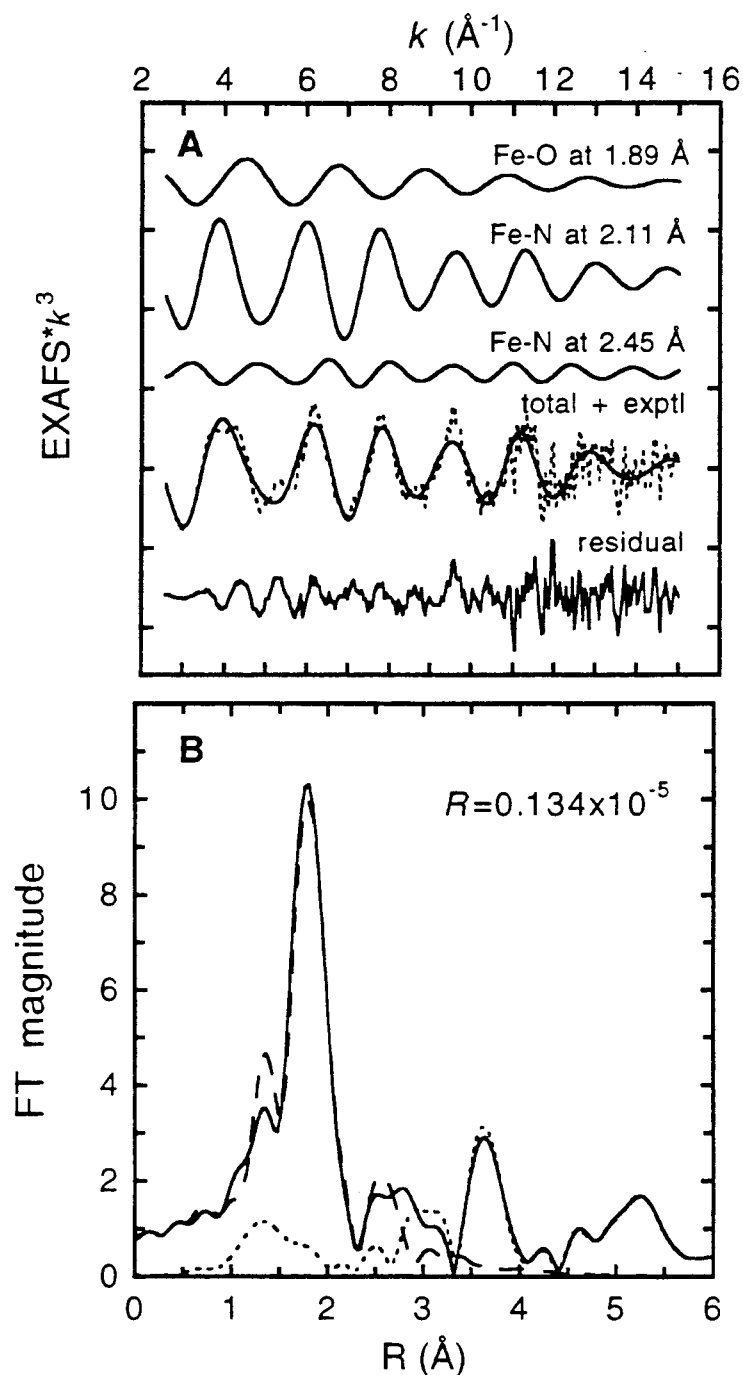


Figure 5.26. Comparison of the theoretical and experimental signals of the k^3 -weighted EXAFS data and the FT of the best two-body fit for FePCD-NO. Part A contains the individual EXAFS contributions where the total signal (—) is also shown and compared with the experimental data (---). The residual is the difference between the experimental and theoretical EXAFS. (The ordinate scale is 5 between consecutive tick marks.) B) The non-phase-shift-corrected FT of the EXAFS data of the experimental data (—) and that of the total theoretical signal (----). Also shown is the FT of the residual (.....).

Table 5.12. GNXAS Results for FePCD-NO.

Fit	structural feature (CN ^a)	GNXAS distance/ angle	GNXAS	
			bond variance (σ_R^2)/ angle variance (σ_θ^2) ^b	R value
best fit with only first-shell signals	Fe-O (1)	1.89 Å	0.005	0.134x10 ⁻⁵
	Fe-N _s (4)	2.11 Å	0.005	
	Fe-N _l (1)	2.45 Å	0.002	
best fit with three- body signals included	Fe-O (1)	1.89 Å	0.005	0.120x10 ⁻⁵
	Fe-N _s (4)	2.11 Å	0.005	
	Fe-N _l (1)	2.45 Å	0.002	
	N _s -C (4)	1.32 Å	0.004	
	N _l -C (1)	1.37 Å	0.003	
	Fe-N _s -C (4)	125°	1 × 10 ²	
	Fe-N _l -C (1)	145°	6 × 10 ¹	

^a CN = number of configurations in the complex. ^b Bond and angle variances are reported in Å² and degrees², respectively.

good match between the experimental and theoretical signal. Note that an Fe-O signal was used to mimic the Fe-N(O) signal as the shortest Fe-ligand distance in the Fe(III)PCD structure was an Fe-O distance.

To investigate the Fe-N-O bond angle, the distances and σ^2 values of the three first-shell contributions were kept fixed to those values obtained from the best first-shell fit (Table 5.12 and Figure 5.26) while the Fe-N-O angle was varied. The sensitivity of the fit to the Fe-N-O angle was tested by calculating a theoretical EXAFS spectrum with Fe-N-O angles ranging from 90° to 180°. The signal for the Fe-N-O unit was generated from a {FeNO}⁷ model complex, Fe(TACN)(N₃)₂NO (where TACN = *N,N',N''*-trimethyl-1,4,7-triazacyclononane).⁷³ A plot of the log(*R* value) vs. Fe-N-O angle is shown in Figure 5.27A where a minimum in this type of plot is indicative of a better fit to the experimental EXAFS data. The *R* value drops drastically as the Fe-N-O angle is decreased from 180° to 155° and then increases slightly as the angle is lowered to 135°. The *R* value is fairly constant between 140° and 100° and then increases as the Fe-N-O angle is lowered to 90°. A comparison of the FTs of the experimental data and calculated spectra at 180°, 155°, and 140° are presented in Figure 5.28 where the *R* value was largest at 180°, lowest at 155°, and had leveled off by 140°. The FT of the calculated spectrum with the Fe-N-O angle equal to 180° does not match the FT of the experimental EXAFS data at ~2.5 Å (Figure 5.28A) which is the region where the signal from the Fe-N-O multiple-scattering appears.⁷³ The Fe-N-O signal is very strong when the angle is 180° due to the intervening atom focusing effect.⁷³ The Fe-N-O signal has decreased significantly when the angle is at 155° matching the experimental data more accurately (Figure 5.28B). When the Fe-N-O angle is below ~150°, the signal from the Fe-N-O unit is relatively weak.⁷³ Thus, there is not much variation in the match to the experimental data for Fe-N-O angles between 100° and 145° as is indicated by the similar *R* values (Figure 5.27A). The *R* value increases when the Fe-N-O angle is below 100° as the single-scattering signal from the Fe-O of the Fe-N-O unit increases (Figure 5.27A).

The signal from the Fe-N-O configuration was the only three-body contribution that was taken into account in the calculated spectra above. In reality there will also be signals from second-shell carbon atoms in the FT range of ~2.3 - 3 Å. Accordingly, the FePCD-NO data was fit with the three first-shell contributions, Fe-O at 1.89 Å, Fe-N at 2.11 Å (Fe-Ns), and Fe-N at 2.45 Å (Fe-NI), and two second-shell contributions, Fe-Ns-C and Fe-NI-C. The best fit to the FePCD-NO data that included the Fe-N-C contributions had an *R* value of 0.120x10⁻⁵ with the resulting bond distances and angles shown in Table 5.12. The signals (not shown) from the Fe-N-C configurations were very weak as was also observed for the Fe-O-C and Fe-N-C signals for Fe(III)PCD (Figure 5.24C).

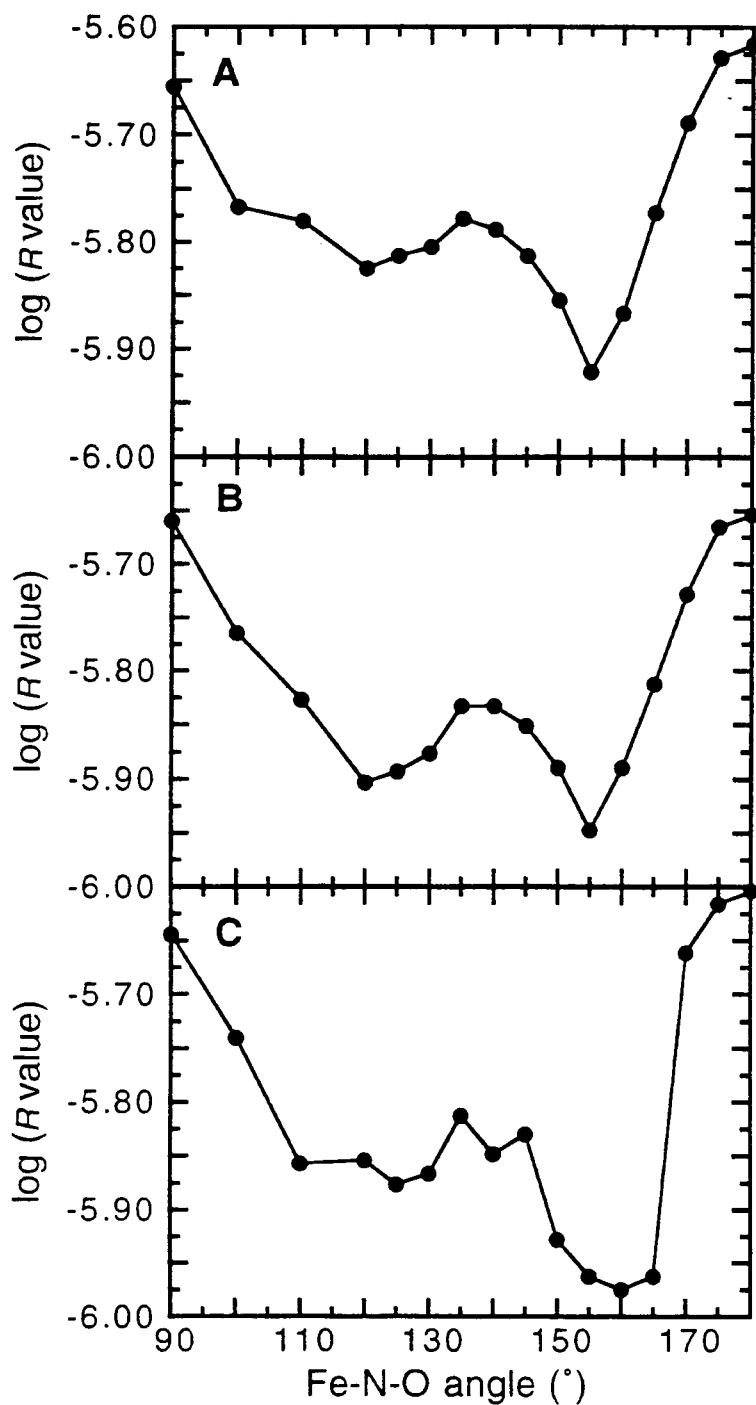


Figure 5.27. Plots of the $\log(R \text{ value})$ vs Fe-N-O angle of FePCD-NO where each point represents a match of the calculated EXAFS spectrum to the data. The lower the R value the better the fit. Plot A contains calculated spectra that included only first-shell contributions and an Fe-N-O contribution while Fe-N-C contributions were included in the spectra of plots B and C with all the Fe-N-C parameters fixed for the calculated spectra in plot B and varied for those in plot C.

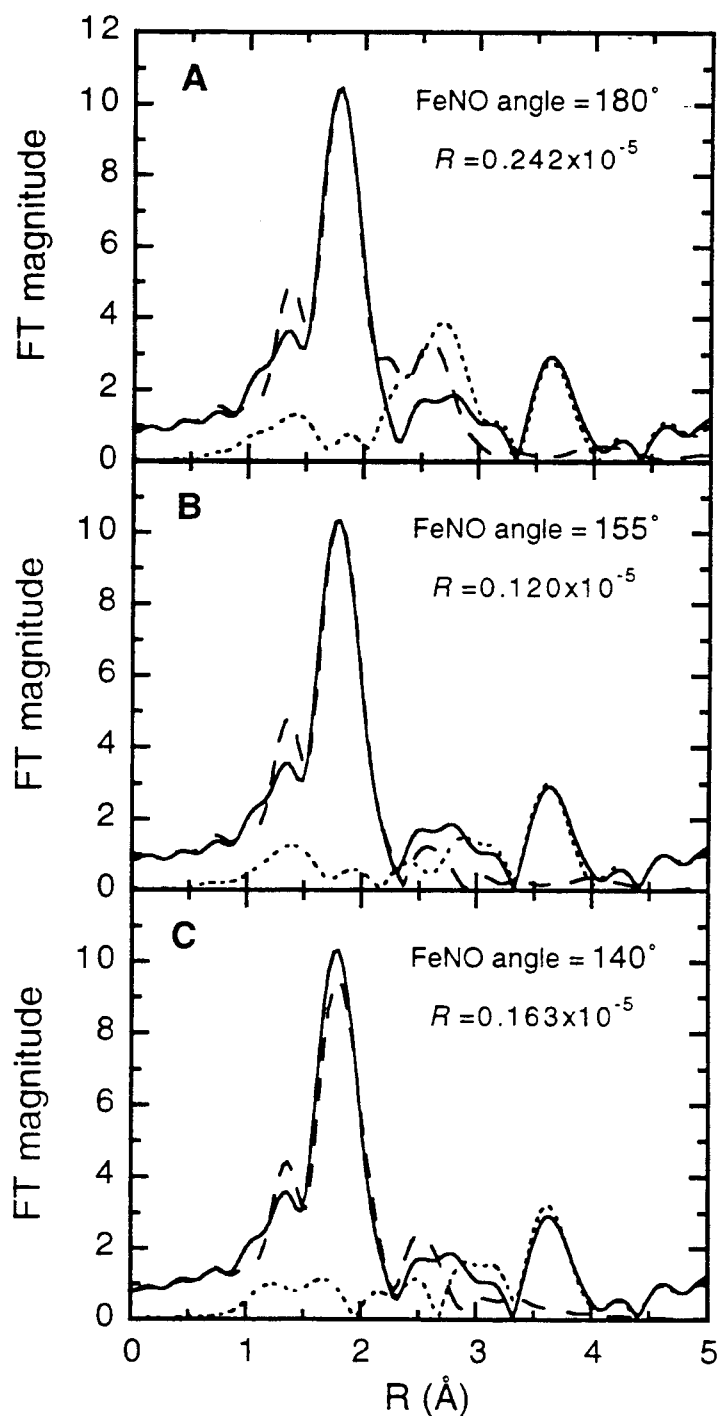


Figure 5.28. A comparison of the theoretical (---) and experimental (—) non-phase shift corrected FT of FePCD-NO EXAFS data, along with the FT of the EXAFS residual (····). The R value is an indication of the goodness of the fit. Calculated spectra for several different Fe-N-O bond angles are shown: A) 180°, B) 155°, and C) 140°. The calculated spectra included the three first-shell contributions and an Fe-N-O contribution.

The sensitivity of this fit to the Fe-N-O angle was tested by fixing all the distances, angles, and variances to the values shown in Table 5.12 and calculating a theoretical EXAFS spectrum with Fe-N-O angles ranging from 90° to 180°. A plot of the log(*R* value) vs. Fe-N-O angle is shown in Figure 5.27B. The *R* value decreases substantially in lowering the Fe-N-O angle from 180° to 155°, rises slightly upon lowering the angle further to 140°, decreases slightly upon lowering the angle further to 120°, and then increases upon lowering the angle to 90°. A comparison of the FTs for the calculated spectra and experimental data are shown for Fe-N-O angles of 180°, 155°, and 140° in Figure 5.29. Again, the FT of the calculated spectrum with the Fe-N-O angle equal to 180° does not match the FT of the experimental EXAFS data at ~2.5 Å due to the strength of the signal from a linear Fe-N-O unit. Once the Fe-N-O angle decreases below ~160°, the signal weakens and the calculated spectra match the experimental data more accurately. The plot of the log(*R* value) vs. Fe-N-O angle shows a double minimum. This double minimum has been observed before for {FeNO}⁷ model complexes⁷³ where the minimum at lower angles is due to the single-scattering (Fe-O) signal having a phase and amplitude that matches the experimental data and the minimum at higher angles is due to the multiple-scattering (Fe-N-O) signal having a phase and amplitude that matches the data.

Since FePCD-NO is not structurally defined, one may be biasing the results by fixing the distances, angles, and variances as was done in the previous set of calculated spectra with varying Fe-N-O angle. Thus, spectra were also calculated for a range of Fe-N-O angles over 90° to 180° allowing the distances, angles, and variances of the Fe-Ns-C and Fe-Nl-C configurations to vary. A plot of the log(*R* value) vs. Fe-N-O angle for the calculated spectra is shown in Figure 5.27C. The *R* value drops dramatically on going from an Fe-N-O angle of 180° to 165° with there being a minimum between 165° and 150°. The *R* value increases slightly when the Fe-N-O angle is decreased from 150° to 145°, is approximately constant for Fe-N-O angles between 145° and 110°, and then increases upon decreasing the Fe-N-O angle from 110° to 90°. A comparison of the FTs for the calculated spectra and experimental data are shown for Fe-N-O angles of 180°, 155°, and 140° in Figure 5.30. Again, the FT of the calculated spectrum with the Fe-N-O angle equal to 180° does not match the FT of the experimental EXAFS data at ~2.5 Å due to the strength of the signal from a linear Fe-N-O unit. In general, the plot of log(*R* value) vs. Fe-N-O angle between the calculated spectra where the Fe-N-C parameters were kept fixed vs. allowed to vary are similar. The one striking difference is the precipitous drop in the *R* value when the Fe-N-O angle is decreased from 170° to 165° in the set of fits where the Fe-N-C parameters were allowed to vary. Comparison of the

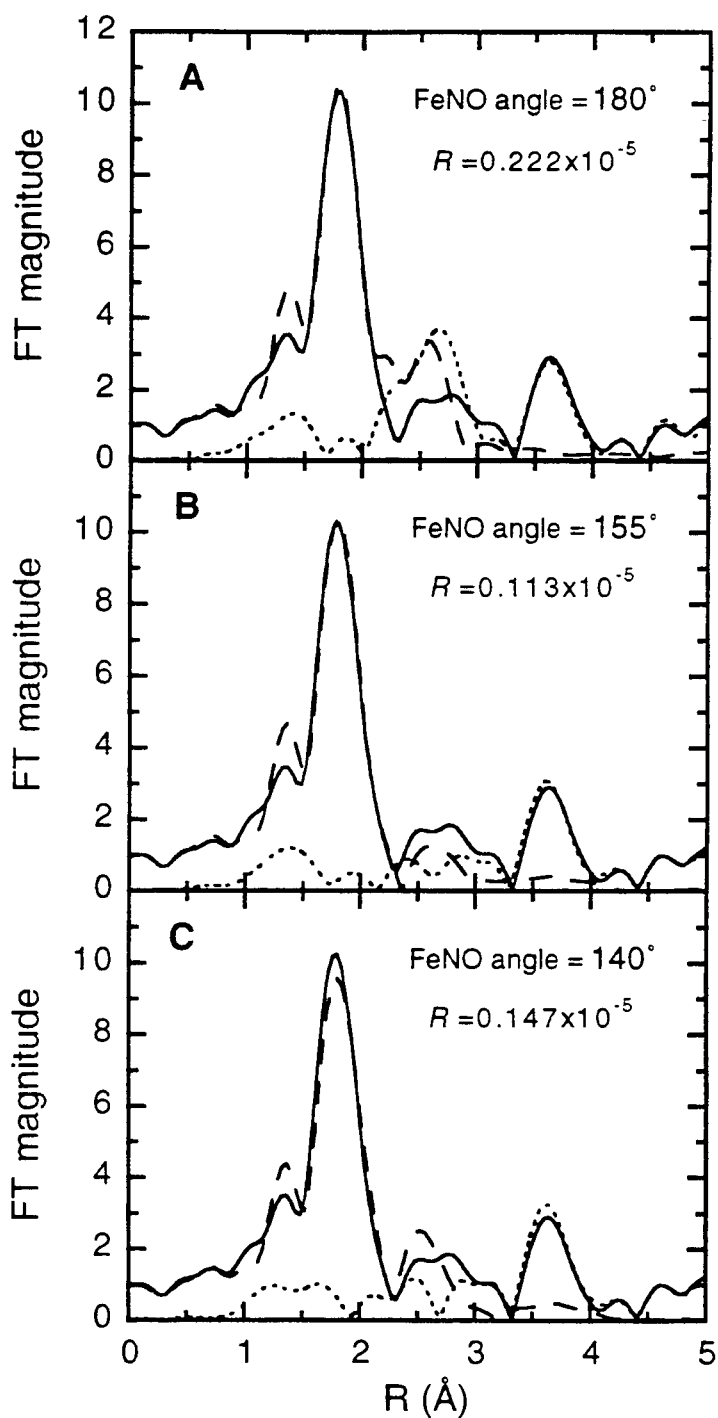


Figure 5.29. Comparison of the theoretical (---) and experimental (—) non-phase shift corrected FT of FePCD-NO EXAFS data, along with the FT of the EXAFS residual (.....). The R value is an indication of the goodness of the fit. Calculated spectra for several different Fe-N-O bond angles are shown: A) 180° , B) 155° , and C) 140° . The calculated spectra included the three first-shell, two Fe-N-C (fixed), and an Fe-N-O contributions.

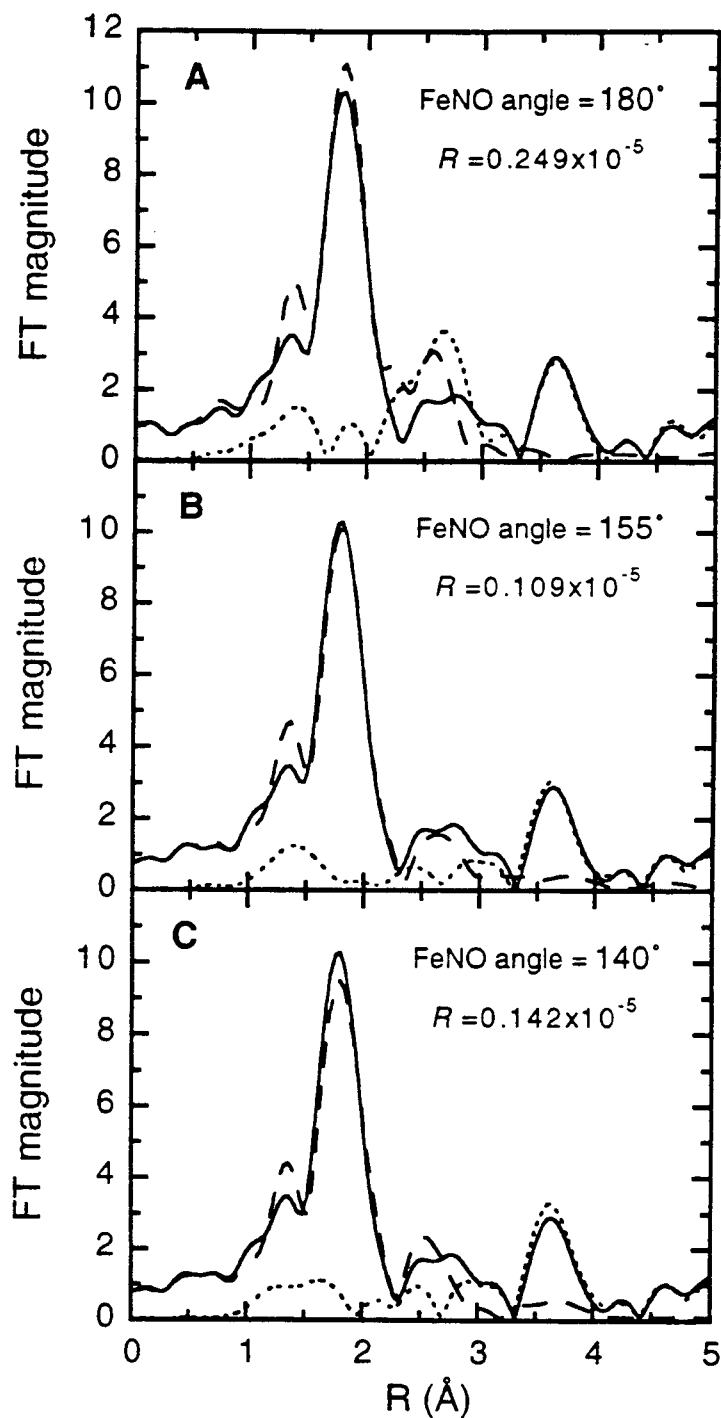


Figure 5.30. Comparison of the theoretical (---) and experimental (—) non-phase shift corrected FT of FePCD-NO EXAFS data, along with the FT of the EXAFS residual (····). The R value is an indication of the goodness of the fit. Calculated spectra for several different Fe-N-O bond angles are shown: A) 180°, B) 155°, and C) 140°. The calculated spectra included the three first-shell, two Fe-N-C (varied), and an Fe-N-O contributions.

individual EXAFS signals for the calculated spectra that had Fe-N-O angles of 165° shows that in the latter set of fits the signal from the Fe-Ns-C configuration has increased dramatically where the strongest portion of the signal is exactly out-of-phase with the strongest portion of the Fe-N-O signal (Figure 5.31). The angle variance of the Fe-Ns-C configuration dropped from 100 (see Table 5.12) down to 1 when the Fe-N-O was fixed to 165° and the Fe-N-C parameters were allowed to vary. An angle variance of 1 for four different Fe-Ns-C angles is physically unreasonable as all four of the Fe-Ns-C angles would have to be identical.

In summary, the signal in the FT of the FePCD-NO EXAFS data at ~ 2.5 Å is very weak. The lack of signal in this region either implies that the Fe-N-O unit is bent or that there is a strong interference effect between the Fe-N-O signal and other Fe-O-C and Fe-N-C signals. Since all the Fe-O-C and Fe-N-C signals in Fe(III)PCD EXAFS data were relatively weak, it is not expected that they would be strong in the data of FePCD-NO. Thus, the FePCD-NO unit appears to be bent. An examination of the minimum in the $\log(R$ value) vs. Fe-N-O angle plots for the three types of fits studied indicates that the Fe-N-O angle is between 110° and 160°. These plots look very similar to those of {FeNO}⁷ model complexes with bent Fe-N-O units and unlike that of a complex with a linear Fe-N-O unit.⁷³ The $\log(R$ value) vs. Fe-N-O angle plot for a complex with a linear Fe-N-O unit shows a minimum at 180° with the R value increasing dramatically as the Fe-N-O angle is lowered from 180° to 150°.

5.7.4. Discussion

The analysis of the XAS pre-edge and edge features of Fe(II)PCD indicate that the iron site is six-coordinate. In addition, the fits to the EXAFS data of Fe(II)PCD show that the iron active site has 5 ± 1 O/N ligation with an average first-shell distance of 2.14 Å which is consistent with a six-coordinate iron site. MCD results for Fe(II)PCD also indicate that the iron site is six-coordinate.⁷⁴ The iron active site of Fe(III)PCD and Fe(III)PCA appear to be five-coordinate as the pre-edge and edge features are similar to those of high spin ferric five-coordinate model complexes. The results are consistent with the crystal structure of Fe(III)PCD from *Pseudomonas aeruginosa* show that the iron active site to be trigonal bipyramidal with tyrosine and histidine residues bound axially and a tyrosine, histidine and water-based molecule bound in the equatorial plane.^{5,6} An analysis of the EXAFS data for Fe(III)PCD shows O/N ligands at 1.92 Å and 2.12 Å. These results agree well with a previous study which reported a best fit to the EXAFS data for Fe(III)PCD of 3 O/N at 1.90 Å and 2 O/N at 2.08 Å and attributed

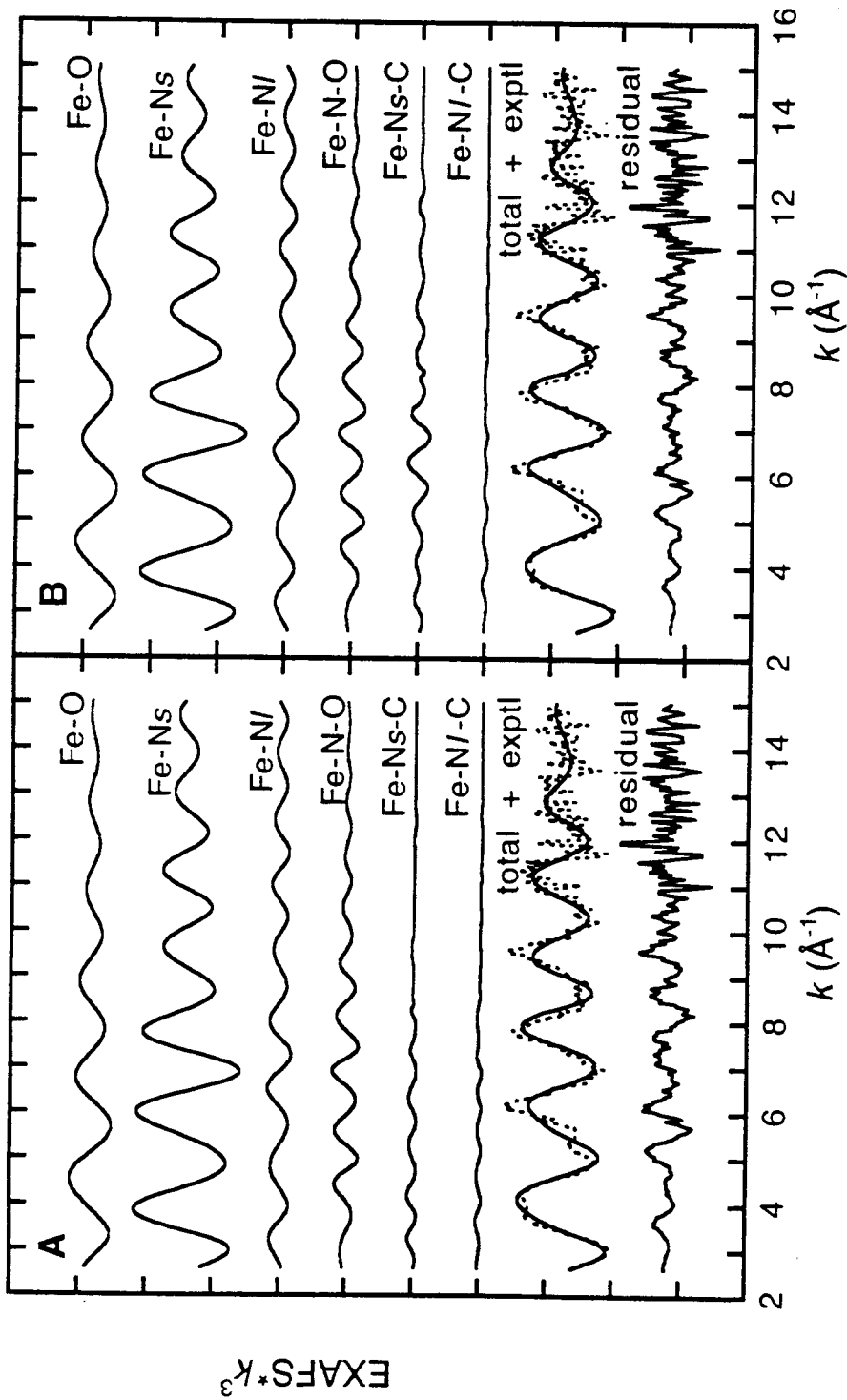


Figure 5.31. EXAFS signals for individual contributions in the GNXAS fits to the FePCD-NO data where the Fe-N-O angle was fixed to 165°. The total signal (—) is also shown and compared with the experimental data (···) with the residual being the difference between the experimental EXAFS and the theoretical EXAFS. (The ordinate scale is 5 between two consecutive tick marks.) Part A contains a fit where the distances, angles, and σ^2 values of both Fe-N-C configurations were kept fixed. Part B contains a fit where those values were allowed to vary. Note the difference in the strength of the Fe-N_s-C contribution in part A vs. B.

the shorter distance to the bound tyrosine and hydroxide ligands and the longer distance to the two histidine ligands.¹³ Thus, the coordination number increases from 5 to 6 upon reduction of the iron site. Addition of an electron may decrease the ability of the Tyr→Fe charge transfer which lengthens the Fe-Tyr bond as is evident by the longer first shell distances observed for Fe(II)PCD. This relaxation of the ligand sphere allows for an additional ligand.

The EXAFS data of Fe(III)PCA could not be fit well without a longer O/N contribution at 2.47 Å in addition to contributions from O/N at 1.97 and 2.10 Å. A fit to the EXAFS data of Fe(III)PCA that includes all three contributions gives a first-shell coordination number of seven which is much higher than value of five indicated by the pre-edge and analysis. The discrepancy in the coordination number between the edge and EXAFS analysis can either be explained by the fact that there are three Fe-O/N EXAFS waves beating against one another causing high correlation and thus high uncertainty in the total coordination number or that the O/N contribution at ~2.5 Å does not effect the local site symmetry of the iron which is probed in the edge and pre-edge region.

A previous EXAFS study examined the binding of terephthalate, a competitive inhibitor, and homoprotocatechuate, a slow substrate, to Fe(III)PCD.¹³ The study showed that when the inhibitor, terephthalate, was bound to Fe(III)PCD the pre-edge feature indicated that the iron site is six-coordinate and the EXAFS data showed a beat pattern which could only be simulated with a long Fe-O/N interaction at 2.46 Å. True *et. al.* suggested that the oxygens of the carboxylate group in terephthalate displaced the hydroxide ligand and chelated to the ferric site, but in an asymmetric fashion. In contrast, a pre-edge analysis of homoprotocatechuate bound to Fe(III)PCD showed the iron site to remain five-coordinate.¹³ There is strong evidence that substrate binds to Fe(III)PCD in a bidentate manner.^{8,75,76} If the coordination number of Fe(III)PCD bound to homoprotocatechuate is five, then the homoprotocatechuate must displace not only the hydroxide but also one of the endogenous protein ligands. True *et. al.* favor substrate displacing the axially histidine ligand, but do not rule out the possibility that the axially tyrosine may be displaced instead. In the present study, the pre-edge feature of Fe(III)PCA also indicates that the iron is five-coordinate. In addition, a long Fe-O/N interaction at 2.46 Å was needed to simulate the EXAFS data (this contribution is readily visible in the FT of Fe(III)PCA at ~2.2 Å (dashed line in Figure 5.22B)). If substrate binds in a bidentate fashion, either it is bound asymmetrically, in which case the long Fe-O/N contribution could be attributed to an oxygen from the substrate, or symmetrically, in which case the long Fe-O/N contribution could be attributed to an oxygen or a nitrogen from the displaced tyrosine or histidine, respectively. A detailed

study of the multiple-scattering pathways in the various binding modes of the substrate may aid in the interpretation of the EXAFS data; however, the signal-to-noise level is too low in the higher k region of the EXAFS data for Fe(III)PCA for such an analysis to be meaningful. Further study is warranted to distinguish between the various binding modes of the substrate.

The differences observed in the Fe(II)PCD, Fe(III)PCD, and FePCD-NO edge spectra are very similar to those in the Fe(II)EDTA, Fe(III)EDTA, and FeEDTA-NO edge spectra.⁵⁸ FePCD-NO has a rising edge position that lies in between that of Fe(II)PCD and Fe(III)PCD with the shape and intensity of the FePCD-NO edge being much more similar to that of Fe(III)PCD indicating that the iron in Fe(III)PCD is in the ferric oxidation state. The rising edge of FePCD-NO is at lower energy than that of Fe(III)PCD due to the highly covalent nature of the Fe(III)-NO⁻ bond.⁵⁸ An analysis of the pre-edge intensity for FePCD-NO predicts that the iron site is five-coordinate with a bent Fe-N-O unit. FePCD-NO having a bent Fe-N-O unit is also supported by the GNXAS analysis of the EXAFS data for FePCD-NO. There is not a strong signal in the FT of the EXAFS data at 2.5 Å which would be evident if the Fe-N-O unit were linear and the multiple-scattering of the Fe-N-O unit was enhanced due to the focusing effect.⁷³ The plot of the log(R value) vs. Fe-N-O angle of the EXAFS data for FePCD-NO is extremely similar to that for the EXAFS data of Fe(TACN)(N₃)₂NO, where Fe(TACN)(N₃)₂NO has an Fe-N-O angle of 156°. ⁷³ Resonance Raman data and self-consistent field-X α -scattered wave calculations have shown that a bent Fe-N-O unit is stabilized by the in-plane bonding interaction of the NO⁻ π^* orbital with the iron d orbital.⁵⁸

The EXAFS data of FePCD-NO were fit well with 1 O/N at 1.89 Å, 4 O/N at 2.11 Å, and 1 O/N at 2.45 Å. The shorter distance is attributed to the Fe-N(O) bond distance. An Fe-N(O) distance of 1.89 Å is much longer than previously observed Fe-N(O) distances for {FeNO}⁷ model complexes⁵⁹⁻⁶¹ and for isopenicillin N synthase-substrate-NO⁷¹ which have Fe-N(O) distances of ~1.75 Å. The nature of the longer Fe-N(O) bond in FePCD-NO needs to be further investigated keeping in mind that tyrosinate \rightarrow Fe(III) charge donation may limit the ability of NO⁻ to donate electron density to the ferric site, thereby weakening the Fe-N(O) interaction. Further, the N-O bond of FePCD-NO should be weaker than that observed for {FeNO}⁷ model complexes as the N-O bond is strengthened in these complexes due to the NO⁻ \rightarrow Fe(III) charge donation through the 4 σ^+ orbital which is antibonding with respect to the N-O bond.⁵⁸

It has been shown that an XAS edge and EXAFS analysis can provide valuable information on the electronic and geometric structure of the iron active site. Further XAS

studies on FePCA-NO and the ferrous and ferric forms of the extradiol dioxygenases, as well as the enzyme-NO, enzyme-substrate, and enzyme-substrate-NO forms can be used to understand the differences of the catalytic mechanisms of the intra- vs. extradiol dioxygenases.

5.7.5. Acknowledgments

PCD was provided by Prof. John Lipscomb's laboratory at the University of Minnesota. Jeff Zaleski prepared and characterized the four forms of the protein in this study. This research was supported by grants from the NIH (GM40392, E. I. Solomon) and NSF (CHE-9423181, K. O. Hodgson). The Stanford Synchrotron Radiation Laboratory is supported by the Department of Energy, Office of Basic Energy Sciences, Divisions of Chemical Science and Materials Science, and in part by the National Institutes of Health, National Center of Research Resources, Biomedical Research Technology Program (RR-01209, K. O. Hodgson) and the DOE's Office of Health and Environmental Research.

5.7.6. References and Notes

- (1) *Microbial Degradation of Organic Molecules*; Gibson, D. T., Ed.; Marcel Decker: New York, 1984.
- (2) Harayama, S.; Kok, M.; Neidle, E. L. *Annu. Rev. Microbiol.* **1992**, *46*, 565.
- (3) Que, L., Jr. In *Iron Carriers and Iron Proteins*; Loehr, T. M., Ed.; VCH: New York, 1989; p 467.
- (4) Lipscomb, J. D.; Orville, A. M. *Metal Ions Biol. Sys.* **1992**, *28*, 243.
- (5) Ohlendorf, D. H.; Lipscomb, J. D.; Weber, P. C. *Nature* **1988**, *336*, 403.
- (6) Ohlendorf, D. H.; Orville, A. M.; Lipscomb, J. D. *J. Mol. Biol.* **1994**, *244*, 586.
- (7) Earhart, C. A.; Radhakrishnan, R.; Orville, A. M.; Lipscomb, J. D.; Ohlendorf, D. H. *J. Mol. Biol.* **1994**, *236*, 374.
- (8) Pyrz, J. W.; Roe, A. L.; Stern, L. J.; Que, L., Jr. *J. Am. Chem. Soc.* **1985**, *107*, 614.
- (9) Que, L., Jr.; Heistand, R. H., II; Mayer, R.; Roe, A. L. *Biochemistry* **1980**, *19*, 2258.
- (10) Que, L., Jr.; Epstein, R. M. *Biochemistry* **1981**, *20*, 2545.
- (11) Felton, R. H.; Barrow, W. L.; May, S. W.; Sowell, A. L.; Goel, S.; Bunker, G.; Stern, E. A. *J. Am. Chem. Soc.* **1982**, *104*, 6132.

- (12) Whittaker, J. W.; Lipscomb, J. D. *J. Biol. Chem.* **1984**, *259*, 4487.
- (13) True, A. E.; Orville, A. M.; Pearce, L. L.; Lipscomb, J. D.; Que, L., Jr. *Biochemistry* **1990**, *29*, 10847.
- (14) Han, S.; Eltis, L. D.; Timmis, K. N.; Muchmore, S. W.; Bolin, J. T. *Science* **1995**, in press.
- (15) Mabrouk, P. A.; Orville, A. M.; Lipscomb, J. D.; Solomon, E. I. *J. Am. Chem. Soc.* **1991**, *113*, 4053.
- (16) Fujisawa, H.; Uyeda, M.; Kojima, Y.; Nozaki, M.; Hayaishi, O. *J. Biol. Chem.* **1972**, *247*, 4414.
- (17) Nozaki, M. In *Molecular Mechanisms of Oxygen Activation*; Hayaishi, O., Ed.; Academic Press: New York, 1974; p 405.
- (18) Que, L., Jr.; Lipscomb, J. D.; Zimmerman, R.; Münck, E.; Orme-Johnson, N. R.; Orme-Johnson, W. H. *Biochim. Biophys. Acta* **1976**, *452*, 320.
- (19) Whittaker, J. W.; Lipscomb, J. D.; Kent, T. A.; Münck, E. *J. Biol. Chem.* **1984**, *259*, 4466.
- (20) Bull, C.; Ballou, D. P.; Otsuka, S. *J. Biol. Chem.* **1981**, *256*, 12681.
- (21) Walsh, T.; Ballou, D. P.; Mayer, R.; Que, L., Jr. *J. Biol. Chem.* **1983**, *258*, 14422.
- (22) Arciero, D. M.; Lipscomb, J. D.; Huynh, B. H.; Kent, T. A.; Münck, E. *J. Biol. Chem.* **1983**, *258*, 14981.
- (23) Tatsuno, Y.; Saeki, Y.; Nozaki, M.; Otsuka, S.; Maeda, Y. *FEBS Lett.* **1980**, *112*, 83.
- (24) Orville, A. M.; Lipscomb, J. D. *J. Biol. Chem.* **1993**, *268*, 8596.
- (25) Arciero, D. M.; Orville, A. M.; Lipscomb, J. D. *J. Biol. Chem.* **1985**, *260*, 14035.
- (26) Arciero, D. M.; Lipscomb, J. D. *J. Biol. Chem.* **1986**, *260*, 2170.
- (27) Whittaker, J. W.; Orville, A. M.; Lipscomb, J. D. *Methods Enzymol.* **1990**, *188*, 82.
- (28) Scott, R. A.; Hahn, J. E.; Doniach, S.; Freeman, H. C.; Hodgson, K. O. *J. Am. Chem. Soc.* **1982**, *104*, 5364.
- (29) Lytle, F. W. In *Applications of Synchrotron Radiation*; Winick, H.; Xiam, D.; Ye, M.-h.; Huang, T., Eds.; Gordon and Breach Science Publishers: New York, 1989; p 135.
- (30) Cramer, S. P.; Tench, O.; Yochum, M.; George, G. N. *Nucl. Instrum. Methods Phys. Rev.* **1988**, *A266*, 586.
- (31) George, G. N.; Pickering, I., to be published.
- (32) Abbreviations used: HB(3,5-*i*Pr₂pz)₃ = hydrotris(3,5-diisopropyl-1-pyrazolyl)borate; TMC = tetramethylcyclam; salen =

N,N'-ethylenebis(salicylideneiminato); acac = acetylacetonate; TACN = *N,N',N''*-trimethyl-1,4,7-triazacyclononane.

- (33) Kitajima, N. private communication.
- (34) Hodges, K. D.; Wollman, R. G.; Barfield, E. K.; Hendrickson, D. N. *Inorg. Chem.* **1977**, *16*, 2746.
- (35) Burbridge, C. D.; Goodgame, D. M. L. *Inorg. Chim. Acta* **1970**, *4*, 231.
- (36) Gerloch, M.; Mabbs, F. E. *J. Chem. Soc. (A)* **1967**, 1598.
- (37) Drummond, J.; Woods, J. S. *Chem. Commun.* **1969**, 1373.
- (38) Kistenmacher, T. J.; Stucky, G.D. *Inorg. Chem.* **1968**, *7*, 2150.
- (39) Cramer, S. P.; Hodgson, K. O.; Stiefel, E. I.; Newton, W. E. *J. Am. Chem. Soc.* **1978**, *100*, 2748.
- (40) Cramer, S. P.; Hodgson, K. O. *Prog. Inorg. Chem.* **1979**, *15*, 1.
- (41) Scott, R. A. *Methods Enzymol.* **1985**, *117*, 414.
- (42) Iball, J.; Morgan, C. H. *Acta Crystallogr.* **1967**, *23*, 239.
- (43) Roof, R. B. J. *Acta Crystallogr.* **1956**, *9*, 781.
- (44) Johansson, L. *Chem. Scr.* **1976**, *9*, 30.
- (45) Johansson, L.; Molund, M.; Oskarsson, Å. *Inorg. Chim. Acta.* **1978**, *31*, 117.
- (46) Filipponi, A.; Di Cicco, A.; Tyson, T. A.; Natoli, C. R. *Solid State Commun.* **1991**, *78*, 265.
- (47) Filipponi, A.; Di Cicco, A. *Synchrotron Radiation News* **1992**, *6*, 13.
- (48) Westre, T. E.; Di Cicco, A.; Filipponi, A.; Natoli, C. R.; Hedman, B.; Solomon, E. I.; Hodgson, K. O. *J. Am. Chem. Soc.* **1995**, *117*, 1566.
- (49) Mattheiss, L. F. *Phys. Rev.* **1964**, *134*, A970.
- (50) Hedin, L.; Lundqvist, S. *Solid State Phys.* **1969**, *23*, 1.
- (51) Krause, M. O.; Oliver, J. H. *J. Phys. Chem. Ref. Data* **1979**, *8*, 329.
- (52) The principal determining factor for E_T is the monochromator and associated vertical slit opening, with the resolution determined by the relationship $\Delta E/E = \cot(\Theta)\Delta\Theta$, where Θ is a function of the Darwin width and the vertical angular acceptance of the monochromator. The value at the Fe K-edge for the experimental conditions used for these experiments were ~1.4 eV (see ref 29).
- (53) Agarwal, B. K. *X-ray Spectroscopy*; Springer-Verlag: New York, 1979; p 276.
- (54) Lytle, F. W.; Gregor, R. B.; Sandstrom, D. R.; Marques, E. C.; Wong, J.; Spiro, C. L.; Huffman, G. P.; Huggins, F. E. *Nucl. Instrum. Methods* **1984**, *226*, 542.
- (55) Tyson, T. A.; Roe, A. L.; Frank, P.; Hodgson, K. O.; Hedman, B. *Phys. Rev. B* **1989**, *39A*, 6305.